

ELECTROCHEMICAL CONCENTRATION MEASUREMENTS  
FOR MULTIANALYTE MIXTURES IN SIMULATED  
ELECTROREFINER SALT

by

Devin Spencer Rappleye

A dissertation submitted to the faculty of  
The University of Utah  
in partial fulfillment of the requirements for the degree of

Doctor of Philosophy

Department of Metallurgical Engineering

The University of Utah

August 2016

Copyright © Devin Spencer Rappleye 2016

All Rights Reserved

# The University of Utah Graduate School

## STATEMENT OF DISSERTATION APPROVAL

The dissertation of Devin Spencer Rappleye  
has been approved by the following supervisory committee members:

<u>Michael F. Simpson</u>	, Chair	<u>01/05/2016</u> Date Approved
<u>Hong Yong Sohn</u>	, Member	<u>01/05/2016</u> Date Approved
<u>Michael L. Free</u>	, Member	<u>01/05/2016</u> Date Approved
<u>Henry S. White</u>	, Member	<u>01/05/2016</u> Date Approved
<u>Azaree T. Lintereur</u>	, Member	<u>01/05/2016</u> Date Approved

and by Manoranjan Misra, Chair/Dean of  
the Department/College/School of Metallurgical Engineering

and by David B. Kieda, Dean of The Graduate School.

## ABSTRACT

The development of electroanalytical techniques in multianalyte molten salt mixtures, such as those found in used nuclear fuel electrorefiners, would enable in situ, real-time concentration measurements. Such measurements are beneficial for process monitoring, optimization and control, as well as for international safeguards and nuclear material accountancy. Electroanalytical work in molten salts has been limited to single-analyte mixtures with a few exceptions. This work builds upon the knowledge of molten salt electrochemistry by performing electrochemical measurements on molten eutectic LiCl-KCl salt mixture containing two analytes, developing techniques for quantitatively analyzing the measured signals even with an additional signal from another analyte, correlating signals to concentration and identifying improvements in experimental and analytical methodologies.

Five binary-analyte mixtures are studied with varying degrees of signal overlap; two mixtures are simulated and three are experimentally investigated. The two simulated mixtures are:  $\text{UCl}_3\text{-PuCl}_3\text{-LiCl-KCl}$  and  $\text{UCl}_3\text{-ThCl}_4\text{-LiCl-KCl}$ . The simulated data demonstrates the capabilities of multivariate analysis in determining concentration, even when electrochemical signals almost completely overlap. The three experimentally measured mixtures are:  $\text{GdCl}_3\text{-LaCl}_3\text{-LiCl-KCl}$ ,  $\text{LaCl}_3\text{-ThCl}_4\text{-LiCl-KCl}$ , and  $\text{UCl}_3\text{-MgCl}_2\text{-LiCl-KCl}$ . In all three mixtures signals were able to be separated, analyzed and correlated strongly with concentration. Standard apparent potentials and diffusion

coefficients are also determined for each analyte in the mixtures from measured data. Multivariate analysis was applied to the experimental data, as well, and is particularly valuable at higher degrees of signal overlap.

The experimental setup included both stationary and rotating electrodes. A rotating cylinder electrode (RCE) was designed and developed for high-temperature molten salt studies. The RCE was used to perform hydrodynamic electrochemical measurements in  $\text{UCl}_3\text{-MgCl}_2\text{-LiCl-KCl}$  mixtures. No similar studies have been found in the literature. Necessary improvements in experimental methods are also identified, specifically measurement of electrode area and development of a stable reference electrode. These improvements will reduce experimental error and improve the accuracy of the concentrations determined from electrochemical measurements.

To my wife, Joslyn, for her patience and support

"...love challenges, be intrigued by mistakes, enjoy effort and keep on learning."

-Carol S. Dweck, 2006, *Mindset: The New Psychology of Success*

## TABLE OF CONTENTS

ABSTRACT.....	iii
NOMENCLATURE .....	x
ABBREVIATIONS .....	xiii
ACKNOWLEDGEMENTS.....	xvi
1. INTRODUCTION .....	1
1.1. Motivation.....	2
1.2. Pyroprocessing Description.....	6
1.3. Pyroprocessing Safeguards.....	10
1.4. Electrochemical Studies.....	18
1.5. Summary .....	26
1.6. Dissertation Structure .....	29
2. ELECTROCHEMISTRY .....	31
2.1. General Overview .....	32
2.2. Thermodynamics .....	33
2.3. Reaction Kinetics.....	35
2.4. Mass Transport .....	38
2.5. Electroanalytical Methods .....	40
2.6. Summary .....	60
3. EXPERIMENTAL METHODS.....	63
3.1. General Equipment and Design.....	64
3.2. Test Matrices.....	69
3.3. Electrochemical Cell Design .....	70
3.4. Experimental Methods.....	75
3.5. Electrochemistry Test Procedures .....	83
3.6. Summary .....	87
4. COMPUTATIONAL WORK.....	88
4.1. ERAD.....	89



4.2. Multivariate Analytical Techniques.....	92
4.3. UCl <sub>3</sub> -PuCl <sub>3</sub> -LiCl-KCl Mixtures.....	97
4.4. UCl <sub>3</sub> -ThCl <sub>4</sub> -LiCl-KCl Mixtures.....	114
4.5. Summary.....	119
5. ELECTROCHEMISTRY OF GdCl <sub>3</sub> -LaCl <sub>3</sub> -LiCl-KCl MIXTURES.....	121
5.1. Electrochemistry of GdCl <sub>3</sub> in LiCl-KCl Eutectic.....	121
5.2. Electrochemistry of LaCl <sub>3</sub> in LiCl-KCl Eutectic.....	123
5.3. Electrochemistry of GdCl <sub>3</sub> and LaCl <sub>3</sub> in LiCl-KCl Eutectic.....	124
5.4. Concentration Correlations.....	129
5.5. Conclusion.....	139
6. ELECTROCHEMISTRY OF ThCl <sub>4</sub> -LaCl <sub>3</sub> -LiCl-KCl MIXTURES.....	140
6.1. Electrochemistry of ThCl <sub>4</sub> and LaCl <sub>3</sub> in LiCl-KCl Eutectic.....	140
6.2. Electroanalytical Concentration Measurements.....	141
6.3. Conclusions.....	143
7. ELECTROCHEMISTRY OF UCl <sub>3</sub> -MgCl <sub>2</sub> -LiCl-KCl MIXTURES.....	145
7.1. Electrochemistry of UCl <sub>3</sub> in LiCl-KCl Eutectic.....	146
7.2. Electrochemistry of MgCl <sub>2</sub> in LiCl-KCl Eutectic.....	146
7.3. Electrochemistry of UCl <sub>3</sub> and MgCl <sub>2</sub> in LiCl-KCl Eutectic.....	150
7.4. Concentration Correlations.....	154
7.5. Discussion.....	170
7.6. Conclusion.....	175
8. DREP VALIDATION—A HYDRODYNAMIC STUDY.....	177
8.1. Model Description.....	177
8.2. Model Parameters.....	180
8.3. Model Results.....	188
8.4. Discussion.....	194
8.5. Conclusion.....	197
9. CONCLUSIONS AND FUTURE WORK.....	198
9.1. Conclusions.....	198
9.2. Future Work.....	199
Appendices	
A: EXPERIMENTAL DETAILS.....	205

B: DENSITY MEASUREMENTS .....	217
REFERENCES .....	218

## NOMENCLATURE

Symbol	Meaning	Symbol	Meaning
$A$	Electrode surface area, Pre-exponential Factor	$M$	Arbitrary metal
$a$	Activity	$m$	Mass
$C$	Concentration	$MW$	Molecular weight
$D$	Diffusion coefficient	$n$	Electrons transferred/valance state
$d$	Electrode diameter	$R$	Universal Gas Constant
$E$	Electrode potential	$r$	Reaction rate
$e$	Semi-differentiated current	$r_o$	Electrode/Rod Radius
$F$	Faraday's constant	$Re$	Reynolds number
$h$	Mass-transfer coefficient	$Sc$	Schmidt number
$I$	Current	$Sh$	Sherwood number
$i$	Current density	$T$	Temperature
$j$	Molar flux	$t$	Time
$k$	Reaction rate constant	$w$	Weight fraction
$l$	Immersion length/depth	$V$	Volume
		$x$	Mole fraction or linear dimension

Symbol	Meaning	Symbol	Meaning
<b>Greek</b>			
$\alpha$	Transfer coefficient	$\eta$	Overpotential
$\Gamma^*$	Amount of adsorb ion	$\mu$	Chemical potential or dynamic viscosity
$\gamma$	Activity coefficient or surface tension	$\bar{\mu}$	Electrochemical Potential
$\Delta$	Change/Difference	$\nu$	Scan rate
$\delta$	Diffusion layer thickness	$\rho$	Density
$\theta$	Contact angle	$v$	Fluid velocity
$\phi$	Absolute/Local Potential	$\omega$	Rotational rate in rpm
<b>Superscripts</b>			
$a$	Anode	$o$	Standard
$b$	Bulk	$o'$	Apparent Standard
$c$	Cathode	$s$	Surface
<b>Subscripts</b>			
$a$	Activation	$L$	Limiting
$b$	Backward	$m$	Measurement
$c$	Concentration	$O$	Oxidized
$d$	Diffusional or double-layer	$o$	Exchange
$eq$	Equilibrium	$op$	Operational
$f$	Forward	$p$	Peak

Symbol	Meaning	Symbol	Meaning
$i$	Initial	$R$	Reduced
$j$	Species	$s$	Solution
$k$	Current step/setting		
<b>Other</b>			
$\bar{e}$	Normalized semi-differentiated current	$\hat{i}$	Modified normalized current
$\Delta G$	Gibb's free energy	$\nabla$	Gradient
$\bar{i}$	Normalized current		

## ABBREVIATIONS

ANL	Argonne National Laboratory
ASV	Anodic Stripping Voltammetry
CA	Chronoamperometry or Chronoamperogram
CE	Counter Electrode
CP	Chronopotentiometry or Chronopotentiogram
CV	Cyclic Voltammetry or Cyclic Voltammogram
DA	Destructive Analysis
DREP	Deposition Rates using Electrode Potential Model
EBR-II	Experimental Breeder Reactor No. 2
ER	Electrorefiner
ERAD	Enhanced REFIN with Anodic Dissolution
FCF	Fuel Conditioning Facility
FP	Fission Products
IAEA	International Atomic Energy Agency
ICP-MS	Inductively Coupled Plasma Mass Spectrometry
ICP-OES	Inductively Coupled Plasma Optical Emission Spectroscopy
IFR	Integral Fast Reactor
INL	Idaho National Laboratory
LSV	Linear Sweep Voltammetry

MSR	Molten Salt Reactor
MTG	Mass Tracking System
NMA	Nuclear Material Accountancy
NNWS	Non-nuclear Weapon State
NPL	Nuclear Pyrometallurgy Laboratory
NPV	Normal Pulse Voltammetry or Normal Pulse Voltammogram
NRT	Near Real-Time
OCP	Open-Circuit Potentiometry or Open-Circuit Potential
PC	Principal Component
PCR	Principal Component Regression
PLS	Partial Least Squares
PUREX	Plutonium Uranium Redox Extraction
RCE	Rotating Cylinder Electrode
RE	Reference Electrode
RSS	Residual Sum of Squares
RT	Real-Time
SBS	Signature Based Safeguards
SCE	Standard Chlorine Electrode
SD	Semi-differentiated
SNM	Special Nuclear Material
SWV	Square Wave Voltammetry
TC	Thermocouple
TRU	Transuranic Elements

UNF      Used Nuclear Fuel  
UW      University of Wisconsin  
WE      Working Electrode



## ACKNOWLEDGEMENTS

This dissertation represents a collective effort by many people, all of which cannot be listed, but the author wishes to recognize some of those who have contributed to the work contained herein, including:

- Dr. Michael Simpson for the opportunity to start the lab and supporting and mentoring me throughout the process
- Dr. Man-Sung Yim for continued interest and support after my master's work
- Dr. Sang-Mun Jeong for his support and assistance, particularly in developing an electrochemical setup and in analyzing electrochemical signals
- Riley Cumberland, Dr. Il-Soon Hwang, and Dr. Man-Sung Yim for the availability and use of ERAD
- Zhonghang Wang for his excellent work on electrochemical measurements in the  $\text{ThCl}_4\text{-LaCl}_3\text{-LiCl-KCl}$  system
- Dennis Romney and Tom Gudmundson at the mechanical shop in the Chemistry Department for consultation on key experimental design components
- All of my current and past colleagues in the lab: Adam Burak, Aliaksei Minko, Avi Jurovitzki, Chao Zhang, David Horvath, Lauryn Hansen, Mario Gonzalez, Milan Štika, Parker Okabe, Prashant Bagri, and Zhonghang Wang
- My wife, Joslyn, for encouragement and support throughout the entire process
- God, my Heavenly Father, for guiding and strengthening me all along the way.

## 1. INTRODUCTION

At the beginning of 1986, the Integral Fast Reactor (IFR) program was just a fledgling government research program testing and characterizing different metal fuel alloys for a fast reactor and performing lab-scale electrorefining, but that all changed when the Chernobyl nuclear accident happened. In the midst of the panic and fear, a columnist by the name of Jerry Bishop put together the Chernobyl story and a press release from the U.S. Department of Energy about a couple tests performed on the Experimental Breeder Reactor No. 2 (EBR-II) three weeks earlier. He reported that when the conditions that led to the Chernobyl incident occurred in EBR-II, “engineers sat quietly, waiting to see what would happen... [and] the atomic reaction stopped and the coolant temperature dropped” (1). His article “caused a sudden increase in support for the IFR” (2) and marked a turning point in the program widening the scope and accelerating the pace.

The IFR program ran from 1984 to 1994 and is chiefly responsible for the current development of the electrometallurgical treatment of used nuclear fuel (UNF), commonly called pyroprocessing. To some extent, pyroprocessing is a misnomer since the core of the process—the electrorefiner (ER)—is based on electrochemistry and operates only at 500°C. However, the name has stuck from the original process from the 1960s which was a true pyrometallurgical process (3). In the original process, the UNF was simply melted and recasted into new fuel elements. This only removed the more volatile fission products

(xenon, krypton, etc.), but that was sufficient to allow the newly constructed EBR-II to run on recycled fuel in 1965 (4).

The concept of the IFR was to develop a self-sufficient nuclear power plant that would generate more fissile material than it consumed. EBR-II would serve as the reactor and an accompanying fuel conditioning facility (FCF) would be installed in place of the original 1960s' process. In order for the IFR to be economical, the process installed in the FCF would need to be compact with minimal processing units and a quick turnaround time. In 1988, the refurbishment of the fuel cycle facility was initiated. By 1994, the pyroprocessing facility was complete, but the IFR program had been cancelled. Now, the FCF processes EBR-II and other sodium-bonded UNF to condition it for disposal (2). As of 2012, the US has treated 4.62 tHM of UNF from EBR-II and the Fast Flux Test Facility using the electrometallurgical process at the FCF, but currently has no plans to produce fuel for fast reactors (5).

### **1.1. Motivation**

Aside from the US, several countries have developed and demonstrated interest in implementing pyroprocessing, including Russia, the European Union (EU), India, United Kingdom, China, Japan, and the Republic of Korea. Russia has treated 40 kg of UNF from the BN-350 and BOR-60 reactors using high-temperature, electrochemical methods. In the future, Russia plans ambitious development of fast reactors and the accompanying fuel recycling technology, pyroprocessing (6). China, like Russia, already has a fast reactor connected to the grid and plans to process UNF from fast reactors using pyroprocessing (7). India is using a 3-stage approach to closing its nuclear fuel cycle which involves transitioning from thermal to fast reactors. By 2020, it is anticipated that

metal fuels will be the primary fuel in their fast reactors and has motivated the development of pyroprocessing at IGCAR (Indira Gandhi Centre for Atomic Research) which has performed electrorefining of uranium alloys on the kilogram-scale (8).

The Republic of Korea “relies on fuel imports for about 97 % of its primary energy demand” (9). Consequently, it seeks secure and sustainable energy sources. Closing the nuclear fuel cycle would increase the utilization of its uranium imports and minimize the waste needed to be stored. The Republic of Korea has conducted significant research on pyroprocessing since 1997. The US is currently involved in some of the research under the Joint Fuel Cycle Study (JFCS) (10). In 2008, “South Korea’s Atomic Energy Commission... issued a long-term research and development plan... The system would be based on pyroprocessing... and fast reactors that operate in ‘burner’ mode” (11). The plan targets 2028 for demonstrating the technical and economic feasibility of pyroprocessing.

Japan, like the Republic of Korea, is another major energy importer. Since 1986, it has performed significant research and development of fast reactors and pyroprocessing in an effort to maximize its fuel utilization (12, 13). It has a pyroprocessing facility constructed which processes a U-Zr alloy at an equivalent rate of 1tHM/yr with plans for 40tHM/yr facility. However, most advanced fuel cycle research activities have stopped since the Fukushima accident because those researchers have been diverted to the study of decommissioning the Fukushima Daiichi Nuclear Power Station (6). Despite the accident, Japan remains committed to “reduce[ing] the volume and harmfulness of radioactive waste and creat[ing] a nuclear fuel cycle that contributes to effective utilization of resources” (14). To achieve those objectives, development of fast reactors

and pyroprocessing will still be pursued. Pyroprocessing is also being considered and researched in Japan for the treatment of fuel debris from the Fukushima Daiich Nuclear Power Station which mainly consists of  $(U,Zr)O_2$  and is difficult to dissolve in nitric acid which is acid used in traditional processing of UNF (15).

Other notable pyroprocessing developments are occurring in Europe. The Institute of Transuranium Elements (ITU) studies both aqueous and pyrochemical reprocessing. In addition to ITU's efforts, General Electric (GE) Hitachi is currently vying for the opportunity to dispose of the United Kingdom's plutonium stockpiles using its PRISM reactor which is based on the IFR and uses pyroprocessing (16, 17). This would mark the first commercially designed and operated pyroprocessing facility in the western world. Thus significant development of and interest in pyroprocessing exists world-wide and possible commercial operation of pyroprocessing is a near-term reality.

A key component to the successful commercialization of pyroprocessing will be effective process monitoring technologies which can be used to optimize process performance, to determine the need for maintenance and cleaning operations, and to ensure safe operation. Monitoring pyroprocessing is especially challenging because it handles UNF with strong radiation fields at high temperatures which requires remote operation behind several feet of concrete. Because of these harsh conditions, robust sensors, detectors, and other monitoring technologies need to be developed for pyroprocessing.

Further motivating the need for monitoring technology is nuclear safeguards. Domestic and, in some cases, international safeguards will need to be applied to the process because it handles special nuclear material (SNM), namely uranium and

plutonium. This is traditionally done by nuclear material accountancy (NMA) which essentially tracks and balances the SNM in the process within an acceptable amount of error. The monitoring of nuclear material is the nexus of process monitoring and safeguards. Process monitoring and safeguards are both interested in the composition of process media for different purposes. Thus sensors that could provide feedback on the composition of uranium and plutonium in the process would be beneficial for both process monitoring and safeguards.

In anticipation of a Non-nuclear Weapon State (NNWS) adopting pyroprocessing, safeguard technology and approaches that International Atomic Energy Agency (IAEA) can implement need to be developed. In developing safeguards, the perspective of both the IAEA and the NNWS should be considered. The IAEA operates on limited funding of \$348M (18) which is comparable to Detroit's or Philadelphia's police department budget (19), but must be sufficient for monitoring all the SNM handled by NNWS with IAEA safeguard agreements across the globe. Thus, the safeguard techniques should seek to minimize the cost-burden on the IAEA while maximizing the probability of detecting the misuse of a facility. The NNWS wants to run their facilities in the most economic and efficient manner. Thus, it too would benefit from accurate monitoring for the optimization and control of process units. However, highly intrusive safeguards requiring excessive plant shutdowns or modifications would reduce the economics of operating the facility by the NNWS. Thus, an ideal method to safeguard a facility would minimize the cost and invasiveness of safeguards while maximizing the reliability of the feedback to optimize the process and to positively detect plant misuse by the IAEA.

Reliable electrochemical and other sensors combined together have the potential

to meet some or all of these requirements. Such sensors could provide key measurements in real-time (RT) or near real-time (NRT) about the composition and conditions at key points in the process. Furthermore, they could reduce the frequency of invasive inspections and plant shutdowns while providing important information to the IAEA to verify the declared use of the facility and to operators to control and optimize the process. Additionally, the use of process monitoring could address some of the key challenges that arise when attempting to apply traditional safeguards approaches, such as NMA.

Pyroprocessing differs fundamentally from traditional reprocessing facilities, namely PUREX (Plutonium Uranium Redox Extraction), currently under safeguards. To illustrate these differences and their impact on international safeguards, the general flowsheet for pyroprocessing and the current method of NMA is reviewed followed by a discussion of safeguard challenges specific to the process.

## **1.2. Pyroprocessing Description**

Several variations of pyroprocessing exist and are detailed elsewhere (2,6,10,13,20,21), but no standard design for a commercial facility has been developed. However, the general features are similar among the process variations and are based on the process developed during the IFR program at Idaho National Laboratory's (INL) FCF. The general pyroprocessing flow diagram is displayed in Figure 1.1. In any current design, the process operates batch-wise and is enclosed in an argon hot cell behind several feet of concrete. There are a limited number of penetrations in the cell through which nuclear material can be exchanged.

The process generally starts with disassembly and chopping of UNF fuel rods into pellets. If the UNF is from oxide fuel, it must first be reduced to its metal form by

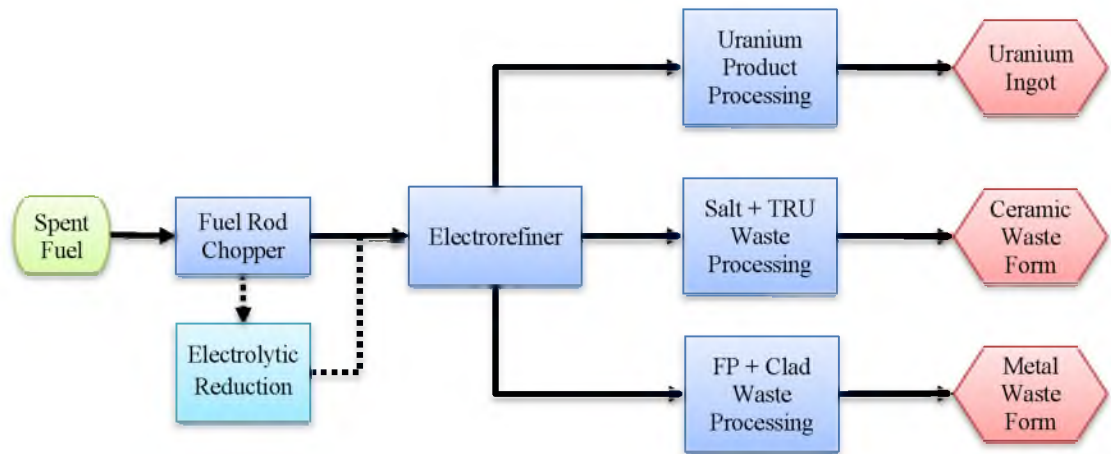


Figure 1.1 General Process Flow Diagram of Pyroprocessing

electrolytic reduction which uses electricity to dissociate  $Li_2O$  and reduce the  $Li^+$  ions to Li metal. The Li metal reduces the oxides in UNF at one electrode while generation  $O_2$  at the other electrode (2). If the UNF is metallic fuel, electrolytic reduction can be bypassed. Once in metallic form, UNF pellets are loaded into baskets which act as the anode(s) in the ER where the constituents of UNF are partitioned into 3 different phases. The separation and distribution of elements in UNF in an ER are illustrated in Figure 1.2. Elements in UNF can remain in the anode baskets, dissolve into the molten salt, or

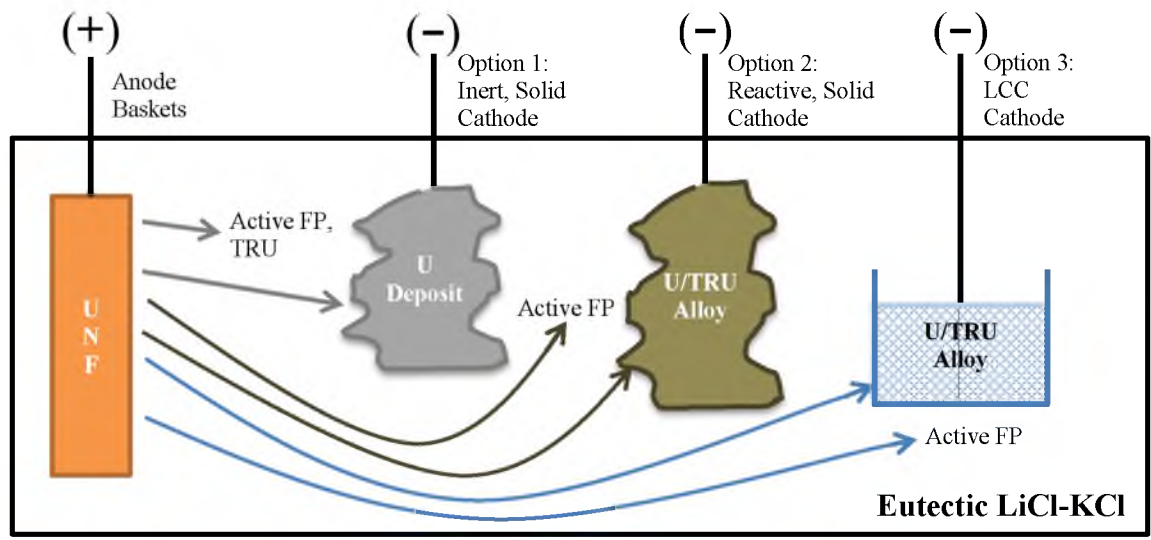


Figure 1.2 Drawing of electrorefiner with 3 options of cathode depicted



deposit at a cathode. The standard reduction potential ( $E^o$ ) and activity of an element are the primary determinants of an element's location after electrorefining. An abbreviated electromotive force series (EMF) for the eutectic LiCl-KCl system at 450°C in Table 1.1 illustrates how  $E^o$  determines the location. The more prevalent ions of each type of element (active fission products (FP), TRU, U, cladding hulls, or noble FP) in UNF based on INL's experience at FCF are listed in Table 1.1 with the type of element in parenthesis (23). It should be noted that those elements found on any cathode are also found in the salt as these elements must be electrotransported through the salt to the cathode. The active metal FP and TRU are oxidized into the molten eutectic LiCl-KCl salt. Noble metal FP and cladding hulls remain in the anode baskets. U and/or TRU can be electrodeposited at the cathode(s).

There are principally two modes in which an ER can operate. In one mode, the ER is designed to solely recover U at a solid, inert cathode. In the other mode, the ER is designed to simultaneously recover U and TRU as a codeposited U/TRU alloy in a liquid cadmium cathode (LCC) or solid, reactive electrode (e.g., aluminum, nickel, etc.). Figure 1.2 depicts all three options, but only one type of electrode is employed at a time.

Initially, only U metal is recovered until the TRU accumulate significantly in the

Table 1.1 EMF for Eutectic LiCl-KCl at 450°C with selected ions common in processing UNF (22)

Couple	$E^o$ (V vsCl <sub>2</sub> /Cl)*	Location
Li <sup>+</sup> /Li	-3.63	Salt
La <sup>3+</sup> /La (Active FP)	-3.13	
Pu <sup>3+</sup> /Pu (TRU)	-2.79	Salt or Reactive Cathode
U <sup>3+</sup> /U (U)	-2.47	Inert or Reactive Cathode
Fe <sup>2+</sup> /Fe (Cladding)	-1.39	Anode
Mo <sup>3+</sup> /Mo (Noble FP)	-0.85	
*Adjusted from Pt/Pt <sup>2+</sup> scale by subtracting 0.216 V		

salt. Then a reactive electrode is employed to recover the U/TRU product. The product from the ER, whether U or U/TRU, is then heated to distill the residual salt and/or cadmium and consolidated into an ingot for waste storage or fabrication into fuel. The variations in the process largely deal with salt treatment, waste form fabrication, and recycle of actinides.

The important things to note from the pyroprocessing flowsheet and electrorefining descriptions are: (1) it is a batch process, (2) it is remotely operated in an argon cell enclosed by thick concrete walls, (3) UNF is not homogeneous and is only partially dissolved in the ER, and (4) plutonium is never isolated in the process. These features complicate the application of traditional safeguards, but can also make proliferation and misuse more difficult and easier to detect. If the approach to safeguards is modified, certain features of process can be leveraged to assist in NMA.

#### 1.2.1. Nuclear Material Accountancy at FCF

The current method of NMA for pyroprocessing is employed at FCF at INL. A mass tracking system (MTG) was initially developed by Argonne National Laboratory (ANL) to continually track the location and inventory of items in the FCF (23). For input accountancy, INL uses ORIGEN calculations and the Physics Analysis Database (PADB) to estimate UNF composition and later makes corrections in the MTG based on dissolution and DA of fuel segment samples (24,25). FCF consists of multiple units including two ERs, two fuel choppers, a cathode processor, and a casting furnace. In units, such as the ER, where the inventory of items are partitioned between different phases and locations, the changes in item compositions and masses are modeled using the MTG. A description of the MTG treatment of the ERs in FCF has been reported

elsewhere (26). The predictions made by the MTG are either verified or updated by sampling and DA upon availability and the MTG system is subjected to replays to update the process inventories. However, the DA of molten salt samples can take several weeks to complete. This delay could result in operating at nonoptimal settings for prolonged periods of time. Additionally, there would be problems with the time scale for closing material balances if the facility were to be monitored by the IAEA. The significance of these issues would increase with scale or throughput of the facility. For example, INL's FCF is currently sized to only process up to about 2 t/yr of spent fuel. A commercial facility would likely have a throughput of at least 100 t/yr.

### **1.3. Pyroprocessing Safeguards**

Safeguards can be applied domestically by an organization, like the Nuclear Regulatory Commission in the US, or internationally by the IAEA. The requirements and nature of domestic safeguards vary by country and would need to be addressed on a case-by-case basis. Therefore, only the more universal requirements and methods used by the IAEA are discussed in this section.

The main objective of safeguards according to the IAEA is “the timely detection of the diversion of significant quantities of nuclear material from peaceful nuclear activities to the manufacture of nuclear weapons or of other nuclear explosive devices or for purposes unknown, and deterrence of such diversion by the risk of early detection” (27). Safeguards are applied to facilities that handle SNM. These include enrichment plants, fuel fabrication plants, nuclear reactors, and reprocessing plants among others. Pyroprocessing is considered a reprocessing plant. Traditionally, the IAEA objective of early detection of diversion is accomplished in a reprocessing plant by performing mass

balances on material balance areas (MBA). This is accomplished by calculating the material unaccounted for (MUF):

$$MUF = In - Out - HU \quad (1.1)$$

where *In* and *Out* are the amounts of SNM going into or out of an MBA and *HU* is the hold-up of SNM in the MBA. This calculation is done periodically during MBA close-outs. If the MUF exceeds a significant quantity for a SNM (see Table 1.2), then “the possibility of manufacturing a nuclear explosive device cannot be excluded” (27).

Furthermore, there is a detection time defined as “the maximum time that may elapse between diversion of a given amount of nuclear material and detection of that diversion by IAEA safeguards activities” (27). Thus, not only is detection of diversion required, but it must occur within a certain timeframe. In pyroprocessing, the SNM would be low-enriched, and possibly high-enriched, uranium and plutonium in irradiated fuel at the beginning of the process putting the detection time around a month for plutonium and multiple months for uranium. However, after some processing, direct use SNM, particularly plutonium, would exist as compounds and mixtures throughout the process reducing the detection time to the order of weeks.

With PUREX, mass balances are more readily accomplished. At the beginning of the process, UNF is completely dissolved in a dissolution tank commonly referred to as the “accountability tank.” This tank provides a homogeneous sample from which the composition of the feed can be determined with minimal uncertainty. Because PUREX uses an aqueous solvent that is liquid at room temperature, the process can be easily flushed out to further reduce uncertainty and SNM hold-up.

Table 1.2 Significant quantities and detection times for SNM (27)

Material	Amount	Detection Time
<i>Direct Use Nuclear Material</i>		
Pu (containing less than 80% $^{238}\text{Pu}$ )	8 kg	Pure Metal (7-10 days)
$^{233}\text{U}$	8 kg	Compound (1-3 weeks)
Highly Enriched Uranium (HEU) – $^{235}\text{U} \geq 20\%$	25 kg*	UNF (1-3 months)
<i>Indirect Use Nuclear Material</i>		
Low-Enriched Uranium (LEU) – $^{235}\text{U} < 20\%$ ,	75 kg*	3-12 months
Natural Uranium	10 t	
Depleted Uranium	20 t	
Thorium	20 t	3-12 months
*Amount refers to mass of the $^{235}\text{U}$ isotope		

As discussed, several aspects of pyroprocessing provide challenges for the use of the NMA approach of mass balances used on PUREX. First, the feed material, UNF, is not homogeneous. Second, there is a large amount of SNM hold-up in the ER by design. Lastly, the batch nature of pyroprocessing means that accumulation of SNM in the ER occurs over a series of inputs and outputs which makes mass balances more complex. Flush-outs would be onerous due to the batch and high-temperature nature of the process and would also interfere with the objective of accumulating TRU in the ER salt for co-extraction with uranium. Several solutions have been proposed for addressing the safeguard challenges associated with pyroprocessing.

### 1.3.1. Input Accountability

The feed to pyroprocessing, UNF assemblies, are inhomogeneous—their elemental and isotopic composition varies spatially. Thus, each chopped fuel rod pellet has a unique composition. As described earlier, at INL's FCF the amount of each nuclide fed to the process is predicted using ORIGEN calculations and are adjusted based on random sampling which introduces high uncertainty (>5%) and a time delay (28). In a commercial facility, this level of error could quickly amount to a significant quantity. A

couple approaches have been proposed to resolve the issue of an inhomogeneous input.

The lack of an accountability tank could be resolved by simply making a homogenized melt of the UNF (28,29). This would result in the simplest sampling and measurement methods yielding highly accurate composition values from mass spectrometry. However, this would introduce additional processing for a system that is designed to be compact and simple so that UNF can be economically processed on-site and, if desired, quickly recycled back into a fast reactor. Significant costs and engineering challenges would be associated with homogenizing UNF. Additionally, sampling and analyzing the melt would introduce some lag time in determining the compositions. While this method may yield the lowest uncertainties in SNM input, it would disrupt the process and increase the cost of pyroprocessing for a NNWS.

Another approach is passive gamma ray spectroscopy which may potentially provide more rapid feedback (30). It will require a standard to which the measurement can be calibrated. This method is also dependent on extensive knowledge of the fuel history such as burnup, cooling time, and neutron poison histories.

### 1.3.2. Neutron Balance

SNM, particularly plutonium, has been proposed to be tracked using neutrons (29). This would involve a total neutron measurement of each pin of UNF introduced into the process, the ER, the metal waste form, the ceramic waste form, and the uranium product. The bulk of the neutrons in UNF are attributed to curium. The plutonium-to-curium ratio of UNF can be determined using DA, possibly from the homogenized UNF melt or randomized sampling methods. If that ratio is assumed to be constant throughout

the process, the amount of plutonium can be determined from neutron count and tracked throughout the process using neutron counting.

However, it is not certain that “[curium] would completely transfer with [plutonium] in a pyroprocessing facility” (31). INL performed curium measurements which demonstrated the difficulty of tracking plutonium using curium. In the experiments, there was not a significant accumulation of curium in salt to be detected using DA. Additional calculations were performed at the University of Utah that demonstrates the possibility of variations in plutonium-to-uranium ratio when using reactive electrodes or codepositing U/Pu on an inert electrode (32). This may preclude quantitative measurements of plutonium content, in some cases; however, it may still provide valuable qualitative information (i.e., verifying presence of plutonium, increasing or decreasing plutonium content).

### 1.3.3. Actinide Hold-up

A significant amount of U, TRU, lanthanides, and FP can build up in the eutectic LiCl-KCl salt in the ER. This is intentional because pyroprocessing was designed to harvest the fissionable actinides and recycle them back into a reactor. This achieves two objectives: (1) produce more energy and (2) transmute long-lived actinide radioisotopes into shorter-lived radioisotopes.

The accumulation of actinides in the ER over time can create a large inventory of SNM held up in the process. This amount could be quantified using DA methods such as Inductively Coupled Plasma Mass Spectrometry (ICP-MS), but as discussed significant time and sample preparation is required. Various techniques such as voltammetry, potentiometry, hybrid K-edge densitometry and laser induced breakdown spectroscopy

(LIBS) could provide RT or NRT accountancy of SNM in the ER.

LIBS is a promising optical method of measuring molten salt composition, but still has a long and uncertain development path (33,34). Practical challenges associated with high-temperatures, repeatability and representative sampling need to be resolved so that it can be applied in situ on molten salt media. Hybrid K-edge densitometry has been used extensively in aqueous reprocessing and is being examined for application to pyroprocessing (30). However, the high-temperature and high-radiation environment would prohibit in situ measurements by hybrid K-edge densitometry. Thus mechanisms for sampling and sample preparation need to be developed. Depending on the amount of sample preparation need, it may also have a significant lag-time.

Electroanalytical techniques utilizing electrode probes (cyclic voltammetry, square wave voltammetry, etc.) have been applied in molten salts and show promise for making quantitative measurements of the elemental composition of molten salts. These probes would be constructed out of durable material (i.e., tungsten, ceramics, etc.) that can withstand the harsh conditions of the ER enabling in situ measurements. Furthermore, little to no sample preparation would be required. However, there has yet to be developed a complete and reliable electrochemical sensor for an UNF ER.

#### 1.3.4. Digital Cloud Chamber and Inverse Spectroscopy Algorithm

INL has developed a method by which nonhomogeneous samples can be characterized (31). It uses a digital cloud chamber (DCC) to record the pathways of gamma rays and neutrons. Using the data from the DCC in conjunction with the inverse spectroscopy algorithm, the energy and originating location of the incident radiation can be determined. This tool could be used for quantifying plutonium in UNF or other



containers in pyroprocessing (35). It should be noted that this detection method requires a long measurement time making it better suited for evaluating feed and product inventory rather than intermediary products in pyroprocessing.

#### 1.3.5. Goals Driven Safeguards

One of the proposed alternatives to traditional safeguards is Goal Driven Safeguards (36). This approach takes advantage of the batch nature of pyroprocessing. The material is moved between process units in containers. Each container would be weighed and numbered marking the creation of an “item.” Each item would be tracked through the system. The movement of the item would be recorded and monitored. In pyroprocessing under normal operation, there is a unique set of motions between each unit of operation. If a movement was recorded outside of the normal operating paths, it would signify abnormal operations and the possibility of diversion.

The location of the process in a shielded hot cell is also advantageous. The hot cell has a limited number of portals. These portals could be monitored using non-destructive assay methods to ensure that products leaving the cells are consistent with their declaration. Lack of accuracy in nondestructive assay methods would be compensated by the item and motion tracking within the cell.

#### 1.3.6. Signature-Based Safeguards

Signature-Based Safeguards (SBS) build upon the principles of Goals Driven Safeguards and adds a process model to identify measurable indicators (signatures) of the diversion of SNM (37). This approach could include some of the methods previously mentioned (i.e., neutron counts, electrochemical measurements) as signatures. It could

also include other signals such as temperature, density, voltages, current, and so forth.

The process model would simulate potential diversion scenarios to identify combinations of measurements, movements, and other conditions that are indicative of diversion. This model would run in real-time in parallel to the actual process.

SBS can complement traditional NMA by acting as a trigger to pause operation or initiate cleanout of ER systems. If a combination of real time sensors yields a high probability that a diversion event may have occurred, it can justify the stoppage of operations with exhaustive sampling and analysis to close the mass balances. This type of rigor in mass tracking is unlikely to be practical in a production facility, but it may ultimately be necessary. However, SBS could limit the frequency of such operations. Hypothetically, SBS could be used to select when such a stoppage and complete system accountability is needed. Additionally, this approach could also prove beneficial to product optimization and process control by providing information about the compositions of different process phases in real-time.

In order to accomplish SBS, chemically and physically correct representations of each unit operation should be built. Additionally, some of the other safeguards methods mentioned previously will require or benefit from process monitoring. The ER is the most important and complex unit of operation because it partitions the UNF. Understanding the behavior and interactions of key ions, such as uranium and plutonium ions, in the ER is crucial to process monitoring and SBS. It would be the ideal location for process monitoring and for potential proliferators to alter the flow of material making it a key location to monitor and model.

#### 1.4. Electrochemical Studies

In order to reliably monitor and simulate an ER, fundamental data, such as diffusion coefficients and standard potentials, for major ions in the salt need to be measured and their dependence on concentration, temperature, and other factors accurately quantified and characterized. Additionally, robust sensors need to be developed. Because ER is already an electrochemical environment, electroanalytical techniques utilizing electrode probes (cyclic voltammetry, chronoamperometry, etc.) can be readily applied to probe the behavior of ions and to make in situ, RT and/or NRT quantitative measurements of ER salt composition. Electrochemical sensors could provide a wealth of information about the behavior of ions in the ER, the composition of the salt and the performance of electrorefining operations.

Several techniques are available for measuring key parameters and estimating concentration. Cyclic voltammetry (CV) is a favorable method because of its reliability over a broad range of concentrations and studies have been performed demonstrating its ability (38,39). Chronoamperometry (CA) has also been studied as a possible means to estimate the concentration of an ion in molten LiCl-KCl eutectic (38). Normal pulse voltammetry (NPV) and square wave voltammetry (SWV) have been applied to the measurement of actinide ion concentrations in molten LiCl-KCl eutectic, but SWV is limited to lower concentrations which are likely to be exceeded during ER operation (40).

Aside from these studies, many other studies have been performed on ternary molten salt systems. These studies have used eutectic LiCl-KCl as the matrix salt and another metal chloride, commonly a rare earth or actinide, as the analyte. These single-analyte studies have been reviewed by Zhang (41) and provide an excellent

understanding and database of electrochemical properties for individual ions.

Unfortunately, these metal ions are not isolated in eutectic LiCl-KCl in an ER; rather, several analytes will be present at significant concentrations. Based on INL's experience in processing UNF in ERs at FCF, the most prevalent actinide in the ER salt is known to be U (3.5- 6.9 wt%) while other actinides and lanthanides, most notably plutonium, are also present in small amounts (<1 wt%), but can accumulate higher over time (42–44). The presence of multiple ions can interfere with each other's signals and could possibly affect ionic properties (activity coefficient, standard potentials, etc.).

Most of the available studies in literature have focused on electrochemical measurement in a ternary system. The development of experimental and analytical methods for obtaining reliable ion properties and concentrations in quaternary salt (i.e., eutectic LiCl-KCl with two metal chloride analytes) is generally unexplored in the literature and is the main objective of this work. Studies that have made electrochemical measurements in eutectic LiCl-KCl with multiple analytes or have focused on making concentration correlations in eutectic LiCl-KCl using electrochemical data are reviewed to demonstrate that lack of knowledge in multianalyte electrochemistry in molten LiCl-KCl eutectic. This review is not meant to explain basic electrochemistry. The reader is referred to Chapter 2 for a more comprehensive review of electrochemical principals relevant to this work.

#### 1.4.1. Single-Analyte Studies

##### *1.4.1.1 Neodymium*

Researchers from the Korean Atomic Energy Research Institute and Korea University investigated applying electrochemical techniques at higher concentrations

(38). Specifically, they studied eutectic LiCl-KCl containing up to 9 wt%  $\text{NdCl}_3$  (5.38 wt% Nd) as a surrogate for  $\text{UCl}_3$ . Using CV and CA, they obtained linear plots with concentration. They ran CV at 200 mV/s from 0.5 to 9 wt%  $\text{NdCl}_3$  and found that the cathodic peak current and charge were both linear with  $\text{NdCl}_3$  concentration. With CA, “the current obtained at 0.9 s linearly increases with the  $\text{NdCl}_3$  concentration up to 9 wt%, whereas the value at 10 s increases in a nonlinear manner beyond a 4 wt% concentration” (38). This nonlinearity may have resulted from “the acceleration of Nd electrodeposition on electrodeposited Nd surface or the [growth] of the surface area by Nd electrodeposition” (38). To apply CA to monitoring an ER, they suggested repeating CA which applies a reducing potential then an oxidizing potential repeatedly. With Nd metal, they found that within 0.2 s most of the metal is reoxidized, even at 9 wt%  $\text{NdCl}_3$  implying that repeating CA could provide rapid feedback.

This study highlights several challenges associated with high concentrations of metal ions such as the growing metal deposit and provides good guidance for setting parameters for CV and CA to manage these issues. However, this study only accounts for one analyte which is not representative of a UNF ER and only applies simple, traditional analytical techniques.

#### *1.4.1.2 Uranium*

In the US, researchers at INL and University of Wisconsin—Madison (UW) investigated the electrochemistry of  $\text{UCl}_3$  in the concentration range of 1 to 10 wt%  $\text{UCl}_3$  (7.13 wt% U) (39). They used CV, chronopotentiometry (CP), and anodic stripping voltammetry (ASV) on the LiCl-KCl- $\text{UCl}_3$  mixtures. CP was used mainly to determine diffusion coefficients and was not applied to making concentration measurements. In

their CVs, they found 3 pairs of anodic and cathodic peaks. The most positive peaks (approx. -0.5 V vs Ag/AgCl [5 mol%]) was assigned to the oxidation of  $U^{3+}$  to  $U^{4+}$  and the reduction of  $U^{4+}$  back to  $U^{3+}$ . The second pair of peaks was separated significantly. The anodic peak at -0.7 V and cathodic peak at -1.5 V were attributed to the desorption and adsorption of  $U^{3+}$ . The most negative pair of peaks (-1.6 V) was interpreted to be the reduction of  $U^{3+}$  to  $U^0$  and oxidation back to  $U^{3+}$ . Using the last pair of peaks, they found the cathodic peak to be very linear with concentration, but they did not force the y-intercept through zero. The anodic peak was more inconsistent than the cathodic peak. They did not provide a reason for the inconsistency, but anodic peaks in CVs depend on the surface deposit morphology and the scan reversal potential. Thus the anodic peak has more dependencies unrelated to concentration than the cathodic peak making it less repeatable.

The suitability of ASV was also examined for making concentration measurements. However, over this broad of a composition, it was difficult to tune ASV parameters to yield a distinguishable peak at each concentration. The settings used by the researchers are described as follows (39):

At the higher concentrations (7.5 wt% & 10.1 wt%), a 60 s plating time at -2.3 V produced large deposits with no distinct stripping peak; therefore, a 5 s plating time was used. At the lower concentrations (1.0 wt% and 2.5 wt%), a plating time of 5 s did not allow for enough reduction of material onto the working electrode to give a clear stripping peak. Due to this issue, a 60 s plating time was used for the (1.0, 2.5, and 5.0) wt% UC13 salt mixtures and a 5 s plating time was used for the (5.0, 7.5, and 10.1) wt% UC13 runs.

The inability to keep the parameters consistent resulted in a poor correlation between ASV peaks and concentration. However, ASV may be a good candidate for more trace elements in a UNF ER.

Like the publication on neodymium, the INL and UW researchers found good correlation between CV peak height and concentration. This publication gives excellent insight into the electrochemical behavior of uranium over a broad concentration range. However, again, only a single-analyte is present and the analysis involves simple, traditional analytical techniques.

#### 1.4.2. Multianalyte Studies

##### *1.4.2.1 Uranium and Plutonium*

Japan's Central Research Institute of Electric Power Industry (CRIEPI) and Japan Atomic Energy Research Institute (JAERI) tested the idea of using electrochemical techniques, particularly voltammetry, to monitor actinide concentration in molten LiCl-KCl eutectic (40). The techniques examined were SWV and NPV. They tested mixtures containing  $\text{UCl}_3$ ,  $\text{PuCl}_3$ ,  $\text{NpCl}_3$ , and  $\text{GdCl}_3$  in eutectic LiCl-KCl. Initially, they tested SWV on the LiCl-KCl- $\text{PuCl}_3$  mixture. Based on their results, the height of SWV peaks deviated from linearity at very low concentrations (0.1 wt%  $\text{Pu}^{3+}$ ). The authors concluded that (40):

Below the deposition potential, the surface area of the working electrode is expected to be a little larger when reverse step current is measured than when forward step current is measured due to the deposition of plutonium metal. Because SWV output is obtained by subtracting the reverse current from forward current in each step, the final output value would be smaller than expected especially at higher concentration. This is considered to be the reason for the non-linearity of the peak current to the plutonium concentration.

Due to the waveform of SWV the surface area of the electrode is altered as the scan progress, especially at higher concentrations.

Next, CRIEPI and JAERI researchers examined NPV. NPV differed from SWV

in that it returns to the same “rest” or “base” potential as the “pulse” potential varies. If the base potential is held sufficiently long and set more positive than the reduction potentials of metals present, then the deposited metal should be completely removed before the next pulse. The time from the beginning of one pulse to the beginning of the next pulse is referred to as the measurement time,  $t_m$ , and the time from the beginning of one pulse to its end is referred to as the pulse time,  $t_p$ . The authors reported that the “reduction current was found to decrease to some extent after the current once reached the maximum value when  $t_m$  was shorter than about 10 times  $t_p$ ” (40). They also observed a delay of about 0.09s in the “reduction current rise” of uranium and plutonium. This delay was attributed “to over 10 m of wiring from the electrodes through the plutonium glove box wall to the potentiostat” (40). Thus, they used a  $t_p$  of 0.1 s and a  $t_m$  of 2 s and used a potential window of -1 to -2.2 V. This resulted in a turnaround time of 10 min.

They performed NPV in a mixture containing LiCl-KCl- $\text{UCl}_3$ - $\text{PuCl}_3$  in which the concentrations range for 0.15 to 2.48 wt% U (0.22 to 3.55 wt%  $\text{UCl}_3$ ) and 0.12 to 1.67 wt% Pu (0.17 to 2.40 wt%  $\text{PuCl}_3$ ). Their NPV measurements maintained linearity within the concentration range of their experiments with the exception of 2.40 wt%  $\text{PuCl}_3$ . Again, the cause of nonlinearity was attributed to a growing surface area by the authors. However, it should be noted that this was the concentration at which the U and Pu signals overlapped the most. No treatment was performed by the authors to separate the signals. They also investigated the possible interference from FP and other actinides. They used  $\text{GdCl}_3$  to represent the FP because it had the most positive standard potential of active FP. Also, they used  $\text{NpCl}_3$  to represent actinides. The signals for  $\text{GdCl}_3$  occurred after (more



negative than) the Pu signal and the researchers observed that “the reduction current of uranium and plutonium were not influenced by the addition of gadolinium” (40) even at the highest concentration tested of 0.57 wt% Gd (0.95 wt% GdCl<sub>3</sub>). The signal for NpCl<sub>3</sub> lay in between the U and Pu signals resulting in significant interference.

CRIEPI’s and JAERI’s research shows that NPV is a promising method for concentration measurements. However, their work was limited to 2.48 wt% U and 1.67 wt% Pu which is on the low end for U in a UNF electrorefiner. Also, they performed limited analytical work on the collected data. Due to the advancement in computers, more powerful and advanced analytical techniques are readily available to treat interferences from other analytes.

In addition to the Japanese publication, ANL published a paper in 2015 on measuring the concentration of U and Pu ions in LiCl-KCl using cyclic voltammetry (45). They found that proper cleaning potentials and waiting periods are necessary for repeatable results, especially at high concentrations. In order to minimize error associated with characterizing the area, they measured the peak potential at multiple working electrode immersion depths and related the slope of peak current versus immersion depth to concentration. When the normalized peak height of U was plotted versus the concentration of uranium, they found that it was only linear up to 2 wt% U (~2.9 wt% UCl<sub>3</sub>). They concluded “because the diffusion coefficient depends on the salt composition... a different method is needed to measure the diffusion coefficient independently [*sic*] of concentration and to detect any changes in its value caused by changes in concentration or salt composition” (45). This not observed in the INL-UW work, possibly because they did not force the y-intercept through zero. They also

analyzed four samples with both U and Pu present, in which a narrow range of Pu concentration (1.28-1.44 wt% Pu) was tested. Semidifferentiation of the CV measurements created a more identifiable baseline which resulted in measurements more consistent with ICP-OES for the Pu<sup>3+</sup> ion concentration.

#### *1.4.2.2 Gadolinium and Dysprosium*

CV, SWV, and open-circuit potentiometry (OCP) were performed by Chinese researchers on GdCl<sub>3</sub> and DyCl<sub>3</sub> (46). However, their research was mostly focused on the selective extraction of dysprosium on a solid electrode. Therefore, their analysis of the electrochemical data is mostly qualitative and mainly interested in quantifying the potential window which would yield a high extraction efficiency. No attempts were made at calculating ion properties or relating the signals to concentration.

#### *1.4.2.3 Zirconium and Copper*

CV, SWV, and OCP were used to monitor the reaction progress of metal zirconium rods with copper ions in eutectic LiCl-KCl (47). The researchers used the cathodic peak height from CV to monitor the concentration of Cu and found a very good agreement with ICP-AES measured concentrations. However, no information was provided on the relation between the electrochemical signals and concentration of Zr ions. Cu is more noble than Zr, thus its electrochemical signal can be recorded without interference from Zr ion signals making Cu peak height measurement fairly straight forward to determine.

#### *1.4.2.4 Other Work*

INL is currently performing studies on electrochemical measurements of LiCl-KCl-UCl<sub>3</sub>-PuCl<sub>3</sub> mixtures. Some results have been shared via conference presentations and personal communication, but no formal publications have been made available. INL is investigating NPV and developing a potentiometric sensor (48, 49). One of their difficulties in NPV is distinguishing the onset of plutonium deposition. They have developed a model to predict where plutonium deposition should begin. The model predictions are used to guide their selection of the baseline for the plutonium deposition. The potentiometric sensor is being developed with an ion-selective membrane to allow the open-circuit potentials of individual ions to be measured.

### **1.5. Summary**

It is apparent from the global trends and interest in pyroprocessing that commercial operation of pyroprocessing is a near-term reality and eventual adoption by a NNWS is highly probable. Thus, process monitoring sensors and techniques need to be developed to control the process, to ensure safe operation, to optimize process parameters, and to support NMA for both domestic regulatory organizations and the IAEA. In situ, RT, and NRT accountancy may minimize the intrusiveness and cost of safeguards for pyroprocessing while providing valuable monitoring capabilities for the IAEA, NNWS and nuclear weapon states (NWS). A key unit to monitor in pyroprocessing is the ER where UNF is refined into three phases. Because it is already an electrochemical environment in the ER, electroanalytical techniques utilizing electrode probes (cyclic voltammetry, chronoamperometry, etc.) can be readily applied to make in situ, RT/NRT quantitative measurements of ER salt composition and to investigate ion

behavior. Such a sensor would be beneficial to NNWS, NWS, and the IAEA.

Surveying the existing work, it becomes apparent that mixtures of a single analyte in LiCl-KCl eutectic have been examined at low and high concentrations. Only a couple publications tested multianalyte mixtures which were limited to lower concentrations, a narrow concentration range, qualitative analysis, or quantitative analysis of the more noble species. Additionally, only a limited number of tests were performed. The analysis of the electrochemical data has been limited to simple, traditional analytical techniques. Thus, this work seeks to fill the gap of existing publications by testing binary-analyte mixtures over a broad range of concentrations with multiple combinations of elements as the analyte. The electrochemical signals measured in the binary-analyte mixture will be analyzed and assessed in their ability to correlate to concentration. Additionally, this work will also take advantage of advanced computational tools now available which will allow for more rigorous and quantitative analysis of the signals for both ions.

The existing literature has identified CV, CA, and NPV as possible electrochemical techniques that maintain a good correlation between its signal and the concentration of metal ions. CP has not been tested extensively for concentration measurements. It has mainly been used to determine diffusion coefficients. SWV was shown to have limited applicability at low concentrations. Thus, it is planned to apply CV, CA, NPV, and OCP to mixtures containing two elements of interest in LiCl-KCl eutectic. As has been observed in the literature, overlap of signals may be an important issue that may pose a challenge to reliable concentration measurements. The standard reduction potential is the most significant factor in determining if signals will overlap. A list of apparent standard reduction potentials ( $E^{o'}$ ) of key elements in a UNF ER is

provided in Table 1.3. Of the elements listed, Np, Pu, Cm, and Am are difficult to obtain and unavailable from commercial chemical companies.

In order to test the limits of the electrochemical methods in measuring concentrations in binary-analyte systems, multiple redox couple pairings have been tested with various differences in  $E^{o'}$  values that are similar to important pairings in a UNF ER. The tested pairings are displayed in Table 1.4. The key elements to measure in the ER are uranium and plutonium, but the FP, rare earths, and actinides have the potential to interfere with the signals of uranium and plutonium.

Using these pairings, the merit of an electrochemical sensor as a means to provide reliable concentration estimates of key ions in an ER can be more fully evaluated.

Additionally, the optimal techniques, parameters and the effect of multiple ions on the

Table 1.3 Standard Apparent Reduction Potentials at 500°C

Redox Couple	$E^{o'}$ (V vs Cl <sup>-</sup> /Cl <sub>2</sub> )
Zr <sup>2+</sup> /Zr	-1.98 (41)
U <sup>3+</sup> /U	-2.49 (41)
Th <sup>4+</sup> /Th	-2.55 (41)
Np <sup>3+</sup> /Np	-2.67 (41)
Pu <sup>3+</sup> /Pu	-2.75 (41)
Mg <sup>2+</sup> /Mg	-2.85 (50)
Cm <sup>3+</sup> /Cm	-2.86 (41)
Am <sup>2+</sup> /Am	-2.88 (41)
Gd <sup>3+</sup> /Gd	-2.95 (41)
La <sup>3+</sup> /La	-3.11 (41)

Table 1.4: Proposed Redox Couple Pairings

Pairing	Active Couple	Noble Couple	$\Delta E^{o'}$ (V)	Similar Pairing
1	La <sup>3+</sup> /La	Gd <sup>3+</sup> /Gd	0.16	Pu/Am OR Pu/Rare Earth
2	La <sup>3+</sup> /La	Th <sup>4+</sup> /Th	0.56	U/Rare Earth
3	Mg <sup>2+</sup> /Mg	U <sup>3+</sup> /U	0.36	U/Pu

signals can be observed and evaluated. Furthermore, key parameters of ions can be calculated for binary-analyte mixtures. This can provide insight to the extent to which additional analytes affect the behavior of each individual analyte. Additionally, these parameters and effects can be encapsulated in models that could be used in SBS or as a means to measure ion compositions and behavior. The experimental work scope seeks to examine the effect of standard reduction potential spacing on the capability to electrochemically measure concentrations and model ion behaviors. The analysis will involve the separation of ion signals, the application of multivariate analysis to electrochemical data, and the validation of an electrochemical model, DREP (Deposition Rate using Electrode Potentials) which was derived specifically for metal electrodeposition in eutectic LiCl-KCl. By using multiple approaches to electrochemical measurements and their analyses, concentrations can be determined for both ions and promising approaches can be identified.

## **1.6. Dissertation Structure**

Aside from Chapters 2 and 3, the remainder of the dissertation is presented in chronological order of when the work was performed. Therefore, earlier chapters represent work that was performed first. Chapter 2 discusses key electrochemical relations, theory, and considerations specifically relating to electrodeposition. These equations and principles will be used and referenced throughout the chapters involving the analysis and interpretation of the data. Chapter 3 discusses the practical aspects and details of the experimental setup and procedures. Before the experiments were performed, some computational modeling was performed to guide the design of experiments and test ideas for analyzing experimental data. The computational work is

discussed in Chapter 4 and includes a detailed description of the multivariate technique, Principle Component Regression (PCR), used throughout this dissertation. The LiCl-KCl-GdCl<sub>3</sub>-LaCl<sub>3</sub> mixture was the first quaternary salt system that was tested and the results of that investigation are presented first in Chapter 5. Then the next salt matrix, LiCl-KCl-ThCl<sub>4</sub>-LaCl<sub>3</sub>, is presented and discussed in Chapter 6. The last salt matrix to be tested and presented is the LiCl-KCl-UCl<sub>3</sub>-MgCl<sub>2</sub> system in Chapter 7. A specific discussion for each system is found in respective chapters. Chapter 8 presents the hydrodynamic electrochemical measurements made for the intent of validating DREP. Chapter 9 concludes the dissertation with a general discussion about the application of studied electrochemical techniques to actual ER salt and the future work needed to apply these techniques in an ER.

## 2. ELECTROCHEMISTRY

About 230 years ago, an anatomist, Luigi Galvani, accidentally touched his steel scalpel to a brass hook holding a frog leg in place. Upon contact, the frog leg twitched and the first observation of electrochemistry was made in a laboratory. Galvani chalked it up to biological processes that he termed “animal electricity.” Meanwhile, Alessandro Volta replicated his experiments and contended that the electricity was generated by the two dissimilar metals, not from some process inside the animal. He demonstrated his theory by building voltaic piles, essentially alternating metal plates sandwiched by cardboard soaked in salt water. Both were right. Galvani’s approach gave birth to neurophysiology, while Volta’s approach made him the father of modern day electrochemistry (51).

The voltaic pile was the first form of continuous electric current, a necessity for the development of electrochemistry and most modern technologies. A string of scientists picked up Volta’s work, and the field of electrochemistry has grown to include applications in almost every field. To describe the behavior of ions in electrochemical cells, electrochemistry blends three fundamental subjects: (1) thermodynamics, (2) reaction kinetics, and (3) mass transport. From these fundamental matters, all electrochemical relations and techniques are derived. To facilitate the discussion of the fundamentals matters in the context of electrochemistry, some general terms and concepts of electrochemistry need to be introduced.



## 2.1. General Overview

Electrochemical studies are usually carried out in an electrochemical cell. An electrochemical cell consists of four main components: a power supply, an anode, a cathode, and an electrolyte. The power supply drives the reaction. Material is oxidized at the anode and reduced at the cathode. The electrolyte serves as a conducting medium to allow the flow of ions in the cell. In electroanalytical work, the power supply is replaced by a potentiostat which can manipulate and measure the potential and/or current at an electrode. This electrode is called the working electrode (WE) and can function as either the anode or cathode depending upon the conditions imposed. A counter electrode (CE) serves as the other electrode to close the electrochemical circuit. An additional electrode called a reference electrode (RE) is commonly used in electroanalytical work. The RE provides a stable potential to which the WE can be compared or referenced. In molten LiCl-KCl eutectic, the RE is commonly based on the silver-silver chloride (Ag/AgCl) redox couple or a chlorine ion and gas [Cl<sup>-</sup>/Cl<sub>2</sub> (1 atm)] redox couple.

Typically, electroanalytical techniques are interested in the reaction of a certain species, called an analyte, that liberates (oxidation) or consumes (reduction) electrons at the WE. These reactions are generally represented by the following reaction and written so that the forward reaction is the reduction reaction.



In molten LiCl-KCl eutectic, the analyte is usually a monoatomic metal ion, which applied to (2.1) results in the following equation



Of primary concern, in this work, is the reduction of metal ions to metal in the zero

valance state or the reverse reaction of oxidation from metal to a metal ion. Applying the assumption of zero valance state to (2.2) (i.e.,  $p = 0$ ), the equation simplifies to the following expression



The current flowing in an electrochemical cell can be a result of two processes: faradaic or nonfaradaic. A faradaic process involves the transfer of electrons across the electrolyte-electrode interface, like the reactions previously discussed. Nonfaradaic processes do not transfer electrons, such as adsorption and desorption of ions or double-layer (capacitive) charging. Hence, Faraday's law cannot be applied to these processes.

The potential applied to a cell or an electrode can drive a reaction to occur if the voltage is sufficient. However, a portion of the applied potential is devoted to overcoming resistances, the most significant often being solution resistance. This loss of or drop in applied voltage is referred to as ohmic or IR drop and can be calculated with Ohm's law:

$$E = IR_s \quad (2.4)$$

If the ohmic drop is uncompensated and significant, then it can introduce errors in measurements and analysis.

## 2.2. Thermodynamics

Thermodynamics provides information concerning the possibility of a certain reaction or phase formation. Typically, the spontaneity of a reaction is determined using the change in Gibbs free energy ( $\Delta G$ ) which can be calculated as follows:

$$\Delta G = \Delta G^{\circ} + RT \ln(Q) \quad (2.5)$$

where  $Q$  is the reaction quotient which is the product of the activity of products raised to their stoichiometric coefficient divided by the product of the activity of the reactants raised to their stoichiometric coefficient. In electrochemistry, a reaction typically involves oxidation or reduction via electron transfer. If (2.5) is adapted for (2.3), it becomes the following equation

$$\Delta G = \Delta G^\circ + RT \ln \left( \frac{a_{M^{p+}}}{a_{M^{n+}}} \right) \quad (2.6)$$

The activity of an electron in a metal “can be disregarded because the electron concentration never changes appreciably” (52).

In electrochemistry, it is more convenient to work with potential ( $E$ ) than  $\Delta G$ . The reversible (infinite resistance) potential is related to  $\Delta G$  by the charge passed, as shown below

$$\Delta G = -nFE \quad (2.7)$$

The negative sign is due to the electrochemical convention that a positive potential corresponds to a spontaneous process. Combining (2.6) and (2.7) results in the *Nernst* equation:

$$E = E^\circ - \frac{RT}{nF} \ln \left( \frac{a_{M^{p+}}}{a_{M^{n+}}} \right) \quad (2.8)$$

The potential obtained with this equation can be considered the equilibrium potential or open-circuit (i.e.,  $I = 0$ ) potential of a redox reaction. The activity can be defined by (2.9) and (2.10)

$$a = \gamma x \quad (2.9)$$

$$a = \gamma_c \frac{C}{C^o} \quad (2.10)$$

If  $p = 0$  in (2.8) and the reduced metal does not interact with the electrode or another reduced metal, then its activity can be assumed to be one. However, if multiple metals are deposited and form an alloy, then activity cannot be assumed to be one. In molten salt electrochemistry, (2.9) is prevalently used.  $C^o$  is the concentration at which the standard reduction potential ( $E^o$ ) is defined which is commonly 1 molal (53). It is common for the activity coefficient to be grouped with  $E^o$  to form the apparent or formal standard reduction potential ( $E^{o'}$ )

$$E^{o'} = E^o - \frac{RT}{nF} \ln \left( \frac{\gamma_{M^{p+}}}{\gamma_{M^{n+}}} \right) \quad (2.11)$$

Thus,  $E^{o'}$  is only constant if the activity coefficients do not depend strongly on composition over the concentration range of interest. Again, if  $p = 0$ , then activity coefficient is assumed to be unity unless an intermetallic forms in the deposit.

### 2.3. Reaction Kinetics

For a single-step, elementary reaction, its net rate is given by the resulting law as applied to (2.3)

$$r = k_f C_{M^{n+}} - k_b C_{M^{p+}} \quad (2.12)$$

Rate constants are known to have an Arrhenius relationship with temperature and activation energy

$$k = A e^{-\frac{E_a}{RT}} \quad (2.13)$$

If the reaction is occurring in a condensed phase, then activation energy can be related to a “standard Gibb’s free energy of activation” (52) which can be related to potential, as

expressed in (2.14) and (2.15)

$$k_f = k^o \exp \left[ -\frac{\alpha n F}{RT} (E - E^{o'}) \right] \quad (2.14)$$

$$k_b = k^o \exp \left[ \frac{(1-\alpha) n F}{RT} (E - E^{o'}) \right] \quad (2.15)$$

The transfer coefficient ( $\alpha$ ) accounts for the amount of the potential that promotes the reduction (forward) reaction. The standard rate constant ( $k^o$ ) is the forward and backward rate constants at equilibrium under the special conditions that  $E = E^{o'}$  and the bulk concentrations are equal ( $C_{M^{n+}}^b = C_{M^{p+}}^b$ ). If (2.14) and (2.15) are substituted into (2.12) and Faraday's law is applied ( $I = nFAr$ ), then the faradaic current related to the reaction in (2.3) is given by (2.16)

$$I = nFAk^o \left( C_{M^{n+}} \exp \left[ -\frac{\alpha n F}{RT} (E - E^{o'}) \right] - C_{M^{p+}} \exp \left[ \frac{(1-\alpha) n F}{RT} (E - E^{o'}) \right] \right) \quad (2.16)$$

This expression is very useful, but can be expressed more conveniently. This is done by introducing a term called the exchange current density ( $i_o$ ). This is derived by evaluating (2.16) at equilibrium (i.e.,  $I = 0$ ) and results in the equation below

$$i_o = nFAk^o \left( C_{M^{n+}}^b \right)^{1-\alpha} \left( C_{M^{p+}}^b \right)^\alpha \quad (2.17)$$

Substituting (2.17) into (2.16) and multiplying by negative one yields the *current-overpotential* relationship in the IUPAC convention (53)

$$I = i_o \left( \frac{C_{M^{p+}}}{C_{M^{p+}}^b} \exp \left[ \frac{(1-\alpha) n F}{RT} \eta \right] - \frac{C_{M^{n+}}}{C_{M^{n+}}^b} \exp \left[ -\frac{\alpha n F}{RT} \eta \right] \right) \quad (2.18)$$

If the surface and bulk concentrations are assumed to be equal, (2.18) simplifies to the more common *Butler-Volmer* equation. The overpotential ( $\eta$ ) is defined as the offset of

potential from the equilibrium potential

$$\eta = E - E^{o'} + \frac{RT}{nF} \ln \left( \frac{C_{M^{p+}}^b}{C_{M^{n+}}^b} \right) \quad (2.19)$$

### 2.3.1. Metal Electrodeposition Kinetics

In the case of  $p = 0$ , a metal is deposited onto the electrode. In this case, the concentration of reduced metal ( $C_M$ ) becomes a common term in the derived kinetic expressions because most literature assumes that the reduced product is soluble when deriving kinetic expressions. However, this can be confusing because most metals are insoluble in molten salts and other electrolytes. Various methods of handling the deposited metal concentration have been proposed when deriving the kinetic expressions. The simplest approach is to assume that the bulk and surface concentration of the deposited metal are the same (54). Another option is to use the standard concentration as a “scaling concentration” (55). However, the first approach only resolves the problem in a few situations and neither approach may hold when two metals deposit and alloy with each other. A more general, albeit more complicated, approach derives an alternative current-overpotential relation by starting with a slightly different rate law (56):

$$R = k_f a_{M^{n+}} - k_b a_M \quad (2.20)$$

By following the same steps in the previous derivation in Section 2.3, this modification of the *current-overpotential* relation is derived in the American or polarographic convention (56):

$$I = i_o \left( \frac{a_{M^{n+}}}{a_{M^{n+}}^b} \exp \left[ -\frac{\alpha nF}{RT} \eta \right] - \frac{a_M}{a_M^b} \exp \left[ \frac{(1-\alpha)nF}{RT} \eta \right] \right) \quad (2.21)$$

where the modified definitions of  $i_o$  and  $\eta$  are given in (2.22) and (2.23).

$$i_o = nFAk^o \left( a_{M^{n+}}^b \right)^{1-\alpha} \left( a_M^b \right)^\alpha \quad (2.22)$$

$$\eta = E - E^o + \frac{RT}{nF} \ln \left( \frac{a_M^b}{a_{M^{n+}}^b} \right) \quad (2.23)$$

In this case, activity of the metal deposits can be assumed to be one if the metal deposits are pure. This assumption is not valid when less than a monolayer of a metal is deposited on a foreign substrate or when two metals deposit and interact to form a metallic solution. In such cases, the activity of the metals would need to be determined for (2.21) to be applied. A simple model for activity of a monolayer of metal is that the activity of the metal is proportional to the fraction of the electrode surface covered by the metal (52)

$$a_M = \frac{\gamma_M A_M}{A} \quad (2.24)$$

However, this ignores nucleation effects which are common for deposited metals. For co-deposition of two metals, this would require significant study of the metal-metal interactions under the electrochemical cell conditions to determine the activities of metals.

## 2.4. Mass Transport

The kinetic expressions in (2.18) and (2.21) have two separate terms for concentrations or activity in the bulk and at the electrode surface illustrating that the conditions are different at the surface of an electrode than in the bulk solution. These differences are the result of mass transport mechanisms, namely diffusion, convection, and migration. All of these mechanisms are encapsulated in the flux ( $j$ ) of an ion.

The flux is driven by the difference in the electrochemical potential ( $\bar{\mu}$ ) which is related to the chemical potential ( $\mu$ ).

$$\bar{\mu} = \mu^{\circ} + RT \ln(a) + nF\phi \quad (2.25)$$

The last term accounts for electrical properties of the ion's environment and is related to the charge of the ion and absolute potential ( $\phi$ ) of the ion's location. Ions in a solution will move or generate a flux to relieve gradients in the electrochemical potential. Thus molar flux can be calculated from the gradient of electrochemical potential and any convective flow

$$j = -\frac{CD}{RT} \nabla \bar{\mu} + Cv \quad (2.26)$$

Substituting (2.25) into (2.26) yields this general equation

$$j = -CD \nabla \ln(a) - CD \frac{nF}{RT} \nabla \phi + Cv \quad (2.27)$$

By introducing a few assumptions to (2.27), it simplifies to the *Nernst-Planck* equation

$$j = -D \frac{dC}{dx} - CD \frac{nF}{RT} \frac{d\phi}{dx} + Cv \quad (2.28)$$

The assumptions in (2.28) include one-dimensional transport and the equivalence of activity and concentration. The three terms in equations (2.27) and (2.28) represent first diffusion, then migration, and lastly convection. Using Faraday's law ( $I = nFAj$ ), the flux can be related to current.

In certain cases, flux equations can be simplified by neglecting migration, convection or both. The convection term can be neglected in stagnant fluids. The migration term is less significant at low currents due to a weaker electric field (i.e., lower overpotentials). The addition of a supporting (i.e., not electroactive) electrolyte can almost completely remove migration effects. Supporting electrolytes can also reduce the effects of ohmic drop in the solution. If the convection and migration terms are neglected,



then the Nernst-Planck equation reduces to Fick's first law

$$j = -D \frac{dC}{dx} \quad (2.29)$$

Fick's second law is derived from the first law and is the origin of almost every electroanalytical expression derivation

$$\frac{dC}{dt} = D \frac{d^2C}{dx^2} \quad (2.30)$$

Thus, it should be noted that derived electroanalytical expressions in the next section apply the assumption of a stagnant fluid and negligible migration unless otherwise noted.

## 2.5. Electroanalytical Methods

Electroanalytical methods are techniques that investigate the behavior of an ion of interest called an analyte by manipulating potential or current and measuring the other. Four terms are frequently used when describing electroanalytical techniques: amperometry, potentiometry, voltammetry, and coulometry. Amperometry controls the potential, usually holding it steady at one setting, and measures the current. It can be considered a subclass of voltammetry. Potentiometry measures potential while controlling the current. Voltammetry, like amperometry, measures current and controls potential, but voltammetric techniques involve more than fixing the potential at a set value. It can include scanning the potential or a series of potential steps with a certain pattern. Coulometry measures the charge under potential controlled conditions and can affect the bulk characteristics of the electrochemical solution. The first three techniques are carried out under small  $A/V$  conditions meaning that the area of the electrode is small enough that the current passed does not alter the properties of bulk volume. Coulometric techniques can pass sufficient current to alter the conditions in the bulk solution.

As discussed in Section 1.4, the techniques of interest in this project are chronoamperometry (CA), cyclic voltammetry (CV), open-circuit potentiometry (OCP) and normal pulse voltammetry (NPV). The derivations of key relations for each of the listed techniques are reviewed in this section along with key assumptions. These methods involve applying a waveform and measuring the response which can typically be described by a derived equation. A summary of each technique is provided in Table 2.1.

### 2.5.1. Chronoamperometry

CA involves stepping the potential from an initial potential level at which no faradaic current flows to a potential at which faradaic current flows and is diffusion-limited. The diffusion-limited current can be determined by solving Fick's second law with the accompanying boundary conditions

$$\frac{dC_{M^{n+}}}{dt} = D_{M^{n+}} \frac{d^2C_{M^{n+}}}{dx^2} \quad (2.31)$$

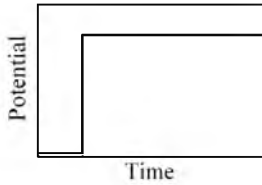
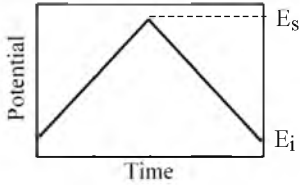
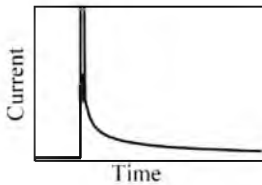
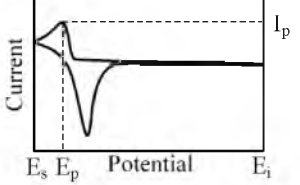
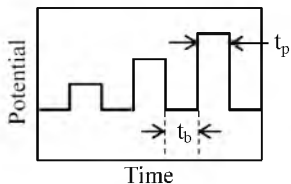
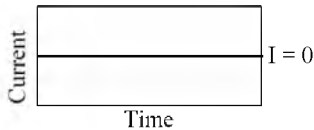
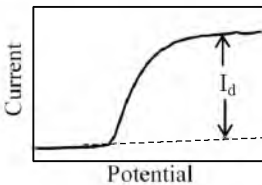
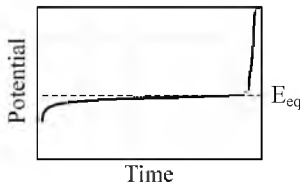
$$C_{M^{n+}}(x, 0) = C_{M^{n+}}^b \quad (2.32)$$

$$\lim_{x \rightarrow \infty} C_{M^{n+}}(x, t) = C_{M^{n+}}^b \quad (2.33)$$

$$C_{M^{n+}}(0, t) = 0 \quad (2.34)$$

From (2.31), it is evident that one-dimensional semi-infinite linear diffusion is assumed. Also, the diffusion coefficient is assumed to be spatially independent and, therefore, independent of concentration, because concentration is varying with location as demonstrated by the boundary conditions, (2.33) and (2.34). The time, at which the potential is stepped, is considered zero (i.e.,  $t = 0$ ) and no faradaic current is flowing. Thus, metal ions are uniformly distributed throughout the solution as indicated by the

Table 2.1 Summary of electroanalytical methods

	<b>Chronoamperometry (CA)</b>	<b>Cyclic Voltammetry (CV)</b>
<b>Waveform</b>		
<b>Response</b>		
<b>Key Equations</b>	$I(t) = nFA \sqrt{\frac{D}{\pi t}} C$	$I_p = 0.6105A \sqrt{\frac{(nF)^3 D v}{RT}} C$
	<b>Normal Pulse Voltammetry (NPV)</b>	<b>Open-Circuit Potentiometry (OCP)</b>
<b>Waveform</b>		
<b>Response</b>		
<b>Key Equations</b>	$I_d = nFA \sqrt{\frac{D}{\pi t_p}} C$	$E_{eq} = E^{o'} + \frac{RT}{nF} \ln \left( \frac{x_o}{x_R} \right)$

initial condition, (2.32). After the potential is stepped, the concentration of metal ions in the bulk solution is unaffected, if the small A/V conditions hold. If the potential step is large enough, the metal ions at the surface will be immediately and completely reduced resulting in diffusion controlling the rate of reduction.

The solution to (2.31) is obtained by using Laplace transforms and the initial and boundary conditions which results in a temporal concentration profile. The concentration profile can be differentiated and substituted into Fick's first law which can be related to current by Faraday's law. This results in the *Cottrell* equation

$$I(t) = nFAC_{M^{n+}}^b \sqrt{\frac{D_{M^{n+}}}{\pi t}} \quad (2.35)$$

According to the equation, the current approaches infinity at very short times and zero at very long times. However, in practice, this is not observed. At longer times, natural convection can prevent the current from completely decaying away. For metal electrodeposition, the area can also increase substantially which can cause the current to depart from Cottrellian behavior. On a short timescale, limitations in the equipment can prevent measurement and recording of very large currents. Additionally, double layer charging can significantly distort the current signal at very short times.

To illustrate these important limitations and considerations, a CA measurement as part of the experiments in this work (mixture D6) is displayed in Figure 2.1 along with the current predicted by the Cottrell equation. Initially, it can be seen that the potentiostat and its software is unable to capture the high current predicted by the Cottrell equation. Then after 1 s, the magnitude of the current ceases to decay and actually grows. This is due to the growth of metal deposits on the WE, which increases its surface area.

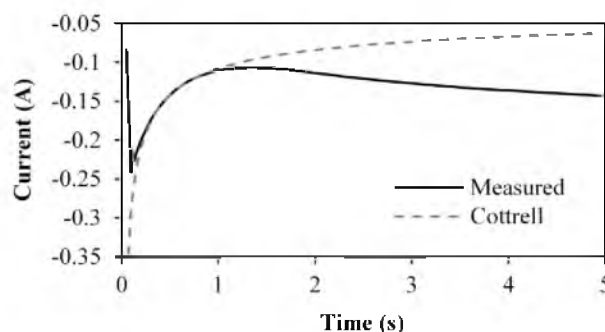


Figure 2.1 Chronoamperogram at  $E = -2.08$  V vs Ag/AgCl(1 wt%) for mixture D6 (4.69 wt% GdCl<sub>3</sub>, 2.45 wt% LaCl<sub>3</sub>,  $T = 500^{\circ}\text{C}$ , Area = 0.35 cm<sup>2</sup>)

### 2.5.1.1 Double-Layer Charging

The interfaces between the electrode and solution tend to behave as capacitors due to excess charges in the vicinity of the interface. When the interface is perturbed from its initial state, significant amount of the current is consumed by the nonfaradaic process of charging the double layer. For a potential step, the resulting charging current is given by the following expression

$$I(t) = \frac{\Delta E}{R_s} e^{-t/R_s C_d} \quad (2.36)$$

The change in potential or the size of the potential step is represented by  $\Delta E$ . The product of  $R_s$  and  $C_d$  is commonly referred to as the time constant. Until the time is equivalent to 5 time constants, the current due to double layer charging cannot be neglected.

The eutectic LiCl-KCl salt has been found to have a resistance from 0.4-2  $\Omega/\text{cm}$  depending on the analytes present and their concentration based on published results (57–60). Additionally, the reported capacitance of the double layer in molten LiCl-KCl is 0.1-2.0 mF/cm<sup>2</sup> (57,59). The absolute resistance for a particular setup depends upon the distance between the RE and WE. The absolute capacitance depends on the surface area of the WE. Two approaches to reduce the effect of capacitive current are, first, to sample

the current at sufficiently long time that capacitive currents can be neglected and second, to design your cell to reduce the time constant for capacitive currents. Table 2.2 shows the variation of the  $R_s C_d$  (RC) time constant with WE and RE spacing and WE surface area, if the largest values of  $2 \Omega/\text{cm}$  and  $2.0 \text{ mF}/\text{cm}^2$  are assumed for a conservative estimate of the RC time constant. It should be noted that the reduction of the RC time constant has practical limitations. For example, too close of spacing could cause shorting when metal deposits form on the WE or inhibit diffusion of ions to the WE surface.

### 2.5.1.2 Semi-Infinite Linear Diffusion

Cylindrical electrodes are commonly used for electrochemical measurements in molten LiCl-KCl eutectic. If the cylindrical electrode is small enough radially or the current is sampled for a short enough time, then the semi-infinite linear diffusion assumption may introduce significant error. To illustrate the possible error that could be introduced by assuming linear diffusion at cylindrical electrodes, the current response for CA was calculated for diffusion at a planar electrode using (2.35) and at a cylindrical electrode at various diameters using the following approximation which is accurate within 1.3% (52)

Table 2.2 Variation of the time constant (in ms) with electrode spacing and WE area

		Surface Area ( $\text{cm}^2$ )				
		0.2	0.4	0.6	0.8	1
Electrode Spacing (cm)	0.2	0.2	0.3	0.5	0.6	0.8
	0.4	0.3	0.6	1.0	1.3	1.6
	0.6	0.5	1.0	1.4	1.9	2.4
	0.8	0.6	1.3	1.9	2.6	3.2
	1	0.8	1.6	2.4	3.2	4.0

$$I = \frac{nFADC}{r_o} \left[ \frac{2 \exp\left(-0.05\sqrt{4\pi Dt}/r_o\right)}{\sqrt{4\pi Dt}/r_o} + \frac{1}{\ln\left(5.2945 + 0.7493\sqrt{4Dt}/r_o\right)} \right] \quad (2.37)$$

The calculated current responses for planar and cylindrical diffusion at the WE with a diameter of 0.5 mm are plotted in Figure 2.2. Initially, the current responses are identical. However, at longer times, the current responses diverge. Thus, if the current was measured using a 0.5 mm WE and sampled at 1 s, but analyzed using the Cottrell equation, which assumes planar diffusion, the current would be underestimated by about 10%. This would in turn overestimate the concentration of ions in the molten salt by 11%. As shown in Figure 2.3, the error can be reduced by sampling at shorter times or using a cylindrical WE with a larger diameter. This could also be resolved by using the same diameter WE for measuring the diffusion coefficients and determining concentrations which would effectively embed the error in the diffusion coefficient.

Further analysis of Figure 2.2 reveals another approach that could minimize the error introduced by using cylindrical WE. If the current is plotted versus the inverse of the square root of time, then the slope would be proportional to concentration according to the Cottrell equation. The slopes of both curves are nearly identical (<0.001%) in Table 2.3. Practically, all of the difference between the curves is found in the y-intercept.

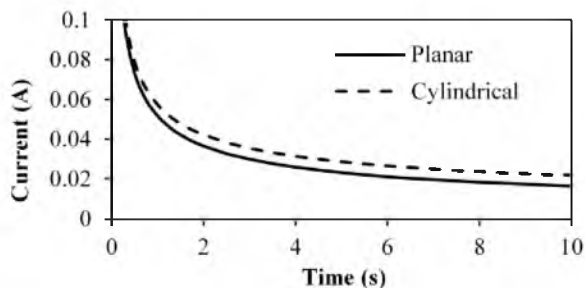


Figure 2.2 Calculated current response with planar and cylindrical diffusion for CA

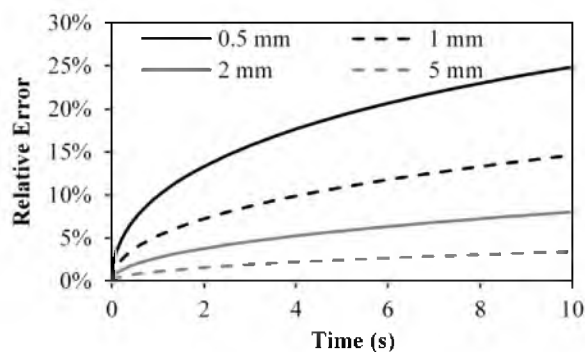


Figure 2.3 Relative error of the calculated current at a cylindrical WE of various diameters (0.5-5 mm) as a function of sampling time

Table 2.3 Comparison of the regressions of current with  $t^{-1/2}$

Planar		Cylindrical	
Slope	Y-int	Slope	Y-int
0.051642	0	0.051643	0.005713

### 2.5.2. Cyclic Voltammetry

The general concept of CV is to scan the potential over a range of potential values at a certain rate and measure the current response. As the potential reaches values at which species in the solution or on the electrode will react, the changes in the current are measured accordingly. When the maximum or minimum potential is reached the direction of the scan is reversed creating a cycle of the potential. A closely related technique called linear sweep voltammetry (LSV) simply scans in one direction and terminates when the end potential is reached.

By scanning the potential, a wealth of information is obtained about the system. However, to extract meaningful quantitative information from CV, the analysis can become extensive and complex. The derivations of key analytical expressions and their assumptions are dependent on the standard rate constant of an ion ( $k^0$ ), the scan rate ( $\nu$ )



and solubility of the reduced species in the electrolyte. The parameter,  $\Lambda$ , which is the ratio of intrinsic reaction rate to mass transfer rate, is often used to determine whether the reaction is reversible, quasi-reversible or irreversible, as shown in Table 2.4. Thus, reversible processes are characterized by fast reaction kinetics relative to mass transfer, and irreversible processes are characterized by slow reaction kinetics relative to mass transfer. Quasi-reversible processes are in between the two extreme conditions and use certain functions/profiles to blend the reversible and irreversible functions. This classification of reversibility is specific to electrochemistry and should not be confused with *chemical* reversibility. In fact, this kind of reversibility is frequently referred to as *electrochemical* reversibility/irreversibility.

Once a system has been properly identified, the appropriate equations can be applied to characterize the properties of the ions or determine concentrations. These equations are summarized in Table 2.5. The derivations, assumptions, characteristics and application of these functions are discussed in the following sections.

### 2.5.2.1 Reversible

The listed conditions for determining the type of CV define reversibility by the speed of the electron transfer process relative to the scan rate ( $\nu$ ) of the potential. The rationale is that if electron transfer is fast, then equilibrium is achieved rapidly and can be assumed at the electrode surface. In such a case, the Nernst equation can be applied

Table 2.4 Criteria for Reversibility, Quasi-reversibility and Irreversibility (61)

Reaction Type	Dimensionless	For T=773 K, D=10 <sup>-5</sup> cm <sup>2</sup> /s, $\alpha=0.5$
Reversible	$\Lambda > 15$	$k^o > 0.32\sqrt{n\nu}$ cm/s
Quasi-Reversible	$15 > \Lambda > 10^{-2(1+\alpha)}$	$0.32\sqrt{n\nu} > k^o > 2.12 \times 10^{-5}\sqrt{n\nu}$ cm/s
Irreversible	$\Lambda < 10^{-2(1+\alpha)}$	$k^o < 2.12 \times 10^{-5}\sqrt{n\nu}$ cm/s

Table 2.5 Summary of expressions used for CV

Reversible (soluble-soluble) (63)	Reversible (soluble-insoluble) (64)
<i>Randles-Sevick</i>	<i>Berzins-Delahay</i>
$I_p = 0.4463A \sqrt{\frac{(nF)^3 D_o v}{RT}} C$	$I_p = 0.6105A \sqrt{\frac{(nF)^3 D_o v}{RT}} C$
$E_p = E^{o'} + \frac{RT}{nF} \ln \left( \sqrt{\frac{D_R}{D_o}} \right) - 1.109 \frac{RT}{nF}$	$E_p = E^{o'} + \frac{RT}{nF} \ln(x_o) - 0.854 \frac{RT}{nF}$
$\Delta E_p =  E_p - E_{p/2}  = 2.20 \frac{RT}{nF}$	$\Delta E_p =  E_p - E_{p/2}  = 0.774 \frac{RT}{nF}$
Quasi-Reversible (soluble-soluble) (61)	Irreversible (soluble)* (65)
$\Lambda = \frac{k^o}{\sqrt{D_o^{1-\alpha} D_R^\alpha \frac{nFv}{RT}}}$	<i>Delahay</i>
$I_p = I_p(rev)K(\Lambda, \alpha)$	$I_p = 0.4958nFA \sqrt{\frac{\alpha nF D_o v}{RT}} C$
$E_p = E^{o'} + \frac{RT}{nF} \ln \left( \sqrt{\frac{D_R}{D_o}} \right) - \varepsilon(\Lambda, \alpha) \frac{RT}{nF}$	$E_p = E^{o'} + \frac{1}{b} \left( 0.780 + \ln \left( \frac{\sqrt{D_o b v}}{k^o} \right) \right) b = \frac{\alpha nF}{RT}$
$\Delta E_p =  E_p - E_{p/2}  = \Delta(\Lambda, \alpha) \frac{RT}{nF}$	$\Delta E_p =  E_p - E_{p/2}  = 1.857 \frac{RT}{\alpha nF}$
* An irreversible peak assumes that the potentials are such that anodic processes are negligible	

$$E = E^{o'} - \frac{RT}{nF} \ln \left( \frac{C_{M^{p+}}}{C_{M^{m+}}} \right) \quad (2.38)$$

This version of the Nernst equation uses the concentration convention for activity and the standard apparent potential which includes the activity coefficients. The potential in this case is also a function of time

$$E = E_i - vt \quad (2.39)$$

For simplicity only the LSV potential function is included here. The CV function only varies slightly and has been demonstrated elsewhere (62). The steps and assumptions are identical with only the modified CV function of potential inserted.

**2.5.2.1.1 Soluble product.** A potential scan can be thought of as a series of

infinitesimally small potential steps. Hence, (2.31)–(2.33) are applied for the oxidized species. The last boundary condition, (2.34), is not applied because the small potential steps do not necessarily produce complete diffusion control. Instead, another boundary condition is formulated by substituting (2.39) into (2.38) resulting in an equation that can relate the oxidized and reduced species to one another as a function of time.

Another difference is that the flux of the reduced species needs to be considered, because the overpotential may not be large enough to neglect it. Thus, boundary conditions for the reduced species are similar to the oxidized species, except that the bulk concentration of the reduced species is replaced by zero, if it is initially absent. The sum of the flux of the oxidized and reduced species is then set equal to zero

$$D_{M^{n+}} \frac{dC_{M^{n+}}}{dx} + D_{M^{p+}} \frac{dC_{M^{p+}}}{dx} = 0 \quad (2.40)$$

This is solved using Laplace transforms and results in a function whose maximum (i.e., peak current) can be characterized by the *Randles-Sevcik* equation (62,63)

$$I_p = 0.4463A \sqrt{\frac{(nF)^3 D_{M^{n+}} \nu}{RT}} C_{M^{n+}} \quad (2.41)$$

**2.5.2.1.2 Insoluble product.** However, if the product is a deposited metal which is insoluble in the solution, there is no flux due to the reduced species which alters the solution. Since no reduced species is present in the solution, (2.40) is replaced by (2.31). The initial condition and first boundary condition are (2.32) and (2.33) respectively. The second boundary condition is formulated from a modified form of (2.38)

$$E = E^{\circ'} + \frac{RT}{nF} \ln(C_{M^{n+}}) \quad (2.42)$$

(2.39) is substituted into (2.42) and solved for  $C_{M^{n+}}$  to formulate the second boundary

condition. Again, Laplace transforms are performed to obtain an equation that describes the reduction peak of the oxidized metal ion. The peak current of the resulting function is described by the *Berzins-Delahay* equation (64)

$$I_p = 0.6105A\sqrt{\frac{(nF)^3 D_{M^{n+}} \nu}{RT}} C_{M^{n+}} \quad (2.43)$$

Both for soluble and insoluble, the Nernst equation is invoked to generate the needed boundary conditions. Thus, it is assumed that the potential is scanned at a slow enough rate to allow equilibrium to be achieved at the electrode surface. If  $k^o$  is large, this can be achieved at high scan rates. Inevitably, as scan rate increases, the assumption of equilibrium at the WE surface will become invalid. This is well demonstrated by  $\text{UCl}_3$  in LiCl-KCl eutectic, as shown in Figure 2.4 which plots the peak current versus the square root of scan rate from mixture N1 (see Section 3.3.2 and Appendix A for more details). Initially, the peak current is linear with the square root of scan rate, as predicted by (2.41) and (2.43). However, between 0.2 and 0.3 V/s, the peak begins to depart from the linear trend, this is most likely due to the transition from reversibility to quasi-reversibility (59,66,67). As a result, the peak heights are lower. Thus the limits of reversibility and irreversibility need to be known and well understood so that the correct equations are applied to determine concentrations.

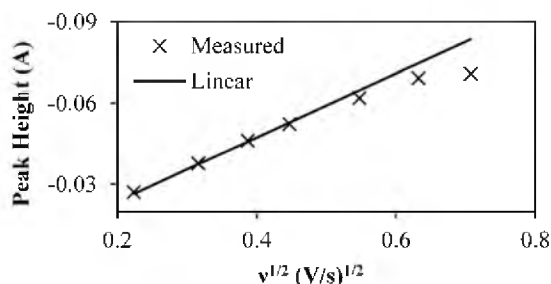


Figure 2.4 Plot of  $\text{U}^{3+}$  reduction peak height versus square root of scan rate for mixture N1 (0.83 wt%  $\text{UCl}_3$ , WE Area =  $0.73 \text{ cm}^2$ ,  $T = 500^\circ\text{C}$ )

Linearity of peak height with scan rate is insufficient to deduce reversibility. As seen in Table 2.5, reversible and irreversible expressions are proportional to the square root of scan rate. The unique feature of electrochemical reversibility is the independence of peak potential ( $E_p$ ) with scan rate. The half-peak width ( $\Delta E_p$ ) can also be used to determine reversibility, irreversibility, or quasi-reversibility. However, at these potentials, a significant amount of current could be flowing which may require compensation for ohmic drop to accurately diagnose the reversibility of the system. Thus (2.4) must be applied to determine the contribution of resistance to the potential at the WE. Once quantified, that amount needs to be subtracted from the observed or applied peak potential to obtain the accurate peak potential value.

Neglecting to account for ohmic drop may result in mischaracterizing the reaction mechanism, as demonstrated for mixture N1 in Figure 2.5, which plots the peak potential of  $UCl_3$  in LiCl-KCl at different scan rate with and without accounting for ohmic drop. The resistance of the salt was measured to be  $0.3 \Omega$  using the current interrupt method. When the potential is not adjusted for ohmic drop, it appears that the peak potential is a function of scan rate. However, if the adjustment is made, peak potential has almost no

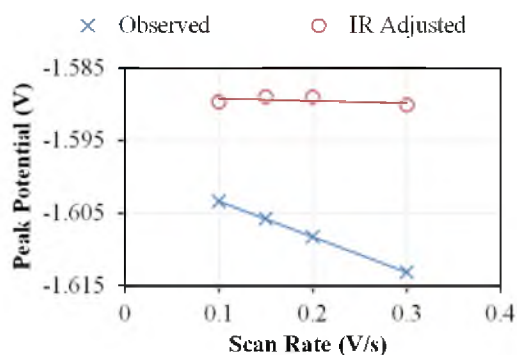


Figure 2.5 Peak potential of  $U^{3+}$  with and without adjustment for ohmic (IR) drop for mixture N1

trend with scan rate. This adjustment is also required in order to obtain accurate  $E^{o'}$  values from the peak potential.

### 2.5.2.2 Quasi-Reversible

Quasi-reversible peaks are the most difficult to analyze. The analysis essentially attempts to characterize the peak by blending the reversible and irreversible functions in Table 2.5 by using the  $K$ ,  $\mathcal{E}$ , and  $\Delta$  functions or profiles, which are available in literature (52,61). These profiles were derived by solving (2.40) with same initial and boundary conditions that were used for the reversible and soluble product CV case with the exception that the Nernst equation cannot be applied. Instead the flux is equated to reaction rate as derived in (2.16). This results in the following expression

$$D_{M^{n+}} \frac{dC_{M^{n+}}}{dx} = k^o \left( C_{M^{n+}} \exp \left[ -\frac{\alpha nF}{RT} (E - E^{o'}) \right] - C_M \exp \left[ \frac{(1-\alpha)nF}{RT} (E - E^{o'}) \right] \right) \quad (2.44)$$

By solving (2.40) with the new boundary condition, Masuda and Ayabe (61) showed that the peak shape was a function of  $\alpha$  and a parameter,  $\Lambda$

$$\Lambda = \frac{k^o}{\sqrt{D_o^{1-\alpha} D_R^\alpha \frac{nFv}{RT}}} \quad (2.45)$$

As seen in Table 2.5, the  $K$ ,  $\mathcal{E}$ , and  $\Delta$  functions depend on  $\alpha$  and  $\Lambda$ . Unfortunately, only limited work has been done on quasi-reversible systems that involve an insoluble product. Only the anodic dissolution peak has been characterized, because the deposition peak is complicated by nucleation which inhibited the application of the expression derived by Avaca (55) for quasi-reversible electrodeposition. Unfortunately, the anodic peak for metal dissolution is not as repeatable as the cathodic peak since it depends on the potential at which the CV was reversed and the morphology of the metal deposit. Thus,

the applicability of the quasi-reversible equations in Table 2.5 is questionable for the soluble-insoluble reaction.

By examining the properties of the  $K$  function, which is a scaling function for peak current, some insight can be gained into its applicability to soluble-insoluble systems. At sufficiently low scan rates,  $K$  is equal to one and constant making the peak current function equivalent to the reversible expression. At a sufficiently high scan rate,  $K$  is equal to a constant value which depends on the value of  $\alpha$  so that the resulting peak current expression is equivalent to the irreversible case. Essentially, at high scan rates,  $K$  is the ratio of the irreversible over the reversible peak function. By comparing the reversible and irreversible equations in Table 2.5, it can be seen that the only variations in the peak current expression are the leading constants and the  $\alpha$  term in the irreversible expression. Thus, a constant ratio results if the irreversible expression is divided by the reversible expressions which results in 0.78 for soluble-soluble reactions and 0.57 for soluble-insoluble reactions, if  $\alpha = 0.5$ . Hence, theoretically,  $K$  function will not result in the irreversible expression if applied to the Berzins-Delahay equation.

This theoretical exercise can be verified using experimental data. Marsden and Pesic (68) studied cerium electrodeposition and plotted the peak height for the reduction of  $\text{Ce}^{3+}$  to Ce metal versus the square root of scan rate from a very low scan rate ( $\sim 5$  mV/s) to a very high scan rate ( $\sim 1.5$  V/s) at 653 K. This plot is reprinted here in Figure 2.6 in which the peak current clearly transitions from one linear curve to another linear curve as the scan rate increases. They explained that this is “characteristic of a quasi-reversible system where the system displays Nernstian behavior at low scan rates but transitions to irreversibility at high scan rates” (68). They also calculated that at 653 K,

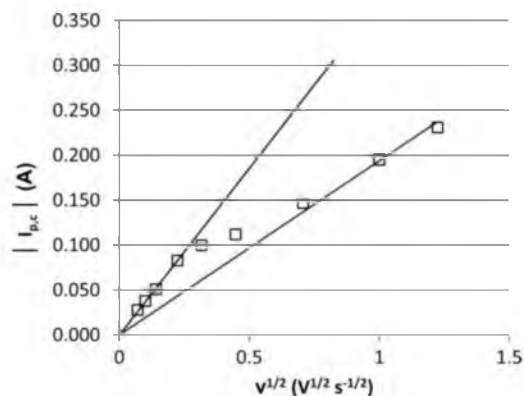


Figure 2.6 Reduction peak height of  $\text{Ce}^{3+}$  as a function of the square root of scan rate (Figure 5 in original work) (68). Reproduced by permission of The Electrochemical Society.

$\alpha = 0.48$ . Thus, the slope at high scan rates (irreversible region) divide by the slope at low scan rates (reversible region), should be close to 0.78 for the  $K$  function to apply.

The slopes of the reversible and irreversible lines were determined to be 0.369 and 0.193 respectively, by digitizing the two lines in Figure 2.6. This results in a ratio of 0.52 which is much closer to 0.57 calculated earlier. Thus, it appears that the  $K$  function is inapplicable to soluble-insoluble reactions in theory and practice.

### 2.5.2.3 Irreversible

The irreversible system is simplified by the assumption that the backward reaction is negligible reducing (2.44) to the following expression

$$D_{M^{n+}} \frac{dC_{M^{n+}}}{dx} = k^c \left( C_{M^{n+}} \exp \left[ -\frac{\alpha n F}{RT} (E - E^o) \right] \right) \quad (2.46)$$

The same problem is solved, (2.40), with the same boundary and initial conditions, as was done for the quasi-reversible process with the exception that (2.46) is used instead of (2.44). The benefit of irreversible peaks is that kinetic information can be calculated. As seen in Table 2.5, the kinetic parameters,  $\alpha$  and  $k_o$ , are found in the expressions for



irreversible CV peaks. In addition to those expressions, another equation for the peak current can be derived in terms of the peak potential, as shown below

$$I_p = 0.227nFAC_{M^{n+}}k_o \exp\left[-\frac{\alpha nF}{RT}(E_p - E^{o'})\right] \quad (2.47)$$

Thus, a plot of the  $\ln(I_p)$  versus  $E_p - E^{o'}$  should yield a linear plot with a slope and an intercept proportional to  $\alpha n$  and  $k_o$ , respectively.

### 2.5.3. Normal Pulse Voltammetry

Since the waveform for NPV is more complex than other techniques, it is reprinted and enlarged in Figure 2.7 for convenience. NPV is essentially a series of CA tests with a “rest” time in between during which no species is electroactive with exception of reduced species reoxidizing. This is particularly important for metal electrodeposition at nonpolarographic (i.e., nonrenewing) electrodes. By holding the potential for an extended period of time ( $t_b$ ) at a base potential ( $E_b$ ) sufficiently positive, the deposited metal can reoxidize and the nonpolarographic electrode can return to its original state. However, not only does the electrode surface need to be allowed to return to its original state, the diffusion layer needs to as well. Otherwise, an accumulation or depletion of ions in the diffusion layer could cause the magnitude for the diffusion-limited current ( $I_d$ ) to be artificially increased or decreased. In the case of depletion, the

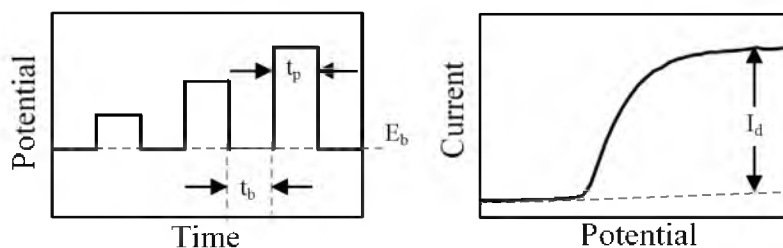


Figure 2.7 Enlargement of NPV waveform (left) and response (right) from Table 2.1

curve takes on a peak shape, like in CV. In some cases, the time required to renew the conditions near and at the electrode can require more than 10 s, resulting in a much slower turnaround time for NPV (>10 min) than for CV (<1 min).

After renewing the electrode surface and diffusion layer, the potential is pulsed into the region where the species of interest are electroactive for a short amount of time ( $t_p$ ), and the current is sampled at the end of the pulse. Because this is a potential step method, all of the considerations and limitations discussed for sampling CA also apply here. Thus,  $t_p$  should be long enough that nonfaradaic currents do not significantly contribute, but should also be short enough that electrode area does not increase.

The measured response for NPV is on the right in Figure 2.7 and plateaus when the current is diffusion limited.  $I_d$  is directly proportional to concentration as predicted by the Cottrell equation, (2.35), except that  $t$  is replaced by  $t_p$ .

#### 2.5.4. Open-Circuit Potentiometry

OCP is facilitated by the Nernst equation, (2.8). Thus equilibrium conditions need to be imposed (i.e., zero current) while the potential is measured. Either the mole fraction or molar concentration convention can be used. It may be advantageous to remain in the molar concentration convention, since all the other methods were derived based on the molar concentration convention. In the case of metal deposition, some metal needs to be initially present on the electrode in order to record its open-circuit potential with its ion. This could be done by using an electrode made of the metal of interest or by pre-depositing some metal on an inert electrode, then enforcing an open-circuit. The measured potential at open-circuit should vary logarithmically with concentration or mole fraction. If this behavior can be verified for molten salt mixtures of interest, then it could

be used to determine concentration.

#### 2.5.4.1 Reference Electrode Conversions

When applying the OCP method, there is a logarithmic relation between concentration and measured potential. This approach to concentration measurement can be highly sensitive to small errors in experimental setup or analysis approach. For example, the conversion between reference electrode potentials can be critical, but there is inconsistency in the literature regarding that conversion. The potential at a  $\text{Cl}^-/\text{Cl}_2(1 \text{ atm})$  electrode, the standard chlorine electrode (SCE), is the de facto reference potential that can be directly related to standard free energy of formation. But it is impractical to use such an electrode as the reference. Alternatively, an Ag/AgCl reference electrode is a popular choice for molten chloride systems. But to compare studies on the same basis and calculate activity coefficients, the potential of such an Ag/AgCl reference electrode must be converted to the SCE scale. The potential of an Ag/AgCl electrode depends upon the concentration of AgCl in the RE. Thus, in most works, the potentials measured versus an Ag/AgCl RE are converted to the SCE potential. In literature there are a couple formulas and data sets for converting from the Ag/AgCl to the SCE. Unfortunately, they are inconsistent as shown in Table 2.6.

Table 2.6 Potential difference from Ag/AgCl to SCE

Source	1 wt% (0.39 mol%)	1 mol%	5 mol %
Yang-Hudson (69)	-1.223	-1.167	-1.071
Shirai et. al. (70)	-1.073	-1.017	-0.921
Shirai et. al.*	-1.182	-1.119	-1.012
Mottot (71)	-1.368	-1.305	-1.198
Lantelme-Berghoute (58)	-1.201	---	-1.049
*Corrected for sharp density increase near 100 mol% AgCl			

The Yang-Hudson reference measured the potential of the Ag/AgCl potential experimentally against a SCE and is commonly cited in published experimental studies of ions in molten LiCl-KCl eutectic. Shirai et al. (70) performed similar work to Yang-Hudson, but measured significantly different potential values under similar conditions. However, when extrapolated with respect to molarity as opposed to mol% to account for the density variations, their value for  $E^{o'}$  produced results more consistent with Yang-Hudson. An expression derived by Mottot has also been used and is quite different from the other sources. The Lantelme-Berghoute reference measured the reduction potentials of  $\text{La}^{3+}$  and  $\text{Gd}^{3+}$  ions directly with a SCE. The reduction potentials of these ions were measured by the author using a 1 wt% and 5 mol% AgCl RE. The values reported in the last row of Table 2.6 are the calculated difference between the measured and reported values by Lantelme and Berghoute which agree well with the Yang-Hudson reference.

Such large variation in reported potentials is problematic. This could indicate that small changes in experimental conditions could drastically affect the recorded potential values. To demonstrate the impact of small potential variations, a hypothetical situation is proposed. If a  $E^{o'}$  value is converted to the SCE using the Yang-Hudson data by an author, then it will need to be converted back to the Ag/AgCl scale to be applied to an open-circuit potential measured versus Ag/AgCl RE. However, if the factor used to convert  $E^{o'}$  is inconsistent, off calibration or the potential of the RE has slightly shifted, then the concentration determined from the open-circuit potential could be quite inaccurate. In this case, the error relative to the Yang-Hudson source introduced by inconsistent conversion values are reported in Table 2.7, but a shift in the RE potential would have the same effect. The errors are quite large even when the conversion factors

Table 2.7 Effect of RE conversion on mol% measurement

Source	Shirai et. al.	Shirai et al.*	Mottot	Lantelme-Berghoute
Relative Error	86000%	1300%	-100%	169%

used only varied by tens of millivolts. Thus, if OCP is to be employed as a concentration measurement technique a highly stable RE needs to be employed.

## 2.6. Summary

This chapter has reviewed the known fundamental theory of electrochemical kinetics, transport, and thermodynamics from literature and has discussed its application to the study of electrodeposition of metal, which is the main subject of interest for this thesis. Derived equations for electroanalytical techniques have been reviewed, examining their assumptions and applicability to electrodeposition. It is essential to examine the measured data to ensure that assumptions applied are consistent across all data sets and concentrations and with the method employed (i.e., CA, CV, etc.); otherwise, variations in data will be manifested that are unrelated to concentration variations. This could skew calibration curves or alter diffusion coefficient values. Thus, before calculating key parameters or constructing calibration curves, certain checks have been revealed to be necessary from examining the assumptions of the electrochemical methods. The checks, equations, and theory will be applied and referenced in Chapters 5-7 in which electrochemical data is analyzed.

### 2.6.1. Chronoamperometry

The key assumption in CA is that semi-infinite linear diffusion limits the process. Diffusion limitation can be checked by overlaying the temporal current profile measured

at various potentials. When the profiles overlap, then the process is confirmed to be diffusion limited since the Cottrell equation is independent of potential. The semi-infinite linear diffusion assumption can introduce error into this work since cylindrical electrodes are used for the WE. Thus, the diameter of WE was held constant within each test matrix to standardize the error.

### 2.6.2. Cyclic Voltammetry

Key characteristics of CVs vary with scan rate resulting in three categories: (1) reversible, (2) quasi-reversible, and (3) irreversible. Plotting the peak height versus the square root of scan rate can be used to identify transitions from reversibility to quasi-reversibility or from quasi-reversibility to irreversibility. Linear trends of peak height with the square root of scan rate indicate either a reversible or irreversible region. The CVs need to be further classified by analyzing the trend of peak potential with scan rate. If the peak potential is independent of scan rate then reversibility can be concluded, otherwise the system is irreversible. Since expressions for quasi-reversible soluble-insoluble cyclic voltammetry have not successfully been derived and derivation of such expression is beyond the scope of this dissertation, the quasi-reversible region is avoided.

### 2.6.3. Normal Pulse Voltammetry

The key to NPV is the assumption that the WE surface and diffusion layer has been restored to the original state. The main inhibitor to the renewal of the WE surface is persistent metal deposits. If significant deposits accumulate the NPV signal will not plateau, but continually increase. The depletion of ions is most likely to be cause of non-renewal of the diffusion layer since it is conducted in stagnant media. This would be

indicated by the current slightly decreasing at more extreme potentials. Thus, these phenomena are observed, the base time will be increased, to the extent possible, which will allow more time for the renewal of the WE surface or diffusion layer.

#### 2.6.4. Open-Circuit Potentiometry

OCP measurements are subject to shifts in potentials due to drift over time or differences in the composition of AgCl in the REs used. To check the consistency of the RE potential, the potential of lithium ion deposition and/or dissolution of the WE will be used. These values should be consistent because their bulk properties change very little from one experiment to another.

It is clear from examining the theory that the behavior of ions at each concentration needs to be determined to avoid introducing variances in the data unrelated to concentration. Thus, in addition concentration measurements, the analyses and verification methods discussed will also be performed as part of the results when clear boundaries between signals are discernable.

In addition to the theory or electrochemistry, some limited practical considerations have been mentioned for applying electrochemistry to molten salt cells. The next chapter covers in more detail the practicalities of designing and performing electrochemical experiments in molten salts. Furthermore, the application of the electroanalytical theory discussed in this chapter on multi-analyte mixtures depends upon good separation of the signals. The method of separating the signals is particular to analyte pairings and is discussed in the chapters relevant to the pairing results.

### 3. EXPERIMENTAL METHODS

In 1907, having characterized alpha particles ( $\alpha$ -particles) (i.e., stopped by paper, positively charge), Ernst Rutherford used them to investigate the atom. Rutherford commissioned Hans Geiger and Ernst Marsden to perform some experiments saying: “Why not let [Marsden] see if any  $\alpha$ -particles can be scattered through a large angle?” (72). The popular model of the atom at the time was the plum pudding model in which the atom is supposed to be electrons surrounded by a soup of equal positive charge, much like blueberries in a muffin or plums in pudding. If the plum pudding model was accurate, then alpha particles would travel more or less straight through the gold foil. Indeed, Rutherford later confessed that “I may tell you in confidence that I did not believe that [ $\alpha$ -particles] would be [scattered through a large angle]” (72).

Undaunted, Marsden and Geiger shot alpha particles through a gap in a lead screen at gold foil and observed the scatter of  $\alpha$ -particles which produced a flash on ZnS screen. They surrounded the gold foil almost completely with ZnS, not to neglect any scattering angle. To their surprise, they observed flashes on the same side from which the  $\alpha$ -particles were emitted. This was physically impossible in the plum pudding model. It would be “as if you fired a 15-inch shell at a piece of tissue paper and it came back and hit you” (72). After two years of stewing over the results of the experiment and trying to reconcile them with various models of the atom including a negatively charged core model, Rutherford proposed a new model of the atom—a dense core or nucleus of



positive charge surrounded by electrons—and verified it with further experiments.

Key to the discovery of the nucleus of the atom was thorough and sound experimental methods. As in Rutherford's work, rigorous and methodical experimental work is needed to verify and develop electrochemical models for determining the composition of electrorefiner (ER) salt. This chapter describes the efforts made to establish the appropriate mix of capabilities in a new academic laboratory, called the Nuclear Pyrometallurgy Laboratory (NPL), so that the electrochemical behavior of multi-analyte mixtures in eutectic LiCl-KCl can be observed, measured and compared to theories and models. Several models may be needed to adequately describe the behavior of the molten salt samples depending on the conditions. Thus, this chapter discusses the considerations and adjustments made in designing and conducting experiments in order to improve the control of experimental conditions and the repeatability of measurements. This control and repeatability helps elucidate which models best measure molten salt compositions under certain conditions.

### **3.1. General Equipment and Design**

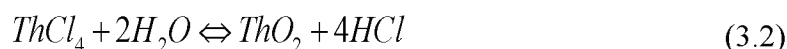
#### **3.1.1. Inert Atmosphere Glovebox**

The chloride salts used in these experiments can be highly hygroscopic, particularly LiCl and ThCl<sub>4</sub>. Most chloride salts will react with water at or below 500°C to form oxides and oxychlorides (MOCl<sub>x</sub>) which will precipitate out or create additional electrochemical signals causing possibly interference. Either case is undesirable. Even the presence of oxygen in the molten salt can have undesirable effects. Willit et al. reported that cathode deposits containing UO<sub>2</sub> were observed in the electrorefining of uranium due to residual oxygen in the system which reacted to form UO<sub>2</sub><sup>2+</sup> (73). The precipitation or

presence of oxides or oxychlorides in the salt complicates and may prevent the accurate determination of ion concentrations in the salt. The formation of oxides and oxychlorides is well illustrated by  $\text{ThCl}_4$ .

A stock of  $\text{ThCl}_4$  was received (Fisher Scientific) that had been grossly contaminated by water. A mass of 26 g of that salt was dried in an inert argon atmosphere at  $300^\circ\text{C}$  for 36 h. A mass of 11 g was lost and the remaining salt was porous and flakey. The salt was ground up and 0.28 g of the dried  $\text{ThCl}_4$  was added to 58.34 g of eutectic  $\text{LiCl-KCl}$  and CVs were applied to the molten salt at  $500^\circ\text{C}$ . The resulting cathodic peak current density at a scan rate of 100 mV/s was one-tenth of the reported (74) peak current density at the same scan rate, temperature and concentration (0.43 wt%).  $\text{ThO}_2$  is insoluble in eutectic  $\text{LiCl-KCl}$  (75). Thus, it is probable that only one-tenth of the salt remained as  $\text{ThCl}_4$  or  $\text{ThOCl}_2$  after drying.

Further analysis revealed that  $\text{ThCl}_4$  undergoes oxidation reactions when heated in the presences of water, as shown below



These reactions are both thermodynamically favorable at or below  $300^\circ\text{C}$  as evidenced by their change in free energy plotted in Figure 3.1 (76). At about  $225^\circ\text{C}$ , the formation of  $\text{ThO}_2$  becomes more favorable, but both are favorable before moisture can be driven off at  $100^\circ\text{C}$ . The thermal gravimetric analysis (TGA) in Figure 3.2 reveals that significant weight is lost when wet  $\text{ThCl}_4$  is heated to  $300^\circ\text{C}$ . The thermodynamic and TGA data are strong indicators that reaction (3.1) and/or (3.2) did occur during the heating process.

The  $\text{ThCl}_4$  case is not unique, in fact, most metal chlorides have favorable

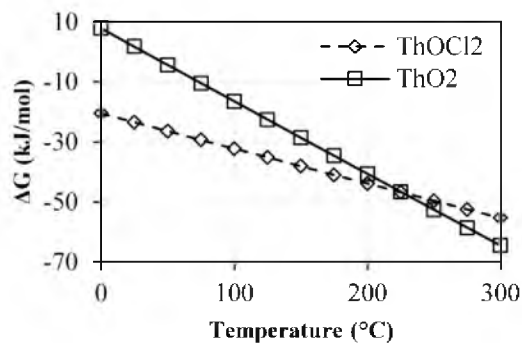


Figure 3.1 Gibb's free energy change for formation of  $\text{ThOCl}_2$ , (3.1), and  $\text{ThO}_2$ , (3.2), from 0 to 300°C

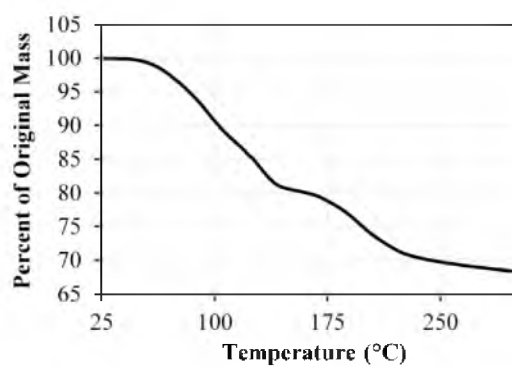


Figure 3.2 Weight loss of wet  $\text{ThCl}_4$  when heated from 25 to 300°C at 5°C/min in a TA Instruments Q600 TGA-DSC with ultra high purity argon cover gas flowing at 100 mL/min

thermodynamics for the formation of either oxides or oxychlorides when moisture or oxygen is present, even in small amounts (76,77,78). Thus, the electrochemical studies in this work were carried out in a PureLab HE glovebox obtained from Innovative Technologies, as pictured in Figure 3.3. Ultra-high purity argon was used as the working gas for the glovebox which is equipped with gas purification module to scrub out  $\text{O}_2$  and  $\text{H}_2\text{O}$ . This provided a highly pure inert atmosphere for the electrochemical experiments in this work. The  $\text{O}_2$  and  $\text{H}_2\text{O}$  levels were always maintained below 1 ppm and in most cases at 0.1 ppm.



Figure 3.3 Picture of glovebox in which electrochemical test were conducted

### 3.1.2. Chiller

Heating of salts in the glovebox necessitate an adequate heat removal system. The recirculation line of the glovebox was fitted with a heat exchanger. A 50/50 mix of water and ethylene glycol acted as the coolant and was fed into the shell-side of the heat exchanger. The coolant was recirculated by a Polyscience WhisperCool™ Chiller (Item No. 6160M21A130D) which was typically maintained at 2°C if only one furnace was running and -15°C if two furnaces were running in the glovebox. The glovebox at all times was maintained below 120°F to avoid the degradation of seals on the glovebox.

### 3.1.3. Potentiostat

An Autolab PGSTAT302N potentiostat/galvanostat was used to conduct the electroanalytical procedures. Six copper posts on the back of the glovebox allowed for the connection of the potentiostat leads to patch cords (McMaster-Carr, Part No. 6927K44) inside the glovebox, which were connected to the electrodes. The potentiostat

leads were configured in a 3-probe setup, as shown in Figure 3.4. The sense electrode (S) lead was coupled with the working electrode (WE) lead and connected to the copper post that was connected to the WE with a patch cord. The reference electrode (RE) and counter electrode (CE) leads were connected to their respective copper posts and electrodes, as well.

A Gamry Interface 1000 was also used momentarily with mixture R4 to measure the uncompensated resistance using electrochemical impedance spectroscopy (EIS) for comparison to current interrupt (*i*-interrupt) measurements of resistance. As shown in Table 3.1, the values for resistance differed slightly depending on the method.

#### 3.1.4. Electrochemical Cell

Some specifics of the electrochemical cell varied as improvements were made and different analytes were used, but general design of the cell remained the same. The specific variations are discussed later. All electrochemical tests were performed in a Kerr Electro-melt Furnace (Model No. 35224) which heated the salt to 500°C +/- 2°C. A K-

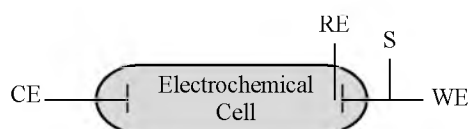


Figure 3.4 Potentiostat lead configuration

Table 3.1 Comparison of resistance value obtained by *i*-interrupt and EIS

Test	Resistance (mΩ)	
	<i>i</i> -interrupt (-1.65 V)	EIS (-1.65 V)
1	302.8	373.4
2	309.8	370.1
3	316.3	372.3
Avg	309.6	371.9
Std Dev	6.783	1.686

type thermocouple from Omega (Part No. KQXL-116G-12) was used to monitor the temperature of the salt. Control of the furnace was maintained with the preinstalled Pixsys ATR142 controller. The interior of the furnace consists of a graphite crucible and heating element. A large 99.6% alumina crucible (AdValue Technology, Part No. AL-2250) was inserted into furnace to act as liner in case of cracking in the primary crucible containing the molten salt. The primary crucible was a smaller 99.6% alumina crucible (AdValue Technology, Part No. AL-2100). A 2-in. hole was drilled into the lid of the furnace. Then a plug was inserted into the hole in the furnace lid. The plugs have ports to allow for sampling and the passage of electrodes and thermocouples.

### 3.2. Test Matrices

In order to test the limits of the electrochemical methods in measuring concentrations in binary-analyte systems, multiple redox couple pairings were tested with various differences in  $E^{o'}$ . The tested pairings are displayed in Table 3.2 along with the difference in their  $E^{o'}$  values ( $\Delta I$ ). These pairings were selected to simulate possible pairings of interest in an actual ER. In an ER, the elements that oxidize into the salt are active fission products (FP), rare earths and actinides. The key elements to measure are uranium and plutonium, but the FP, rare earths and actinides have the potential to interfere with the signals of uranium and plutonium. The pairings possibly simulated are listed in Table 3.2.

Table 3.2 Redox couple pairings

Pairing	Active Couple	Noble Couple	$\Delta E^{o'}$ (V)	Simulated Pairings
1	La <sup>3+</sup> /La	Gd <sup>3+</sup> /Gd	0.16	Pu/Am, Pu/Rare Earths
2	La <sup>3+</sup> /La	Th <sup>4+</sup> /Th	0.56	U/Rare Earths
3	Mg <sup>2+</sup> /Mg	U <sup>3+</sup> /U	0.36	U/Pu

The targeted concentrations for each pairing are displayed in Tables 3.3-3.5. Each pairing has a unique set of alphanumeric IDs to identify the crucible used and test number in the crucible. This ID is used throughout the dissertation to identify each mixture tested and referred to as the mixture ID. The salt added to each crucible was weighed out on a scale (A&D FX-3000i) inside the glovebox. The La/Gd pairing was the first pairing tested since the chemicals were readily available. Next, tests on the La/Th pairing were initiated by another researcher (see Acknowledgments). Simultaneously, tests on the Mg/U pairing were conducted. It should be noted that the weight percent of  $\text{MgCl}_2$  is much lower than the other elements due to the significant difference in molecular weight. Also, the  $\text{ThCl}_4$  concentrations are slightly lower due to the significant loss during the drying processes. During tests on the La/Gd pairing, certain drawbacks in the experimental design and procedures were identified and altered. The La/Th tests started before these changes were implemented, but the alterations were fully implemented for the Mg/U pairing. These changes are discussed in the next section. Additionally, a detailed list of experimental conditions and setup for each mixture is listed in Appendix A.

### **3.3. Electrochemical Cell Design**

Two designs were used which differed slightly from one another. The initial experimental design was used for the La/Gd and La/Th pairings, and the final experimental design was used for the Mg/U pairings. All of the general design considerations discussed earlier in Section 3.1.4 apply to both designs. Only the differences in designs are discussed here.

Table 3.3 Targeted concentration values for the La/Gd pairing (X = not tested)

		LaCl <sub>3</sub> (wt%)				
		0.0	1.0	2.0	2.5	3.0
GdCl <sub>3</sub> (wt%)	0.0	X	C1	X	X	X
	1.5	E1	D1	B3	X	B4
	1.7	E2	D2	X	X	X
	3.0	X	D3	A3	X	A4
	3.5	X	X	X	D7	X
	4.5	X	D4	D5	X	D6

Table 3.4 Targeted concentration values for La/Th pairing (X = not tested)

		LaCl <sub>3</sub> (wt%)				
		1.0	2.0	3.0	4.0	5.0
ThCl <sub>4</sub> (wt%)	0.5	U1	U2	U3	U4	U5
	1.0	V1	W7	X	X	U6
	1.5	V2	X	W6	X	U7
	2.0	V3	X	X	W5	U8
	2.5	W1	W2	W3	W4	U9

Table 3.5 Targeted concentration values for Mg/U pairing (X = not tested)

		MgCl <sub>2</sub> (wt%)					
		0.0	0.3	0.6	0.9	1.2	1.5
UCl <sub>3</sub> (wt%)	0.0	X	R1	X	X	M1	X
	1.0	N1	N2/O1	O2	O3	O4	O5
	2.0	X	P1/S1	R2	X	X	Q1
	3.0	X	P2/S2	X	R3	X	Q2
	4.0	X	P3/S3	X	X	S8	Q3
	5.0	X	P4/S4	P5/S5	P6/S6	P7/R4	P8/S7



### 3.3.1. Initial Design

In this configuration, the plug used was a solid alumina block with three holes for each electrode. Photos of the alumina plug (AdValue Tech) are provided in Figure 3.5. The temperature was checked before and after a test by removing the WE and inserting the thermocouple (TC) through the same hole. Samples would be taken after removing the CE.

A picture and drawing of the complete electrochemical cell are displayed in Figure 3.6.  $\text{GdCl}_3$  (99.99% anhydrous, Alfa-Aesar),  $\text{LaCl}_3$  (99.99% anhydrous, Alfa-Aesar), and  $\text{ThCl}_4$  (Fisher Scientific, Cat. No. T-110) were added to eutectic  $\text{LiCl-KCl}$  (99.99% anhydrous, SAFC Hitech) salt to form mixtures of various compositions. The RE consisted of a thin-walled, 10 mm OD, borosilicate NMR tube (Sigma-Aldrich, Part No. Z274771-1PAK), a 1 mm Silver Wire (99.9%, Alfa-Aesar), and salt mixture consisting of eutectic  $\text{LiCl-KCl}$  and 1 wt%  $\text{AgCl}$  (99.9% anhydrous, Strem Chemicals) for La/Gd pairings. For La/Th pairing, the concentration of  $\text{AgCl}$  (99.997% Premion®, Alfa-Aesar) was increased to 5 mol% (0.83 mol/kg). The WE was a 1 mm Mo wire (99.94%, Alfa-Aesar) for La/Gd pairing and 2 mm W rod (99.95%, Alfa-Aesar) for La/Th pairing. In either case, the WE was sheathed in alumina tubes, excluding the ends, and immersed 0.6-1.8 cm in the salt. The 1 mm Mo wire was sheathed in 1.6 mm ID



Figure 3.5: Top (left) and side (right) view of alumina plug

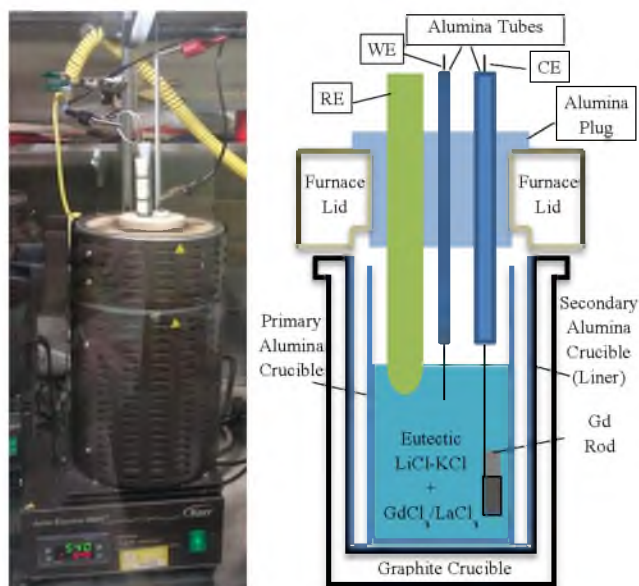


Figure 3.6 Initial electrochemical cell design used for La/Gd and La/Th pairings

alumina tube (McMaster-Carr, Part No. 8746K11) and the 2 mm W rod was sheathed in a 1/8" ID alumina tube (McMaster-Carr, Part No. 8746K14). The WE was rinsed in 3N HCl, polished by 2000-grit silicon carbide paper and anodically cleaned before conducting electrochemical tests. The CE was a stainless steel rod and basket containing the more noble metal in each pairing—a 6.35 mm x 25.4 mm Gd metal rod (99.9% Alfa-Aesar) or Th metal turnings (International Bio-Analytical Industries Inc., Part No. T-1002-50). For tests on only  $\text{LaCl}_3$  in LiCl-KCl, the CE was a 2 mm W rod fully immersed in the salt. The salt depth ranged from 3.0-3.5 cm. Electrodes were all held in place on the plug using Viton® Fluorelastamer O-rings (McMaster-Carr) that fit snug on the electrodes or alumina sheaths.

A couple of issues with the initial experimental setup came to light while performing electrochemical tests on La/Gd pairing and the first couple of experiments on La/Th pairing. Slight alterations to the experimental setup in Figure 3.6 were made before commencing tests on U/Mg pairings to address these issues.

### 3.3.2. Final Design

In the final design, the alumina plug was replaced. The holes in the alumina plug were not precise or straight. There was a slight slant to the WE/TC hole which caused the WE to be at an angle. The imprecise holes also allow electrodes to sway, making it difficult to align the electrode precisely and consistently. The alumina plug is expensive to machine and customize. Thus, straightening the WE/TC hole was cost-prohibitive, and only one hole configuration was possible. This limited the configuration and type of electrodes that can be used.

The replacement plug was two steel plates (Sharpe Products, Part No. 9445) which were machined to have identical port configurations that aligned precisely, preventing the tilting and swaying of electrodes. The two plates sandwiched the furnace lid and were attached using all-thread and nuts. Alumina tubes (McMaster-Carr) that fit snug in the holes were cemented in place. A photo of the new plug configuration is shown in Figure 3.7. Steel is easy to machine and alumina tubes are affordable and readily available from multiple suppliers. Thus customization and repair of the lid is quick and affordable. In this case, four ports were used to allow for sampling, additions

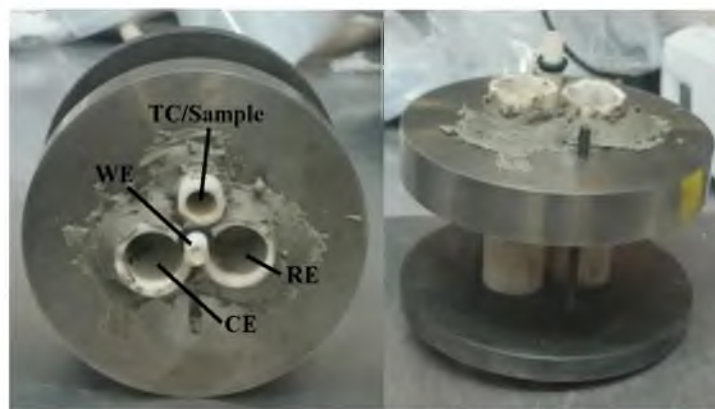


Figure 3.7 Top (left) and side (right) view of final plug design with steel plates and alumina tubes used for Mg/U pairing

and temperature measurements without disturbing the electrode setup.

Salt mixtures were made using  $\text{MgCl}_2$  (99.99% anhydrous, Alfa-Aesar) and  $\text{UCl}_3$  (received from Y-12) and eutectic  $\text{LiCl-KCl}$ . The CE electrode contained U metal sheets (International Bio-Analytical Industries Inc.). The U metal sheets came with a black layer that flaked off easily. The black layer was supposed to be an oxide layer and was polished in the glovebox until the U metal was silvery-gray.

### **3.4. Experimental Methods**

#### 3.4.1. Surface Area Measurement

The WE area is challenging to quantify because the electrochemical measurements are carried out inside the furnace without any means of visually confirming the immersion depth of the WE. Two methods were used to measure the WE area. The dip method was used for the La/Gd and La/Th pairings. The vertical translator was used for the U/Mg pairing.

##### *3.4.1.1 Dip Method*

The surface area was initially measured by immersing a cold WE into the molten salt, then withdrawing it immediately. The molten salt would freeze to the surface indicating the immersion depth of the electrode. This coupled with the radius of the WE rod ( $r_o$ ) enabled the quantification of the WE surface area. However, this method depends upon the consistency of WE placement. Furthermore, surface tension effects may affect the frozen salt length resulting in incorrect characterization of the immersion depth. For example, when the rod is inserted it takes some force to break the surface of the salt, this may result in the depression of the surface as in aqueous media (see Figure

3.8a). Moreover, if the molten salt is a wetting fluid, some wicking of the fluid up the WE rod may occur over time (see Figure 3.8b).

Observations of the WE indicated that depression of the surface and wicking may be a possibility. After being immersed in molten salt bearing  $\text{UCl}_3$  for prolonged periods, the WE was marked, removed, and allowed to cool, then reimmersed the same distance and removed quickly. An image of a WE after this process is displayed in Figure 3.9 which shows a thick frozen layer on a 2 mm diameter rod with a thin layer of salt to the right approximately 2 mm long. If that length is assumed to be the wetting height ( $h$ ), then the contact angle ( $\theta$ ) of wetting can be calculated using the surface tension ( $\gamma$ ) for LiCl-KCl ( $0.117 \text{ J/m}^2$ ) (79), density ( $\rho$ ) of eutectic LiCl-KCl ( $1.62 \text{ g/cm}^3$ ) (60) and the equation derived for a meniscus on a small cylinder (80)

$$h = r_o \sin \theta \left[ \ln \left\{ \frac{4}{\sqrt{\rho g / \gamma r_o}} (1 + \cos \theta) \right\} - 0.55721 \right] \quad (3.3)$$

This results in a contact angle of  $71^\circ$ . Assuming a triangular shape, the width of wetting at half-height is 0.69 mm. This is significantly wider than the diffusion layer thickness ( $\delta$ ) which grows with time (i.e.  $\delta = \sqrt{D\pi t}$ ) in a stagnant fluid. A  $\delta$  of 0.69 mm is not achieved until 152 s assuming a diffusion coefficient of  $10^{-5} \text{ cm}^2/\text{s}$ . Thus, significant electrochemistry can occur in the wetted region of the WE. Typically, an immersion



Figure 3.8 Illustration of surface tension effect for (a) immersing WE into salt and (b) wetting on a static WE



Figure 3.9 Picture of WE after prolonged and quick immersion

depth of 1 cm was used resulting in a possible 20% error.

This error may have caused a slight increase in the calculated diffusion coefficients, but the concentration measurements should still be valid since the same method to measure area was employed for all La/Gd and La/Th tests. However, the inconsistency of this surface area measurement may have introduced additional variance into the data resulting in less precise measurements.

#### *3.4.1.2 Vertical Translator*

In order to improve the surface area measurements, a vertical translator (Velmex Inc., Part No. XN10-0012-M02-71) was equipped with an arm to hold the WE so that the immersion depth of the WE could be incremented with a precision of 0.005 mm. The initial arm design was two eighth-inch steel rods with alligator clips attached at the ends. However, friction between the alumina sheath and the WE would cause the steel rods to bend. Thus, two half-inch aluminum rods were used as the arms and the WE was secured with nylon tipped set screws. The new experimental configuration is pictured in Figure 3.10 with the final plug and vertical translator. The interior of the furnace is configured exactly as it is illustrated in Figure 3.6.

Using the vertical translator, the WE immersion depth was incrementally decreased. At each immersion depth, cyclic voltammetry (CV) was performed. Highly



Figure 3.10 Photo of final experimental setup used for Mg/U pairings

linear plots of peak height versus the change in immersion depth of the WE in the molten salt, similar to the one shown in Figure 3.11, were obtained using this technique. The absolute immersion depth of the WE is obtained from the y-intercept of the regression of the change in the WE depth with respect to peak height. This method has been compared to the initial method of dipping a cold WE into molten salt. When compared to the thick frozen layer, significant differences (1-2 mm) in the immersion depth between the two methods have been observed. However, agreeable results are obtained when the wetted length, as shown in Figure 3.9, is compared to the immersion depth calculated from the

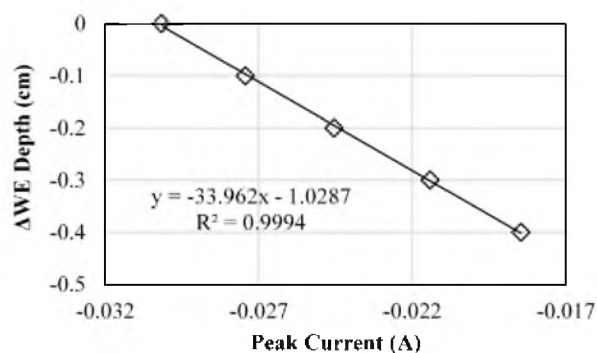


Figure 3.11 Immersion depth calibration curve

vertical translator calibration curve. The method was employed on the WE in Figure 3.9 and agreed with the wetted length within 0.78%— $6.0 \pm 0.5$  mm (dip method) versus  $6.29 \pm 0.28$  mm (vertical translator). This high level of agreement is not always achieved, but has not been observed to differ by more than 12%. Discrepancies may be caused by surface tension effects and the combined error of each measurement method.

### 3.4.2. Reference Electrode

Initially, a AgCl concentration of 1 wt% (0.070 mol/kg) in eutectic LiCl-KCl was used in the RE for the La/Gd pairing because most previous work had used that ratio of AgCl. However, the stability of the RE at that low concentration is questionable. Shirai et al. (70) report a drift in RE potential when AgCl was below 1 mol% (0.18 mol/kg). From a practicality standpoint, it is more difficult to consistently construct a RE with a very low AgCl content. Additionally, in dilute AgCl solutions, slight deviations in the AgCl concentrations result in a greater shift in potential, as shown in Figure 3.12. The potential of the AgCl/Ag RE versus the standard chlorine electrode (SCE) decreases sharply as the AgCl concentration approaches zero, as illustrated by the logarithmic trendline. Thus, for La/Th and Mg/U pairings, a concentration of 5 mol% AgCl was used to increase the

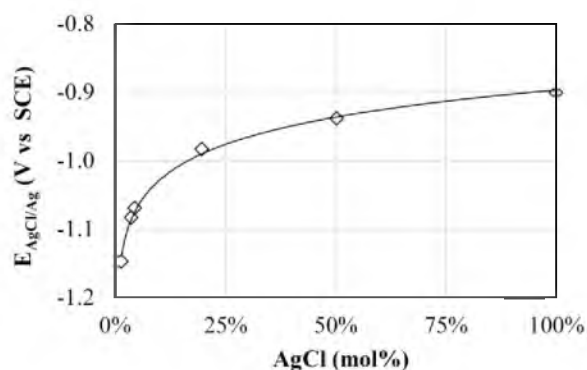


Figure 3.12 Potential of the Ag/AgCl RE versus the SCE (69)



stability and repeatability of the RE potential.

For both La/Gd and La/Th pairings, glass NMR tubes served as the membrane between RE solution and the binary-analyte mixture. These tubes would occasionally crack. If the crack occurred while cooling, the RE would be suspended above the main salt mixture and the RE salt would be solid. Thus, no contamination would occur in the salt mixture being analyzed. However, cracks would also occur while the RE was immersed in the mixture and the RE solution was still molten. In this case, the salt would become contaminated and have to be discarded. Thus, multiple REs were used for one test matrix. The contamination of mixtures was inconvenient for La/Gd and La/Th systems, but would be obstructive for samples containing  $\text{UCl}_3$  due to its limited supply. Thus, a 7 mm OD and 5 mm ID mullite tube (Ceramic Solutions, Item No. MLCOE7A) served as the membrane for the U/Mg pairing.

#### 3.4.3. Sampling

Molten salt samples were collected by dipping all-thread into the molten salt and immediately removing it. The frozen salt would then be weighed and collected in a small sealable bag or bottle. Depending on the amount of salt desired, a quarter-inch or 6-32 all-thread would be used. The quarter-inch all-thread would collect about 0.25g and the 6-32 would collect 0.1g.

Zone freezing was a concern with the all-thread sampling method. Thus, an alternative sampling method was performed and compared to the all-thread method. The alternative approach was to immerse an alumina tube in the salt for a minute. Then the top was sealed and the alumina tube was withdrawn. Very soon after withdrawing the alumina tube, the top was unsealed and molten salt dripped into an aluminum weigh boat

solidifying immediately. Three different salt mixtures containing various amounts of  $\text{MnCl}_2$  were sampled three times by each sampling method at  $500^\circ\text{C}$ . ICP-OES was performed and returned results within the standard error of each other, as shown in Table 3.6, with the exception of sample No. 3 in salt mixture B using the all-thread method. This may have been due to a dilution error since all other samples are consistent with each other.

All molten salt samples collected were weighed and dissolved in a certain volume (15-45 mL) of diluted nitric acid (2-7.14 vol%). If needed, further dilutions would be performed using pipettors (Ependorf) so that the analyte concentration would be between 1 and 100 ppm. Calibration solutions were created using ICP standards purchased from Inorganic Ventures.

After the solutions were made and dilutions performed, their concentrations would be analyzed using a Spectro Genesis FES (Model No. 20.05.2009) ICP-OES (Inductively Coupled Plasma Optical Emission Spectrum) machine or by the ICP-MS Metals Lab at the University of Utah. ICP-OES and ICP-MS analysis would return concentrations in ppm which would then be converted to weight fraction ( $w$ ) in the salt

Table 3.6 Comparison of all-thread (frozen) and alumina tube (molten) sampling methods

Sample No.	All-Thread Samples			Alumina Tube Samples		
	A	B	C	A	B	C
1	0.269%	0.544%	0.764%	0.252%	0.536%	0.771%
2	0.266%	0.557%	0.722%	0.262%	0.512%	0.756%
3	0.275%	0.872%	0.699%	0.270%	0.556%	0.706%
Avg	0.270%	0.658%	0.729%	0.262%	0.534%	0.744%
Std. Dev.	0.004%	0.186%	0.033%	0.009%	0.022%	0.034%
David Horvath took the samples and Lauryn Hansen performed the dilutions and ICP-OES measurements						

using the following equation

$$w_{MCl_n} = (ppm) \frac{\mu g_M}{g_{sol'n}} \rho_{sol'n} V_{sol'n} \frac{g_M}{10^6 \mu g_M} \frac{MW_{MCl_n}}{MW_M \cdot m_{sample}} \quad (3.4)$$

where *ppm* is the ICP measured concentration value in ppm ( $\mu\text{g/g}$ ) for one of the metal analytes in nitric acid solution. The density of the solution ( $\rho_{sol'n}$ ) varied depending on the amount of nitric acid and sample present in solution, but typically was very close to 1.0 g/mL. The volume of the solution ( $V_{sol'n}$ ) was known from the dissolution and dilution of samples. It is important to note that ICP-OES and ICP-MS measure the concentration of metal ions in solution. Thus, the molecular weights (*MW*) of the salt and metal were used to obtain the amount of the salt present in the original sample. Lastly, the total mass of the salt sample is placed in the denominator to yield weight fraction.

The molar concentration of each mixture was calculated by using the assumption of additive volumes, as shown below:

$$\frac{1}{\rho_{salt}} = \sum_j \frac{w_j}{\rho_j} \quad (3.5)$$

where *j* represents each metal-chloride species present in the salt mixture. This assumption introduces little error (<1.5%) as demonstrated by the density measurements in Appendix B.

#### 3.4.4. Additions

Salt mixtures were made by initially introducing a small amount of each analyte into eutectic LiCl-KCl, then progressively adding more of each analyte in turn. With the La/Gd pairing each addition of analyte was performed after a salt mixture had cooled and solidified. Then, the salt was remelted and the electrodes reinserted. For La/Th and Mg/U

pairing, analytes were added while the salt was molten to minimize the disturbance of electrodes and heat cycles in the glovebox. After adding an analyte, the salt would be stirred for one minute and then allowed to settle for 30-60 min. CVs were recorded every 6 min. When 3 or more CVs overlapped, the salt would be considered equilibrated and a new set of electrochemical experiments would be performed.

### 3.5. Electrochemistry Test Procedures

Electrochemical measurements were performed using Autolab NOVA (version 1.10) software. The general procedure is as listed:

1. Anodically clean WE.
2. Run full CV from W/Mo dissolution to Li deposition.
3. Apply current interrupt to measure cell resistance.
4. Run CV at 5 or more scan rates (50-500 mV/s).
5. Run CA at 10 or more potential steps.
6. Measure OCP.
7. Run NPV (Mg/U and La/Th only).

After these electrochemical tests were performed then a sample would be taken. Then more of one or more analyte would be added and the tests were repeated.

#### 3.5.1. Anodic Cleaning

CV and linear sweep voltammetry (LSV) were typically used for initial anodic cleaning of the WE, typically scanning from 0 to 1.1 V versus Ag/AgCl (5 mol%), careful to avoid high current densities ( $<50 \text{ mA/cm}^2$ ) so that the WE geometry would not be significantly altered by anodic dissolution. After the initial anodic cleaning,

chronoamperometry (CA) would be used by holding the WE potential significantly greater than the equilibrium potential of the more noble analyte, but negative enough to avoid dissolution of the WE—typically 0 to 0.5 V versus Ag/AgCl(5 mol%). Mixtures containing  $\text{UCl}_3$  were cleaned using CA at potentials more negative than the transition from the 3+ to the 4+ valance state.

### 3.5.2. Cyclic Voltammetry

After cleaning the electrode, a full CV was collected because it can provide two stable points to use to check for RE potential drift. The potential of lithium deposition and tungsten dissolution varies very little with changes in the analyte concentrations and, therefore, provide excellent reference points when comparing data from other experiments. Unfortunately, molybdenum dissolution is complicated by the formation of  $\text{K}_2\text{MoCl}_6$  (81) which creates an anodic peak that shifts, even in the same mixture at the same concentrations.

After running a full CV, current interrupt (i-interrupt) is applied at the peak potentials of the analyte reduction peaks observed in the full CV to measure the solution resistance. Three or more measurements are made with anodic cleaning to remove deposited metals in between each interrupt measurement.

The CV is then shortened to avoid both Li deposition and W or Mo dissolution. Usually, the upper vertex of the CV was 0 V versus Ag/AgCl (5 mol%) and lower vertex  $\sim 100\text{mV}$  more negative than the reduction peak of the more active analyte. At each scan rate, three scans would be performed. The first scan typically differed slightly from scans 2 and 3. If scans 2 and 3 overlapped, then the next scan rate was tested. If not, an additional scan was performed.

### 3.5.3. Chronoamperometry

A type of repeating CA, similar to normal pulse voltammetry (NPV), was used in this work. Like NPV, the pulse potential is decreased with each pulse and a cleaning or base potential is applied to renew the WE and diffusion layer. However, unlike NPV, the entire temporal current profile is recorded rather than just at end of the pulse.

First, the peak potential of the more noble species was applied for 2-5 s. Then, a more positive potential, typically 0-0.5 V, was applied for 20 s or more to clean the WE. For  $\text{UCl}_3$ , the cleaning potential was more negative to avoid excessive oxidation of  $\text{U}^{3+}$  to  $\text{U}^{4+}$ . Next, the potential was stepped 0.1 V more negative than the peak potential, then cleaned again. This cycle was repeated 5 or more times. This whole process was repeated for the more active species.

### 3.5.4. Open-Circuit Potentiometry

OCP was performed two ways. First, the chronopotentiometry was run until Li deposition ( $\sim -2.5$  V vs Ag/AgCl) occurred, then a zero current imposed and the potential recorded until plateaus for both species were clearly defined ( $\geq 180$  s). This allowed for the equilibrium potential of the more active species to be recorded. The other method was to switch the WE and CE leads so that OCP was performed with the metal basket containing the more noble metal. Using this method, there was no need to pre-deposit metal on the electrode and a more stable equilibrium potential was recorded. However, only the equilibrium potential of the more noble species could be recorded.

### 3.5.5. Normal Pulse Voltammetry

NPV was performed using a step potential of 5 mV, a pulse time of 0.25 s and interval time of 5-15 s. The potential range was selected by examining the CVs. The initial potential was about 0.1 V more positive than the reduction peak of the more noble species. The end potential was typically 0.2 V more negative than the cathodic peak of the more active analyte.

### 3.5.6. Rotating Cylinder Electrode

In all of the aforementioned techniques, the WE is static. In addition to these tests, a rotating cylinder electrode (RCE) was implemented to perform hydrodynamic electrochemical tests. The use of the RCE creates a well-defined boundary layer and allows for the study and characterization of kinetic behaviors. The RCE was made using the rotator from Autolab's RDE-2 and accompanying motor controller. A custom adapter was machined to connect the RDE-2 to a 2 mm tungsten rod. Initially, the adapter was only 2 in. long, as pictured in Figure 3.13 on the left. However, this required the WE to be 9 in. long and resulted in excessive whipping above 200 RPM. The adapter was

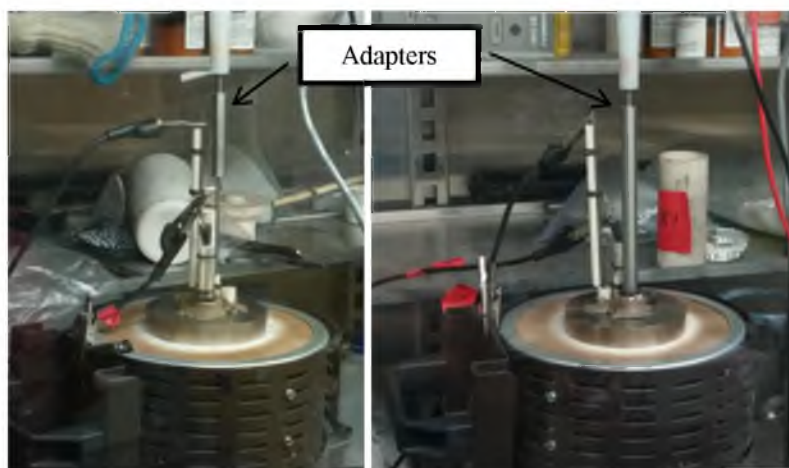


Figure 3.13 Experimental setup for RCE with short (left) and long (right) adapter

lengthened to 8 in., and the WE was shortened to 3 in., as pictured in Figure 3.13 on the right. This resulted in the adapter extending into the furnace, but whipping was minimal until 750 RPM. The WE was secured in the adapter using a pair of 2-56 set screws. LSV was performed from 100-500 RPM. For the RCE studies, the static WE was merely replaced by RCE. A schematic of the cell setup is shown in Figure 3.14.

### 3.6. Summary

The experimental setup was developed and improved over time and with experience. Efforts were made to maintain consistency within a test matrix so that results would be directly comparable. Further development is still needed particularly in characterization of WE surface area and the experimental setup for RCE tests. Possible improvements to these experimental approaches are discussed in Chapter 9.

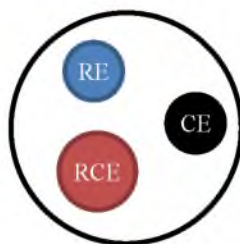


Figure 3.14 Schematic of RCE electrochemical cell



#### 4. COMPUTATIONAL WORK

During World War II, two developments occurred that produced the first computer simulations of scientific problems, namely neutron transport. In 1945, the first nuclear bomb was detonated at Alamogordo, New Mexico and the first electronic computer, EINAC, was built at the University of Pennsylvania. The nuclear physics at Los Alamos grappled with neutron velocity spectra with “various peaks and valleys [which are] difficult to handle mathematically” (82). Thus, Stan Ulam and John Von Neuman developed a statistical method that involved intense amount of computations and called it the Monte Carlo method. Using EINAC, they solved neutron transport problems which reduced the amount of expensive tests that they had to perform. However, “[Enrico] Fermi had invented, but of course not named, the present Monte Carlo method when he was studying the moderation of neutrons in Rome. He did not publish anything on the subject, but he used the method to solve many problems...” (83). In fact, “Fermi took great delight in astonishing his Roman colleagues with his remarkably accurate, ‘too-good-to-believe’ predictions of experimental results” (82). This was around a decade before EINAC. Thus Fermi performed these calculations himself “whenever insomnia struck in the wee morning hours!” (82).

Computer simulations have been used since these first applications to predict experiments in almost every field. They can help guide experiments and select key experimental parameters, possibly reducing the number of experiments. Models for a

used nuclear fuel (UNF) electrorefiner (ER) have been developed since the late 1980s including: PYRO (84), TRAIL (85), GPEC (86), and REFIN (56). ERAD (Enhanced REFIN with Anodic Dissolution) is a more recent model that built upon the experience and knowledge of these models and additional experimental information (87). Before experiments ERAD was used to simulate data which could be used to evaluate and compare the usefulness and capabilities of several analytical techniques. Additionally, the effects of certain experimental conditions on the simulated data were observed. This guided the preparation and types of the experiments conducted.

Two systems were simulated: LiCl-KCl-UCl<sub>3</sub>-ThCl<sub>4</sub> and LiCl-KCl-UCl<sub>3</sub>-PuCl<sub>3</sub>. These systems were selected because U, Pu, and Th are key elements to monitor in pyroprocessing. The U/Pu pairing is particularly important in the treatment of reactor fuel cycles that are based on an initial feed of uranium fuel. The U/Th pairing will become more relevant with the development of the thorium cycle, in particular the molten salt reactor (MSR). These two pairings also provide a stark contrast in standard reduction potential spacing.

#### 4.1. ERAD

ERAD is a versatile one-dimensional electrochemical simulation code package.<sup>1</sup> The general features of ERAD are only discussed here, more details about ERAD and its methodologies and assumptions have been reported elsewhere (87–89). ERAD can simulate CVs or electrorefining. ERAD simulations of experimental CVs of either UCl<sub>3</sub>

---

<sup>1</sup>ERAD was developed in two parts. First, Byung Gi Park developed REFIN at Seoul National University under Il-Soon Hwang's advisement. Then, Riley Cumberland modified REFIN at the Korean Advance Institute of Science and Technology (KAIST) under Man-Sung Yim's advisement.

or  $\text{PuCl}_3$  in eutectic  $\text{LiCl-KCl}$  from open literature have shown good agreement (87,90). The electrorefining feature has also been benchmarked with gram-scale electrorefining tests (87,91).

As shown in Figure 4.1, the initial conditions (i.e., compositions, cell current, electrode potentials, etc.) of the electrochemical cell are specified by the user in an input file. Depending on the mode of operation (current-controlled or potential-controlled), ERAD uses the cell current or electrode potentials as boundary conditions to solve for the flux of the ions through the cell using fundamental electrochemical relations, such as: the Nernst, Butler-Volmer and Nernst-Planck equations (see Chapter 2). Because ERAD is based on fundamental electrochemical relations, it requires several well-characterized properties for each element, including: standard reduction potentials, activity coefficients, diffusion coefficients, oxidation state, transfer coefficients, and exchange current density.

ERAD was developed by modifying REFIN in a number of ways (56). A model was added to describe the dissolution of SNF from a solid anode, solubility limits were enforced at the anode surface, geometry of the anode was altered to account for a porous layer of noble metals (92), the differential equation solver was replaced, and a package

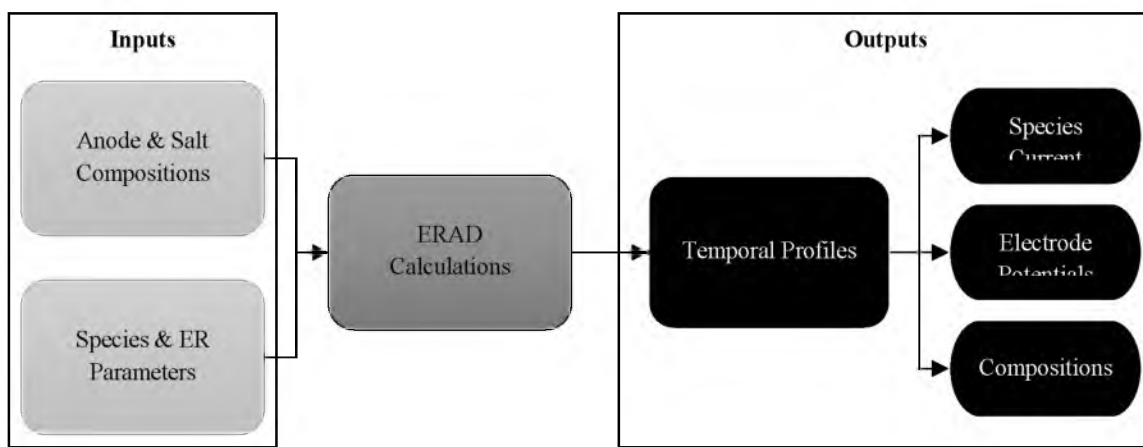


Figure 4.1 Inputs and outputs of ERAD

was inserted to account for fast reactions occurring before the application of an external power source. ERAD has the capability to account for up to 10 elements counting the three present in the eutectic LiCl-KCl melt.

The phases simulated in ERAD are shown in Figure 4.2. Active elements in UNF need to diffuse through the bulk anode and the depleted, porous layer consisting of noble metals to the anode surface where they are oxidized into the anode diffusion layer. The oxidized elements diffuse to the bulk solution which is well-mixed and assumed to be homogenous. Then the oxidized elements diffuse through the cathode diffusion layer and are reduced at the cathode surface.

It is important to note that ERAD is spatially one-dimensional. It assumes a uniform potential distribution and current density at the surface of electrodes. However, it can account for differences in electrode surface area. Thus, ERAD performs particularly well in the geometric configuration of concentric cylinders. Also of note is that ERAD has not been benchmarked for multielement deposition. Thus, ERAD does not account for possible alloying effects that can result in underpotential deposition and prepeaks of metal ion deposition. According to the phase diagram of U and Pu, there is a possibility that alloys do form at 500°C (93). Previous work has also shown that at 500°C no

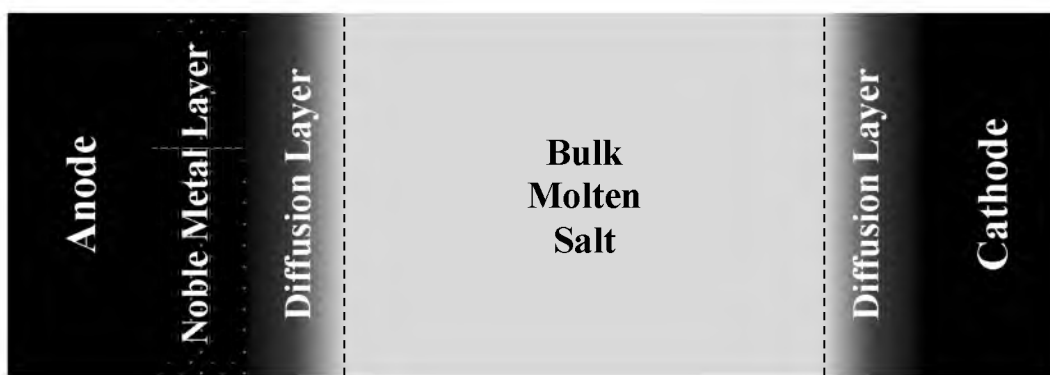


Figure 4.2 Representation of the ER phases simulated by ERAD

intermetallic is formed between U and Th and the solubility of U in Th is low (94,95). Thus the simulation may omit peaks and slight shifts in peak potentials, particularly in the case of U and Pu. However, these simulations can still lend insight into the challenges associated with multi-analyte mixtures and help evaluate analytical techniques.

#### 4.2. Multivariate Analytical Techniques<sup>1</sup>

As detailed in Section 2.5, steady-state current, peak current, diffusion current or potential can be related to concentration and is fairly straight forward for a single-analyte mixture. However, if multiple actinides are present, their peaks or currents could overlap making it difficult to establish baselines for peaks or attribute the measured current to a single species. For example, in CV, current peaks are formed by scanning the potential at a sensing electrode. As long as these peaks are strongly related to the concentration of a species, they can be reliably used to determine the concentration. However, if another species is present and forms a peak in close proximity to the other species, the peaks will overlap. The peaks will need to be deconvoluted in order to extract reliable concentration measurements. This could involve stalling the scan just after the peak potential or semi-differentiating the CV curve, but these methods require a certain amount of separation between the peak potentials and discard a majority of the data (52,96). Alternatively, multivariate analytical techniques, which utilize the complete CV curve rather than a couple data points at the peaks, could provide more reliable and accurate correlations, potentially even when peak almost completely overlap (97). Multivariate analytical

---

<sup>1</sup>This section includes text and figures from the author's preprints of an article published in *Annals of Nuclear Energy* at <http://dx.doi.org/10.1016/j.anucene.2014.11.023> (144) and a paper in the proceedings of the INMM 55<sup>th</sup> Annual Meeting (97). Reprinted with permission of the Institute of Nuclear Materials Management. Copyright 2014. All rights reserved.

techniques could also provide additional insights into the conditions of the ER and the measurement device. The performance of traditional peak heights and diffusion currents are compared to multivariate analytical techniques in the following sections.

Two closely related multivariate analytical techniques are investigated in this chapter: (1) principal component regression (PCR) and (2) partial least squares (PLS). Only a brief explanation of PCR and PLS will be provided here which is specific to the analysis of voltammograms. Readers are referred elsewhere for more detailed and general descriptions (98,99). However, it is worth noting the PCR and PLS can be applied to any signal that is affected by any set of variables in any process.

PCR and PLS are multivariate analysis methods which use a greater amount of the data collected in voltammograms than the univariate analysis of peak height. PCR and PLS analyze a set of data, called a training set, to determine the main contributors to variance, called principal components (PCs). In this work, a training set is an  $n \times m$  matrix of voltammetric curves with  $n$  data points collected at  $m$  different species concentrations that span the expected range of concentrations for each species. A PC is calculated from the training set,  $A$ , using singular value decomposition, as shown below.

$$A = USV^T \quad (4.1)$$

$U$  is an  $n \times n$  matrix containing the PCs, or the eigenvectors of  $AA^T$ ,  $S$  is an  $n \times m$  matrix containing the eigenvalues on its diagonal, and  $V^T$  is an  $m \times m$  matrix containing the eigenvectors of  $A^T A$ . The important thing to note is that  $U$  is orthonormal and the columns of  $U$  are the PCs. Thus, a PC is a vector that is transformed from  $A$  into a space where it is uncorrelated from all other PCs which helps mitigate covariance when regression is performed. Also, the PCs in  $U$  are ranked according to the amount of the

variance captured from  $A$  by the PC. Thus, column 1 of  $U$  is the PC that accounts for the most variance. The main difference between PCR and PLS are the considerations made when determining the PCs. In PCR, the PCs are selected and ranked based on the amount of variance that they capture from the training set without considering the relation between the data and concentration. In PLS, the values of concentration are taken into account when calculating the PCs from the training set, which can result in slightly more accurate determination of concentration.

Once the PCs are determined, the number of PCs to be retained needs to be determined. The method used for selecting the number of PCs to retain will be discussed later. For now,  $k$  will represent the number of PCs retained. It should be noted that  $k$  cannot exceed the number of observations ( $m$ ). The PCs are related to concentration by a least-squares regression. First, voltammetric curves in the training set are projected onto the retained PCs forming a  $k \times m$  matrix,  $A_{proj}$

$$A_{proj} = U_k^T A \quad (4.2)$$

$U_k$  is an  $n \times k$  matrix containing columns 1 through  $k$  of  $U$ . The PCs are related to a concentration matrix,  $C$  ( $l \times m$ ), by a vector of regressed coefficients,  $B$

$$B = CA_{proj}^T [A_{proj} A_{proj}^T]^{-1} \quad (4.3)$$

$C$  contains  $l$  species at  $m$  different concentrations. Subsequently, voltammetric curves of unknown samples can be projected on the PCs and related back to concentration by (4.4)

$$C_{unk} = B [U_k^T X] \quad (4.4)$$

$C_{unk}$  is a vector of length  $l$  containing the determined concentrations of the unknown sample and  $X$  is a vector of length  $n$  containing the voltammetric curve of the unknown

sample.

As mentioned, not all of PCs are used in the regression. Rather only some ( $k$ ) PCs are retained for the regression. In this way, PCR and PLS also act as a filter to remove noise from signals which could lead to an increased error in the correlated variables. A common method for determining the number of PCs to retain is called predicted residual error sum-of-squares (PRESS) which, in this work, is simply the residual sum of squares (RSS) between the determined and actual concentrations of a known sample, as shown below:

$$RSS = \sum_{i=1}^I (C_i - C_{unk,i})^2 \quad (4.5)$$

$C_i$  represents the actual concentration of the  $i$ -th species and  $C_{unk,i}$  is the determined concentration of the unknown sample.

When selecting a value for  $k$ , it is important to reduce the error in the correlated variables and include all important features of the CV while excluding noise and not over fitting the data. For example, Run 16 of the simulated LiCl-KCl-UCl<sub>3</sub>-ThCl<sub>4</sub> system (see page 117) was used to select a value for  $k$ . The concentration of Run 16 was predicted using (4.4) and the RSS was computed. This calculation was repeated for  $k = 1$  to 15 and the RSS of U and Th concentrations was plotted versus  $k$  for Run 16. As seen in Figure 4.3, the error is greatly reduced after the first 2 PCs making 3 a tempting choice for  $k$ . However, inspection of the residuals of predicted and actual i-E curves in Figure 4.4 show that for  $k = 3$  features of the CV are not accurately captured, such as the tail of reduction peak which occurs after -1.4 V. At  $k = 6$ , all of the features of the CV are captured. Thus, 7 PCs were used to determine the concentrations of the unknown runs for the simulated LiCl-KCl-UCl<sub>3</sub>-ThCl<sub>4</sub> data.



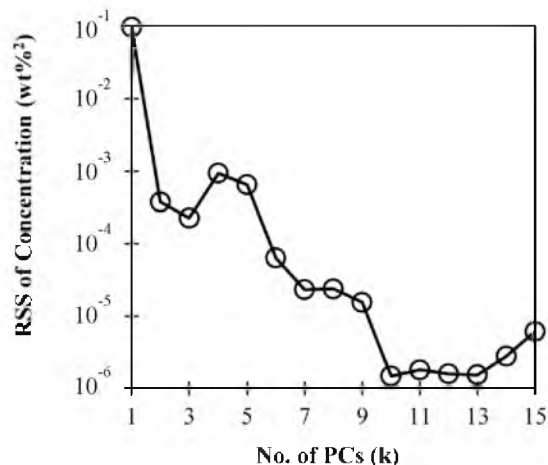


Figure 4.3 Semi-log plot of RSS of concentration for Run 16 of the LiCl-KCl-UCl<sub>3</sub>-ThCl<sub>4</sub> ThCl<sub>4</sub> system (see page 117)

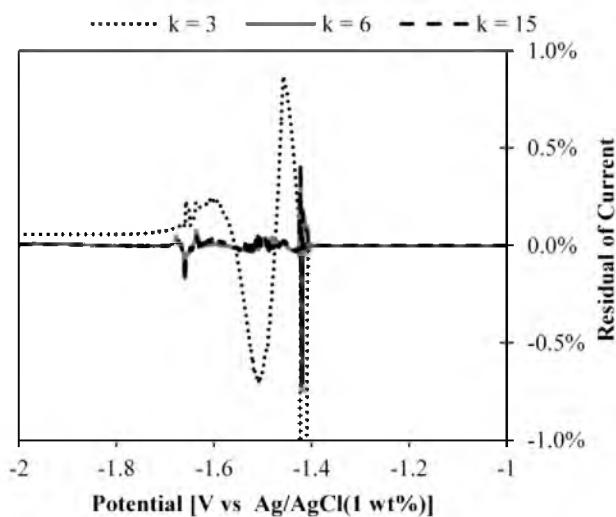


Figure 4.4 Residuals of the reconstructed current for Run 16 of the LiCl-KCl-UCl<sub>3</sub>-ThCl<sub>4</sub> system (see page 117)

Lastly, just like any other analysis method, in order to determine concentrations accurately using PCR or PLS, the conditions (e.g., electrode material, elements present, etc.) under which the unknown data is collected needs to be the same as the conditions of the training set. In this paper, PCR and PLS are applied to both experimental and simulated data. The determined concentrations from PCR and PLS are compared to concentrations obtained from peak height regression.

### 4.3. UCl<sub>3</sub>-PuCl<sub>3</sub>-LiCl-KCl Mixtures<sup>1</sup>

#### 4.3.1. Experimental Data

The experimental data used in this section was obtained by digitizing differential normal pulse voltammetry (NPV) curves in Figure 12 of the cited work (40). The NPV data was collected in an inert argon glovebox at 773 K with a 1 mm W wire as the WE and Ag/AgCl (1 wt%) RE. The immersion depth of the electrode was estimated to be 1 cm, but wetting effects prevented the exact determination of immersion depth. The concentrations of U and Pu ions in the eutectic LiCl-KCl mixtures are provided in Table 4.1 for each NPV curve. The differential NPV curves were digitized using Plot Digitize 2.6.4 (100) and linearly interpolated using Matlab (101) so that data would be uniformly distributed. Figure 4.5 displays the resulting digitized and interpolated curves which compare favorably to Figure 12 of the original work (40). As can be seen in Figure 4.5, there are two sets of peaks. The reduction of U and Pu correspond to the peaks around -1.4 and -1.75V, respectively.

Table 4.1 ICP-OES measured composition of eutectic LiCl-KCl salt mixtures for NPV curves from (40)

Curve	U (wt%)	Pu (wt%)
A	0.15	0.12
B	0.40	0.14
C	0.72	0.16
D	1.69	0.18
E	1.66	0.58
F	1.67	0.91
G	1.62	1.63

<sup>1</sup> This section includes text and figures from the author's preprint of an article published in *Annals of Nuclear Energy* at <http://dx.doi.org/10.1016/j.anucene.2014.11.023>. Reprinted from (144), Copyright 2015, with permission from Elsevier.

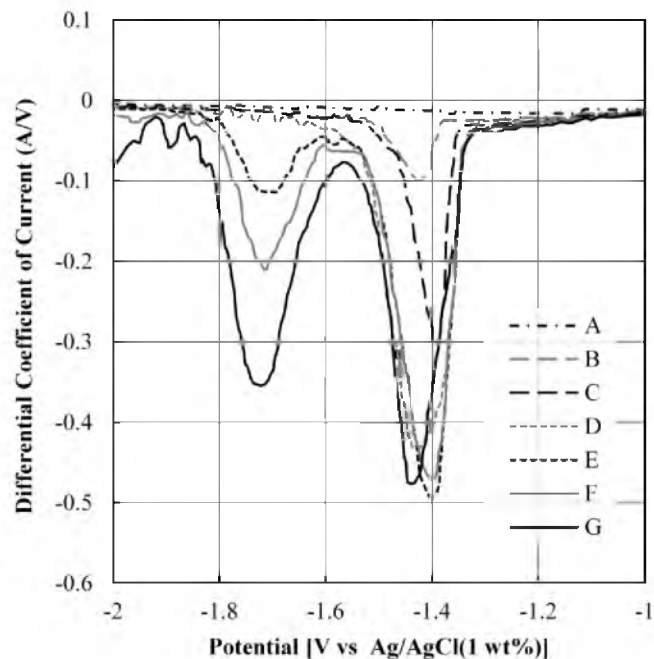


Figure 4.5 Digitized and interpolated NPV curves measured at 773 K on a 1 mm W wire WE (Area  $\approx 0.31 \text{ cm}^2$ ) versus a Ag/AgCl (1 wt%) RE from Figure 12 of (40)

Four analytical techniques were applied to the digitized data: peak height, peak area, PCR, and PLS. For each of these analyses, the data from curves B-F were removed one at a time from the training set of data and treated as an unknown, also known as cross-validation in PCR. For the peak height analysis, the heights of the peaks were determined using the built-in findpeaks function in Matlab. A simple linear regression was performed on the height of the peaks around -1.4 and -1.75V and the weight percent of U and Pu, respectively. The regressed slope and y-intercept were used to determine the concentration of the removed curve. Peak area was already determined in the original paper. Thus, the data from the paper was regressed and used to determine the concentration. For PCR, a function was written in Matlab which performed matrix operations detailed in Section 4.2. The number of PCs used for PCR was 5 and was determined by cross-validation and minimizing the RSS values of curves B-F. PLS was

performed using the built-in `plsregress` function in Matlab and the weight percent of U and Pu were regressed on the differentiated NPV curves using 6 PLS components.

#### 4.3.1.1 Results

The performance of each analytical technique was assessed by plotting the determined weight percent versus the actual weight percent as measured by ICP-OES (40). Thus, if an analytical method determines the weight percent in complete agreement with ICP-OES, the plot should be linear with a slope of 1, y-intercept of 0, coefficient of determination ( $R^2$ ) of 1, and an estimated variance ( $\sigma^2$ ) of 0 (102). These linear regression statistics of each series in each plot are displayed in Table 4.2. Figure 4.6 and 4.7 are plots of electroanalytical versus ICP-OES measured weight percent of U and Pu, respectively. The dashed line in each figure is an ideal linear line (i.e.,  $y = x$ ).

It is evident from Table 4.2 that the U and Pu concentrations determined by peak area, PCR and PLS are consistently more accurate across the range of U and Pu concentrations than the concentrations determined by peak height regression. The slope and  $R^2$  values are closer to 1 and the y-intercept and  $\sigma^2$  values are closer to 0 than for peak height. In this case, peak height is a less accurate indicator of concentration because the U and Pu peaks overlap in some cases making it difficult to determine the baseline of

Table 4.2 Regression statistics for plots in Figure 4.6 and 4.7

Statistic	Uranium (Figure 4.6)				Plutonium (Figure 4.7)			
	Peak Height	Peak Area	PCR	PLS	Peak Height	Peak Area	PCR	PLS
Slope	0.829	0.986	0.953	0.980	0.798	0.946	0.966	0.965
Intercept	0.233	0.010	0.053	0.020	0.039	0.021	0.033	0.037
$R^2$	0.860	0.988	0.989	0.992	0.986	0.991	0.993	0.991
$\sigma^2$	0.073	0.006	0.006	0.004	0.010	0.002	0.002	0.002

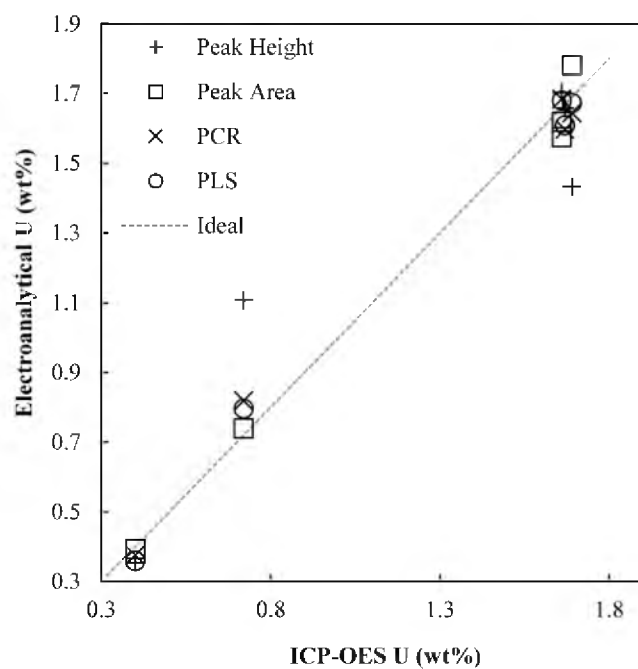


Figure 4.6 Plot of electroanalytical versus ICP-OES measured U concentration using multiple analytical techniques on NPV curves in Figure 4.5 to determine concentration

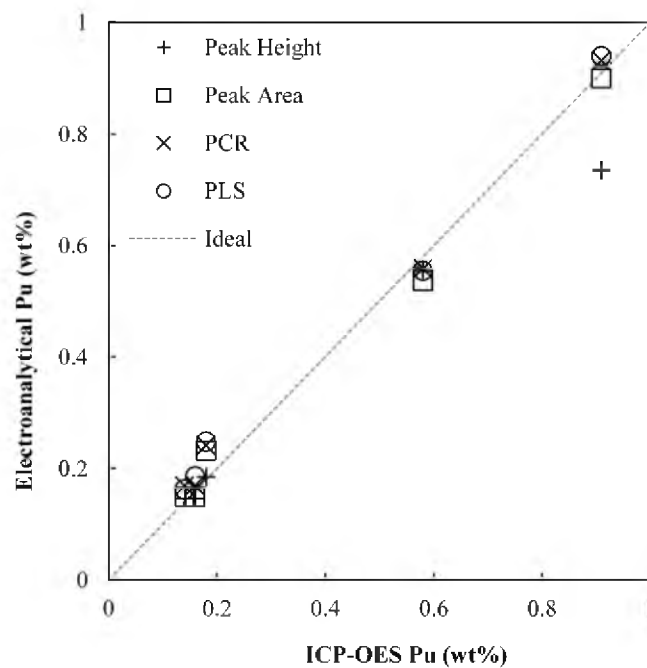


Figure 4.7 Plot of electroanalytical versus ICP-OES measured Pu concentration using multiple analytical techniques on NPV curves in Figure 4.5 to determine concentration

the Pu peak and, hence, the actual peak height. Additionally, at low concentrations of U and Pu, the peaks were difficult to identify. While peak area performed similarly to PCR and PLS in determining the concentration, the difficulty of identifying peaks and their boundaries still exists which becomes increasingly more difficult at higher concentrations. Additionally, by evaluating peak area solely, certain features of the voltammetric curve are lost which could be useful in evaluating the performance of concentration correlations and measurement conditions, as will be demonstrated later.

#### 4.3.2. Simulated Data

Ideally, PCR and PLS are performed using a much larger training set at more evenly distributed concentrations. However, experimental results of multiactinide mixtures are scarce and expensive to obtain. Thus, as a preliminary investigation and demonstration of the merits of PCR and PLS in determining the concentration of actinides in actual ER salt, CVs of eutectic LiCl-KCl containing  $\text{UCl}_3$  and  $\text{PuCl}_3$  were simulated using ERAD.

The general parameters of the simulated electrochemical cell are displayed in Table 4.3. All voltages listed, unless otherwise specified, are versus the  $\text{Cl}_2/\text{Cl}^-$  reference electrode. The diffusion layer thickness values were obtained by fitting ERAD simulated data with experimental data (87,88). The values of the apparent standard potential ( $E^{\circ}$ ), diffusion coefficient ( $D$ ), exchange current density ( $i_0$ ) and transfer coefficient ( $\alpha$ ) for  $\text{UCl}_3$  and  $\text{PuCl}_3$  used in ERAD are listed in Table 4.4. Using these parameters, several CVs were generated at various  $\text{UCl}_3$  and  $\text{PuCl}_3$  compositions. The training set was composed of 24 simulated CVs with U and Pu salt composition varying from 0 to 8 wt% and 0 to 4 wt% in 2 and 1 wt% increments, respectively. The compositions of the

Table 4.3 General parameters of the electrochemical cell for U/Pu and U/Th simulations

Parameter	Value	Parameter	Value
Temperature	500 °C	<i>Diffusion Layer Thickness</i>	
<i>Interfacial Area</i>		Anode	150 μm
Anode	45.23 cm <sup>2</sup>	Cathode	150 μm
Cathode	1 cm <sup>2</sup>	<i>CV settings</i>	
<i>Initial Masses</i>		Upper Vertex	-2.25 V
Anode	9.6 g	Lower Vertex	-3.25 V
Electrolyte	1065 g	Scan Rate	0.1 V/s

Table 4.4 ERAD parameters for simulated species in the LiCl-KCl-UCl<sub>3</sub>-PuCl<sub>3</sub> system

	$E^{\circ}$ (V)	$D$ ( $10^{-5}$ cm <sup>2</sup> /s)	$i_0$ (A/cm <sup>2</sup> )	$\alpha$
<b>UCl<sub>3</sub></b>	-2.501 (87)	2.00 (87)	1.0 (87)	0.5*
<b>PuCl<sub>3</sub></b>	-2.760 (41)	1.12 (41)	0.8 (87)	0.5*
<b>NpCl<sub>3</sub></b>	-2.670 (41)	2.41 (41)	0.8*	0.5*
*assumed value				

“selection” (Sel) run and unknown runs are displayed in Table 4.5. The selection run was used for selecting the number of PCs to retain by minimizing RSS.

Again, the data was interpolated and three analytical methods were used to determine the weight percent for U and Pu: peak height, PCR, and PLS. The peaks were found using the same method previously used on the experimental data in Section 4.3.1. The only difference being that the height of U peak tail at the commencement of the Pu peak was subtracted from the Pu peak height. Using the training set data, a linear

Table 4.5 Salt compositions of selection and unknown simulations

Run	U (wt%)	Pu (wt%)	Run	U (wt%)	Pu (wt%)
Sel	5.0%	1.5%	4	2.5%	2.5%
1	1.0%	0.5%	5	3.0%	1.5%
2	1.0%	3.5%	6	7.0%	0.5%
3	1.5%	3.0%	7	7.0%	3.5%

regression was performed to relate U and Pu weight percent to their respective peak heights and the composition of unknown simulation runs were determined using the regressed coefficients. PCR and PLS were performed in the same manner as described for the experimental data with one exception. Cross-validation was not needed because the selection run was used for determining the number of PCs to retain which was 11 for PCR and 12 for PLS.

#### *4.3.2.1 Results*

A representative plot of the simulated CVs is provided in Figure 4.8. The U, Pu and total current are plotted in the figure. It should be noted that current values in ERAD are in American convention (i.e., positive current = reduction). The depositions of U and Pu occur at potentials more negative than their respective  $E^0$  due to concentration effects as captured by the Nernst equation. As can be seen in Figure 4.8, the Pu reduction peak sits right on the tail of U reduction peak. The U reduction peak is still decaying when the Pu reduction peak begins resulting in a baseline for Pu peak that varies as the potential is scanned more negatively. Furthermore, as the U concentration changes, the position of the Pu peak on top of the U peak varies. Thus, not only does the Pu peak baseline change with potential, but also with U concentration. This results in an inconsistent baseline for determining the Pu peak height.

The relative errors of the determined weight percent of U and Pu for each analytical method are plotted in Figure 4.9. For peak height analysis, the relative error of the determined U wt% is relatively low with an average of 2.7% and a high of 4.8%. The relative error of the determined Pu wt% is quite large with an average of 21% and a high of 74%. This is due to the inconsistent baseline of the Pu peak which is a result of



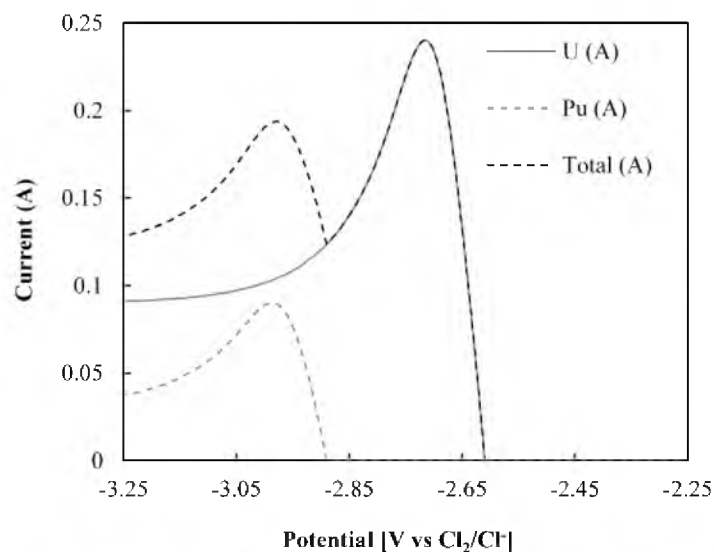


Figure 4.8 Representative plot of simulated CVs for Run 5 from Table 4.5

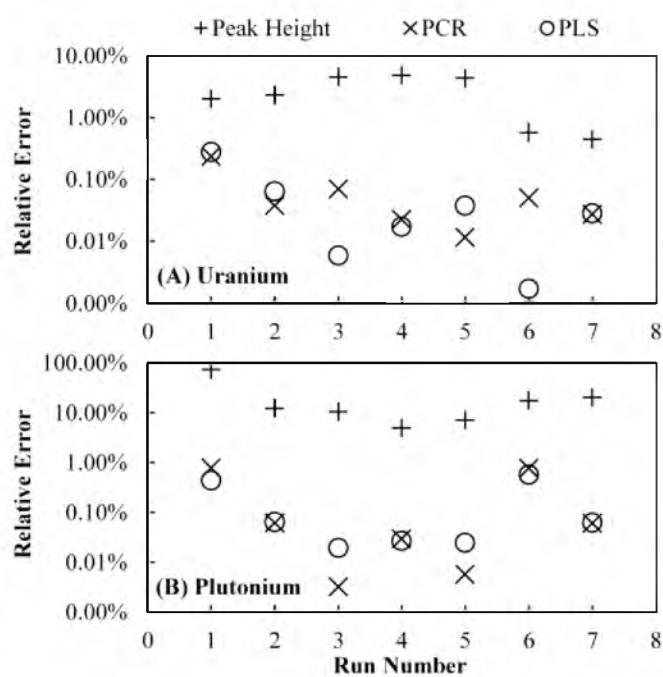


Figure 4.9 Relative errors of the (A) U wt% and (B) Pu wt% determined by each analytical method using simulated data with the parameters in Tables 4.3-4.5

interference from the U peak. In both cases, however, the uncertainty could exceed the significant quantity established by the International Atomic Energy Agency (IAEA) for a nuclear facility under international safeguards. For example, a significant quantity of plutonium is 8 kg. A commercial sized-electrorefiner would likely contain 500-1000 kg of salt. If the actual plutonium concentration was 5 wt%, this would correspond to 25 to 50 kg. Thus, error of the plutonium concentration measurement needs to be much less than 16%.

On the other hand, significantly lower errors are achieved by using PCR and PLS on the same set of data. For PCR, the relative error of the determined U wt% is on average 0.065% with a high of 0.24% and, in the case of Pu, the average error is 0.24% with a high of 0.78%. The errors for PLS are very similar to PCR with an average error of 0.062% and 0.17% and a high of 0.28% and 0.57%, for U and Pu, respectively.

#### 4.3.3. Application to Safeguards

To facilitate a discussion on the application of electrochemical techniques to safeguarding an electrorefiner (ER), it is helpful to envision a general setup of the electrochemical sampling in an ER. Ideally, voltammograms of the ER salt would be collected in a small electrically and physically isolated cell adjacent to or inside the ER to limit interference from process operations, such as the mixing of the electrolyte or electric fields in the ER. A small amount of salt would be drawn into the cell and voltammograms would be collected. Then the salt could be returned to the ER and a new sample would be drawn into the cell. A separate sampling cell would allow continuous operation of the ER while continuously collecting voltammograms. Inside the cell would be three electrodes: a reference, working, and counter electrode. The IAEA would

occasionally require some control over the operation of the sampling cell to verify and control the conditions in the cell. Using the voltammograms collected in the cell with PCR or PLS, concentrations of actinides in the ER salt could be determined.

Beside better concentration correlations, another benefit of PCR and PLS is that the measured voltammogram can be reconstructed from the PCs. The residuals of the reconstructed voltammograms can be compared to the residuals of historical or known-composition voltammograms to qualitatively assess the accuracy of the determined concentrations and the validity of the data. The residuals ( $\varepsilon$ ) of reconstructed data are calculated according to the following equation:

$$\varepsilon(E) = i_m(E) - i_r(E) \quad (4.6)$$

where  $i_m$  and  $i_r$  are, respectively, the measured and reconstructed current, both of which are functions of potential,  $E$ . If the reconstructed data closely matches the measured data, the residuals are small. However, if the measured data is collected under conditions different from the training set, the PCs selected from the training set will not accurately reconstruct the measured data. The trends of the residuals could be used to discern whether changes in the determined concentrations are due to actual changes in salt composition or variations in cell conditions. In order to examine the trends of the residuals, the ERAD simulated current is treated as the measured current ( $i_m$ ) and the reconstruction of the simulated current using PCs is used as the reconstructed current ( $i_r$ ). The use of residuals in determining the source of change in determined concentrations is demonstrated in a couple examples.

In these examples, the electrode surface area, diffusion layer thickness and amount of species in the cell were altered, but the training set used to determine

concentrations and reconstruct the CVs was generated using the original conditions (see Table 4.3). This should cause the determined concentration and the reconstructed data to not be as accurate because training set data from certain cell conditions are being applied to measured data from different conditions.

#### 4.3.3.1 Concentration

Before any alterations are made to simulated cell conditions, it is helpful to know the variations of residuals with changing concentrations. If the concentrations are actually changing, then certain changes in residuals occur. For example, if the concentration of U increases, the residuals in the potential range of the U reduction peak should be reduced (see Figure 4.10A). As U concentration increases, the reduction peak of U increases and accounts for more variation in the spectrum making it easier to capture with PCR. The same holds true for Pu and its reduction peak (see Figure 4.10B). Thus, an increase in concentration should result in a decrease in the magnitude of the residuals, particularly in

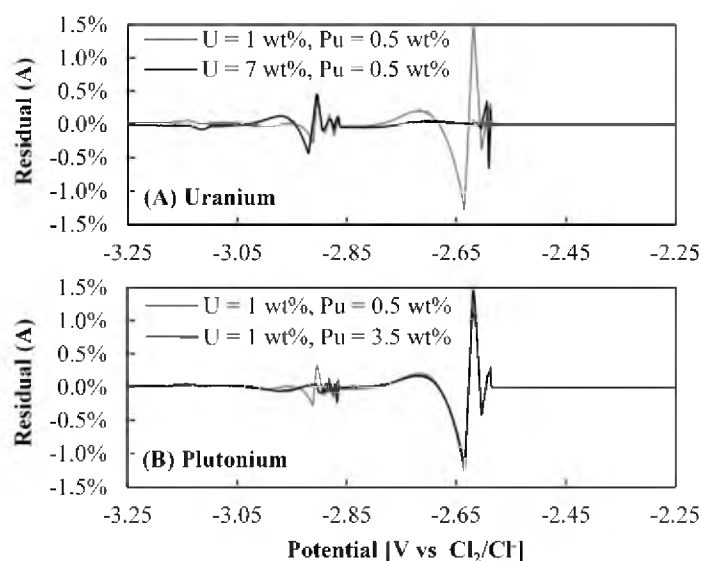


Figure 4.10 Residuals of reconstructed CVs using 12 PCs at varying (A) U and (B) Pu concentration levels

the region where the species is electroactive. It should also be noted that the magnitude of the residual spectrum does not change uniformly with concentration; rather its effect is most pronounced within the region around its peak.

#### 4.3.3.2 Surface Area

One critical parameter for electrochemistry is the active surface area of the working electrode (WE). The surface area could increase due to thick deposits or dendrites forming on the WE and could decrease due to fouling. To simulate the effect of a changing surface area on the concentrations determined by PCR, the WE surface was altered from 1 cm<sup>2</sup> to 0.5, 0.75, 1.5 and 2 cm<sup>2</sup>. Then run 6 from Table 4.5 was re-simulated in ERAD. Then the concentrations were determined and CVs were reconstructed using the training set that was generated with a WE area of 1 cm<sup>2</sup>.

As shown in Figure 4.11, the surface area can affect the determined concentrations. The values for U and Pu concentration are, respectively, found on the left and right vertical axes. The dashed horizontal lines represent the actual concentrations of U and Pu. The PCR determined concentration increases as the surface area increases. For

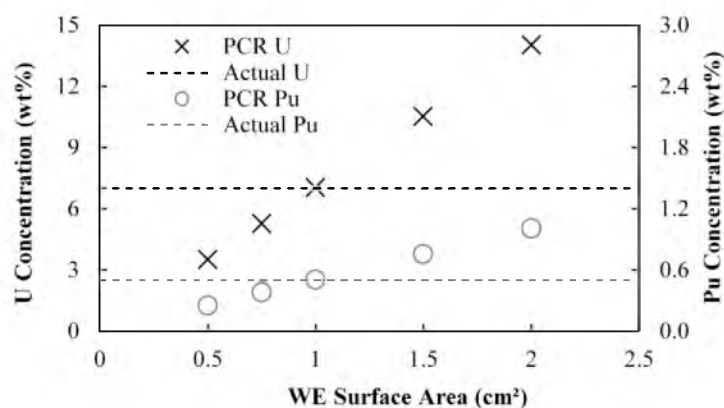


Figure 4.11 Effect of WE surface area on the concentration determined by PCR for Run 6 from Table 4.5 with a nominal area of 1 cm<sup>2</sup>

a 1% increase in surface area, the PCR concentration increases by 1%. This is reasonable because current is linearly related to surface area and is also related to concentration.

The effect of surface area on determined concentrations could trigger a false alarm to the diversion of special nuclear material (SNM) or be used to manipulate measurements. For example, if the WE gradually began to foul and the effective surface area of WE is decrease, then the determined U and Pu concentrations would decrease. This could trigger a false alarm that the host country is drawing down its Pu and TRU undeclared. On the other hand, an operator could gradually increase the surface area of WE to offset the decrease of U or Pu in ER salt due to diversion. This would lead the IAEA to think there is more U or Pu in the ER than the actual amount allowing the host country some margin of U and Pu to divert.

Manipulation or unintentional changes to the WE can be investigated in two ways: (1) the assumption of IAEA control in cell and (2) a residual analysis. In the first option, the IAEA could insert its own probe or adjust the existing probe to various immersion lengths. Based on the height of the cyclic voltammetry (CV) curves at different immersion lengths, the actual area could be regressed. However, this requires additional sampling. For the second option, a residual analysis can be done using existing data from the current sample and past samples. If the residual analysis can identify anomalies in the reconstruction of the data and their source, then the IAEA may not need to collect additional samples.

The analysis of the residuals of the reconstructed CVs with a WE area of 0.5, 0.75, 1, 1.5, and 2 cm<sup>2</sup> reveals a distinct trend. In Figure 4.12, the residuals for a WE area of 0.5, 1 and 2 cm<sup>2</sup> are plotted versus potential. For clarity, WE areas of 0.75 and 1.5 cm<sup>2</sup>

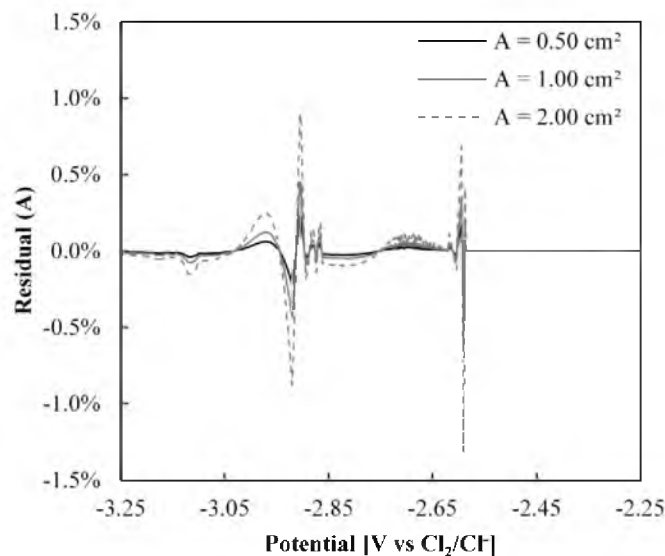


Figure 4.12 Variation of residuals with WE area

were omitted from the plot, but follow the same trend noted here. As can be seen in the plot, the magnitudes of the residuals are increased across all potentials as WE area is increased. This should not be the case, if the concentrations of U and Pu are actually changing. The residuals would be different, but not altered in the same manner across the entire spectrum. Thus, this type of trend in the residuals could be indicative of alterations in the WE area rather than actual changes in the salt composition.

One could envision a rare scenario where the actual concentrations for U and Pu in ER are both changing uniformly (e.g. addition of fresh LiCl-KCl eutectic) leading to a uniform change in the residuals, as in Figure 4.12. However, it was noted in Figure 4.11 that an increase in surface area leads to an increased concentration measurement. Furthermore, in Figure 4.12, an increase in surface area leads to an increase in the residuals' magnitude. Therefore, when the surface area is changing, an increase in the residuals' magnitude is correlated to an increase in the determined concentrations. As noted in Figure 4.10, the residual magnitude should decrease, if the concentrations are

actually increasing. Thus, scenarios that could obscure the cause of changes in the determined concentrations can be deciphered by combining the trends of concentrations and the residuals.

#### 4.3.3.3 Diffusion Layer Thickness

The hydrodynamic conditions of the sampling cell can also affect the determined concentrations. Variations in the hydrodynamic conditions could occur if insufficient settling time is allowed after drawing in a sample from the ER or the cell experiences excessive vibrations from neighboring process equipment. In actual experimental work, rotational rate of an electrode or a stirrer would be a convenient parameter to vary to study the effect of hydrodynamics on the residuals. However, the diffusion layer thickness is the parameter in ERAD that is related to hydrodynamics. Thus, ERAD re-simulated run 6 with diffusion layer thicknesses of 140, 145, 155, 160  $\mu\text{m}$ , and PCR was applied using a training set that contained data simulated with a thickness of 150  $\mu\text{m}$ . The effect of diffusion layer thickness on the PCR determined concentrations is shown in Figure 4.13, which has the same format as Figure 4.11. The PCR concentrations for both

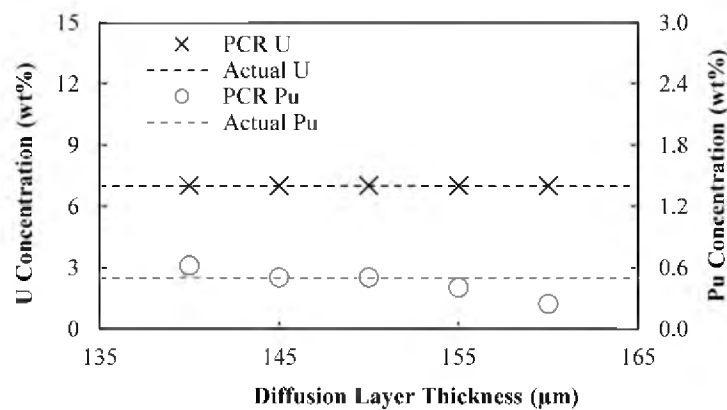


Figure 4.13 Effect of diffusion layer thickness on the concentration determined by PCR for Run 6 from Table 4.5 with a nominal thickness of 150  $\mu\text{m}$



U and Pu decrease with increasing diffusion layer thickness, although, for U, the decrease is very small ( $<0.01$  wt%) and imperceptible in this plot. As with area, this may trigger a false alarm or be used to manipulate concentration measurements. For example, a gentle stirrer could be clandestinely installed and operated in a sampling cell which could make the Pu content appear larger than the real amount.

Again, the examination of residuals could elucidate the cause of the variations in determined concentrations. By examining Figure 4.14, it can be seen that residuals are larger in the regions of the tails of U and Pu peaks. For clarity, again, the intermediate values were omitted, but follow the same trend. This makes sense, because the tails of the reduction peaks are under diffusion control. Thus, if residuals show an increase in the regions of the reduction peak tails, it could be indicative of alterations of the hydrodynamic environment of the measurement cell rather than changes in the salt composition.

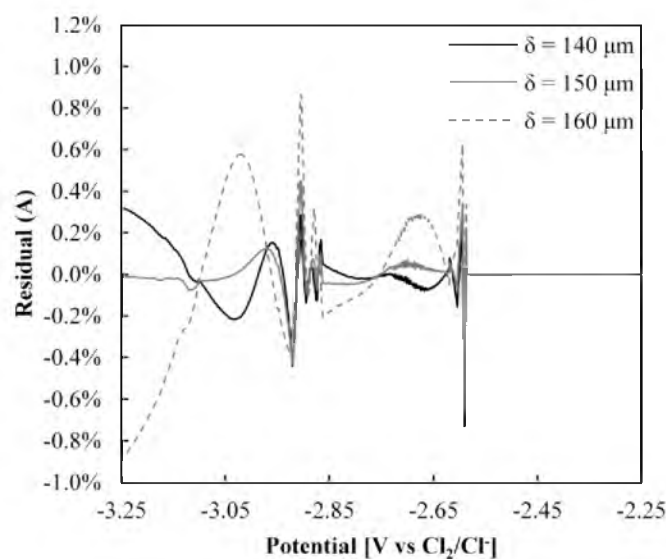


Figure 4.14 Variation of residuals with diffusion layer thickness

#### 4.3.3.4 Additional Species

If a species is present in a sample that is not accounted for in the training set, then it can also cause errors in the determined concentration. A prime candidate to interfere with U and Pu concentration measurements is neptunium (Np). It is common in UNF and has a standard reduction potential in between U and Pu, as can be seen in Table 4.4. Run 6 was resimulated in ERAD with 0.01, 0.05, 0.1, 0.2, 0.3 wt% Np in the ER salt. PCR was applied with the original training set which does not contain Np. The effect of the unaccounted presence of Np on the PCR determined U and Pu concentrations is shown in Figure 4.15. The PCR weight percent of U is mostly unaffected and only increases by 0.02 wt%. However, the PCR weight percent of Pu varies considerably. These variations in the determined weight percent are explained by examining the residuals in Figure 4.16. For clarity, only 0.0, 0.2 and 0.3 Np wt% are plotted to illustrate the overall trend. The residuals remain mostly unchanged until approximately -2.7 V when Np begins to deposit. Thus, the U peak is mostly unaffected by the presence of Np because Np deposition occurs after the U peak, but the Pu peak is affected as evidenced in the change in residuals after -2.7 V. Thus, the departure of the residuals at a certain point could be

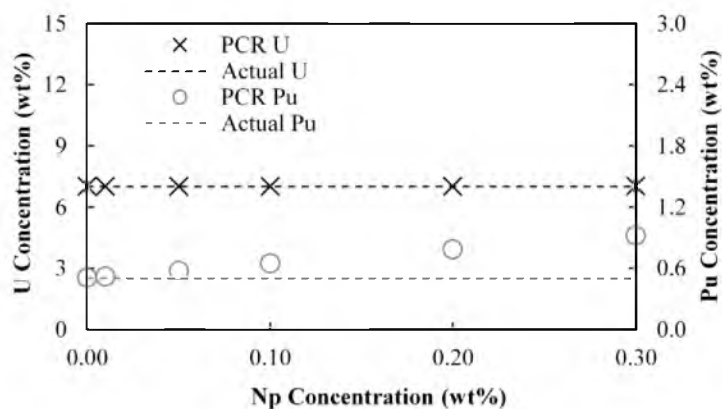


Figure 4.15 Effect of unaccounted Np on the concentration determined by PCR for Run 6 from Table 4.5

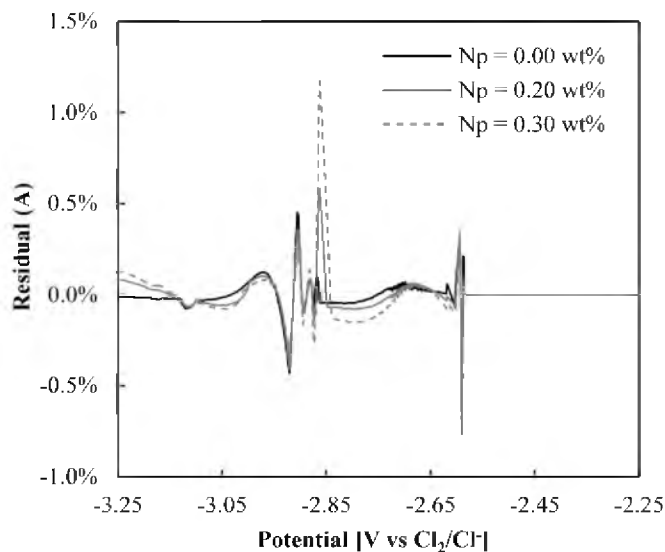


Figure 4.16 Variation of residuals with Np content in salt

indicative of an unexpected species being present rather than an actual change in U or Pu composition. If the residuals are clear enough, the unexpected species could be determined by examining the potential at which the residuals depart from historical trends or calibration data and comparing that to the standard reduction potentials of metal ions in molten LiCl-KCl.

#### 4.4. UCl<sub>3</sub>-ThCl<sub>4</sub>-LiCl-KCl Mixtures<sup>1</sup>

##### 4.4.1. The Molten Salt Reactor

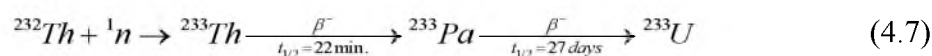
Various designs of MSR exist (103–106). In general, the MSR is designed to operate at high temperatures (650–850°C) and use molten LiF, LiF-BeF<sub>2</sub> (FLiBe), LiF-NaF-KF (FLiNaK), or another fluoride salt loaded with U and/or Th. Some designs even

---

<sup>1</sup>This section includes text and figures from the author's preprint of a paper in the proceedings of the INMM 55<sup>th</sup> Annual Meeting (97). Reprinted with permission of the Institute of Nuclear Materials Management. Copyright 2014. All rights reserved.

use chloride salts (107). A thorium-fuel MSR can be a single- or two-salt system, operated in either the thermal or fast neutron spectrum. As shown in Figure 4.17, in a two-salt system, a thorium-rich or “blanket” salt surrounds the reactor core. The other salt is uranium-rich and forms the core of the reactor.

In a thorium fueled reactor, U-233 is produced when Th-232 absorbs a neutron and undergoes two beta decays, as shown below:



The first beta decay from Th to protactinium (Pa) has a half-life of 21.83 min and can be assumed to primarily occur in the reactor. Subsequently, Pa-233 is removed from the reactor salt since it has a longer half-life of 27 days and a high neutron absorption cross section. Then, Pa-233 is allowed to decay to U-233 outside of the reactor in a hold-up tank. At this point, U-233 could be returned to the salt containing Th, if the MSR uses a one-salt system, or it could be loaded into the core salt. In either system, U will be present with Th. In a one-salt system, the weight percent of U and Th could be 1 and 40 wt%, respectively (108). In the two-salt system, a small amount of Pa-233 will have decayed to U-233 while still in the reactor or some Th may be coextracted with U. Thus, an ability to detect the presence and concentration of U in the presence of Th would be vital for any measurement technique.

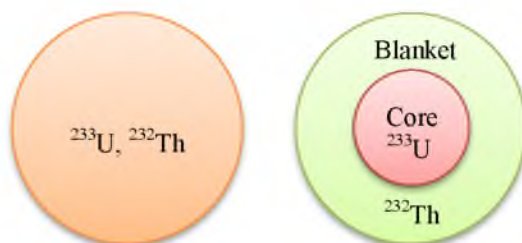


Figure 4.17: Depiction of a single-salt (left) and a two-salt (right) reactor

The MSR employs several distinct features—it is a high-temperature liquid-fuel system with breeding capability in a thorium-uranium fuel cycle. The liquid nature of the fuel permits the employment of on-line refueling and recycling. These features bring advantage in economy and safety, as well as a substantial reduction of hazardous waste. The processing media for the on-line treatment of MSR fuel is still undecided. However, in Oak Ridge National Laboratory's conceptual design, portions of the fuel treatment loop use fluoride salts (109) and chloride salts may also be used in MSR operating in the fast neutron spectrum. Thus, the LiCl-KCl-UCl<sub>3</sub>-ThCl<sub>4</sub> may be an important system to understand and monitor using electrochemistry as the MSR develops. As noted earlier, there exists a likely possibility that, in a MSR, small amounts of U would be found in mixtures containing significantly more Th. Therefore, the ability to make quantitative measurements of the concentration of U in a mixture containing a significant amount of Th using voltammetry is of particular interest in this work.

#### 4.4.2. Voltammetry Simulation

The properties used to simulate the electrochemical behavior of U and Th in eutectic LiCl-KCl salt at 500°C are displayed in Table 4.6. The number in brackets indicates the reference from which the value was taken. The electrochemical cell parameters were the same as those used in the LiCl-KCl-UCl<sub>3</sub>-PuCl<sub>3</sub> system (see Table 4.3) with exception of the working electrode (cathode) and CV vertex potentials. For each simulation of U/Th CVs, the potential was scanned from -1 to -2 V versus Ag/AgCl (1 wt%) at a rate of 0.1 V/s, essentially linear sweep voltammetry (LSV), and the current was calculated based on a surface area of 4.53 cm<sup>2</sup> for the sensing (working) electrode. Several simulations were performed at varying levels of U and Th concentration. The

Table 4.6: Properties used for simulations

Property	U	Th
$E^{\circ}$ (V vs Ag/AgCl)	-1.274 (110)	-1.325 (74)
$D$ ( $\times 10^5$ cm <sup>2</sup> /s)	2.00 (90)	4.46 (74)
$z$	+3	+4
$i_o$ (A/cm <sup>2</sup> )	1.00 (90)	0.8*
$\alpha$	0.5*	0.5*
*Assumed Value		

concentration values used for each run are displayed in Table 4.7. The first 16 simulations were used as the training set. The last 3 simulations were used as unknowns to test the performance of voltammetry in making concentration measurements.

The  $i$ -E curve for Run 13 is provided in Figure 4.18 to illustrate key features of the reduction peak that are common to all runs. Due to the proximity of U's and Th's apparent standard potentials to each other ( $\Delta E^{\circ} = 51$  mV), the reduction peaks of U and Th almost completely overlap, as seen in Figure 4.18. This makes deciphering their separate peaks and respective peak heights impossible. Thus, the traditional method of relating peak height to concentration cannot be used. An alternative analysis method must be used.

Table 4.7: Compositions of simulated runs

Training Set								
Run	U (wt%)	Th (wt%)	Run	U (wt%)	Th (wt%)	Run	U (wt%)	Th (wt%)
1	0.00	1.00	8	0.50	0.00	15	1.00	3.00
2	0.00	1.50	9	0.50	1.00	16	0.60	1.40
3	0.00	3.00	10	0.50	1.50	<b>Unknowns</b>		
4	0.10	0.00	11	0.50	3.00	Run	U (wt%)	Th (wt%)
5	0.10	1.00	12	1.00	0.00	17	0.05	2.00
6	0.10	1.50	13	1.00	1.00	18	0.25	1.25
7	0.10	3.00	14	1.00	1.50	19	0.75	0.50

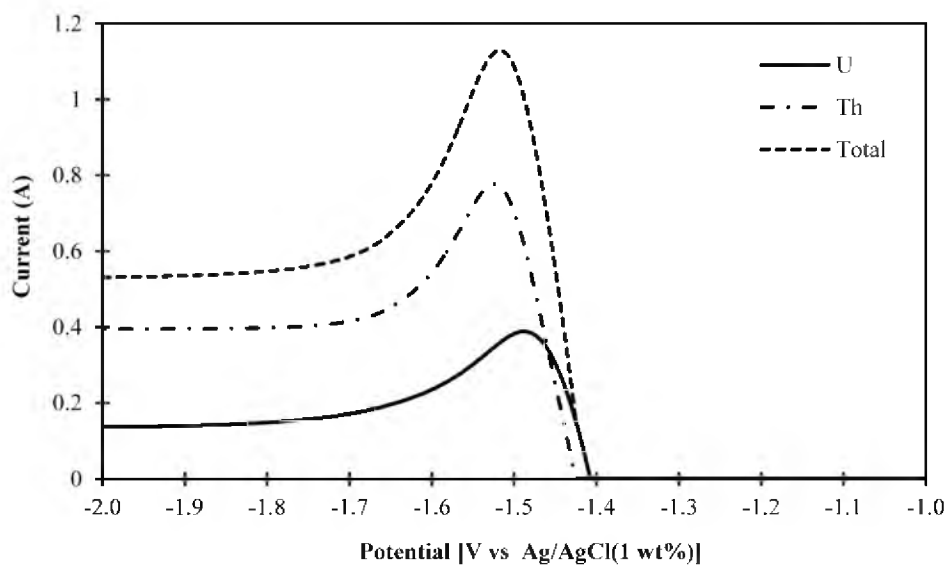


Figure 4.18: *i*-E curve for Run 13 from Table 4.7

#### 4.4.2.1 Results and Discussion

Using PCR with 6 PCs, as described earlier, the concentrations of U and Th were determined for Runs 17-19. As shown in Table 4.8, the determined weight percent of U and Th are very close to the actual for each run with the exception of U in Run 17. Excluding the error of U in Run 17, the average error was 1.1% with a maximum of 2.8%.

The ability of PCR to accurately determine the concentrations of U and Th from the simulated, overlapping reduction peaks of U and Th is promising, but practical application of voltammetry to MSRs has several challenges. First, the detection of trace

Table 4.8: Weight percent of U and Th determined by PCR

Run	U (wt%)		Th (wt%)	
	PCR	Actual	PCR	Actual
17	0.025	0.050	2.012	2.000
18	0.257	0.250	1.248	1.250
19	0.757	0.750	0.494	0.500

amounts U with Th present needs to be addressed, as the concentration of U in Run 17 had an error of 50%. Anodic stripping voltammetry may be more suitable for detecting trace amounts of U. Greater accuracy may be achieved in fluoride salts because, the apparent standard potentials ( $E^{\circ'}$ ) of U and Th in fluorides could have greater separation. For example, at 773 K, according to thermodynamic calculations, the difference in the standard apparent potentials of U and Th ( $\Delta E^{\circ'}$ ) is 366 mV in FLiBe and preliminary measurements show that  $\Delta E^{\circ'} = 320$  mV in FLiNaK (111, 112). Further measurements have confirmed the greater spacing of U and Th CV peaks in LiF (113). In this work,  $\Delta E^{\circ'} = 51$  mV (see Table 4.6). However, this could come at a cost, the greater separation is created by  $E^{\circ'}$  of Th becoming even more negative than the  $E^{\circ'}$  of U, possibly causing the Th reduction peak to overlap with alkali metal reduction. A CV of Th in FLiNaK shows only a shoulder due to the commencement of reduction of one of the alkali metals in the matrix salt (112). Another issue is that voltammetry is best suited for dilute concentrations (i.e. <10 wt%). As mentioned earlier, Th concentration could be as high as 40 wt%. This could be resolved by diluting the sample with a known amount of matrix salt (e.g., FLiBe). Although, this would make the ability to accurately detect trace amounts of U even more important.

#### 4.5. Summary

The use of PCR and PLS to determine U and Pu concentrations in ER salt was demonstrated extensively on simulated data and on limited experimental data from literature. In both cases, PCR and PLS more accurately determined the concentrations of U and Pu in eutectic LiCl-KCl melts than a traditional peak height analysis. Additionally, a residual analysis could be used to discern whether changes in the determined



concentrations are due to actual changes in ER salt composition or due to changes in cell conditions. However, further work is merited. Further analysis on experimental data is required in order to more conclusively determine the accuracy of PCR and PLS in determining concentrations of multianalyte melts. Furthermore, the residuals of experimental data will certainly be noisier than the residuals from simulated data. If the additional noise is small enough, the trends used to identify sources of error (i.e., changes in WE area, etc.) could still be identified.

Voltammetry is also a candidate method for the online monitoring of the concentrations of U and Th in a MSR. However, LSV simulations of the U and Th reduction peaks in LiCl-KCl showed that the peaks can potentially overlap completely. Thus, traditional peak height analysis could not be used to determine the concentrations. PCR was used to determine the concentrations of U and Th. It was found that PCR provided accurate evaluations of concentration, except at low U concentrations. The evaluation of U and Th concentrations in fluoride salts may be easier due to a greater separation of their standard potentials. However, there may still be complications due to interference from the matrix salt. In either case, PCR provides a powerful tool that can be used to better capture the variance of the voltammetry signals with changes in the concentrations of U and Th.

## 5. ELECTROCHEMISTRY OF $\text{GdCl}_3$ - $\text{LaCl}_3$ - $\text{LiCl}$ - $\text{KCl}$ MIXTURES

Irene Curie was tantalizingly close to solving the mystery of nuclear fission. She performed fractional crystallization on her uranium sample after bombarding it with neutrons and found lanthanum present. She was perplexed by this finding since it was well-established for other elements that they only transmute by 1 or 2 atomic numbers and lanthanum was a difference of 35 atomic numbers from uranium. She could not bring herself to challenge years of nuclear physics experiments with her chemical analysis. So, she concluded that “this substance can not be anything except as transuranic element, possessing very different properties...” (114). Even Otto Hahn, who later discovered fission with Lisa Meitner and Fritz Strassman, thought that she was “very muddled up” (115). Lanthanides continue to perplex and confuse researchers and this is particularly true for their electrochemical behavior in eutectic  $\text{LiCl}$ - $\text{KCl}$  as will be demonstrated by the previous work reviewed and original work presented in this chapter.

### 5.1. Electrochemistry of $\text{GdCl}_3$ in $\text{LiCl}$ - $\text{KCl}$ Eutectic

The ternary system of  $\text{LiCl}$ - $\text{KCl}$ - $\text{GdCl}_3$  has been studied extensively. Chronopotentiometry was first used to calculate the diffusion coefficient of  $\text{Gd}^{3+}$  ions in molten eutectic  $\text{LiCl}$ - $\text{KCl}$  (116). The first voltammetric study (58) was published a year later, although the major focus of the study was measuring the electromotive force of both  $\text{LaCl}_3$  and  $\text{GdCl}_3$ . However, it did calculate the diffusion coefficients and activation

energy. The next study (117) verified the nucleation phenomena for Gd metal deposits and the one-step reduction mechanism for  $\text{Gd}^{3+}$  ions. Using SWV, an asymmetry was noted due to nucleation, thus the more negative half of the peak was used to measure the number of electrons transferred which was calculated to be 2.7.

The following study (71) verified the single-step reduction mechanism and identified voltammograms of  $\text{Gd}^{3+}$  to be reversible until a scan rate of 100 mV/s, above which it becomes quasi-reversible. The authors noted that a discrepancy in diffusion coefficient between published values and those calculated from CVs using the Berzins-Delahay equation, which, as discussed in Section 2.5.2, is for reversible equation. This discrepancy is attributed to quasi-reversibility of Gd reduction. Thus, as noted in Chapter 2, understanding the reduction mechanism and reversibility of the system is crucial to obtaining consistent and accurate results. The authors discount the diffusion coefficients calculated from cyclic voltammetry (CV), but convolute the CV measurements to calculate the diffusion coefficient which “is more reliable since it uses the whole curve instead of only the peaks” (71).

A more recent investigation (118) confirms the single-step reduction of  $\text{Gd}^{3+}$  ions and identifies the quasi-reversible region for voltammetry between 50 and 1000 mV/s. In addition to calculating the diffusion coefficient and standard reduction potential of the Gd(III)/Gd couple, the study examines reaction kinetics and estimates the exchange current density and standard rate constant. Additionally, it identifies Gd metal nucleation mechanism to be progressive at low concentration (i.e., 0.5 wt%  $\text{GdCl}_3$ ) and instantaneous above 2 wt%  $\text{GdCl}_3$ . Unfortunately, the transition point from reversibility to quasi-reversibility was not confirmed or investigated at the NPL.

## 5.2. Electrochemistry of $\text{LaCl}_3$ in LiCl-KCl Eutectic

The ternary system of LiCl-KCl- $\text{LaCl}_3$  may be one of the most widely studied systems in the eutectic LiCl-KCl system. Only three works are summarized which performed extensive electrochemical analysis of  $\text{LaCl}_3$  in eutectic melts to investigate its behavior (119–121). All three works conclude that  $\text{La}^{3+}$  ions reduce to La metal in a single-step mechanism. However, significant discrepancies in the electrochemical reversibility of the  $\text{La}^{3+}$  reduction exist in the general literature. Tang and Pesic (121) provide a great review of the conclusion drawn in the literature regarding the reversibility of  $\text{La}^{3+}$  reduction. At 733K, Tang and Pesic concluded that from 50-700 mV/s the reduction of  $\text{La}^{3+}$  ions is quasi-reversible. However, the method used for determining reversibility was developed for soluble/soluble systems and as demonstrated in Section 2.5.2.2 may not be applicable to soluble/insoluble systems. Vandarkuzhali et al. (120) concluded that from 25-150 mV/s at 798 K that reduction of La(III) ions is quasi-reversible and irreversible above 150 mV/s. However, they also observed at 698-798K “a linear dependence of the cathodic peak current on the square root of scan rate” (120) from 25-150 mV/s which is slightly confusing since nonlinearity of peak height with square root of scan rate is characteristic of the quasi-reversible region. They also note that the convoluted CV curves obeyed reversible reduction from 25-50 mV/s. Cyclic voltammetry measurements made by another researcher (122) at NPL show that  $\text{La}^{3+}$  reduction transitions from reversible to quasi-reversible between 100 and 200 mV/s as shown in Figure 5.1. Thus,  $\text{La}^{3+}$  reduction is assumed to be reversible up to 150 mV/s in this study, because of similarities in experimental methods.

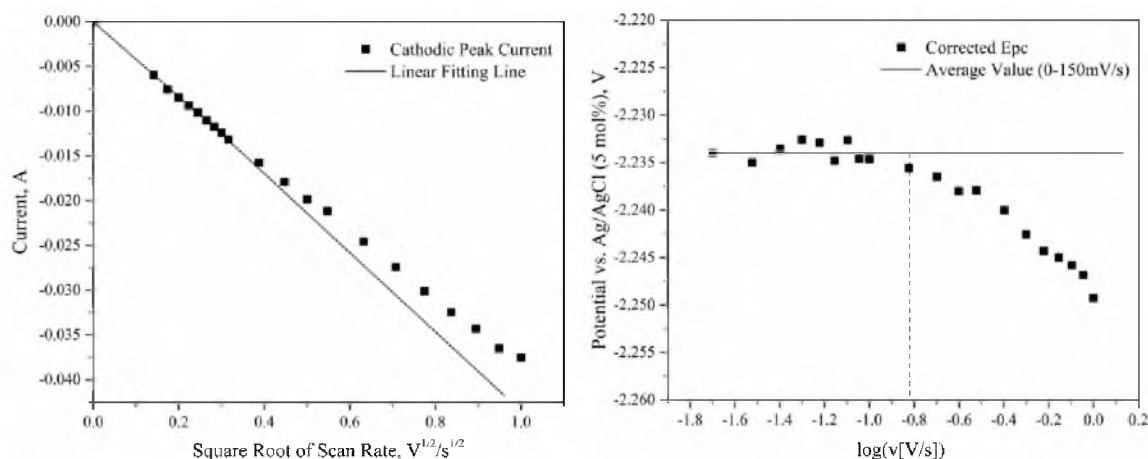


Figure 5.1 Peak current (left) and potential (right) of  $\text{LaCl}_3$  ( $3.29 \times 10^{-5} \text{ mol/cm}^3$ ) in eutectic  $\text{LiCl-KCl}$  at 773 K on a 2 mm W rod. Reprinted from (122) with permission from Elsevier

### 5.3. Electrochemistry of $\text{GdCl}_3$ and $\text{LaCl}_3$ in $\text{LiCl-KCl}$ Eutectic

A representative CV of the  $\text{GdCl}_3$ - $\text{LaCl}_3$ - $\text{LiCl-KCl}$  mixtures is plotted in Figure 5.2. On the forward (reducing) scan, the current is flat and nearly zero until the reduction potential of  $\text{Gd}^{3+}$  ions which forms the first peak at about -1.94 V. Immediately after the  $\text{Gd}^{3+}$  reduction peak decays,  $\text{La}^{3+}$  ions begin to deposit and the peak corresponding to  $\text{La}^{3+}$  reduction closely follows the  $\text{Gd}^{3+}$  reduction peak. Lastly, a sharp decrease in the current near -2.4 V is indicative of  $\text{Li}^+$  ions reducing which establishes the lower limit of the electrochemical window for eutectic  $\text{LiCl-KCl}$ . Then, the scan is reversed and Li metal is oxidized forming the peak at -2.3 V. The expected oxidation peak for the oxidation of La metal is absent and a prominent peak only forms where Gd metal oxidizes. The phenomenon is better illustrated in Figure 5.3 which overlays CVs from the single-analyte mixtures on the CV from mixture D2. It is clear in Figure 5.3 that the La oxidation peak is missing or unnoticeable on the black curve which corresponds to mixture D2, and the remaining oxidation is in the position of the Gd oxidation peak.

Two possible causes are speculated for the absence of the La oxidation peak.

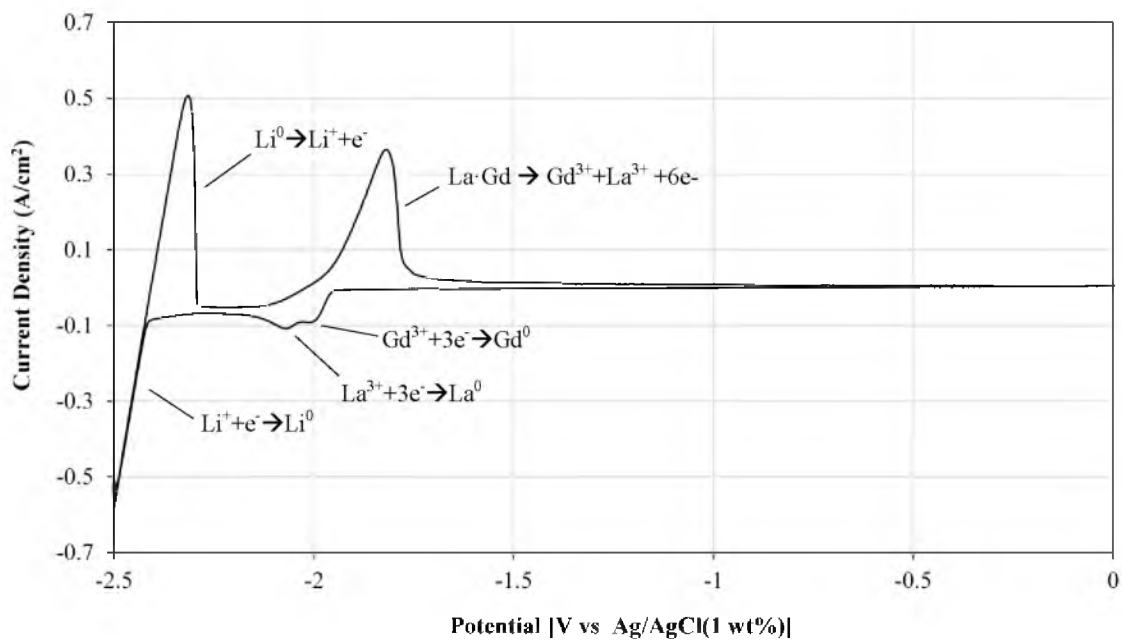


Figure 5.2 CVs for mixtures D1 (1.53 wt%  $\text{GdCl}_3$  0.89 wt%  $\text{LaCl}_3$ ) at 100 mV/s and 773 K on 1mm Mo wire (Area = 0.28  $\text{cm}^2$ )

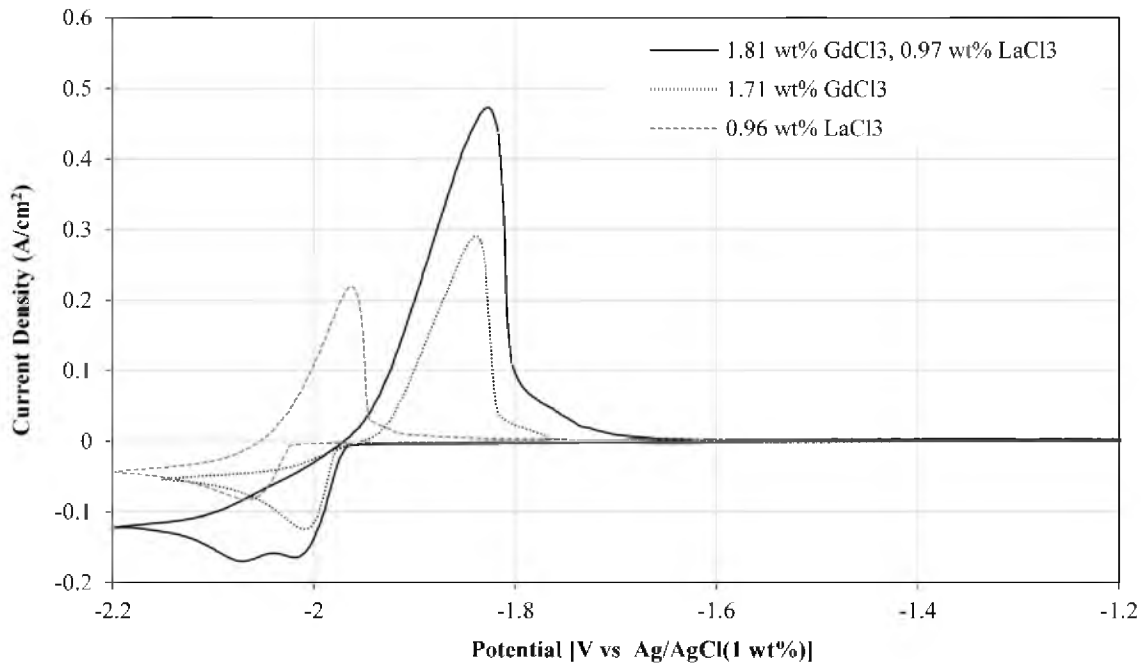


Figure 5.3 CVs for mixtures C1, D2, OCP-Gd3 (see Appendix A) at 100 mV/s and 773 K on 1mm Mo wire

First, it is feasible that Gd and La form a metal alloy when both are present on the WE. Indeed, phase diagrams show that at 500°C alloys readily form between Gd and La metals (123). Attempts were made to outpace the supposed alloying reaction by increasing the CV scan rate incrementally up to 2 V/s. No indication of a second oxidation step was observable from the CV at any of the scan rates. Alternatively, La metal could begin to oxidize, but could become covered by Gd metal since Gd deposition is still favored at La oxidation potentials. This could be the cause of the slight bump around -2.1 V in Figure 5.3. This bump is more prominent when the amount of  $\text{LaCl}_3$  exceeds  $\text{GdCl}_3$  in LiCl-KCl eutectic which is the case for mixture B4. A CV for mixture B4 is displayed in Figure 5.4. A clear bump is observed between -2.1 and -2.0 V. Semi-differentiation of the CV reveals two distinct peaks indicating the possible convolution of two oxidation peak in the CV. In either case, further investigation into the cause of the absence of La oxidation peaks is warranted. Thus, only the cathodic peaks were investigated in this chapter.

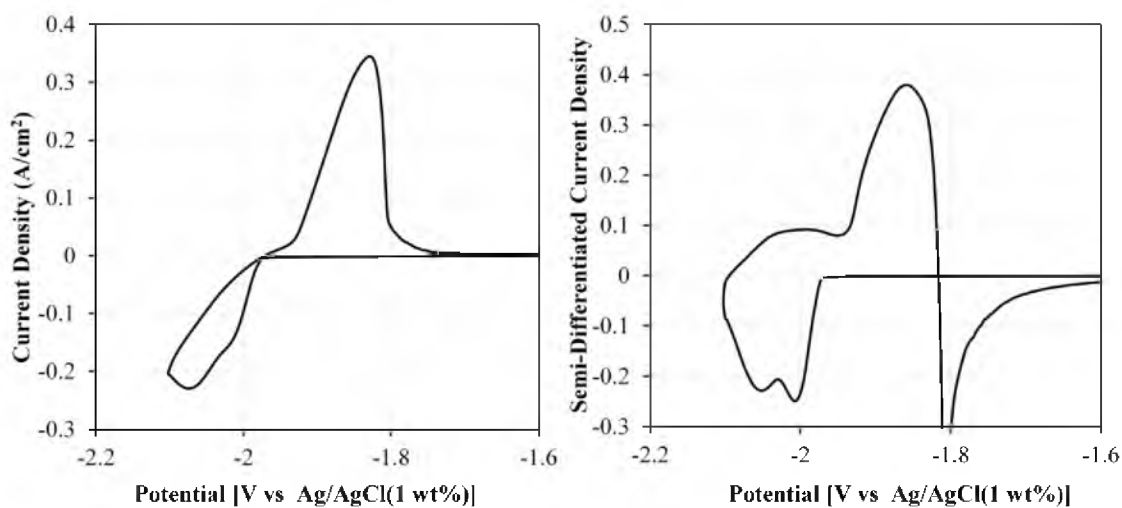


Figure 5.4 CV (left) and semi-differentiated CV (right) of mixture B4 (1.65 wt%  $\text{GdCl}_3$  and 2.21 wt%  $\text{LaCl}_3$ ) at 100 mV/s and 773 K on 1 mm Mo Wire (Area = 0.50 cm<sup>2</sup>)

The absence of the La metal oxidation peak was further investigated using chronopotentiometry (CP). A current of -80 mA was applied to the cell for 4 s, then the cell was held at open circuit and the potential was measured. The resulting potential profiles are plotted in Figure 5.5 with a magnification of the first 0.75 s. There is a slight bend in the plot when a reducing current of -80 mA is charged indicating the onset of the deposition of La from  $\text{La}^{3+}$  ions. However, when the open-circuit potential is measured afterward, there is no step or bend in the potential profile to indicate oxidation of La metal. Ideally, three potential plateaus should appear for Li, La, and Gd metal oxidation while the cell is held at open-circuit. In Figure 5.5, this is not the case. Only two plateaus appear corresponding to the open-circuit potentials measured for  $\text{Li}/\text{Li}^+$  and  $\text{Gd}/\text{Gd}^{3+}$  redox couples.

In  $\text{LiCl-KCl-GdCl}_3\text{-LaCl}_3$  mixtures,  $\text{La}^{3+}$  ions deposit on Gd metal because  $\text{Gd}^{3+}$  ions reduce first. This may affect the standard apparent potential of the  $\text{La}^{3+}/\text{La}$  redox couple because Gd metal alloys with La metal, unlike the Mo wire. For this reason, the

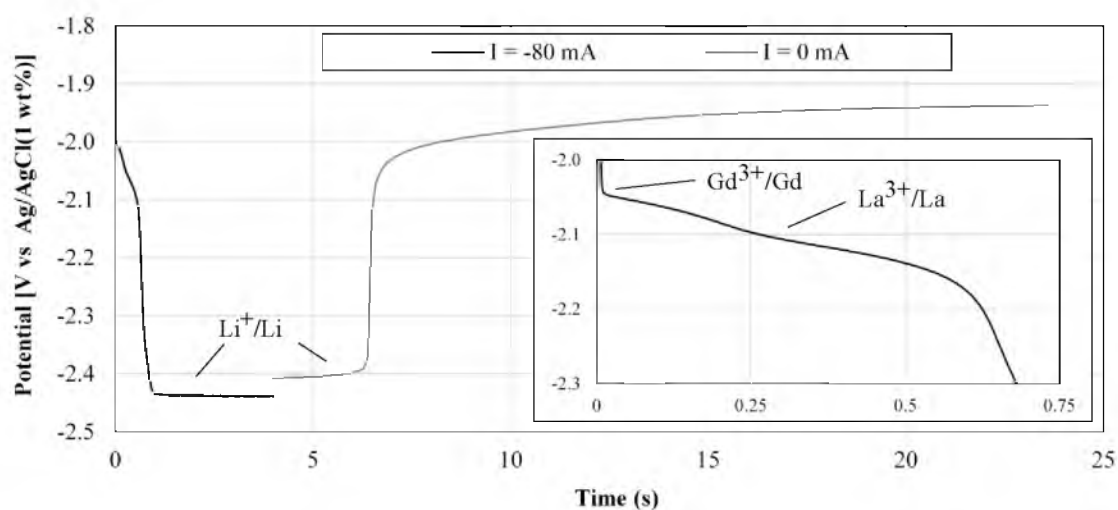


Figure 5.5 CP and OCP for mixture D2 (1.81 wt%  $\text{GdCl}_3$  and 0.97 wt%  $\text{LaCl}_3$ ) with inset inset magnification of first 0.75s



open-circuit potentials of the  $\text{Gd}^{3+}/\text{Gd}$  and  $\text{La}^{3+}/\text{La}$  redox couples were measured by preparing the single-analyte salt mixtures with the IDs: OCP-Gd, OCP-Gd2, OCP-La, and OCP-La2 (see Appendix A). Multiple OCP measurements were made in these mixtures after predepositing Gd or La metal on a Mo wire. Using (2.8) with (2.9), the standard apparent potential ( $E^{o'}$ ) was calculated for each measurement and averaged (see Table 5.1). After making OCP measurements with the Mo wire, a clean Gd rod was inserted into the OCP-La2 mixture and used as the WE to measure the open-circuit potential of  $\text{La}^{3+}$  on Gd metal. Even though the cell was set zero, it was never precisely zero. The current measured would fluctuate from positive to negative and was less than or on the order of  $1 \mu\text{A}$  which allowed for the exchange of  $\text{La}^{3+}/\text{La}$  on the Gd rod. Initially, the potential decayed rapidly as the Gd rod was brought up to 773 K, but eventually settled out to a steady value. Using that value with (2.8) and (2.9), the  $E^{o'}$  for  $\text{La}^{3+}/\text{La}$  on a Gd rod was calculated and is reported in Table 5.1 along with the average single-analyte values and their 99% confidence intervals. The difference in the  $E^{o'}$  value for  $\text{La}^{3+}/\text{La}$  on a Gd rod exceeds the 99% CI demonstrating a high likelihood that the  $E^{o'}$  of  $\text{La}^{3+}/\text{La}$  is affected by the presence of Gd metal. Additionally, it shows that the presence of Gd metal on the WE will cause  $\text{La}^{3+}$  to deposit sooner in a CV because of the more positive  $E^{o'}$  value. The potential values were converted to the chlorine electrode using the values in Table 2.6 from Lantelme-Berghoute (58).

The activity coefficient of La metal on Gd metal can be calculated by the

Table 5.1 Calculated standard apparent reduction potentials with literature values

Redox Couple	$E^{o'}$ (V vs Cl/Cl <sub>2</sub> )	±99% CI	Literature Values		
<b>Gd<sup>3+</sup>/Gd</b>	-2.999	±0.0072	-3.008 (118)	-2.948 (41)	-3.065 (71)
<b>La<sup>3+</sup>/La</b>	-3.086	±0.0055	-3.116 (120)	-3.106 (41)	
<b>La<sup>3+</sup>/La(Gd)</b>	-3.068	0.0173*	*Difference in $E^{o'}$ from $\text{La}^{3+}/\text{Gd}$ to $\text{La}^{3+}/\text{La}$		

following equation

$$\ln(\gamma_{La(Gd)}) = \frac{nF}{RT} (E_{La^{3+}/La}^{o'} - E_{La^{3+}/La(Gd)}^{o'}) \quad (5.1)$$

This assumes that the activity of La metal is one when  $E^{o'}$  is calculated from the OCP after predepositing pure La metal and the difference in  $E^{o'}$  values is solely caused by the change in the La metal activity. It also implies a mole fraction of one for La metal. Under these assumptions, the activity coefficient of La metal on Gd metal is 0.485 at 773 K and  $La^{3+}$  concentration of 0.22 mol%.

As shown in Figure 5.2-5.5, the electrochemical signals of  $Gd^{3+}/Gd$  and  $La^{3+}/La$  redox couples overlap significantly. Thus, in order to make concentration estimations, a method needs to be developed to separate the signals or analyze them together. The signals recorded for CP and OCP have already been shown to have very minimal or no separation between the two redox couples making them poor candidates for signal separation. The other electrochemical techniques applied to LiCl-KCl-GdCl<sub>3</sub>-LaCl<sub>3</sub> mixtures were chronoamperometry (CA) and CV.

#### 5.4. Concentration Correlations

CV and CA are evaluated in this section on two criteria: (1) separability and (2) correlation with concentration. If the separability of the  $Gd^{3+}$  and  $La^{3+}$  reduction signals appeared promising, then correlations were developed, key parameters calculated and concentration determined.

##### 5.4.1. Cyclic Voltammetry

The separation between reduction peaks is dependent on scan rate, as shown in Figure 5.6. At slower scan rates, there is greater resolution and separation between peaks.

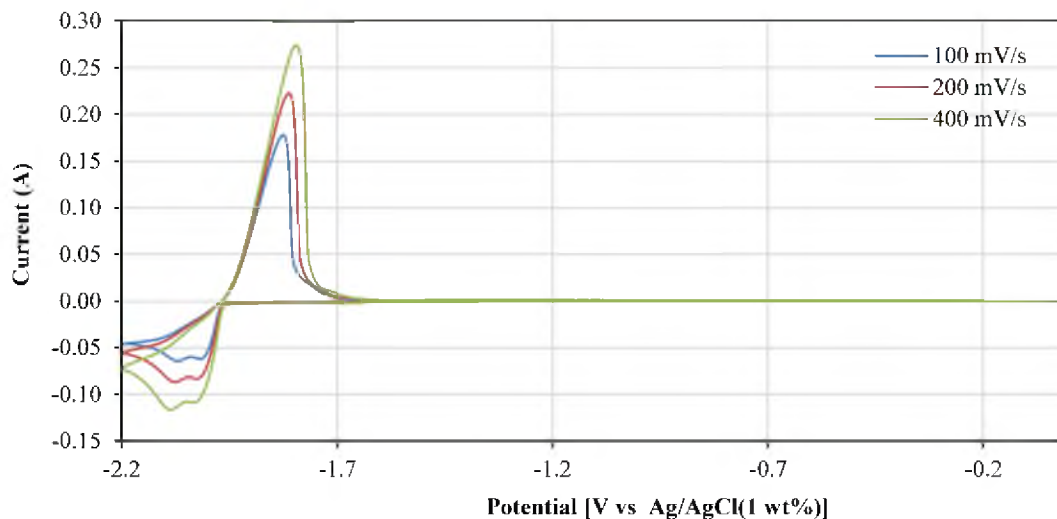


Figure 5.6 CVs at various scan rate on 1 mm Mo wire (Area = 0.38 cm<sup>2</sup>) for mixture D2 (1.81 wt% GdCl<sub>3</sub> and 0.97 wt% LaCl<sub>3</sub>) at 773 K

At faster scan rates, there is less separation. A slight dip can be seen after the Gd<sup>3+</sup> reduction peak at 100 mV/s. That dip becomes more of a plateau as scan rates increase. The scan rates 100, 150, 200, 300, 400, and 500 mV/s were applied in all mixtures. For some mixtures CVs at 50 mV/s and 250 mV/s were recorded. Ideally, 50 mV/s would be used because it has the clearest separation of peaks and would be within the reversibility region for both Gd<sup>3+</sup> and La<sup>3+</sup> reduction. However, area growth affected the peaks at higher concentrations and CVs were not recorded at this scan rate on all mixtures. Thus, CVs recorded at 100 mV/s were selected for analysis because area growth did not appear to occur, separate peaks are still clearly visible, and reversibility conditions are likely still met. Although separate peaks are visible, additional treatment was necessary to establish baselines and obtain accurate peak heights.

The peak separation technique involved both the semidifferentiation and curve fitting as detailed by Palys et al. (96). First, the reduction peaks of the CVs were semidifferentiated (SD) using Autolab's potentiostat software, NOVA 1.11.2.

Semidifferentiation creates sharper and more symmetrical peaks. A representative plot of SD peaks is shown in Figure 5.7. While the peaks in Figure 5.7 look sharper and are more symmetrical than those in Figure 5.3 and 5.6, there is still some overlap and asymmetry to them, unlike the peaks fitted by Palys et al. (96), who fitted symmetrical peaks with the inverse of the hyperbolic cosine squared. In this case, due to asymmetry, a Bifurcated Gaussian (Bigaussian) distribution was fitted to the semi-differentiated peaks using Fityk 0.9.8 (124), as shown in Figure 5.7.

Once the peaks had been separated, the fitted SD peak current density for  $\text{Gd}^{3+}$  and  $\text{La}^{3+}$  reduction were correlated to concentration, as shown in Figure 5.8. The regressed linear parameters, coefficient of determination ( $R^2$ ), and 95% CI for both the  $\text{Gd}^{3+}$  and  $\text{La}^{3+}$  peak height correlations are given in Table 5.2. Diffusion coefficients were also calculated from the slope of the correlations using the following expression for SD peak current ( $e_p$ ) (45)

$$e_p = \frac{n^2 F^2 A v \sqrt{D_{M^{n+}}}}{2RT} C_{M^{n+}} \quad (5.2)$$

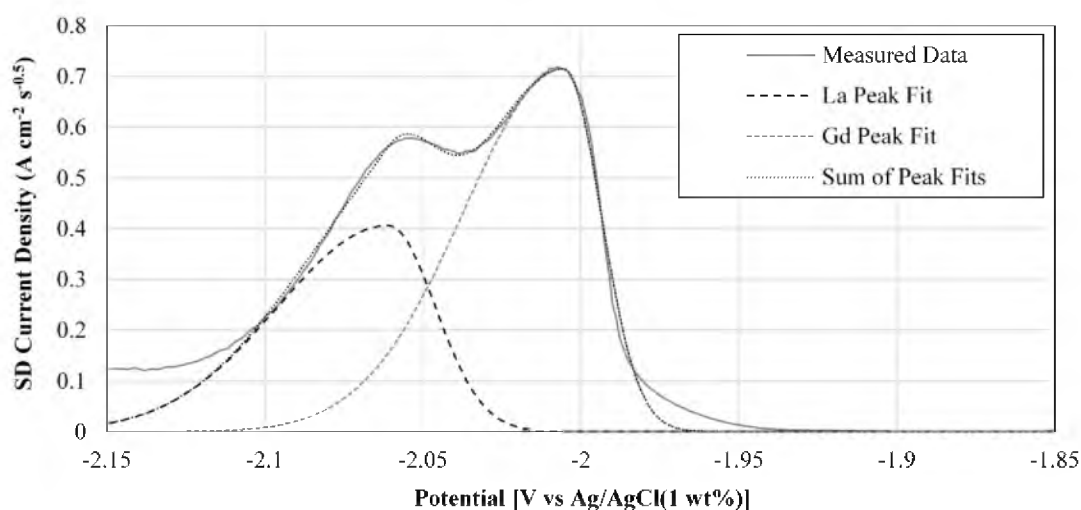


Figure 5.7 Semidifferentiated reduction peaks on 1 mm Mo wire (Area = 0.31 cm<sup>2</sup>) from mixture B3 at 100 mV/s

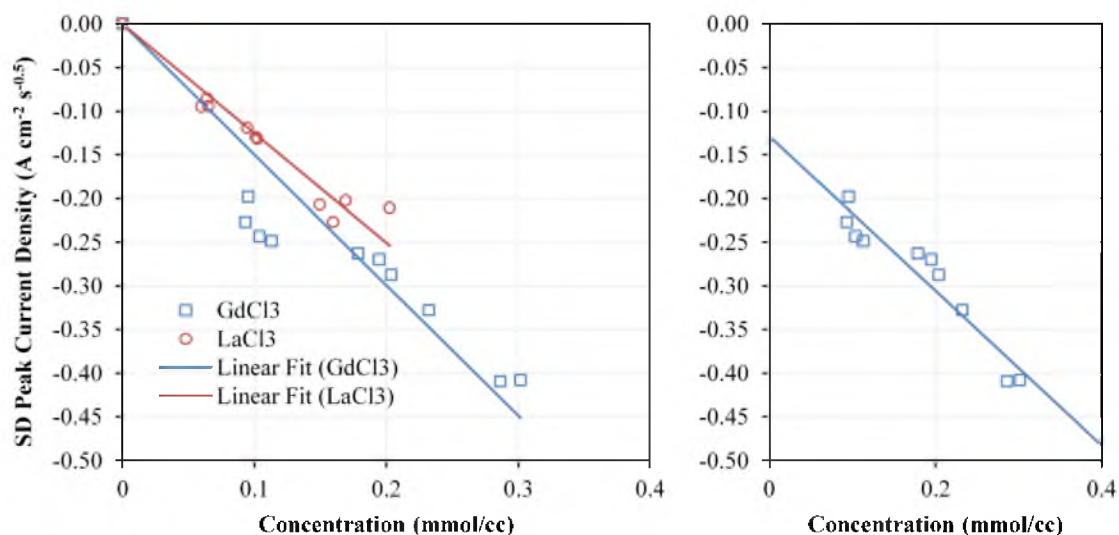


Figure 5.8 Concentration correlations for  $\text{Gd}^{3+}$  and  $\text{La}^{3+}$  SD reduction peak currents at 100 mV/s and 773 K with (left) and without (right) intercept forced to zero

Table 5.2 Regressed coefficients and calculated diffusion coefficient with literature values

	Slope $\pm$ 95% CI ( $\text{A cm mol}^{-1} \text{s}^{-0.5}$ )	Intercept $\pm$ 95% CI ( $\text{A cm}^{-2} \text{s}^{-0.5}$ )	$R^2$	Diffusion Coefficient ( $10^{-5} \text{ cm}^2/\text{s}$ )			
				Calculated $\pm$ 95% CI	(120)	(125)	(58)
$\text{La}^{3+}$	$-1252 \pm 114.2$	N/A	0.92	$0.369 \pm 0.003$	1.37	1.85	2.02
$\text{Gd}^{3+}$ (y-int $\neq$ 0)	$-885.5 \pm 230.3$	$-0.1286 \pm 0.0449$	0.91	N/A	(116)	(71)	(58)
$\text{Gd}^{3+}$	$-1496 \pm 205.1$	N/A	0.77	$0.527 \pm 0.010$	1.15	0.53	1.05

The parameters are only valid within the concentration range of 1.49-4.69wt%  $\text{GdCl}_3$  and 0.89-2.45wt%  $\text{LaCl}_3$ . Furthermore, these correlations were developed based on CVs with a scan rate of 100 mV/s.

The correlation for Gd is weaker than the correlation curve for La. At lower concentrations, the Gd peak height does not decrease as sharply with concentration. This could be due to nonideal behavior of its diffusion coefficient. As has been shown for uranium (45) at high concentrations, the diffusion coefficient could be decreasing. However, the decrease appears to occur at lower concentrations ( $<1.5$  wt%  $\text{GdCl}_3$ ) for  $\text{Gd}^{3+}$  than it does for  $\text{U}^{3+}$ . CV peaks need to be recorded at lower concentrations of  $\text{GdCl}_3$

before a definitive conclusion can be offered on the behavior of the diffusion coefficient of  $\text{Gd}^{3+}$ . In this case, the correlation for  $\text{GdCl}_3$  can be improved by not forcing the intercept through zero making the correlation more empirical and less fundamental.

The values for the diffusion coefficients of both  $\text{Gd}^{3+}$  and  $\text{La}^{3+}$  are much lower than those reported in the literature. The presence of an additional ion may be the cause of this decrease from early single-analyte studies. In the case of  $\text{Gd}^{3+}$ , it may be that the slope of peak height with concentration is steeper at concentrations less than 1.5 wt%  $\text{GdCl}_3$ . Also, most of the literature values were determined using CP. Different electroanalytical techniques can yield different values of the diffusion coefficient. It may also be an artifact of the equation, (5.2), used. There is another expression (126) for SD peak height that has a 4 instead of 2 in denominator which results in 4 times larger values for diffusion coefficients. This would bring the value for  $\text{La}^{3+}$  right in line the existing values in literature, but this expression was not derived specifically for metal deposition whereas (5.2) was.

It is important to note that CVs from mixture D4 were not used in this correlation because of evidence that the immersion depth was mischaracterized. The plot of SD peak current density and concentration with mixture D4 included is displayed in Figure 5.9. Both the  $\text{La}^{3+}$  and  $\text{Gd}^{3+}$  peaks are larger than other peaks at similar concentrations. The  $\text{Gd}^{3+}$  and  $\text{La}^{3+}$  peaks are 45% and 41% greater than the peaks predicted by the diffusion coefficients in Table 5.2. This increase would have to be caused by a factor that would affect both peaks similarly. WE surface area is one such factor that would proportionally affect both peaks.

One-by-one each mixture's SD peak and concentration were removed from the

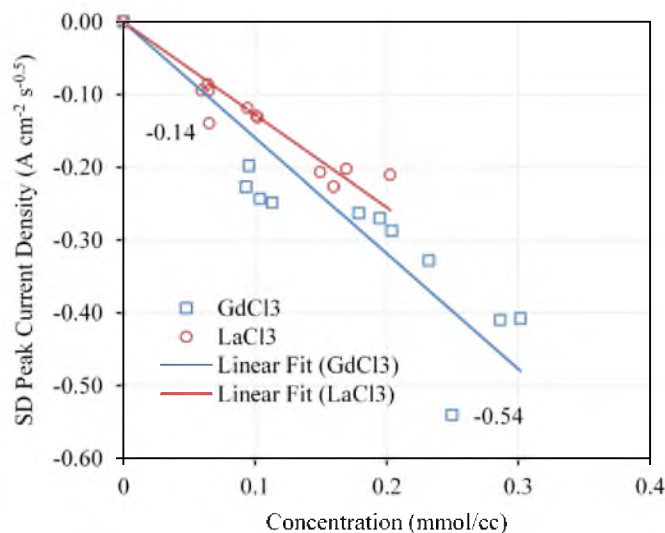


Figure 5.9 Concentration correlations for  $\text{Gd}^{3+}$  and  $\text{La}^{3+}$  with mixture D4 (indicated by SD peak height value) at 100 mV/s and 773 K on 1 mm Mo wire

calibration curve and treated as an unknown sample. After removing a mixture's data, the regression of concentration with SD peak height was redone each time. Then the removed mixture's SD peak height was used to measure its concentration. The electroanalytical concentrations are compared to ICP-OES measured concentrations in Table 5.3. They are also compared to another analytical method, called principle component regression (PCR).

The mathematics and computational procedures of PCR are discussed in Chapter 4. Only the pretreatment of experimental data in preparation for PCR is discussed here. Initially, PCR was performed on raw data with no pretreatment. However, variations not associated with the concentration of the metal ions of interest (i.e.,  $\text{La}^{3+}$  and  $\text{Gd}^{3+}$ ) had a negative effect on the performance of PCR. Possible experimental variations unrelated to concentration of ions are WE surface area and reference potential. Normalizing the CV current by WE surface area is a simple pretreatment that can remove most of the error caused by variations in area. Unfortunately, the reference potential varied across

Table 5.3 Measured GdCl<sub>3</sub> and LaCl<sub>3</sub> concentrations

Mixture ID	GdCl <sub>3</sub> (wt%)				LaCl <sub>3</sub> (wt%)		
	ICP	SD Peak	SD Peak (y-int≠0)	PCR	ICP	SD Peak	PCR
<b>A3</b>	3.08%	2.73%	2.49%	2.77%	1.49%	1.51%	1.38%
<b>A4</b>	3.19%	2.88%	2.77%		2.95%	2.30%	
<b>B3</b>	1.49%	2.40%	1.96%	1.49%	1.52%	1.54%	1.52%
<b>B4</b>	1.65%	2.56%	2.21%	1.89%	2.21%	2.45%	1.98%
<b>D1</b>	1.53%	2.08%	1.36%		0.89%	1.12%	
<b>D2</b>	1.81%	2.63%	2.30%	2.13%	0.97%	1.11%	1.17%
<b>D3</b>	2.84%	2.69%	2.40%	2.73%	0.95%	1.00%	1.25%
<b>D5</b>	4.49%	4.08%	4.98%	4.48%	1.38%	1.37%	1.70%
<b>D6</b>	4.69%	3.97%	4.73%		2.45%	2.28%	
<b>D7</b>	3.64%	3.28%	3.43%	3.69%	2.33%	2.67%	2.83%
<b>Average Relative Error</b>		25.80%	16.92%	6.82%		10.38%	16.38%

mixtures. This was due to the use of a 1 wt% AgCl in the reference electrode (RE). This amount of AgCl is difficult to precisely add to each RE constructed. The use of Pyrex in the construction resulted in frequent cracking and reconstruction of REs. Furthermore, when the concentration of AgCl is low, small changes in the concentration create dramatic shifts in the potential. To resolve this problem, the Gd<sup>3+</sup> reduction peak was aligned across all mixtures. This would remove potential shifts from the data, but preserve the peak spacing between La and Gd peaks which is concentration dependent. Additionally, only the reduction peaks were analyzed; all other data was trimmed out. Lastly, the CV peaks were semidifferentiated to increase the contrast between the two peaks. The concentrations determined using PCR is also compared to ICP-OES measurements in Table 5.3.

The number of principle components was selected by cross-validation. This involved removing a couple data sets from the training set and determining the concentration at all possible number of principle components, then selecting the number of PCs that resulted in the lowest squared error. PCR was not performed on mixtures A4,



D1, and D6 to avoid extrapolation because they were at the extremes of concentration values and PCR is not based on a fundamental equation. Also, D4 was excluded from the training set, just as D4 was excluded from the correlations. The sum of the relative errors in the measured  $\text{La}^{3+}$  and  $\text{Gd}^{3+}$  concentrations are plotted in Figure 5.10 for each analytical method and mixture. While the sum of the relative error of the SD peak current correlations are occasionally lower than PCR's relative error, overall PCR produces a lower and more consistent relative error. PCR especially under performs compared to SD peak current at low  $\text{La}^{3+}$  concentrations.

#### 5.4.1.1 Discussion

Peak height utilizes less data than PCR and relies on the ability to identify and separate peaks. PCR uses multiple data points from one measurement and does not require that peaks are separated. Because of this, peak height is less sensitive than PCR to changes in other variables, such as potential drift. However, in order to use peak heights to estimate concentrations, significant data processing needs to be performed and possible

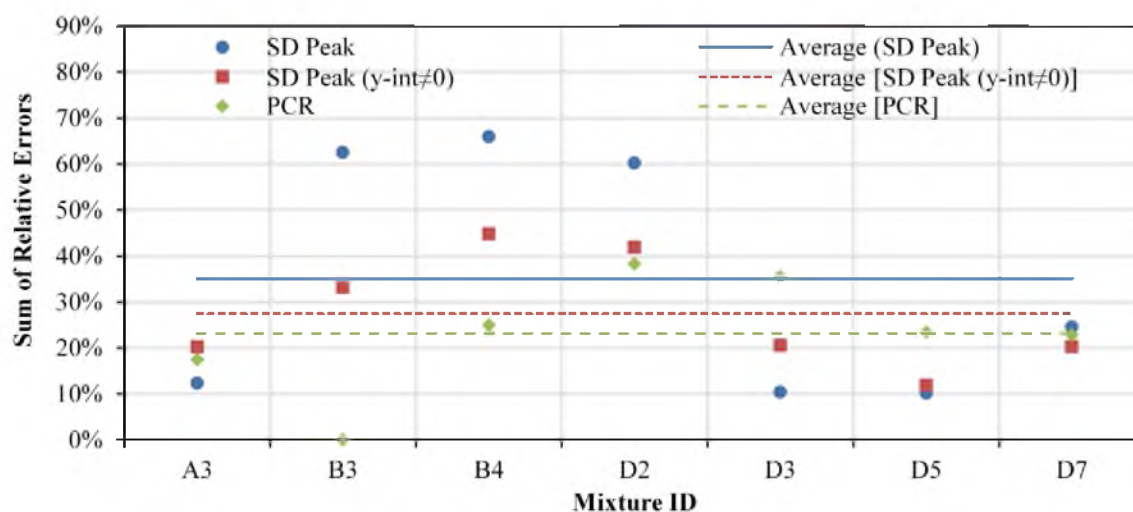


Figure 5.10 Sum of the relative error between ICP-OES and electroanalytical measurements using SD peaks and PCR for each mixture

variations in the diffusion coefficient could further complicate the process. Automating the separation of peaks may prove difficult since the fitting statistically may appear to be good, but may be a poor representation of the physical process, as was the case in some mixtures. Constraints had to be applied to prevent the front of the  $\text{La}^{3+}$  reduction peak from extending all the way out to beginning of the  $\text{Gd}^{3+}$  reduction peak. PCR does not require the separation of signals and potentially could be applied to mixtures containing more than two analytes. It would be fairly straightforward to automate PCR, even with the additional pretreatment of the data. However, fluctuations in the process temperature, WE surface condition and other variables would need to be tightly controlled or their effect characterized and taken into account in the training set. The robustness of PCR would increase as more data is collected throughout the process history.

#### 5.4.2. Chronoamperometry

CA could potentially be used to measure  $\text{Gd}^{3+}$  and  $\text{La}^{3+}$  concentrations, if their currents can be clearly identified and assumed to be additive. To test this, CA was applied at multiple potentials in the region where Gd and La CV peaks were identified. The Cottrell equation predicts that the current will decay with the inverse of the square root to time. For this reason, the slope of the current in each CA measurement was regressed with respect to  $1/\sqrt{t}$  at each potential applied and is plotted in Figure 5.11 for mixture D2.

The assumption of diffusion control in the Cottrell equation is confirmed when the slope is constant with potential, as it is on the far left of the plot. However, the slope does not completely plateau for  $\text{Gd}^{3+}$  reduction before  $\text{La}^{3+}$  begins to reduce. It could be extrapolated that the inflection point in the plot is the starting point of the plateau for

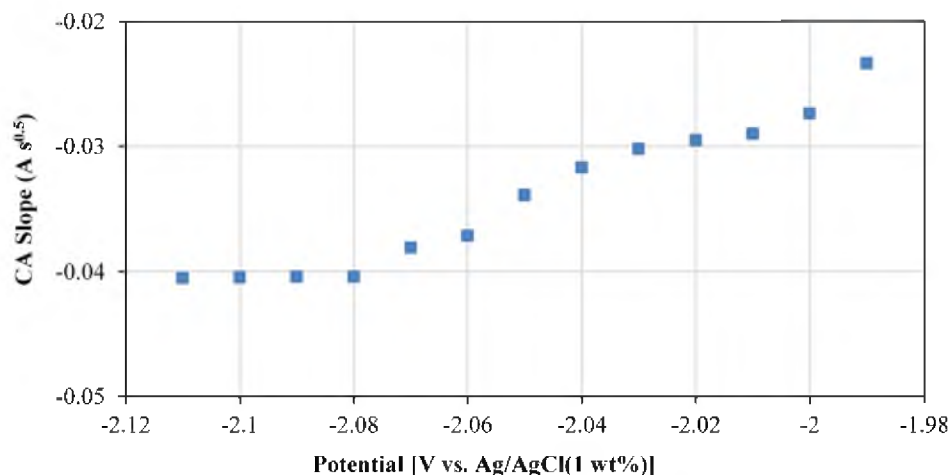


Figure 5.11 Slope of the CA current response versus  $1/\sqrt{t}$  at multiple applied potentials for mixture D2 (1.81 wt%  $\text{GdCl}_3$  and 0.97 wt%  $\text{LaCl}_3$ ) on 1 mm Mo wire (Area=0.38  $\text{cm}^2$ )

$\text{Gd}^{3+}$  reduction. That results in a diffusion coefficient of  $1.72 \times 10^{-5} \text{ cm}^2/\text{s}$  for  $\text{Gd}^{3+}$  and  $0.81 \times 10^{-5} \text{ cm}^2/\text{s}$  for  $\text{La}^{3+}$ . However, when these are compared to the diffusion coefficients calculated from CA in the single-analyte mixtures, C1 ( $1.67 \times 10^{-5} \text{ cm}^2/\text{s}$ ) and OCP-Gd3 ( $0.81 \times 10^{-5} \text{ cm}^2/\text{s}$ ), the diffusion coefficients of  $\text{Gd}^{3+}$  and  $\text{La}^{3+}$  in D2 are almost twice and half, respectively, of those from single-analyte mixtures. This would seem to indicate that CA is not a promising method for concentration measurement in  $\text{LiCl-KCl-GdCl}_3\text{-LaCl}_3$  mixtures. Perhaps, if the CA measurements were taken at more positive potentials and in small potential steps, the profile in Figure 5.11 could have been differentiated to form two peaks and possibly fitted, as can be done for NPV measurements. However, the limited potential range and large potential steps applied to each mixture prohibit this kind of analysis.

## 5.5. Conclusions

CV, CA, CP, and OCP were applied to LiCl-KCl-GdCl<sub>3</sub>-LaCl<sub>3</sub> mixtures. Only CV showed promise for the separation of Gd<sup>3+</sup> and La<sup>3+</sup> signals. Individual peaks were identified by semidifferentiating the CV curve. The SD peaks were fitted using the Biguassian distribution and fitted peaks were used to measure concentrations. The calculated diffusion coefficients were much lower than those reported in the literature for single-analyte studies. The SD peak height for Gd<sup>3+</sup> reduction correlates to concentration poorly when the intercept is forced through zero. This may indicate a change in the diffusion coefficient value at or below 1.5 wt% GdCl<sub>3</sub>. PCR was applied to SD CV curves and reduced the error in the measured concentrations on average.

## 6. ELECTROCHEMISTRY OF $\text{ThCl}_4$ - $\text{LaCl}_3$ - $\text{LiCl}$ - $\text{KCl}$ MIXTURES

It took Jons Jacob Berzelius two attempts to bring honor to the Scandinavian god of thunder, Thor. On his first attempt, he thought that he had discovered a new element and named it thorium in honor of Thor. However, after further analysis and 9 years, he figured out that the element was actually a previously discovered one, yttrium. Four years later, an unidentifiable black mineral was brought to him. This time, Berzelius successfully demonstrated that it contained a new element and he redeemed the name of Thor by naming it thorium (127). Berzelius may have been prophetic in naming thorium after Thor, one of the mighty and powerful Scandinavian gods, because one of the major applications of thorium is nuclear energy of which Berzelius was completely unaware. Indeed, if the thorium nuclear fuel cycle is successfully commercialized, thorium would be an immense source of power. Electrochemical processing could play a key role in the commercialization of the thorium fuel cycle which is part of the motivation for this chapter.

### 6.1. Electrochemistry of $\text{ThCl}_4$ and $\text{LaCl}_3$ in $\text{LiCl}$ - $\text{KCl}$ Eutectic

The experimental work on  $\text{ThCl}_4$ - $\text{LaCl}_3$ - $\text{LiCl}$ - $\text{KCl}$  mixtures was performed by another student in our group and a synopsis of this work has been published (122), no part of which is included here. A complete discussion of the electrochemical behavior, the traditional electrochemical signal analysis and the specific details of  $\text{ThCl}_4$ - $\text{LaCl}_3$ -

LiCl-KCl mixtures are found in that publication. Only the application of principal component regression (PCR) and comparison of results are discussed here.

A cyclic voltammogram (CV) of a  $\text{ThCl}_4$ - $\text{LaCl}_3$ -LiCl-KCl mixture is provided in Figure 6.1 for mixture U1. The peak spacing in the CV is the largest of all the mixtures examined. The reduction of  $\text{La}^{3+}$  usually takes place in a single step and only a single peak reduction peak is observed. However, upon close inspection of the  $\text{La}^{3+}/\text{La}$  redox peaks in the plot on the right in Figure 6.1, there appears to be two pairs of peaks as evidenced by the two oxidation peaks and shoulder on the reduction peak. According to phase diagrams, La and Th metals can alloy (128). Thus, this additional peak may be due to the underpotential deposition of  $\text{La}^{3+}$  on Th metal. The shoulder on the reduction peak changes size, and shape as the concentration of  $\text{La}^{3+}$  and  $\text{Th}^{4+}$  ions vary. Perhaps, capturing this variation along with others with PCR will improve the accuracy of the concentration values determined from electrochemical measurements.

## 6.2. Electroanalytical Concentration Measurements

The concentration measurements were made for mixtures W5-W7 in the publication (122) based on CV, normal pulse voltammetry and chronoamperometry data

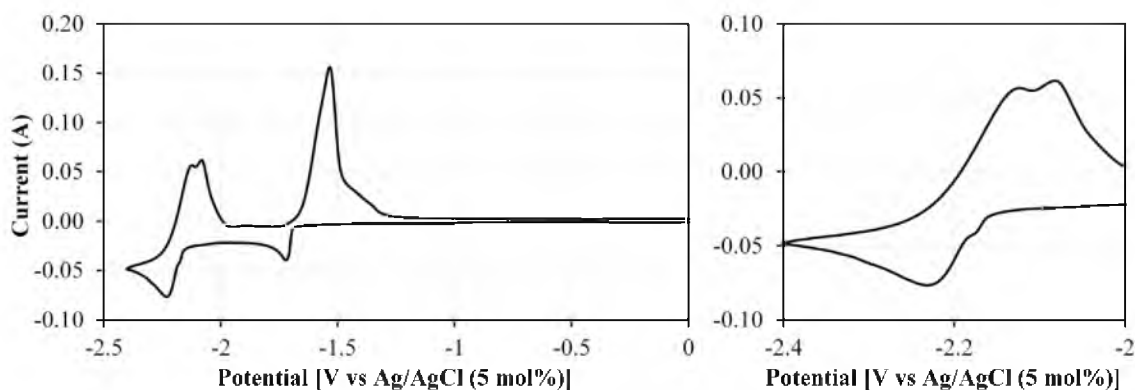


Figure 6.1 Full CV (left) for mixture U1 (0.69 wt%  $\text{ThCl}_4$  and 1.01 wt%  $\text{LaCl}_3$ ) on a W rod (Area=0.47  $\text{cm}^2$ ) at 100 mV/s and 773 K with magnification of La peaks (right)

from mixtures U1-W4. In order to best mirror this approach with PCR, CV curves collected at 200 mV/s in mixtures U1-W4 served as the training set. Cross-validation was performed on the training set to select the number of PCs. Using 5 PCs from the training set, the concentrations of mixtures W5-W7 were determined. They are compared to the electroanalytical measurements made in the publication in Table 6.1.

Initially, PCR was applied to the semidifferentiated (SD) CV curves in same manner described in Chapter 5 with the  $\text{La}^{3+}$  reduction peaks aligned across all mixtures, but this resulted in large errors. The SD data may have brought variations unrelated to concentration to greater prominence. For example, in Figure 6.2, the SD  $\text{Th}^{4+}$  reduction peak shows two peaks. Two peaks or a shoulder on the SD  $\text{Th}^{4+}$  reduction was found in

Table 6.1 Comparison of concentrations measured by peak current and PCR

Mixture ID	ICP-OES mmol/cc		Peak Current mmol/cc		Relative Error		PCR mmol/cc		Relative Error	
	ThCl <sub>4</sub>	LaCl <sub>3</sub>	ThCl <sub>4</sub>	LaCl <sub>3</sub>	ThCl <sub>4</sub>	LaCl <sub>3</sub>	ThCl <sub>4</sub>	LaCl <sub>3</sub>	ThCl <sub>4</sub>	LaCl <sub>3</sub>
W5	0.0417	0.119	0.0464	0.126	11.3%	5.88%	0.0425	0.120	1.93%	3.22%
W6	0.0637	0.179	0.0650	0.174	2.04%	2.79%	0.0642	0.177	0.85%	0.98%
W7	0.0907	0.250	0.0883	0.229	2.65%	8.40%	0.1018	0.295	12.3%	18.0%
	Average				5.3%	5.7%			5.0%	7.4%

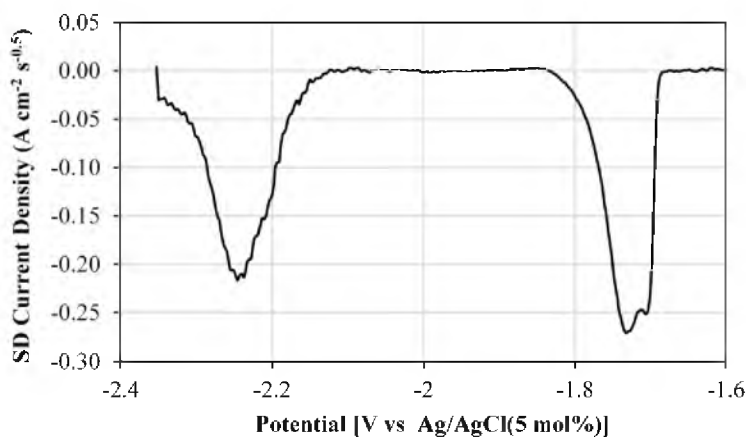


Figure 6.2 Semidifferentiated CV reduction peaks for mixture V2 at 200 mV/s

the other mixtures as well. This may be due to a closely spaced two-step reduction process or it could be due to incomplete removal of oxychlorides and oxides of thorium formed during the drying process. In either case, the increased emphasis of the forked-peak nature may have had deleterious effect on the performance of PCR. Subsequently, PCR was applied to the normal CV curves in the same manner as the SD CV curves which resulted in the more accurate measurements in Table 6.1.

PCR concentration measurements were improved significantly for mixtures W5 and W6, but were dramatically worse for W7. Overall, PCR has a greater relative error than peak height measurements due to large error in W7. Thus, the effectiveness of PCR compared to CV peak height regression is possibly diminished as peak separation increases or as other variations unrelated to concentration are introduced. The possible inference of oxides and oxychlorides were discussed for thorium. In the case of lanthanum, underpotential deposition creates an additional peak which may be more strongly related to thorium metal on the WE rather than the  $\text{La}^{3+}$  concentration. Lastly, W7 may simply be an outlier.

To better gauge the performance of PCR, concentrations were determined for all other mixtures by using the cross-validation technique in Chapter 5. The resulting relative error is plotted in Figure 6.3 which shows that W7 was not an isolated case. There are multiple mixtures with large relative errors, especially V2-W1.

### 6.3. Conclusions

CV measurements of  $\text{ThCl}_4\text{-LaCl}_3\text{-LiCl-KCl}$  mixtures had additional features that may interfere with accurately determining the peak height and may not be related to concentrations, such as: a shoulder on the  $\text{La}^{3+}$  reduction peak and a forked peak on the



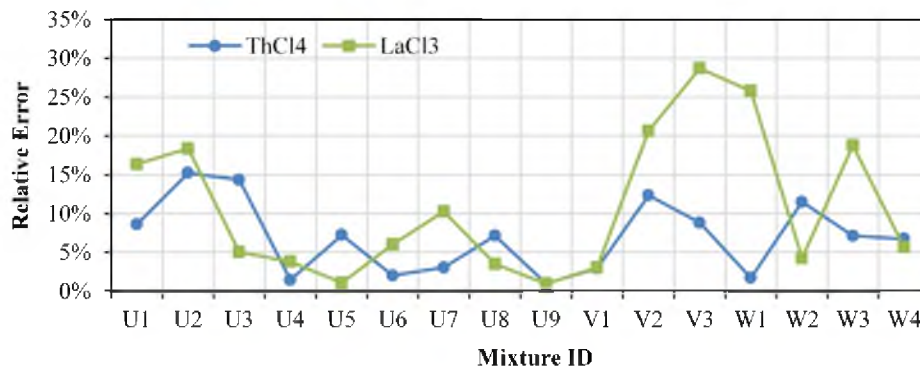


Figure 6.3 Relative error of the concentration determined by ICP-OES and PCR for mixtures U1-W4

SD  $\text{Th}^{4+}$  reduction peak. Because of these interferences, it was proposed that PCR may be able to more accurately determine the concentration. However, PCR did not outperform peak height in determining concentrations. This may be due to the increased peak spacing allowing peak baselines to be clearly identified or due to interferences unrelated to  $\text{Th}^{4+}$  and  $\text{La}^{3+}$  concentration, such as alloying or oxychlorides, which were not observed in  $\text{GdCl}_3\text{-LaCl}_3\text{-LiCl-KCl}$  mixtures.

## 7. ELECTROCHEMISTRY OF $\text{UCl}_3$ - $\text{MgCl}_2$ - $\text{LiCl}$ - $\text{KCl}$ MIXTURES

Uranium is a metal of great interest with unique qualities, most important of which is its ability to fission when bombarded with neutrons. The fissile property of uranium was so unique in the 1930s that no researcher has encountered anything like it before then. Many people studied the half-lives of the daughter products of uranium up to that point, but all assumed that atoms can only transmute by 1 or 2 atomic numbers. This led to elaborate and complicated decay schemes with as many as 16 elements. Some even denied compelling chemical evidence indicating the presence of lighter elements over 30 atomic numbers away from uranium. However, Otto Hahn and Fritz Strassman did not entirely dismiss their chemical evidence. In 1939, they wrote (129):

As chemist we really ought to revise the decay scheme given above and insert the symbols Ba, La, Ce in place of Ra, Ac, Th. However, as “nuclear chemist,” working very close to the field of physics, we cannot bring ourselves yet to take such a drastic step which goes against all previous experience in nuclear physics. There could perhaps be a series of unusual coincidences which has given us false indications.

The key word in that excerpt is ‘*yet*.’ They were still willing to consider it.

When their chemical evidence did not agree with the nuclear physics of their time, they turned to their expatriated colleague Lisa Meitner. She and her nephew, Otto Frisch, used Neils Bohr’s liquid drop model of the nucleus and reasoned that just as a water droplet can elongate when a smaller droplet struck it, so could the nucleus of an atom. If the elongation was enough that protons on either end could repel each other and split the

atom it would explain Hahn's chemical results. Their explanation caused Bohr to exclaim "Oh, what fools we all have been! But this is wonderful. This is just as it must be!" (115). Maybe, in the years to come, researchers may look back on this work and will say, as did Bohr, "Oh, what fools *we...* have been! [emphasis added]."

### 7.1. Electrochemistry of $\text{UCl}_3$ in LiCl-KCl Eutectic

Several studies have been performed on uranium in eutectic LiCl-KCl, some of which are reviewed in Chapter 1. These studies (39,59,66,67,130–132) have found that uranium has two stable valance states, +3 and +4. Uranium reduces from the +4 to +3 in a single step, likewise for the oxidation from +3 to +4. A single-step mechanism has also been observed for the transitions from the +3 ionic state to deposited metal. An additional pair of oxidation and reduction peaks with large spacing between them was reported as well. This pair of peaks was located between the  $\text{U}^{3+} \rightarrow \text{U}^0$  reduction peak and the  $\text{U}^{3+} \rightarrow \text{U}^{4+}$  oxidation peak and was commonly attributed to adsorption/desorption or the formation of a monolayer of metallic uranium. Most of these studies have found the reduction of  $\text{U}^{3+}$  to  $\text{U}^0$  metal to be reversible up to 200 mV/s at 500°C, except for one (39) which reported it as irreversible due to decreasing peak potentials with increasing scan rate. This shift in peak potential was reported more significant at higher concentrations. Diffusion coefficients, standard potentials, activity coefficients, and rate constants have been determined from the electrochemical data in these studies as well.

### 7.2. Electrochemistry of $\text{MgCl}_2$ in LiCl-KCl Eutectic

The behavior of magnesium has received much less attention in the literature than uranium. Only three studies (50,133,134) in the eutectic LiCl-KCl have been identified.

All three studies found  $\text{Mg}^{2+}$  ions to reduce in a single-step and no other stable valance state within the potential window of eutectic LiCl-KCl. The first study (133) found the reduction of  $\text{Mg}^{2+}$  to be reversible up to 2 V/s at 400°C. The second study (134) does not comment on the reversibility of  $\text{Mg}^{2+}$  reduction, but it does use the Berzins-Delahay equation to determine diffusion coefficients. The last study (50) concludes that  $\text{Mg}^{2+}$  reduction is reversible until 300 mV/s from 723 to 908 K. Due to the discrepancy in the boundary of reversible behavior and limited data in the literature, the behavior of  $\text{MgCl}_2$  was investigated.

Three mixtures were prepared containing only  $\text{MgCl}_2$  in eutectic LiCl-KCl—M1, R1 and an additional mixture (R1b) prepared in same manner as R1. The procedures and setup described in Chapter 3 and Appendix A were applied to all three mixtures. A typical voltammogram for these mixtures is displayed in Figure 7.1 from mixture R1. The sharp decrease on the left at about -2.6 V is characteristic of  $\text{Li}^+$  deposition and the far left peak is the reoxidation of deposited Li metal. The small rise of the far right at about 1.0 V

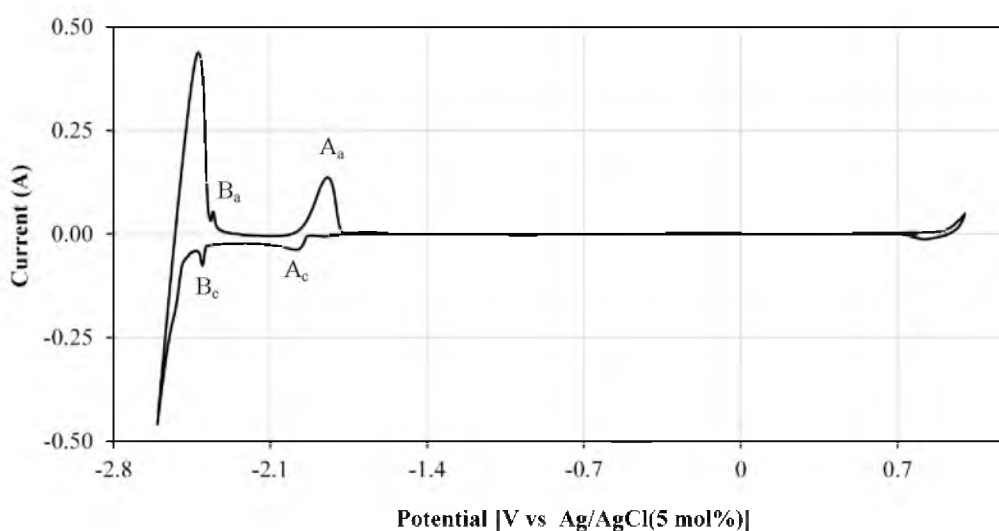


Figure 7.1 Cyclic voltammogram at 300 mV/s from mixture R1 (Area = 0.61 cm<sup>2</sup>, WE = 2 mm W rod, 0.21wt%  $\text{MgCl}_2$ , T = 773 K)

is either due to tungsten dissolution or chlorine evolution. Peaks  $A_a$  and  $A_c$  correspond to the oxidation and reduction of Mg respectively. Peaks  $B_a$  and  $B_c$  are formed due to underpotential deposition of Li on Mg due to alloying (50,134).

Oxidation and reduction peaks of Mg are shown in Figure 7.2 in greater detail for mixture M1 at various scan rates. Only a limited range of scan rates (50-500 mV/s) were applied to mixtures R1 and M1. Thus mixture R1b was prepared to apply a wider range of scan rates (10-2000 mV/s) to more clearly identify the reversibility of  $Mg^{2+}$  reduction. The trend of peak height with the square root of scan rate is displayed in Figure 7.3. Additionally, the behavior of the Mg reduction peak potential with changes in scan rate is shown in Figure 7.4. Each peak current and potential was measured 4 times. The markers on the both plots represent the average of the 4 measurements and the error bars represent 3 standard deviations of the sampled data. In Figure 7.4, the solid black line represents the average measured potential from 25-100 mV/s and the dashed line represent  $\pm 3$  standard deviations ( $\sigma$ ) of that average. The peak potential was corrected for ohmic drop

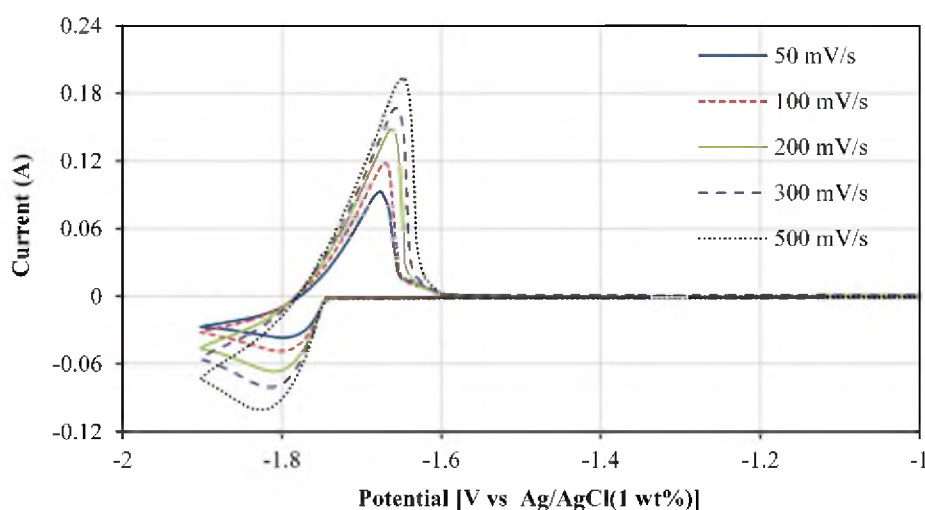


Figure 7.2 Mg oxidation and reduction peaks at various scan rates from mixture M1 (Area =  $0.41 \text{ cm}^2$ , WE = 1 mm Mo wire, 1.17 wt%  $MgCl_2$ , T = 773 K)

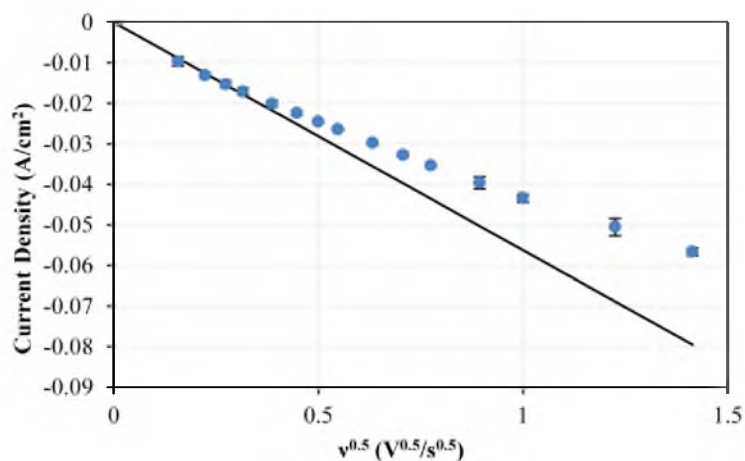


Figure 7.3 Mg reduction peak current density versus the square root of scan rate for mixture R1b (Area = 0.76 cm<sup>2</sup>, WE = 2 mm W rod, 0.30 wt% MgCl<sub>2</sub>, T = 773 K)

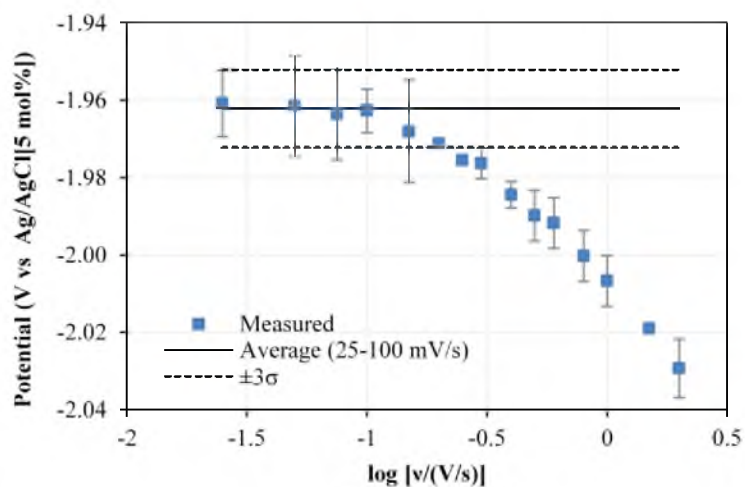


Figure 7.4 Mg reduction peak potential (IR corrected,  $R_u = 0.17 \Omega$ ) at varying scan rates for mixture R1b

by measuring the uncompensated resistance ( $0.17 \Omega$ ) using the current-interrupt method and subtracting  $I_p R_u$  from the observed peak potentials.

As discussed in Section 2.5.2, a reversible cyclic voltammogram (CV) has two important qualities—the peak current has linear relationship with the square root of scan rate and the peak potential is independent of scan rate. The peak current begins to depart from linearity at about 200 mV/s in Figure 7.4. Likewise, the measured peak potential

differs more than 3 standard deviations from the average peak potential between 200 and 250 mV/s. Thus, under these experimental conditions, the reduction of Mg appears to be reversible up to 200 mV/s.

### 7.3. Electrochemistry of $\text{UCl}_3$ and $\text{MgCl}_2$ in LiCl-KCl Eutectic

The presences of both uranium and magnesium ions in eutectic LiCl-KCl could alter the behavior of each other. Thus, before quantitative analyses can be performed, the behavior discussed in the previous two sections need to be verified. To do this, the same analysis that was performed on LiCl-KCl- $\text{MgCl}_2$  mixtures was also applied to LiCl-KCl- $\text{UCl}_3$ - $\text{MgCl}_2$  mixtures.

A representative CV for LiCl-KCl- $\text{UCl}_3$ - $\text{MgCl}_2$  is displayed in Figure 7.5. All features in this CV are found in CVs from all mixtures tested. All of the peaks found in the literature for uranium are present in this CV. There is a pair of peaks corresponding to the transitions of  $\text{U}^{4+}$  to  $\text{U}^{3+}$ , adsorption/desorption of uranium, and the transition of  $\text{U}^{3+}$  to U metal. There is also an additional peak at the potential corresponding to  $\text{Mg}^{2+}$

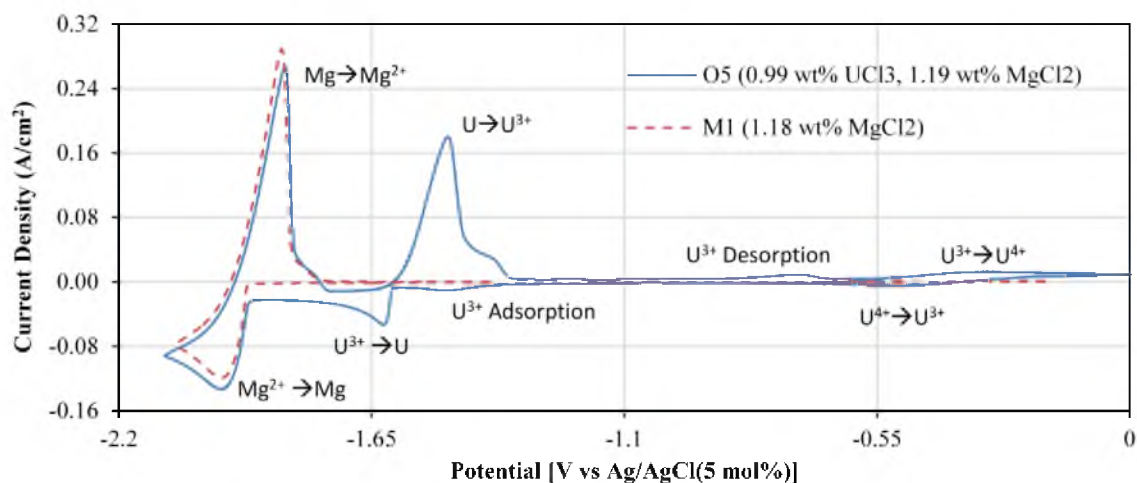


Figure 7.5 Cyclic voltammogram of mixture O5 and M1(see Appendix A) at 100 mV/s (WE = 2 mm W rod, T = 773 K)

reduction. No additional peaks are present due to possible uranium-magnesium interactions. Furthermore, no peaks from literature and single-analyte studies are absent. The signals from U and Mg appear to overlap without any sort of interaction unlike the other two quaternary mixtures. A possible explanation for the limited interaction is that no intermetallic forms between U and Mg (135), whereas La-Gd and La-Th metal pairings do alloy.

Furthermore, the LiCl-KCl-UCl<sub>3</sub>-MgCl<sub>2</sub> mixture electrochemically simulates the LiCl-KCl-UCl<sub>3</sub>-PuCl<sub>3</sub> very well. Tests on mixture RCE1 were carried out under similar conditions that the ANL researchers' published data. The "0.972 cm" curve from Figure 6 of the mentioned publication (45) was digitized using Plot Digitizer (100). The uranium peaks were set to 0 V and the current was normalized by the ratio of uranium peak heights and their respective molar concentrations for a qualitative comparison. The normalized current profiles are presented in Figure 7.6. The Mg reduction peak is slightly more negative and shorter than the Pu reduction peak at similar concentrations. This is due to their differences in standard potentials and valance states. Theoretically, the Mg

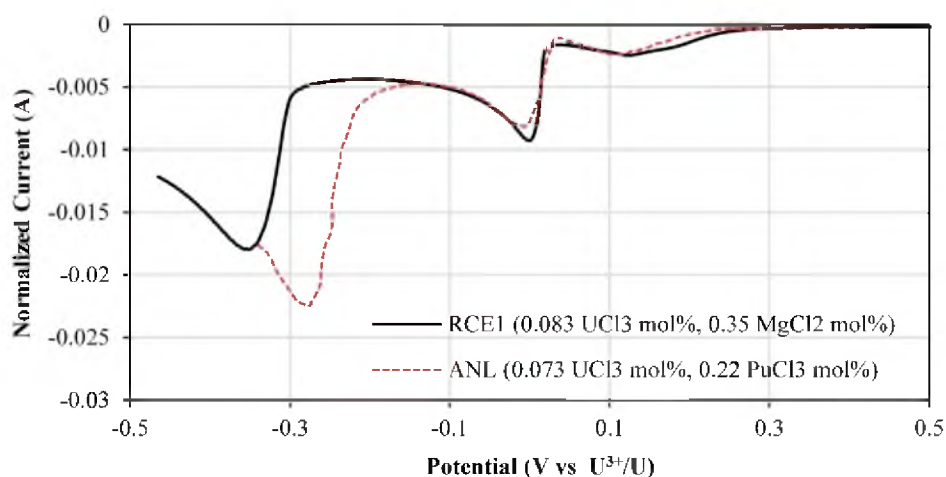


Figure 7.6 Qualitative comparison of reduction peaks in LiCl-KCl-UCl<sub>3</sub>-MgCl<sub>2</sub> and LiCl-KCl-UCl<sub>3</sub>-PuCl<sub>3</sub> (45) mixtures ( $v = 50$  mV/s,  $T = 773$  K) on W WE



peak should about half (0.54) the height of Pu peak at the same concentration. The ratio of the normalized Mg peak and Pu peak in Figure 7.6 is 0.80 which is larger than 0.54, but this is due to the higher  $\text{Mg}^{2+}$  mole fraction compared to  $\text{Pu}^{3+}$ . If the Mg-Pu peak ratio is normalized by ratio of  $\text{Pu}^{3+}$  and  $\text{Mg}^{2+}$  ion concentrations (0.63), a more reasonable Mg-Pu peak ratio of 0.50 is obtained. Thus, to achieve the same peak height, the concentration of  $\text{MgCl}_2$  needs to be increased to about 0.44 mol% which also would move the Mg peak closer to the U peak, theoretically by 8 mV, which would improve the similarity between the two mixtures.

Similar to the R1b mixture, RCE1 was tested over a wide range of scan rates (10-1000 mV/s). CVs measured at select scan rates in the RCE1 mixture are plotted in Figure 7.7. There is a significant amount of shift with scan rate in the CVs. This is due to the change in setup for rotating cylindrical electrode (RCE) tests. First, the working electrode (WE) electrode was coupled to the rotator using a stainless steel adapter which has a higher electrical resistance than tungsten. Second, the adapter is too thick to pass through the usual WE tube in the plug which necessitated the placement of WE further away from

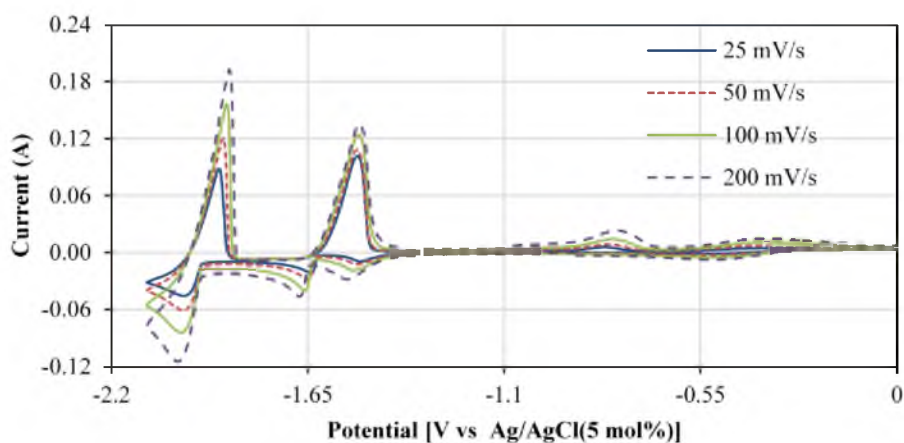


Figure 7.7 Cyclic voltammograms at various scan rates from RCE1 mixture (0.51 wt%  $\text{UCl}_3$ , 0.60  $\text{MgCl}_2$  wt%, Area =  $0.78 \text{ cm}^2$ , WE = 2 mm W rod, T = 773 K) uncorrected for IR drop

the reference electrode (RE). This resulted in a higher resistance (0.55  $\Omega$ ) being measured.

The  $U^{3+}$  and  $Mg^{2+}$  reduction peaks were evaluated as before in Section 7.2 by plotting the trends of peak current and potential with scan rate. The U background current has been subtracted from the Mg peak current. The behavior of the peak currents are shown in Figure 7.8 and the peak potentials are plotted in Figure 7.9. The reduction peak current begins to depart from linearity at 250 and 300 mV/s for U and Mg, respectively. The peak potentials are corrected for ohmic drop and remain relatively flat until 600 and 400 mV/s for U and Mg, respectively. However, it was noted in a previous study (39) that at higher concentrations, the shift in  $U^{3+}$  reduction peak potential was more dramatic. The increase in concentration causes the peak current to increase which in turn would increase the ohmic drop making the peak potential appear to shift. To insure that the process remains reversible at high concentrations, peak potentials at high  $UCl_3$  concentration, mixture P5, were plotted as well. To facilitate the comparison, 16 mV was added to each peak potential value from mixture P5 allowing direct comparison of the trends with scan rate. Even at high concentration, the peak potential is relatively independent of scan rate.

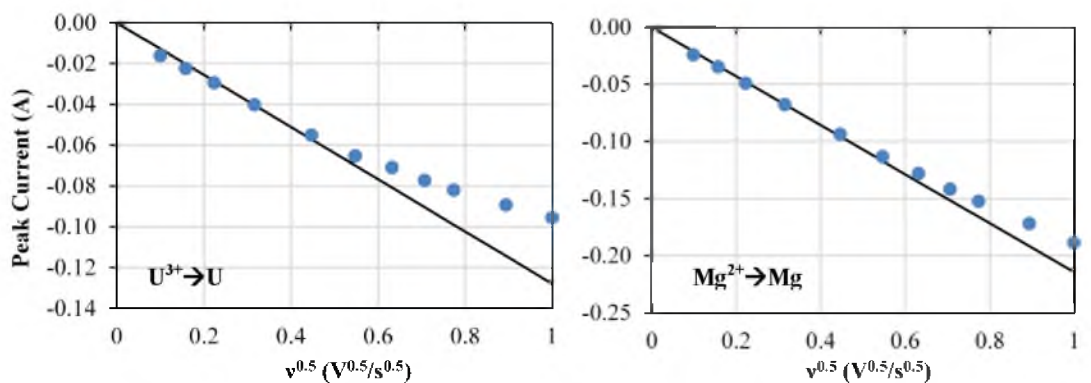


Figure 7.8  $U^{3+}$  (left) and  $Mg^{2+}$  (right) reduction peak currents for mixture RCE1 (0.51 wt%  $UCl_3$ , 0.60  $MgCl_2$  wt%, Area = 0.78  $cm^2$ , WE = 2 mm W rod, T = 773 K)

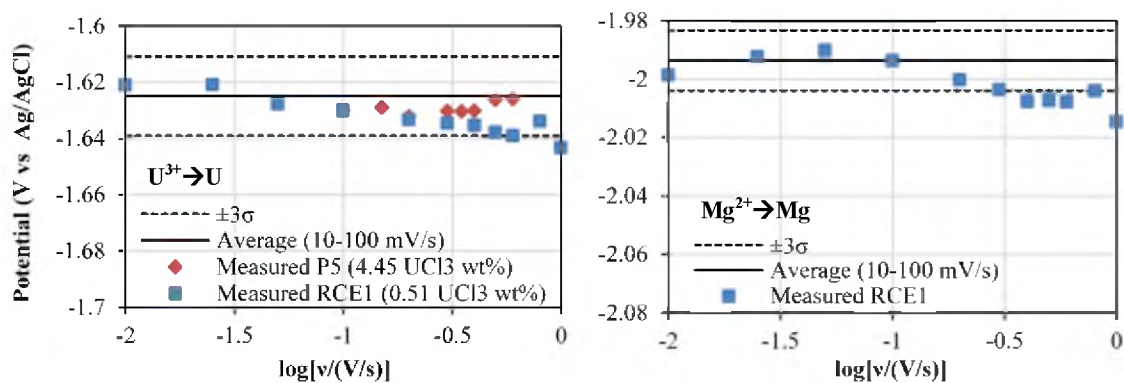


Figure 7.9  $U^{3+}$  (left) and  $Mg^{2+}$  (right) reduction peak potentials for mixture RCE1 corrected for ohmic drop ( $R_u = 0.55 \Omega$ )

However, the U peak currents did not maintain linearity beyond 250 mV/s. To be conservative and more consistent with the literature results, only U reduction peaks measured at or below 250 mV/s are considered reversible and used in the quantitative analysis. For Mg reduction peaks, the reversibility limit is considered to be 300 mV/s.

#### 7.4. Concentration Correlations

The main objective of these electrochemical techniques (CV, CA, NPV, and OCP) is to evaluate their ability to measure concentrations. Each technique is reviewed in turn. First, the key signal of the electrochemical method will be correlated to concentration. This includes some discussion on features unique to each method. Then, by the process of cross-validation—removing one data point, updating the correlation, and determining the concentration of the removed data point from the electrochemical signal—the accuracy of each method will be evaluated. Lastly, challenges specific to evaluating electrochemical signals from LiCl-KCl-UCl<sub>3</sub>-MgCl<sub>2</sub> mixtures will be discussed.

### 7.4.1. Cyclic Voltammetry

CVs were collected at 50, 100, 150, 200, 250, and 300 mV/s with a lower vertex potential of -2.1 V and an upper vertex potential of 0.5 V or 0.0 V (mixtures O1-P4). The upper vertex potentials were above the potential at which  $U^{3+}$  is oxidized to  $U^{4+}$ , but this only generated a small amount of  $U^{4+}$  which was immediate re-reduced to  $U^{3+}$  before the end of the scan. However, to ensure that all the  $U^{4+}$  was re-reduced, the potential was held between the  $U^{3+}/U^{4+}$  and  $U^{3+}/U$  reduction potentials in between each CV procedure.

A normalized peak current was determined for each mixture by dividing the peak current by the geometric area of the WE and the square of scan rate, then averaging the normalized peak values from each scan rate within the reversibility limit. Using the Berzins-Delahay equation, (2.43), the expression for the normalized peak current ( $\bar{I}_p$ ) becomes the following equation

$$\bar{I}_p = \frac{I_p}{A\sqrt{\nu}} = 0.6105\sqrt{\frac{(nF)^3 D_{M^{m+}}}{RT}} C_{M^{m+}} \quad (7.1)$$

The trends of U and Mg peak current with  $U^{3+}$  and  $Mg^{2+}$  concentrations are presented in Figure 7.10, respectively. The statistics on the linear fit of the data in the plots are displayed in Table 7.1. Using the slope and (7.1), the diffusion coefficient for  $U^{3+}$  and  $Mg^{2+}$  were calculated and are compared to literature values in Table 7.1.

The diffusion coefficient for  $Mg^{2+}$  is almost double the literature values. This may be due to the limited work done or possibly because of the method of determining the baseline of the  $Mg^{2+}$  reduction peak height. The baseline was assumed to be relatively flat from the maximum point between the U and Mg reduction points, as shown in Figure 7.11. Theoretically, the current should continue to decay by  $1/\sqrt{t}$ , but this assumes that

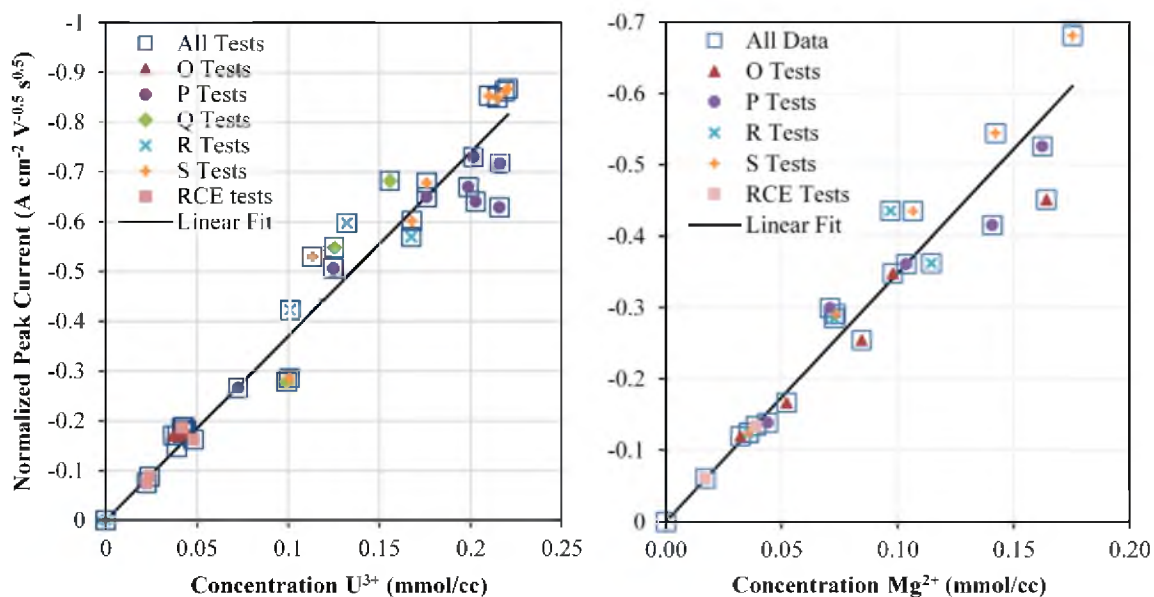


Figure 7.10 Correlation of  $U^{3+}$  (left) and  $Mg^{2+}$  (right) normalized reduction peaks with  $UCl_3$  and  $MgCl_2$  concentration, respectively, on 2 mm W rod at 773 K

Table 7.1 CV linear fitting statistics with calculated and literature diffusion coefficients

	Slope $\pm 95\%$ CI ( $A \cdot cm \cdot mol^{-1} \cdot s^{0.5} \cdot V^{-0.5}$ )	$R^2$	Diffusion Coefficient ( $10^{-5} cm^2/s$ ) at 773 K (*Interpolated)			
$U^{3+}$	$-3702 \pm 162$	0.946	$0.974 \pm 0.0019$	1.448 (67)	2.50 (66)	0.96 (59)
$Mg^{2+}$	$-3478 \pm 224$	0.922	$2.903 \pm 0.0121$	1.57 (50)	1.3* (134)	2.42 (133)

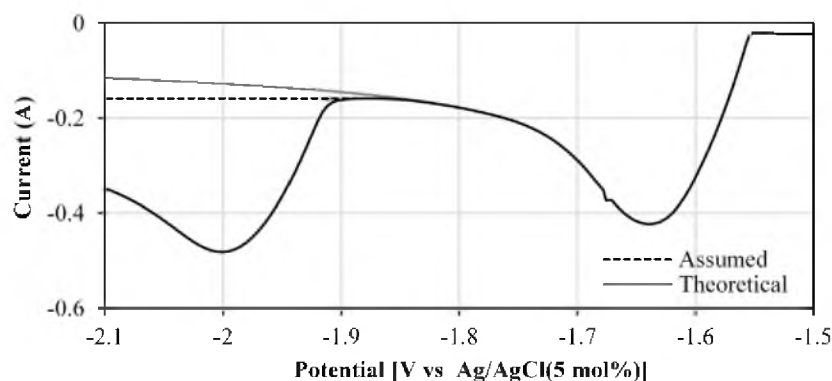


Figure 7.11 Mg reduction peak baselines for mixture S7 at 250 mV/s (4.53  $UCl_3$  wt%, 1.00  $MgCl_2$  wt%, Area =  $0.98 cm^2$ , WE = 2mm W rod, T = 773 K)

natural convection does not limit the decay. Overlap of the Mg reduction peak and the tail of U reduction peak is most significant at high  $\text{UCl}_3$  and  $\text{MgCl}_2$  concentration because the U tail is so large and the Mg peak shifted more closely to the U peak. Thus mixture S7 has the most overlapping CVs. The relative error between the Mg reduction peak current using the different baselines in Figure 7.11 is 8.9%. This effectively estimates the maximum possible error introduced by assuming a constant baseline. This would only result in a 17% decrease in the reported diffusion coefficient.

One possible way to reduce the interference of the U reduction peak tail is to semidifferentiate the CV reduction peaks (45, 126). The expression for the semidifferentiated (SD) peak current is given in (5.2). The shape of the SD peaks for the  $\text{LiCl-KCl-UCl}_3\text{-MgCl}_2$  system is represented in Figure 7.12 using data from mixture S7 in which the highest concentrations of  $\text{Mg}^{2+}$  and  $\text{U}^{3+}$  ions were found. Even in this mixture, the baseline current for SD Mg reduction peak is on the order of 1 mA which is a significant increase in the signal-to-noise ratio. Like CV peak heights, SD peak heights were normalized as shown below.

$$\frac{e_p}{Av} = \frac{n^2 F^2 C_{M^{n+}}^b \sqrt{D_{M^{n+}}}}{2RT} \quad (7.2)$$

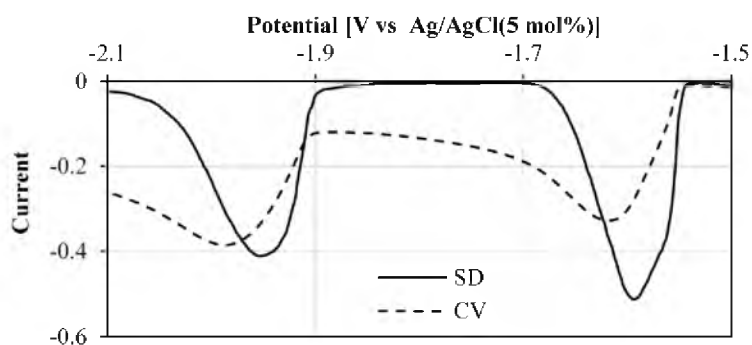


Figure 7.12 Comparison of Mg reduction peak baselines for CV and semi-differentiated CV from mixture S7 at 150 mV/s (Area = 0.98 cm<sup>2</sup>, WE = 2mm W rod, T = 773 K)

The normalized SD peak currents are plotted versus concentration of  $\text{Mg}^{2+}$  ions in Figure 7.13. Unfortunately, the SD peaks appear to be less correlated with concentration, as shown by the statistics in Table 7.2. The cause for this is still unknown and further investigation into the shape and trends of the Mg SD peaks is required.

#### 7.4.2. Chronoamperometry

For each mixture (except S1-S7, and RCE mixtures), chronoamperometry (CA) was applied at various potentials in 10 mV increments from the CV reduction peak potentials to more negative potentials. According the Cottrell equation, (2.35), the current response with time is independent of the potential applied. Thus, the CAs from each

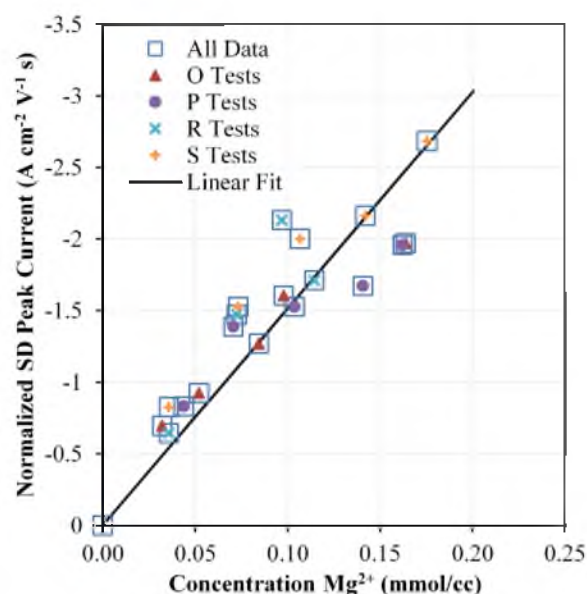


Figure 7.13 Correlation of  $\text{Mg}^{2+}$  normalized SD reduction peaks with  $\text{Mg}^{2+}$  concentration

Table 7.2 SD linear fitting statistics with calculated diffusion coefficient

	Slope $\pm$ 95% CI ( $\text{A}\cdot\text{cm}\cdot\text{mol}\cdot\text{s}\cdot\text{V}^{-1}$ )	$R^2$	Diffusion Coefficient ( $10^{-5} \text{ cm}^2/\text{s}$ ) at 773 K
$\text{Mg}^{2+}$	$-15141 \pm 1457$	0.755	$2.731 \pm 0.0253$

potential applied were compared and the most identical CAs were used. An example of this comparison is shown in Figure 7.14. Once the identical CAs were identified, a normalized current ( $\bar{I}$ ) was calculated by taking the slope of the current versus the inverse of the square root of time and dividing by the area, resulting in the following expression:

$$\bar{I} = \frac{I(t)\sqrt{t}}{A} = nFC_{M^{n+}}^b \sqrt{\frac{D_{M^{n+}}}{\pi}} \quad (7.3)$$

The numerator,  $I(t)\sqrt{t}$ , represents the slope of  $I$  versus  $\sqrt{t}$  curve. The resulting correlations of the normalized current with concentration are plotted in Figure 7.15. The statistics of the linear fit along with calculated and literature diffusion coefficients are shown in Table 7.3.

The Mg normalized current was determined by assuming that the normalized currents of U and Mg were additive. Thus, the normalized  $U^{3+}$  current was subtracted from the total normalized current recorded at potentials beyond the Mg reduction peak potential to obtain the Mg normalized current in each mixture. The Mg data is sparse due to an error in the potentiostat settings. For mixtures P1-P4, the current range was set too low resulting in CAs with odd profiles not typical of the  $1/\sqrt{t}$  decay. Thus, these results could not be used. Furthermore, the measurement of the magnesium concentration with ICP-MS was complicated by the fact that uranium was more prevalent by mass than magnesium. The opposite is usually encountered in analytical chemistry. Thus, magnesium was near the detection limit resulting in large random errors. Select samples were rerun at lower dilutions level yielding more reasonable results, but some mixtures were not run (see Appendix A). Thus, the magnesium concentration was not verified for all test mixtures. This limitation applies to all methods (CV, CA, NPV, and OCP) for Mg.



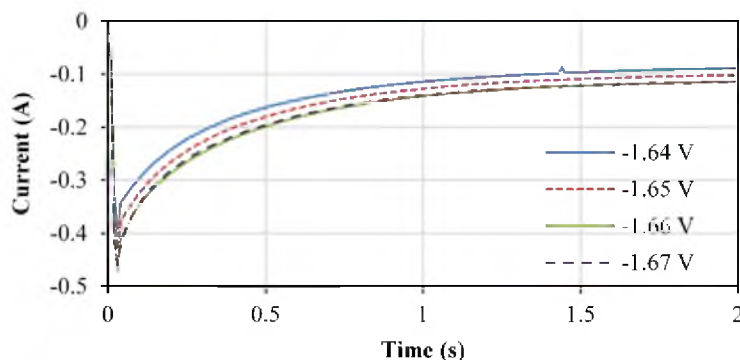


Figure 7.14 Chronoamperograms from mixture P8 (4.18 wt%  $\text{UCl}_3$ , 0.92 wt%  $\text{MgCl}_2$ , Area =  $0.70 \text{ cm}^2$ , WE = 2 mm W rod, T = 773 K)

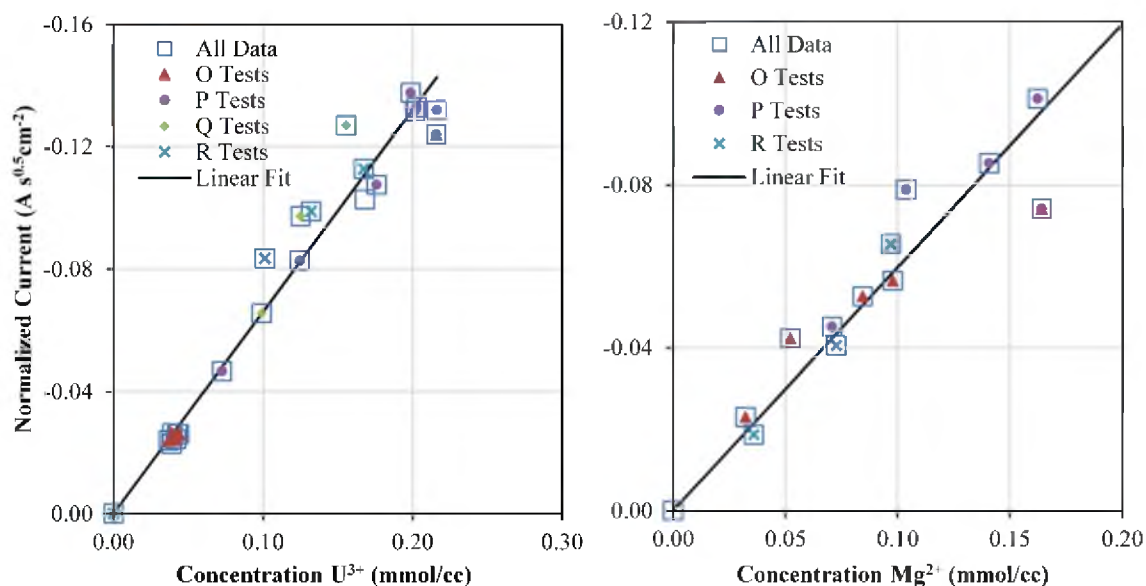


Figure 7.15 Correlation of  $\text{U}^{3+}$  (left) and  $\text{Mg}^{2+}$  (right) normalized current with  $\text{UCl}_3$  and  $\text{MgCl}_2$  concentration, respectively, on 2 mm W rod at 773 K

Table 7.3 CA linear fitting statistics with calculated and literature diffusion coefficients

	Slope $\pm 95\%$ CI ( $\text{A}\cdot\text{cm}\cdot\text{mol}\cdot\text{s}^{0.5}$ )	$R^2$	Diffusion Coefficient ( $10^{-5} \text{ cm}^2/\text{s}$ ) at 773 K		
$\text{U}^{3+}$	$-660.2 \pm 30.9$	0.957	$1.634 \pm 0.0019$	$1.08^\dagger (66)$	$^\dagger 723 \text{ K}$
$\text{Mg}^{2+}$	$-597.1 \pm 59.7$	0.888	$3.008 \pm 0.0300$	$2.3^* (134)$	*Interpolated

### 7.4.3. Normal Pulse Voltammetry

NPV was applied to all mixtures, with exception of S1-S7 and RCE mixtures. For all NPV runs, the pulse time ( $t_p$ ) was set to 0.25 s, base potential ( $E_b$ ) was -0.75 V and a step potential of 5 mV was used. An interval time of 5 s was used for mixtures O1-P2, 10 s for mixture P3, 12 s for mixture P4 and 15 s for all other mixtures. This translates to a base times ( $t_b$ ) of 4.75, 9.75, 11.75, and 14.75 s. The diffusional current ( $I_d$ ) was simply normalized by the physical area of the WE. The resulting correlation of NPV diffusional currents to concentration are shown in Figure 7.16. The statistics of the linear fit and calculated diffusion coefficient are displayed in Table 7.4. No literature values were

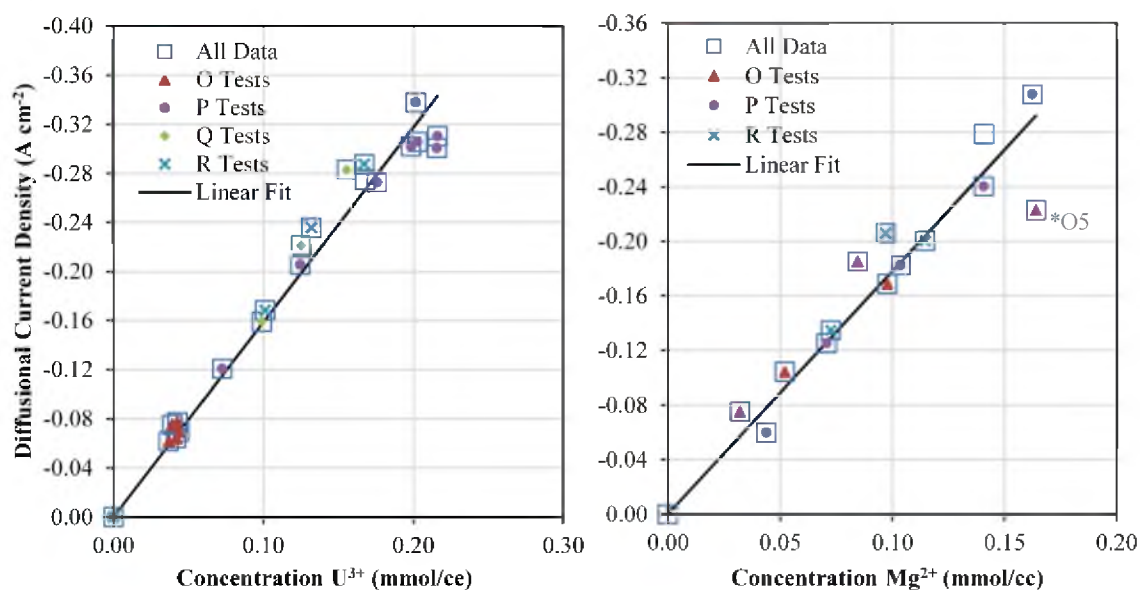


Figure 7.16 Correlation of  $U^{3+}$  (left) and  $Mg^{2+}$  (right) diffusional current density with  $UCl_3$  and  $MgCl_2$  concentration, respectively, on 2 mm W rod at 773 K

Table 7.4 NPV linear fitting statistics with calculated and literature diffusion coefficients

	Slope $\pm 95\%$ CI (A·cm/mol)	$R^2$	Diffusion Coefficient ( $10^{-5}$ cm <sup>2</sup> /s) at 773 K
$U^{3+}$	-1587 $\pm$ 61.1	0.969	2.36 $\pm$ 0.0035
$Mg^{2+}$	-1780 $\pm$ 138	0.906	6.68 $\pm$ 0.0404

found for diffusion coefficients calculated from NPV data.

The  $\text{Mg}^{2+}$  reduction diffusional current was determined by subtracting the  $\text{U}^{3+}$  reduction diffusional current from total diffusional current, as shown in Figure 7.17. In mixtures O2-O3, the diffusional current plateau for magnesium was difficult to identify, possibly due to the short interval time. In these cases, the pulse current was differentiated. This resulted in a pair of peaks as shown in Figure 7.18. The area of magnesium peak was calculated and assumed to be equivalent to the diffusional current of magnesium. As mentioned, a significantly shorter interval time was used for mixtures O1-P2. This may

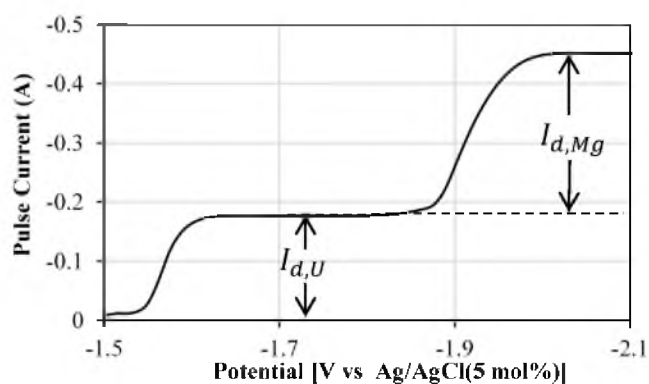


Figure 7.17 NPV from mixture Q2 (see Appendix A) with  $t_p = 0.25$  s,  $t_b = 14.75$  s,  $E_b = -0.75$  V, Area =  $0.80$  cm<sup>2</sup>, WE = 2 mm W rod, T = 773 K

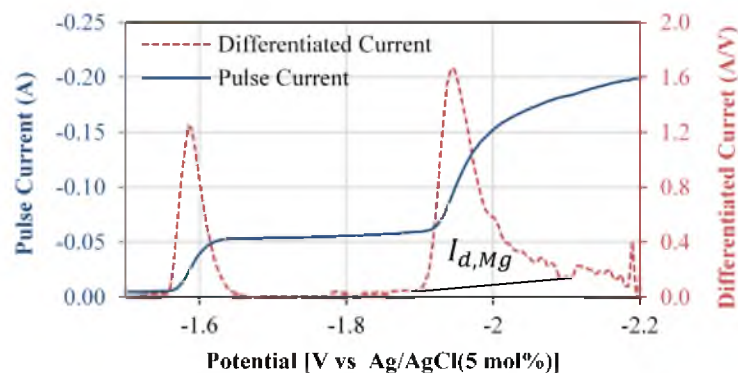


Figure 7.18 Illustration of method for determining diffusional current in the absence of a plateau for mixture O3 ( $t_p = 0.25$  s,  $t_b = 4.75$  s,  $E_b = -0.75$  V, Area =  $0.78$  cm<sup>2</sup>)

have had an effect on diffusional current, particularly at high concentrations, as demonstrated by the O5 data point in Figure 7.16. If that outlier is removed, the slope becomes  $-1854 \pm 89.0 \text{ A}\cdot\text{cm}/\text{mol}$  with a correlation coefficient of 0.974 which results in a diffusion coefficient of  $7.25 \pm 0.0167 \times 10^{-5} \text{ cm}^2/\text{s}$ .

#### 7.4.4. Open-Circuit Potentiometry

In each mixture, the open-circuit potential was measured. For uranium, the open-circuit potential was measured by switching the WE and counter electrode (CE) leads so that the potential was measured at the uranium metal sheets in the stainless steel basket. For magnesium, an Mg rod could not be used in the  $\text{LiCl-KCl-UCl}_3\text{-MgCl}_2$  mixture because Mg metal would reduce the  $\text{U}^{3+}$  ions in the salt. Thus, chronopotentiometry was applied to predeposit uranium and magnesium on the tungsten WE. When the potential reached that of lithium deposition, a zero current was imposed on the cell. A typical chronopotentiogram (CP) is displayed in Figure 7.19 with the subsequent open-circuit potentiometry (OCP) measurement inset. Two clear plateaus are formed: one for the reduction and oxidation of uranium and another for magnesium. Unlike the OCP measurements on the uranium rod, the plateau for magnesium in the inset of Figure 7.19 is not completely flat. The open circuit potential for magnesium was, therefore, assumed to be at the inflection point of the plateau. The resulting OCP measurements are plotted versus the natural logarithm of mole fraction in Figure 7.20. The resulting statistics for the linear fit are shown in Table 7.5. The number of electrons exchanged ( $n$ ) and the standard apparent potential ( $E^{o'}$ ) were calculated from the slopes and y-intercepts, respectively, from Table 7.5 and are displayed in Table 7.6.

The open-circuit potentials were converted to  $\text{Cl}^-/\text{Cl}_2$  reference electrode scale by

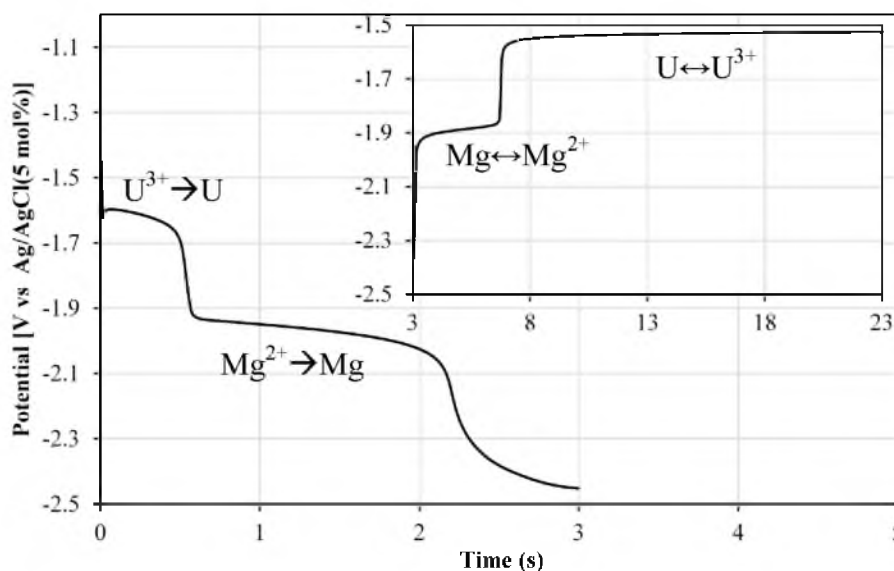


Figure 7.19 CP ( $I=0.32$  A) and subsequent OCP measurement (inset) for mixture S7 (Area =  $0.98$  cm<sup>2</sup>, WE = 2 mm W rod, T = 773 K)

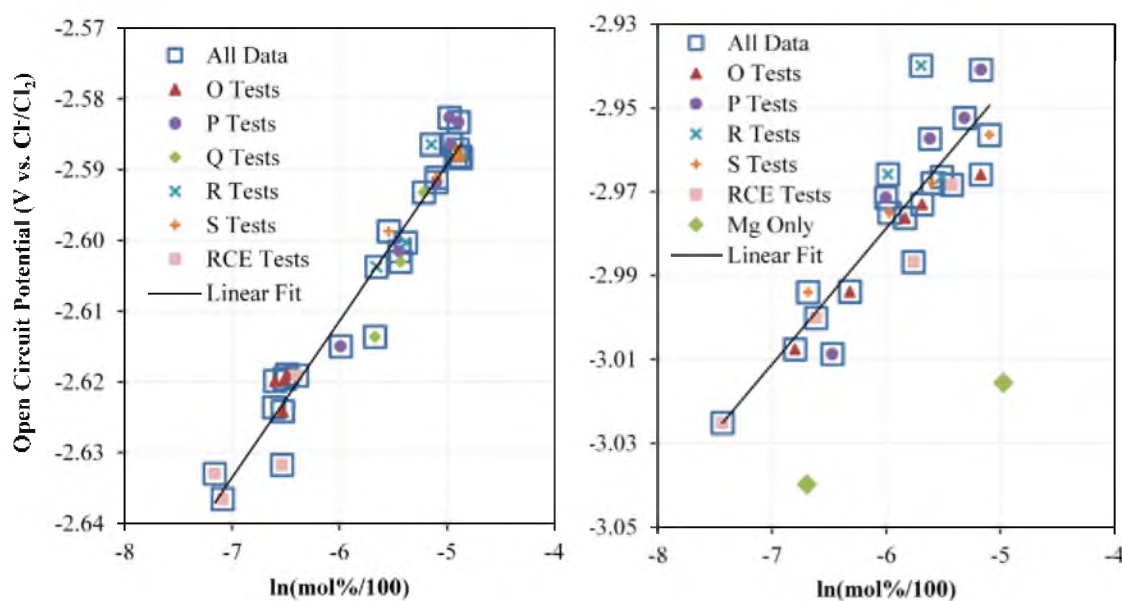


Figure 7.20 Correlation of  $U^{3+}$  (left) and  $Mg^{2+}$  (right) open-circuit potentials with natural log of  $UCl_3$  and  $MgCl_2$  mole fraction, respectively, at 773 K

Table 7.5 OCP linear fitting statistics for Figure 7.20

	Slope $\pm 95\%$ CI (V)	Y-intercept $\pm 95\%$ CI (V)	$R^2$
$U^{3+}$	$0.0221 \pm 0.0021$	$-2.479 \pm 0.012$	0.950
$Mg^{2+}$	$0.0324 \pm 0.0081$	$-2.784 \pm 0.048$	0.785

Table 7.6  $n$  and  $E^{O'}$  values calculated from slope and y-intercept in Table 7.5 with literature values

	$n$ (95% CI)	$E^{O'} \pm 95\% \text{ CI (V vs Cl}^-/\text{Cl}_2)$		
$\text{U}^{3+}$	3.01 (2.75-3.33)	$-2.479 \pm 0.012$	-2.514 (67)	-2.491 (66)
$\text{Mg}^{2+}$	2.05 (1.64-2.74)	$-2.784 \pm 0.049$	-2.849 (50)	

regressing the data from Yang and Hudson with temperature and AgCl mole fraction (69). This resulted in  $E_{\text{Ag}/\text{AgCl}}^{O'} = -1.0702 \text{ V}$  versus  $\text{Cl}^-/\text{Cl}_2$  at 5 mol% AgCl and 773 K. Three different reference electrodes were used. While these electrodes had very similar compositions of AgCl, their potentials varied slightly. Additionally, a high current density was applied to the cell unintentionally on occasion due to improper experimental setup or settings in the potentiostat procedures. This would cause the reference electrode to be polarized after which it would settle to a slightly different reference potential. To account for these shifts or difference in reference potentials, the lithium deposition potential was used to account for these discrepancies, as shown in Figure 7.21. The composition of lithium is very high and relatively constant across all mixtures. Thus, the difference in the sharp decrease corresponding to Li deposition was used to determine the difference in reference potentials. This method of accounting for differences in reference

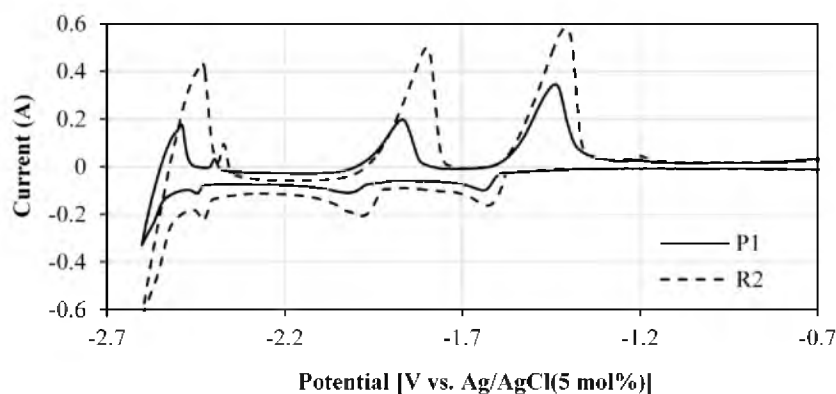


Figure 7.21 Demonstration of difference in Li deposition potentials for mixtures P1 and R2 (See Appendix A) at 300 mV/s and 773 K

potentials is not very precise and demonstrates the need for a truly stable reference electrode if any potential measurement is to be used for measuring concentration.

The correlation for magnesium's OCP is much weaker than it is for uranium. Additionally, it appears magnesium's OCP is affected by the concentration of  $\text{UCl}_3$ . The O and RCE mixtures contain the lowest concentration of  $\text{UCl}_3$  and lie along more negative boundary of OCP data in Figure 7.20. Likewise, P and S mixtures contain higher concentrations of  $\text{UCl}_3$  which consequently shifts their OCPs more positively. Furthermore, two mixtures, M1 and R1 were performed with only  $\text{MgCl}_2$  in eutectic  $\text{LiCl-KCl}$  facilitating the use of Mg rod as the CE. This allowed the OCP to be measured, as it was for uranium, by switching leads and recording the potential at zero current. These two data point, green diamonds in Figure 7.20, are much more negative than all OCP measured in  $\text{LiCl-KCl-UCl}_3\text{-MgCl}_2$  mixtures.

The increase in OCP in the presence of  $\text{UCl}_3$  is mostly likely due to procedure employed. Because uranium is present in the predeposited metal and the salt, the magnesium current is not truly zero; rather it is equivalent to and opposite of the uranium current. If Mg is present on the WE, then the WE potential is much more negative than  $\text{U}^{3+}/\text{U}$  equilibrium potential creating a reducing current for U. Since the Mg current is equal and opposite of that generated by U, then Mg is oxidizing at a rate that would create a cell current of zero which requires a potential more positive than the  $\text{Mg}^{2+}/\text{Mg}$  equilibrium potential. As  $\text{U}^{3+}$  ion concentration increases, then the reducing current of U increases which, in turn, causes the Mg oxidizing current to increase and, therefore, the  $\text{Mg}^{2+}/\text{Mg}$  OCP plateau. Unfortunately, only two points were collected with only  $\text{MgCl}_2$  present. Thus, a regression is not reliable. However, if the Nernst equation applies and the

activity coefficient is equivalent at both compositions, then the  $E^{o'}$  values should be the same and can be calculated as shown below

$$E_{Mg^{2+}/Mg}^{o'} = E - \frac{RT}{nF} \ln(x_{Mg^{2+}}) \quad (7.4)$$

Indeed, the  $E^{o'}$  is -2.850 and -2.817 V versus Cl<sup>-</sup>/Cl<sub>2</sub> for M1 and R1, respectively. These values result in an average of -2.833 V which is much closer to the literature value in Table 7.6. Thus, further refinement of the OCP measurement for the more active ion is needed. The selection criteria for identifying the potential plateau value may need to be reconsidered. Ultimately, the approach being developed by Idaho National Lab (INL) (49), isolating the ion of interest by a selective membrane, may be necessary for the more active ion(s) to achieve true equilibrium

#### 7.4.5. Concentration Measurements

For every electrochemical method in the previous sections, each data point was removed from the concentration correlations (See Figures 7.10, 7.13, 7.15-7.16, and 7.20), in turn, and the regression was redone, but in reverse (i.e.,  $y$  = concentration,  $x$  = electrochemical signal). Then using the new regression the concentration of the removed data point was determined. The composition determined from the electroanalytical methods is plotted versus the ICP-MS measured composition in Figure 7.22 for U and Figure 7.23 for Mg. The figures contain a plot for each electrochemical technique used to measure concentration, plus principal component regression (PCR) as previously described in Chapter 4 and 5. PCR was applied to CVs using 13 PCs for U and 11 PCs for Mg. Two different PCs had to be used due to the limited ICP-MS results for Mg (see Appendix A) restricting the size of the training set of data. The training set was composed



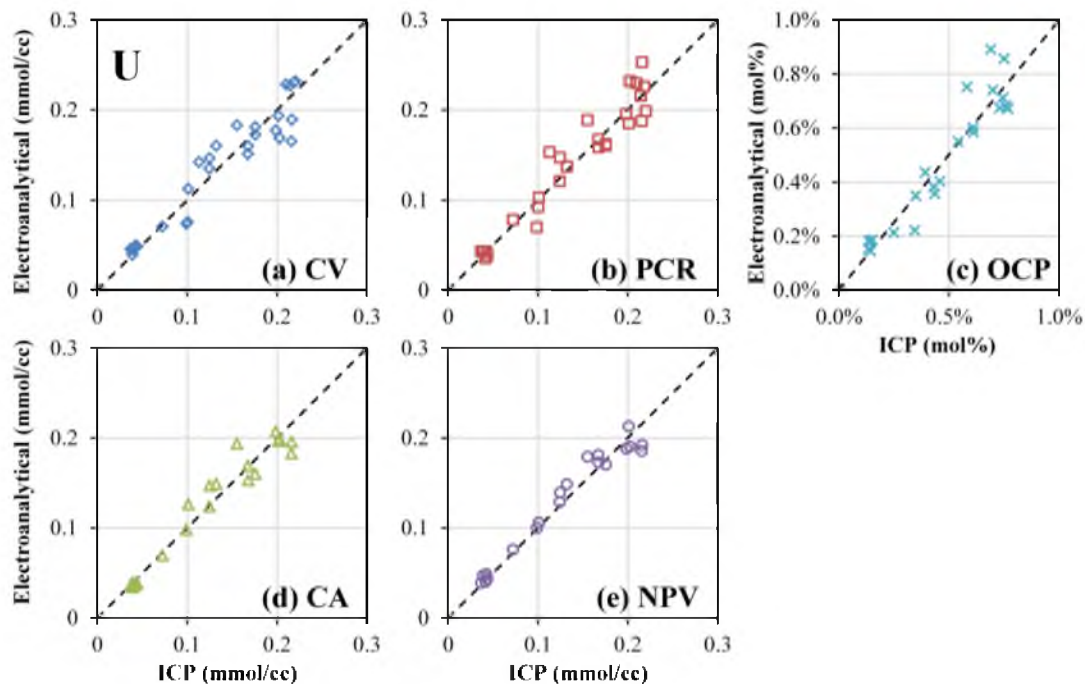


Figure 7.22 Comparison plots of the electroanalytical and ICP-MS measurements of  $U^{3+}$  ion concentration using (a) CV, (b) PCR of CV data, (c) OCP, (d) CA and (e) NPV

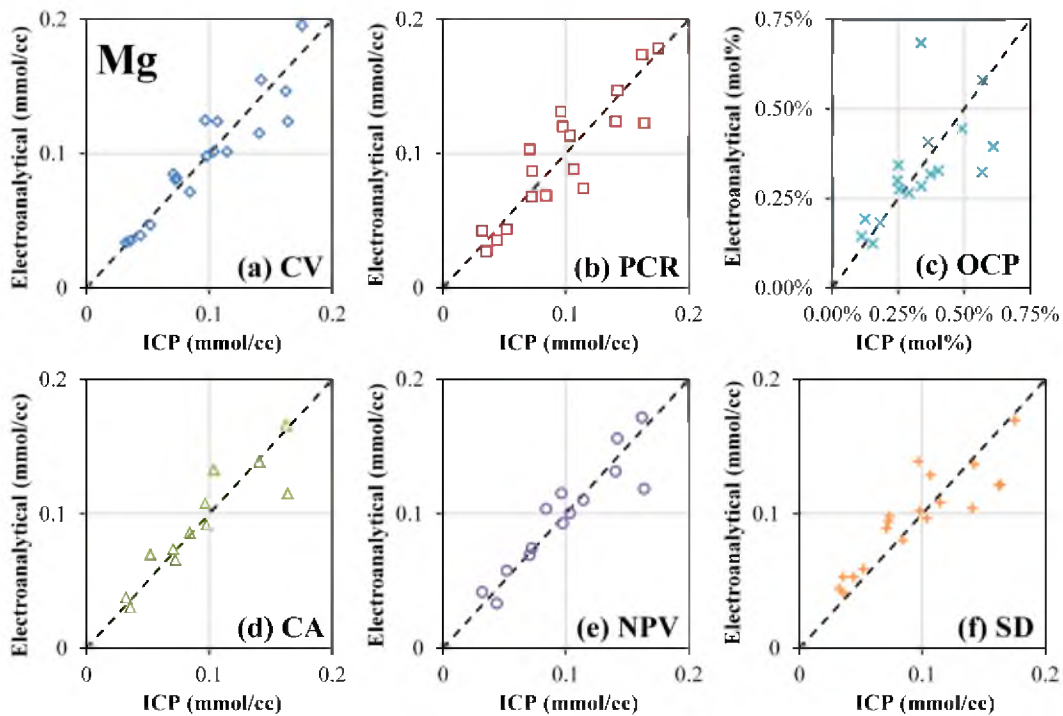


Figure 7.23 Comparison plots of the electroanalytical and ICP-MS measurements of  $Mg^{2+}$  ion concentration using (a) CV, (b) PCR of CV data, (c) OCP, (d) CA, (e) NPV and (f) SD CV data

of CVs from each mixture (O1-Q3 and R2-S8 for U, O1-O5, P4-P8, R2-R4 and S4-S8 for Mg) recorded at 300 mV/s which were aligned at  $U^{3+}$  reduction peak and truncated to include only the  $U^{3+}$  and  $Mg^{2+}$  reduction peaks.

In each plot in Figure 7.22 and 7.23, a black dashed line is included with a slope of 1 and a y-intercept of 0. Ideally, the data points would lie along this line as closely as possible. If the electroanalytical and ICP-MS measurements of the concentration were in complete agreement, then the regressed slope of the data points would be 1 with a y-intercept of 0, correlation coefficient ( $R^2$ ) of 1 and standard error of the y-estimate ( $SE_y$ ) of 0. The actual values for each of these regression statistics for the data points in each plot are provided in Table 7.7 for U and Table 7.8 for Mg. Based on these statistics, NPV has the smallest  $SE_y$  for U and Mg, but its slope and y-intercept are quite far from the ideal of 1 and 0. PCR and OCP have slopes and intercepts close to the ideal for U, but OCP has a weaker correlation. CV and PCR have the closest slopes and intercepts to the ideal for Mg, but CV has a smaller standard error and tighter correlation. A more simplistic, but less holistic way to determine the accuracy of each method is to calculate the average error of the electroanalytical concentration relative to the ICP-MS, as shown in Figure 7.24 which just displays the average, minimum, and maximum relative errors of U and Mg concentration for each technique. The average relative errors are sorted so that the greatest average error is on the left and lowest on the right. On average, NPV and CV yield the smallest relative error, 7.4% and 11.6%, for U and Mg, respectively. However, NPV result for Mg is only slightly larger, 12.4%, whereas the CV error for U is 12.1%.

Table 7.7 Regression statistics for U concentration comparison plots in Figure 7.22

Regression Statistic	CV	PCR	OCP	CA	NPV
Slope	0.9275	1.0054	1.0026	0.9574	0.9248
Y-int. (mmol/cc)*	0.0097	0.0007	-0.0003 mol%	0.0049	0.0107
R <sup>2</sup>	0.9117	0.9253	0.8956	0.9432	0.9609
SE <sub>y</sub> (mmol/cc)*	0.0196	0.0189	0.0810 mol%	0.0160	0.0125
*Unless otherwise indicated					

Table 7.8 Regression statistics for Mg concentration comparison plots in Figure 7.23

Regression Statistic	CV	PCR	OCP	CA	NPV	SD
Slope	0.9225	0.9035	0.5991	0.8321	0.8787	0.6777
Y-int. (mmol/cc)*	0.0067	0.0082	0.1285 mol%	0.0158	0.0117	0.0324
R <sup>2</sup>	0.8734	0.7903	0.4140	0.8250	0.8544	0.7656
SE <sub>y</sub> (mmol/cc)*	0.0166	0.0215	0.1152 mol%	0.0179	0.0161	0.0177
*Unless otherwise indicated						

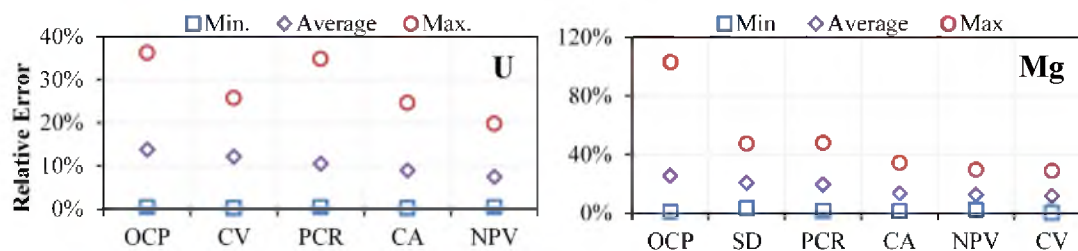


Figure 7.24 Average, minimum and maximum error of electroanalytical concentrations relative to ICP-MS for U (left) and Mg (right)

## 7.5. Discussion

In the previous section, all of the correlations, except for OCP, are tighter at low concentration and more scattered at higher concentration. This may be due to inaccurate determination of the WE surface area. The error in measuring the WE surface area is magnified at higher concentrations because, as shown in (2.43) and other electrochemical relations, the current response is linearly related to both WE area and concentration. Thus as concentration increase, the area and the error in the area measurement is multiplied by

a larger number resulting is more scatter at high concentrations. Interestingly, at least for uranium, the correlation does not appear to widen at higher concentration for OCP which is area independent.

ANL published (132) their method for removing uncertainty from their area measurements which involves the movement of WE to different immersion depths and measuring the peak current. Then, the difference in peak current is used, essentially the slope of peak current versus immersion depth. The peak current was measured at various immersion depth in mixtures N0, O1, P1, P5, Q1, R1, R2, R4, S1, S2, and S8 using the vertical translator detailed in Chapter 3. The slope of the peak current immersion versus the change in peak current, as plotted in Figure 7.25a, was calculated for each of the listed mixtures. The slope values and errors are listed in Table 7.9. A modified version of normalized current in (7.1) is correlated to concentration, as shown below (132)

$$I_p = \frac{\Delta I_p}{\Delta l} \frac{1}{d\sqrt{v}} = 0.6105\pi \sqrt{\frac{n^3 F^3 D_{M^{n+}}}{RT}} C_{M^{n+}} \quad (7.5)$$

where  $l$  is the WE immersion height or depth and  $d$  is the diameter of the WE.

Unfortunately, as shown in Figure 7.25b, this method does not seem to improve the correlation. This may be due to limited number of points, 5 or 6, used to obtain the slopes. ANL used at least twice as many and had a much smaller error in their slopes, 0.85-1.76%, compared to this work, 6.7-55.7% when using a 99.9% confidence interval (CI). Thus, it is recommended that future use of the vertical translator be more extensive. The peak current should be recorded at a greater number of WE immersion depths, at least 10-12. This should increase the accuracy of the slope.

As can be seen in Figure 7.25b, the modified peak current curves downward with

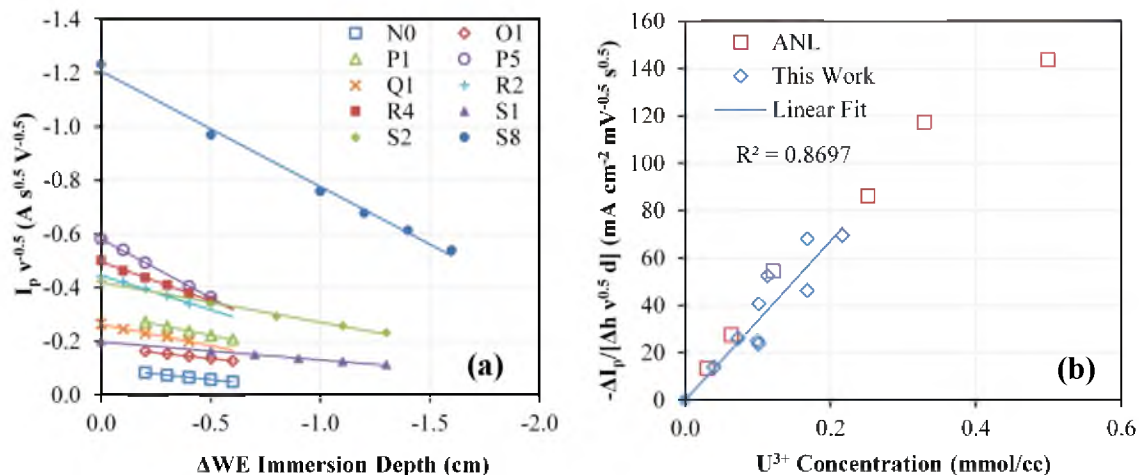


Figure 7.25 Calculation and correlation of the modified peak current,  $\hat{I}_p$  using (a) linear relations between peak current and change in WE depth and (b) correlating the slope of linear relations and  $U^{3+}$  concentration with comparison to ANL data (45)

Table 7.9 Slope of linear relations in Figure 7.25a

Mixture ID	Slope A (V/s) <sup>-0.5</sup> cm <sup>-1</sup>	±99.9% CI	%Error	Mixture ID	Slope A (V/s) <sup>-0.5</sup> cm <sup>-1</sup>	±99.9% CI	%Error
N0	-0.0868	±0.0059	6.7%	R2	-0.2556	±0.1189	46.5%
O1	-0.0868	±0.0135	15.5%	R4	-0.2918	±0.0626	21.4%
P1	-0.1638	±0.0443	27.1%	S1	-0.1494	0.0453	30.3%
P5	-0.4385	±0.0622	14.2%	S2	-0.3309	±0.1842	55.7%
Q1	-0.1579	±0.0717	45.4%	S8	-0.4304	±0.1473	34.2%

increasing  $U^{3+}$  concentration. This is also observed in CVs collected by INL and UW for the  $U^{3+}$  reduction peak. Both INL-UW and ANL data is from eutectic LiCl-KCl mixtures only containing  $UCl_3$ . Data from INL-UW's publication (39) can be compared directly to this work, but ANL's data was reported in the format of Figure 7.25b and needs to be converted by dividing by pi and adjusting the units.

A comparison of data in Figure 7.10 to ANL and INL-UW data is shown in Figure 7.26. The data from this lies right along the ANL and INL-UW data. This may imply that the presence of  $Mg^{2+}$  ions at the concentration levels in this study (0.0171-0.175 mmol/cc) does not affect the behavior of the  $U^{3+}$  ions greatly. This work's data

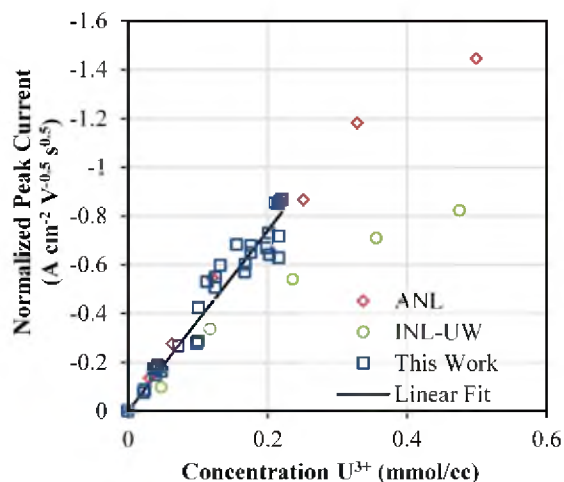


Figure 7.26 Comparison of  $U^{3+}$  reduction peak data to ANL (45) and INL-UW (39) data does not bend downward as the INL-UW data does and follows more closely the ANL data at higher concentrations. However, the data from this work ends at the point where the ANL data begins to bend downward. Thus, this work cannot confirm the decrease in diffusion coefficient proposed by ANL at high  $U^{3+}$  concentrations.

The method developed by ANL may more accurately characterize the geometric area of the WE, but the electrochemically active surface area may yet differ. Factors such as a surface roughness or passivating layers on WEs could affect the effective area on which the metal ions could reduce. The peak before the  $U^{3+}$  reduction peak in Figure 7.5 has been speculated to be the adsorption of  $U^{3+}$  (59) or the formation of a metallic uranium monolayer (66). If the prepeak is due to adsorption, then it would be considered irreversible due to the large separation of the peak pairs and its peak would be characterized by (52)

$$I_p = \frac{\alpha F^2 A \Gamma^*}{2.718 RT} \quad (7.6)$$

$$E_p = E^{o'} + \frac{RT}{\alpha F} \ln \left( \frac{RT}{\alpha F} \frac{k^o}{\nu} \right) \quad (7.7)$$

where  $\Gamma^*$  is the amount of an ion adsorbed on the WE per unit area. Thus, the prepeak current should be linear with scan rate if reversible or irreversible and the prepeak potential should be independent of scan rate, if reversible, or linear with the logarithm of scan rate, if irreversible. Indeed, the peak potential of the supposed  $U^{3+}$  adsorption peak in Figure 7.5 is linear with logarithm of scan rate, as shown in Figure 7.27. However, the prepeak current only exhibits linear behavior at low scan rates in Figure 7.27 and overall is more linear with square root of scan rate. The linearity at low scan rates would seem to suggest reversibility, but peak potential suggests irreversibility. Furthermore, the trend in the prepeak current with square-root of scan rate is highly linear, possibly implying that process may not be adsorption, but rather the formation of a uranium metal monolayer.

In any case, the prepeak current displays almost no dependence on  $UCl_3$  concentration according to the plot in Figure 7.28. It does have a large degree of scatter indicating the repeatability of prepeak may be poor. However, this work was not focused on optimizing CV for the repeatable measurement of the prepeak. Perhaps, the CV parameters could be adjusted to produce more consistent prepeaks. If the prepeak could be demonstrated to be more reproducible, perhaps at lower scan rates, then the  $U^{3+}$  ion

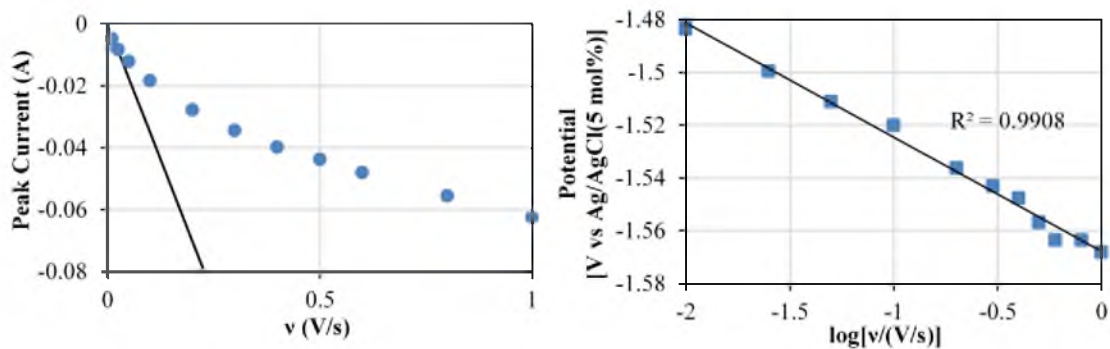


Figure 7.27  $U^{3+}$  reduction prepeak current (left) and potential (right) for mixture RCE1 (0.51 wt%  $UCl_3$ , 0.53 wt%  $MgCl_2$ , WE = 2 mm W rod, Area =  $0.78 \text{ cm}^2$ ,  $T = 773 \text{ K}$ )





and  $\text{Mg}^{2+}$  are linear over the concentration range tested, 0.0224-0.220 mmol/cc for  $\text{U}^{3+}$  and 0.0171-0.175 mmol/cc for  $\text{Mg}^{2+}$ . Using CV data, the diffusion coefficient calculated for  $\text{U}^{3+}$  and  $\text{Mg}^{2+}$  are  $9.74 \times 10^{-6}$  and  $2.90 \times 10^{-5}$   $\text{cm}^2/\text{s}$ , respectively. CV and NPV resulted in the lowest relative error when measuring  $\text{U}^{3+}$  and  $\text{Mg}^{2+}$  concentrations. PCR did improve the concentration measurements for  $\text{U}^{3+}$  when applied to CV data, but did not improve the measurements for  $\text{Mg}^{2+}$ . The recorded CV peaks for  $\text{U}^{3+}$  reduction compared favorably to previous work on LiCl-KCl- $\text{UCl}_3$  mixtures possibly indicating that the presence of  $\text{MgCl}_2$  may not affect the behavior of  $\text{UCl}_3$  at these concentration levels. Using OCP measurements, the apparent standard potential is -2.479 and -2.833 V versus  $\text{Cl}^-/\text{Cl}_2$  for  $\text{U}^{3+}/\text{U}$  and  $\text{Mg}^{2+}/\text{Mg}$ . The OCP measurements of  $\text{Mg}^{2+}$  appear to be dependent on  $\text{UCl}_3$  composition because true equilibrium is not achieved for  $\text{Mg}^{2+}$  due to the exchange of Mg metal with  $\text{U}^{3+}$  ions. The measurement of surface area is possibly a major source of error in measuring concentrations due to the spreading of the electrochemical signals at higher concentration. It is suggested that the pre-peak of  $\text{U}^{3+}$  reduction could be a reliable, built-in indicator of the effective surface area of the WE, if reproducibility can be improved.

## 8. DREP VALIDATION—A HYDRODYNAMIC STUDY

DREP (Deposition Rates using Electrode Potentials) is an inverse model of a UNF electrorefiner (ER) based on the same fundamental equations of ERAD (Enhanced REFIN with Anodic Dissolution), but does not require complete information about the compositions of each phase (i.e., anode, electrolyte, and cathode) in the ER. Rather, it uses the cell current and electrode potential to: (1) determine if more than one ion is reacting at an electrode and (2) calculate the concentration and deposition rates of the electroactive ions. DREP was developed and tested previously by the author (89, 136). The concept of DREP was tested by inputting certain electrolyte compositions of U, Pu and Zr into ERAD, then simulating the current and potential response. The simulated current and potential values were then used in DREP to calculate the composition of U, Pu and Zr in the electrolyte and their deposition rates at the cathode. The results of DREP compared favorably to ERAD demonstrating that the model is theoretically sound (89). However, the model was not validated against experimental data. This chapter details the effort made to validate DREP with experimental data from LiCl-KCl-UCl<sub>3</sub>-MgCl<sub>2</sub> mixtures.

### 8.1. Model Description

DREP was developed by using (2.8), (2.21)-(2.23) with the assumption that deposited metals have an activity of unity and pairs those with the equation below (52).

$$I = nFAh(C_{M^{n+}}^b - C_{M^{n+}}) \quad (8.1)$$

$h$  represents the mass transfer coefficient. The use of (8.1) also introduces the assumption that migration effects are negligible which is the key difference between DREP and ERAD. The migration term in the Nernst-Planck equation, (2.28), is dependent on the potential gradient which can be reduced by decreasing the overpotential. Consequently, the effect of neglecting migration is minimized by using low current densities. By combining (2.8), (2.21)-(2.23) and (8.1), the following equation results when the assumption of unity activity is applied to metal deposits:

$$I_{j,k} = \frac{i_{o,j}^{\circ} A \left\{ \frac{\gamma_j C_j^b}{C_{salt}} \exp \left[ \frac{-(1-\beta_j)n_j F}{RT} (E_k - E_j^{\circ}) \right] - \exp \left[ \frac{-\beta_j n_j F}{RT} (E_k - E_j^{\circ}) \right] \right\}}{\frac{i_{o,j}^{\circ} \gamma_j \exp \left[ \frac{-(1-\beta_j)n_j F}{RT} (E_k - E_j^{\circ}) \right]}{n_j F h_j C_{salt}} + 1} \quad (8.2)$$

$$\beta = 1 - \alpha \quad (8.3)$$

$$i_o^{\circ} = n F k^{\circ} \quad (8.4)$$

where  $C_{salt}$  is molar density or concentration of the entire salt mixture, the subscript  $j$  indicates the metal ion (e.g.,  $U^{3+}$ ) and the subscript  $k$  is the current step index. A complete derivation of this expression is given elsewhere (89). In (8.2)-(8.4),  $F$ ,  $A$ ,  $R$ ,  $T$ , and  $n$  are parameters and properties that have been measured or calculated.  $I_{j,k}$ ,  $i_o^{\circ}$ ,  $E^{\circ}$ ,  $\gamma$ ,  $E_k$ ,  $\alpha$ ,  $h$ , and  $C_{salt}$  are parameters and properties that can be measured or determined. That leaves only  $C_j^b$  as unknowns. If there is only one species (i.e.,  $j$  is a scalar), the concentration can be determined and deposition rate is simply equivalent to the cell current less any inefficiencies. However, if there are 2 or more ions actively reacting at the working electrode (WE), then there are too many unknowns and concentration and

deposition rates cannot be calculated with a single equation.

This problem can be solved by introducing another assumption. Under a small A/V ratio (i.e., WE surface area ( $A$ ) is small compared to the electrolyte volume ( $V$ )) and on short time scales, the bulk concentration is constant and unaffected by the reaction of ions at the WE. Thus, short current steps ( $k$ ) could be taken and the potential measured at each step to create a system of equations, as shown below:

$$I_k = \sum_j I_{j,k}(C_j^b, E_k) \quad (8.5)$$

where  $I_{j,k}$  is the function of  $C_j^b$  and  $E_k$  given in (8.2). Thus, the number of current steps need be equal to the number of electroactive ions in order to solve for concentration and deposition rates. The current steps should be as low in magnitude and as short in duration as possible to minimize the error introduced by the assumption of constant bulk concentration. An illustration of the current step process is shown in Figure 8.1 for a large electrochemical cell.

The model structure, decision making, limitations and characteristics are discussed in detail elsewhere (89), and are only briefly mentioned here. The model does not need knowledge of prior operating history and can determine instantaneous

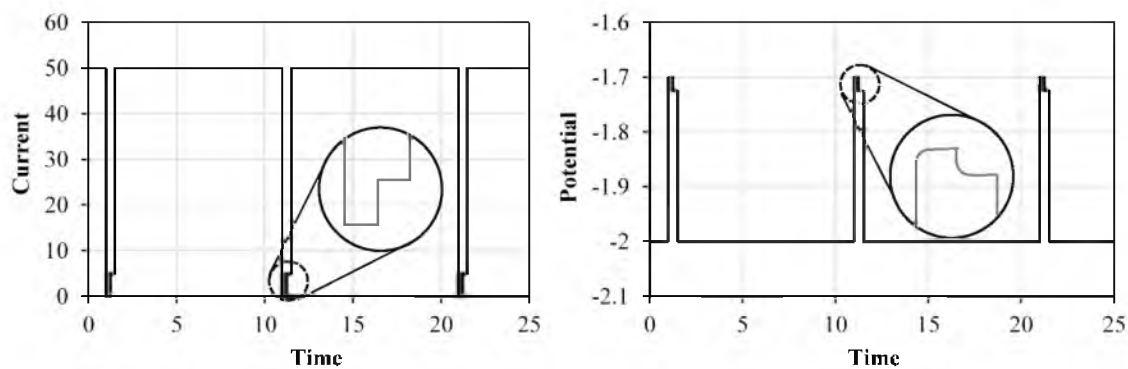


Figure 8.1 Generic illustration of current (left) and WE potential (right) profile for two-species deposition with magnification of current step cycle

deposition rates. The model is capable of independently identifying whether more than one ion is depositing at the WE. As currently developed, the model is one-dimensional and does not have a mechanism to account for growing surface deposits. Only solid, inert cathodes are considered in this model, although the adjustment of some parameters may be able to extend it to solid, reactive electrodes. Additionally, the model assumes the diffusion layer to be static. The model is most sensitive to the  $E^o$  parameter due to its exponential relationship.

## 8.2. Model Parameters

The system selected for validating DREP is the LiCl-KCl-UCl<sub>3</sub>-MgCl<sub>2</sub> mixture. Hence, the diffusion coefficients and standard apparent reduction potentials ( $E^{o'}$ ), from Chapter 7 will be used in DREP. The use of  $E^{o'}$ , as opposed to standard reduction potential ( $E^o$ ), means that the activity coefficient ( $\gamma$ ) accounted for in  $E^{o'}$ . This is accounted for in the model by setting  $\gamma$  equal to one. This leaves  $i_o^o$ ,  $\alpha$ , and  $h$  to be determined for U<sup>3+</sup> and Mg<sup>2+</sup>. Cumberland and Yim (90) already determined  $i_o^o$  and  $\alpha$  for U<sup>3+</sup> by fitting ERAD simulated CVs to CVs in literature. Their values should be equally applicable in DREP, since ERAD and DREP use the same fundamental equation (i.e., current-overpotential equation) for simulating the reaction rates and only differ in the simulation of mass-transfer phenomena. Now, there is only  $i_o^o$  and  $\alpha$  for Mg<sup>2+</sup> and  $h$  for both ions that remain undetermined.

### 8.2.1. Mass Transfer Coefficient

Values for the mass transfer coefficient,  $h$ , were investigated using a rotating cylinder electrode (RCE) and the experimental setup described in Section 3.5.6. Four

tests with the RCE were conducted with the compositions listed in Table 8.1 (see Appendix A for more details). Each mixture was subjected to static cyclic voltammetry (CV) and open-circuit potentiometry (OCP) tests and hydrodynamic (HD) linear sweep voltammetry (LSV) and CP. LSV was used to identify the limiting current at each rotational rate and concentration. CP was used to simulate electrorefining under current control.

When LSV is performed under hydrodynamic conditions, it ideally will take on the shape of a normal pulse voltammetry (NPV) scan—sharp rise followed by a plateau. Similar to NPV, the current plateaus in HD-LSV are due to the complete depletion of an electroactive ion at the electrode surface. However, the plateau in HD-LSV is not time-dependent. The plateau in HD-LSV is called the limiting current ( $I_L$ ), the expression for which is created by setting the surface concentration term to zero in (8.1)

$$I_L = nFAhC_{M^{n+}}^b \quad (8.6)$$

The mass transfer coefficient has been characterized for a RCE in aqueous solutions using the ferrocyanide-ferricyanide couple (137)

$$h = \frac{D}{\delta} = 0.0791 \left( \pi \frac{\omega}{60} \right)^{0.7} d^{0.4} \left( \frac{\mu}{\rho} \right)^{-0.344} D^{0.644} \quad (8.7)$$

$\omega$  represents the rotational rate in RPM,  $\delta$  is the diffusion layer thickness,  $\mu$  is the

Table 8.1 Composition of ICP samples measured by ICP-MS

Mixture ID	UCl <sub>3</sub> (wt%)	MgCl <sub>2</sub> (wt%)
RCE1	0.51%	0.53%
RCE2	0.48%	0.10%
RCE3	1.02%	0.23%
RCE4	0.89%	0.74%

dynamic viscosity of the liquid and  $\rho$  is the density. However, the applicability of this relation to high-temperature molten salt system is unproven. Limited work has been performed with RCEs in eutectic LiCl-KCl and has mostly focused on large-scale ERs and the effect of rotation rates on recovery (138) or has used three-dimensional models to analyze the diffusion layer behavior (139,140). No electroanalytical work using a RCE in high-temperature molten salt was found in the literature. A rotating disc (RDE) and rotating ring-disc electrode (RRDE) have been developed for applications up to 723 K (141).

Initially, HD-LSV was tested in mixture P4 and revealed some issues with the design of the RCE. First, there was significant whipping occurring due to the long, narrow tungsten rod which created excessive noise in the LSV making it difficult to analyze. Second, the hydrodynamics enhanced the deposition rate of uranium significantly which caused significant WE area growth before magnesium could deposit, as shown in Figure 8.2. Lastly, interdependence between scan rate and rotation rate was observed. If the scan rate was too low, the growth of deposits would increase the surface area before a clear plateau would be established resulting in a continuous increase in

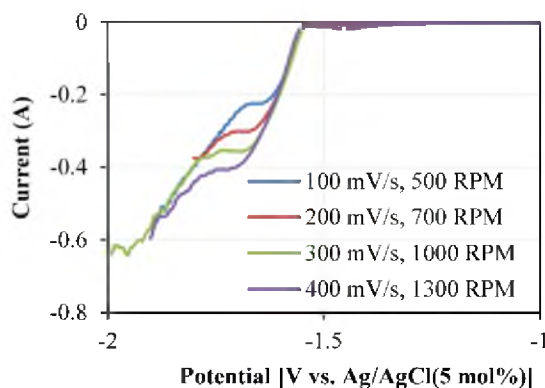


Figure 8.2 HD-LSV shape for mixture P4 (4.16 wt%  $\text{UCl}_3$ , 0.25 wt%  $\text{MgCl}_2$ , Area =  $0.92\text{cm}^2$ , WE = 2 mm W rod, T = 773 K) with short adapter

current. If the scan rate is too fast, the transient effects (i.e., peaks) would be too large and would not decay to a level plateau before the more active ion would start to deposit. Limiting current plateaus were achieved for both uranium and magnesium at lower concentrations in the RCE mixtures. The limiting current plateaus, deposit growth effects and transient effects are all shown in the representative LSVs in Figure 8.3.

As can be seen in Figure 8.3, the limiting current is independent of scan rate, if the reduction process was truly controlled by hydrodynamics. At a very low scan rate, 5 mV/s, the  $U^{3+}$  reduction peak is almost eliminated and the limiting current for  $U^{3+}$  is quickly achieved. As the scan rate increases the peaks grow, but eventually settle to the limiting current value with the exception of 10 and 15 mV/s for  $Mg^{2+}$  and 25 mV/s for  $U^{3+}$ . In the case of 10 and 15 mV/s, the deposited metals begin to significantly increase the surface area before the  $Mg^{2+}$  limiting current can be reached. For 25 mV/s, the  $U^{3+}$  reduction peak is so large that it does not decay to the limiting current before  $Mg^{2+}$  reduction commences. Thus, the limiting current for rotational rate of the RCE was measured by repeating LSV at multiple scan rates and identifying the scan rates at which

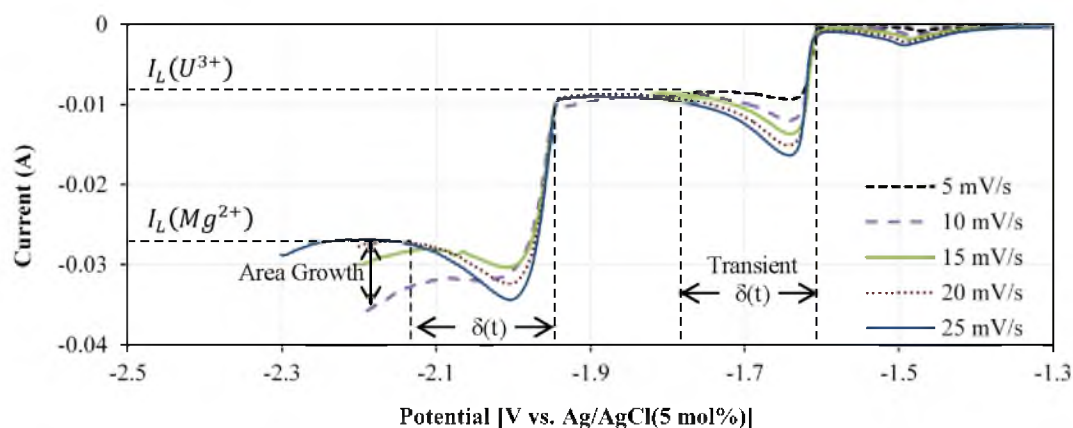


Figure 8.3 HD-LSV for mixture RCE1 (0.51 wt%  $UCl_3$ , 0.53 wt%  $MgCl_2$ ) at 250 RPM (Area =  $0.78 \text{ cm}^2$ , WE = 2 mm W rod, T = 773 K)



the current plateaus at the same value.

The peak formation in HD-LSV is theorized to occur because initially the diffusion layer thickness established by diffusion processes ( $\delta_D$ ) is thinner than the diffusion layer thickness created by the hydrodynamics of the RCE ( $\delta_{RCE}$ ). This tradeoff in diffusion layer control is illustrated in Figure 8.4.  $\delta_D$  is transient and grows with time while  $\delta_{RCE}$  is static. Eventually,  $\delta_D$  increases beyond  $\delta_{RCE}$  and the current switches from being diffusion controlled to hydrodynamic controlled.

The applicability of (8.7) in molten eutectic LiCl-KCl at 500°C was tested by plotting the measured limiting currents for versus  $\omega^{0.7}$  as shown in Figure 8.5. The  $U^{3+}$  limiting current was subtracted from the observed  $Mg^{2+}$  limiting current plateau. If the equation is applicable, then the plot should show a linear trend. The limiting current of  $U^{3+}$  and  $Mg^{2+}$  is linear above 200 RPM and 100 RPM, respectively. At lower rotational rates, the limiting current departs from linearity. This may be due to an incomplete transition from diffusion to hydrodynamic control of the diffusion layer. Using (8.7), the dynamic viscosity ( $2.2 \text{ g m}^{-1} \text{ s}^{-1}$ ) (142) and density ( $1.62 \text{ g/cc}$ ) (60) of eutectic LiCl-KCl, the diffusion coefficient was calculated from the slopes of the plots in Figure 8.5 excluding the nonlinear points at low rotational rates. The values are a little more than

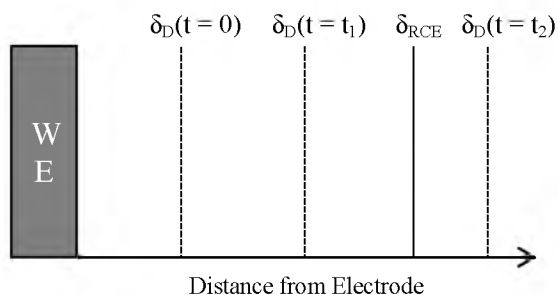


Figure 8.4 Illustration of the transition from diffusion (dashed) to hydrodynamic (solid) controlled diffusion layer where  $t = 0$  at the HD-LSV peak

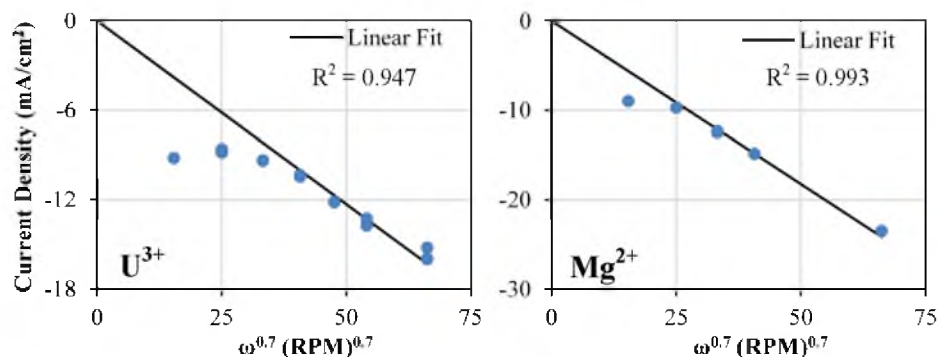


Figure 8.5 Trend of limiting current with  $\omega^{0.7}$  for  $U^{3+}$  (left) and  $Mg^{2+}$  (right) reduction in mixture RCE1 (0.51 wt%  $UCl_3$ , 0.53 wt%  $MgCl_2$ , Area =  $0.63 \text{ cm}^2$ )

double the values determined by CA for both  $U^{3+}$  ( $4.13 \times 10^{-5} \text{ cm}^2/\text{s}$ ) and  $Mg^{2+}$  ( $7.78 \times 10^{-5} \text{ cm}^2/\text{s}$ ) in the previous chapter. This discrepancy could be differences in electrochemical techniques and cell setup. Diffusion coefficients exhibit a high degree of variability in electrochemical tests in molten LiCl-KCl. Nevertheless, the linear trend with  $\omega^{0.7}$  and relatively close diffusion coefficients are promising the evidence that (8.7) is applicable to LiCl-KCl- $UCl_3$ - $MgCl_2$  mixtures at 773 K at rotational rate from 200-500 RPM. Thus, all HD-CP tests were carried out at 250 RPM. The rotational rate was kept below 500 RPM in all RCE mixtures to avoid vortices and nonuniform analyte concentration distributions.

The mass transfer coefficient was calculated via the diffusion coefficient and the diffusion layer thickness, as shown in (8.7). The diffusion coefficients calculated in Table 7.1 were used and the diffusion layer thickness was calculated from limiting currents measured by HD-LSV for each RCE mixture at 250 RPM. This resulted in the diffusion layer thickness values plotted in Figure 8.6 for both  $U^{3+}$  and  $Mg^{2+}$  reduction. The diffusion layer thickness should be constant with concentration, if the limiting current is linearly related to concentration. However, according to Figure 8.7, the limiting current

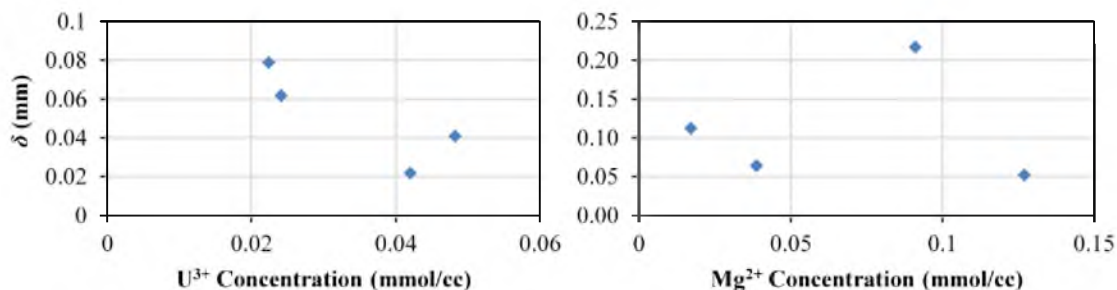


Figure 8.6 Diffusion layer thickness ( $\delta$ ) at 250 RPM, 773 K and each composition of RCE mixtures (see Appendix A)

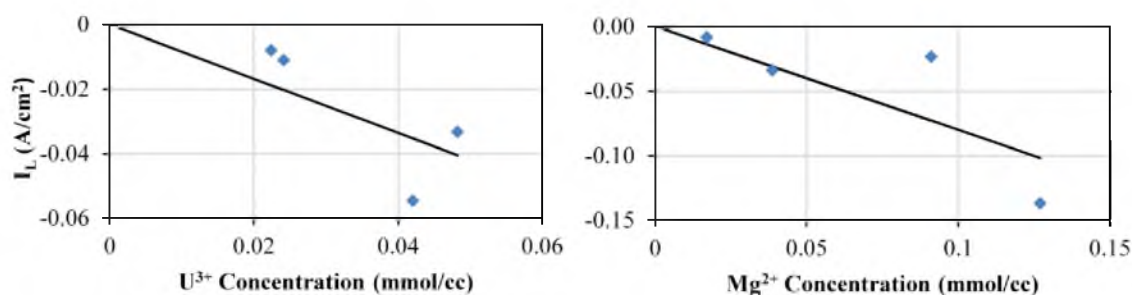


Figure 8.7 Limiting current measured by HD-LSV at 250 RPM, 773 K and each composition of RCE mixtures (see Appendix A)

does not appear to have a strong linear correlation. Consequently, there is a large degree of scatter in the diffusion layer thickness and an averaged value of 0.051 and 0.111 mm was used in DREP for  $U^{3+}$  and  $Mg^{2+}$  ions, respectively. This results in a mass-transfer coefficient of 0.0019 cm/s for  $U^{3+}$  and 0.0026 cm/s for  $Mg^{2+}$ .

### 8.2.2. Kinetic Parameters for $MgCl_2$

The kinetic parameters of  $Mg^{2+}$  ions in eutectic LiCl-KCl were measured by using an approximation of the Butler-Volmer equation at low overpotentials which uses the first two terms of the Taylor series expansion for an exponential function ( $e^x = 1 + x$ ) and the assumption that the bulk and surface concentrations of ions are equal. The approximation yields a the following form of the Butler-Volmer equation which is linear

with overpotential (52):

$$I = -i_o \frac{nF}{RT} \eta \quad (8.8)$$

using DREP's convention and assumptions

$$i_o = i_o^o A \alpha^\beta = i_o^o A (\gamma x)^\beta \quad (8.9)$$

where  $\gamma$  is assumed to be 1 because  $E^{o'}$  is being used instead of  $E^o$ . This approximation deviates from (8.2) by 1% or less for  $\eta = 16.5$  mV, if  $n = 2$ ,  $T = 773$  K and  $\alpha = 0.5$ . The exchange current was measured by regressing the slope of each HD-LSV in every RCE mixture from the commencement of  $\text{Mg}^{2+}$  reduction up to 16.5 mV in the negative direction, as shown in Figure 8.8. The slope for each mixture was taken for multiple HD-LSVs and averaged, then divided by  $nF/RT$  to obtain an exchange current for  $\text{Mg}^{2+}$  for each RCE mixture. The resulting exchange current values are plotted in Figure 8.9.

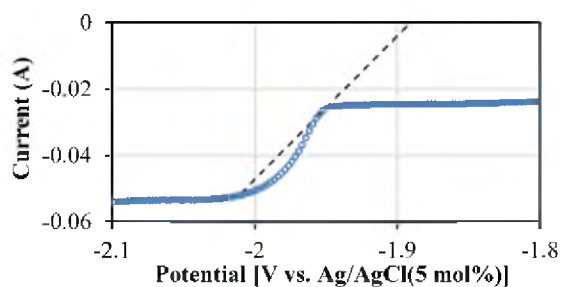


Figure 8.8 Example of slope regression on a 30 mV/s HD-LSV for mixture RCE3

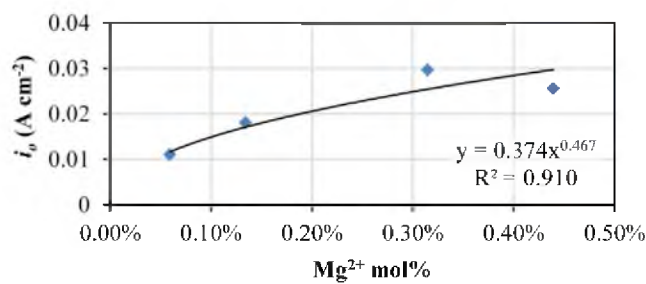


Figure 8.9 Exchange current density dependency on  $\text{Mg}^{2+}$  mole fraction

According to (8.9), the slope should relate to mole fraction by a power law. The natural log of the exchange currents and composition data was regressed to yield the power law displayed in Figure 8.9. As a result of this regression,  $i_o^o = 0.374 \text{ A/cm}^2$  and  $\alpha = 0.533$  ( $\beta = 0.467$ ).

### 8.3. Model Results

ER operation typically occurs under controlled current. Thus, CP was applied to simulate electrorefining. A cycle similar to that shown in Figure 8.1 was applied to cell. First, the cell current was set for 10 s (13 s for mixture RCE2, cycle A) to an “operational” current where U and Mg would codeposit. The operational current was selected by examining the HD-LSV curves. Next, the cell current was set to zero for one second and then set to 5 mA for another second. Then, the cell current was returned to the operational current. This cycle was repeated twice so that the operating current step was applied three times and the one-second open-circuit and 5 mA steps were applied twice. At the end of the third operating current step, the RCE was raised out of the salt while the cell was set to the operational current. The operational current and measured potential at the end of each current step are given in Table 8.2. The letters A and B represent the first

Table 8.2 Operational current setting and measured potential for each RCE mixture

Mixture ID	Current (mA) Operational	Potential [V vs Ag/AgCl (5 mol%)]		
		Operational	Open-Circuit	5 mA
RCE1A	20	-1.951	-1.927	-1.923
RCE1B	20	-1.963	-1.929	-1.929
RCE2A	13	-2.030	-1.971	-1.975
RCE2B	13	-2.030	-1.974	-1.975
RCE3A	40	-1.990	-1.929	-1.926
RCE3B	40	-1.971	-1.928	-1.921
RCE4A	120	-2.027	-1.921	-1.918
RCE4B	120	-2.003	-1.924	-1.920

and second cycle of the current steps. The potential was sampled at the end of each step to avoid interference from possible transient effects. For example, the measured WE potential during the current cycle for mixture RCE2 is given in Figure 8.10. In the first step of cycle A, there are transient effects and the potential response looks like a chronopotentiogram. However, after a couple seconds, the potential settles out to a steady value unlike static CP measurements which continue to decrease until Li deposition. On the last operational step, a sharp decrease in the potential marks the removal of the WE from the cell.

There are two sets of model parameters: species properties (e.g., diffusion coefficient, etc.) and cell settings/measurements. The species properties have all been determined in previous sections or gathered from other references. They are summarized in Table 8.3. For an internal source, the page number where the property is calculated is listed in the source column without parenthesis. For an external source, the reference is cited in parenthesis and italicized. The cell current settings and measured WE potentials

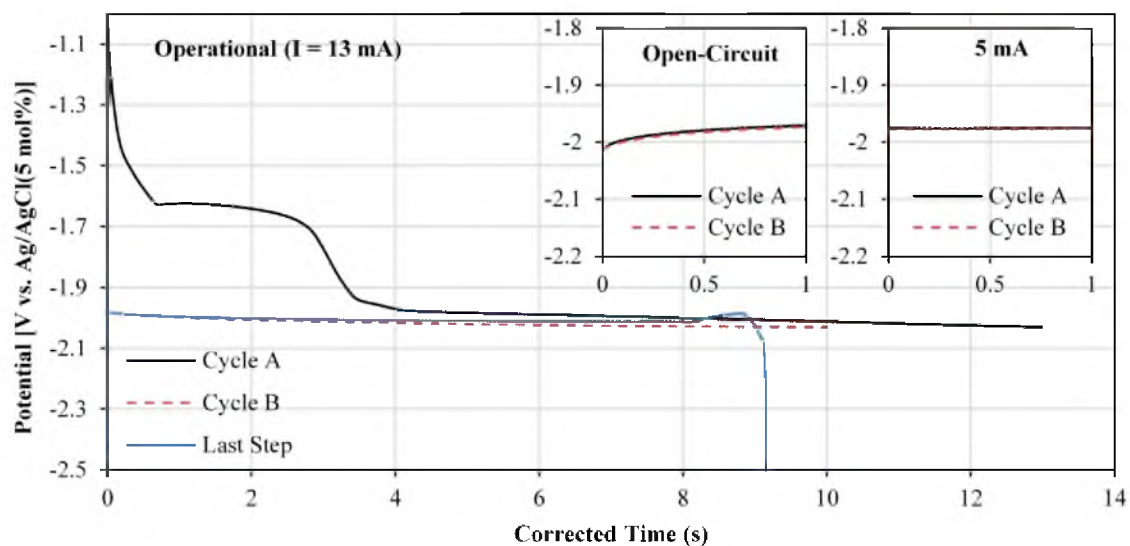


Figure 8.10 HD Chronopotentiogram for the operational (main plot), open-circuit (inset), and 5 mA (inset) steps in mixture RCE2 (Area = 0.74 cm<sup>2</sup>)

Table 8.3 Species property values used in DREP

Parameters	UCl <sub>3</sub>	Source	MgCl <sub>2</sub>	Source
$E^o$ [V vs Ag/AgCl (5 mol%)]	-1.409	p. 165	-1.763	p. 167
$n$	3	p. 165	2	p. 165
$D$ ( $10^{-5}$ cm <sup>2</sup> /s)	0.975	p. 156	2.903	p. 156
$i_o^o$ (A/cm <sup>2</sup> )	1.1	(90)	0.37	p. 187
$\beta$ ( $1 - \alpha$ )	0.5	(90)	0.47	p. 187
$\delta$ (cm)	0.005	p. 186	0.011	p. 186

used in DREP are listed in Table 8.2.

DREP predicts three things with only the information provided in Table 8.2 and 8.3. First, DREP determines if one or more metal ions are being reduced at the WE. Second, it solves the concentration of each depositing metal ion in the bulk electrolyte using the two low current steps (i.e., open-circuit and 5 mA). Lastly, it uses the calculated concentrations and (8.2) to predict the deposition rate at the operational step settings.

DREP succeeds in all mixtures and cycles to identify that more than one metal ion is depositing at the WE. The results of DREP concentration calculations are given in Table 8.4. For RCE1A-RCE2B, the concentrations calculated by DREP agree fairly well with ICP-MS measured values. However, for RCE3B-RCE4B, negative concentrations are calculated and the solutions drastically disagree with ICP-MS values. Essentially,

Table 8.4 Concentrations calculated by DREP

Mixture ID	UCl <sub>3</sub> (mmol/cc)		Relative Error	MgCl <sub>2</sub> (mmol/cc)		Relative Error
	ICP	DREP		ICP	DREP	
RCE 1A	0.0241	0.0326	35%	0.0911	0.1478	62%
RCE 1B	0.0241	0.0322	34%	0.0911	0.1123	23%
RCE 2A	0.0224	0.0213	5%	0.0171	0.0270	58%
RCE 2B	0.0224	0.0210	6%	0.0171	0.0277	62%
RCE 3A	0.0482	0.0102	79%	0.0388	0.2259	482%
RCE 3B	0.0482	$4.26 \cdot 10^3$	$8.82 \cdot 10^6$	0.0388	$-1.45 \cdot 10^8$	$3.74 \cdot 10^{11}$
RCE 4A	0.0420	-0.0382	191%	0.1270	0.5084	300%
RCE 4B	0.0420	-0.0850	302%	0.1270	0.6973	449%

DREP does not converge to realistic solutions for the concentration of the ions. RCE3B has realistic solutions, but are quite inaccurate.

Deposition rates were also calculated by DREP. To gauge the accuracy of the predicted deposition rates, the deposited metal on the WE was dissolved in a known volume of 10 vol% nitric acid and the U, Mg, Li, K content was measured using ICP-MS (see Appendix A). Inevitably, some salt adhered to the metal deposits. The amount of adhering salt was calculated based off of the Li and K content and U and Mg content in the corresponding salt mixture. The amount of U and Mg contained in the adhering salt was calculated by multiplying the ICP-MS concentration measurements of the U and Mg in the salt mixture and the calculated amount of adhering salt. This amount was subtracted from the measured U and Mg content in the dissolution to determine the amount of U and Mg metal deposited. The current efficiency was also calculated from the calculated metal deposit amounts. Key values in these calculations are provided in Table 8.5 (see Appendix A for more details). DREP's deposition rates were multiplied by the summed total duration of the operational steps (i.e., deposition time) and are compared the amount of U and Mg metal deposits calculated from ICP-MS measurements in Table 8.6. It is important to note that the third operational step did not last 10 s because of the early removal. However, the time of removal was marked clearly by a sharp drop in the potential. The early removal is accounted for in the deposition times listed in Table 8.6.

Table 8.5 Calculated amount of salt adhering to metal deposit and current efficiency (see Appendix A)

<b>LiCl (mg)</b>	<b>KCl (mg)</b>	<b>Adhering Salt (mg)</b>	<b>Current Efficiency</b>
2.07	2.66	4.78	122%
2.97	3.98	6.99	131%
3.65	4.93	8.68	118%
5.90	8.06	14.19	122%



Table 8.6 Calculated U and Mg metal deposited

Deposit ID	U deposit (mg)		Relative Error	Mg deposit (mg)		Relative Error	Deposition Time (s)
	ICP	DREP		ICP	DREP		
<b>RCE 1A</b>	0.268	0.316	18%	0.0136	0.0201	48%	27.18
<b>RCE 1B</b>	0.268	0.313	17%	0.0136	0.0206	52%	27.18
<b>RCE 2A</b>	0.229	0.232	1%	0.0077	0.0172	122%	32.16
<b>RCE 2B</b>	0.229	0.229	0%	0.0077	0.0176	128%	32.16
<b>RCE 3A</b>	0.768	0.102	87%	0.0035	0.1328	3721%	29.45
<b>RCE 3B</b>	0.768	-936.2	$1.22 \cdot 10^5$	0.0035	143.59	$4.13 \cdot 10^6$	29.45
<b>RCE 4A</b>	1.583	-0.424	127%	0.0778	0.4887	528%	28.03
<b>RCE 4B</b>	1.583	-0.942	160%	0.0778	0.5681	630%	28.03

Because the predicted deposition rates are dependent on the concentration calculations in DREP, a similar trend is found in the deposition rates. RCE1A-RCE2B are reasonably close while RCE3A is quite inaccurate and RCE3B-RCE4B diverged and returned negative values.

The design of these experiments was to test the ability of DREP to predict deposition rate when two metal ions were depositing. Because of this, the potential range where the CPs were run was slightly more negative than the equilibrium potential. At this region of the current-potential curve (about -2 V in Figure 8.3), uranium is at its limiting current which makes the concentration and deposition rate calculations mostly dependent on the diffusion layer thickness. As a result, the concentration and deposition rate is over-predicted when the actual diffusion layer thickness in a specific mixture (see Figure 8.6) is above the average and under-predicted when the actual diffusion layer thickness is below the average with exception of RCE3B. The diffusion layer thickness does not have the same effect on the magnesium predictions because it is not near its limiting current.

The other important factor at this region of the current-potential curve is the standard apparent potential. The measured potentials (see Table 8.2) shift more positively

in mixture RCE3, even more so in cycle B. In RCE3A, the error in the diffusion layer thickness for uranium offsets the positive shift in potential. However, due to the steep slope of the current-potential curve, the slight shift in potential from RCE3A to RCE3B is enough to slide the predicted magnesium current from reducing to oxidizing which results in the negative concentration. The shift in potential between cycle A and B may have been caused by deposit growth. As the area of the WE increase due to deposits, the current density decreases because the current value is fixed. The lower current density requires a lower overpotential and, in this case, less negative potential. In mixture RCE4, the opposite occurs—a negative shift in the potential—resulting in large positive concentrations for magnesium which then causes the uranium concentration to go negative.

It is apparent that DREP may not be the best method for determining concentration in this particular setup due to potential drifts and unexpected variations in the diffusion layer. It is also clear that the error in the DREP calculations of concentration propagate through to the deposition rates. Therefore, the deposition rate portion of DREP was evaluated by using ICP-MS measured concentration values, essentially eliminating the error propagated by DREP's concentration calculations. The deposition rates predicted by DREP are displayed in Table 8.7. Despite some lingering effects of the variations in diffusion layer thickness and measured potentials, the predicted rates are quite accurate. Thus, it may be sensible to pair DREP with the concentration measurements of a more accurate electroanalytical technique such as CV or NPV.

Table 8.7 Calculated U and Mg metal deposited using ICP-MS concentration values

Deposit ID	U deposit (mg)		Relative Error	Mg deposit (mg)		Relative Error	Deposition Time (s)
	ICP	DREP		ICP	DREP		
RCE 1A	0.268	0.234	13%	0.0136	-0.0059	144%	27.18
RCE 1B	0.268	0.234	13%	0.0136	0.0096	29%	27.18
RCE 2A	0.229	0.244	6%	0.0077	0.0075	4%	32.16
RCE 2B	0.229	0.244	6%	0.0077	0.0073	6%	32.16
RCE 3A	0.768	0.481	37%	0.0035	0.0048	38%	29.45
RCE 3B	0.768	0.481	37%	0.0035	-0.0106	406%	29.45
RCE 4A	1.583	0.466	71%	0.0778	0.1143	47%	28.03
RCE 4B	1.583	0.466	71%	0.0778	0.0879	13%	28.03

#### 8.4. Discussion

The results seem to indicate that variations in experimental conditions, namely hydrodynamic flow and potential drift, significantly affect DREP's calculations. One such variation may be the WE surface area. The vertical translator could not be used with the RCE possibly causing less accurate surface area measurements. The RCE is bulky with many different components and the precise placement of the RCE was difficult. A stand specific for RCE should be constructed to ensure more precise placement of the WE in the salt. The use of a furnace well would also ease the process of position the RCE.

Other experimental variations are also possible. The experimental setup described in Section 3.5.6 takes no measures to ensure that the reference electrode (RE) and CE do not disrupt the flow of the electrolyte. Thus, variations in the placement of the RE and CE could have caused different flow profiles in each mixture. For example, if the CE was placed closer to the WE in one mixture, then the flow disruptions caused by CE would affect the diffusion layer more acutely than in other mixtures. This may be the cause for the wide variation in limiting currents and, consequently, diffusion layer thickness.

In the aqueous study of the RCE (137), special measures were taken to ensure that RE and counter electrode (CE) did not disrupt the flow in the cell. The WE and CE were concentric cylinders and the CE was the outer cylinder. The RE was placed outside of the cell and connected using a liquid junction. This could be similarly accomplished in a molten salt cell by centering the WE in a conductive crucible, such as glassy carbon or steel. The conductive crucible would serve as the CE. A quartz disc with shallow cylindrical recess in the center would be placed in the bottom to accurately center the WE and electrically isolate it from the CE, as shown in Figure 8.11. An external RE may not be feasible, but its effect could be minimized by only slightly immersing it in the molten salt next to the WE.

The ability of DREP to more closely simulate the actual behavior of the  $U^{3+}$  and  $Mg^{2+}$  ions is demonstrated in Figure 8.12 in which the diffusion layer thickness (0.008 mm for U and 0.012 mm for Mg) and the standard apparent potential values (-1.43 V for U and -1.72 V for Mg) specific to mixture RCE2 were used in (8.2). Aside from the transient regions of the HD-LSV, the predicted current is very close to the actual. DREP can be adjusted to account for transient behavior by using a time-dependent diffusion layer thickness, such as in the Cottrell equation

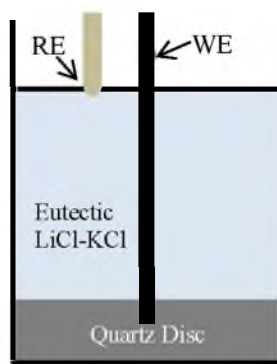


Figure 8.11 Proposed setup for more consistent RCE measurements

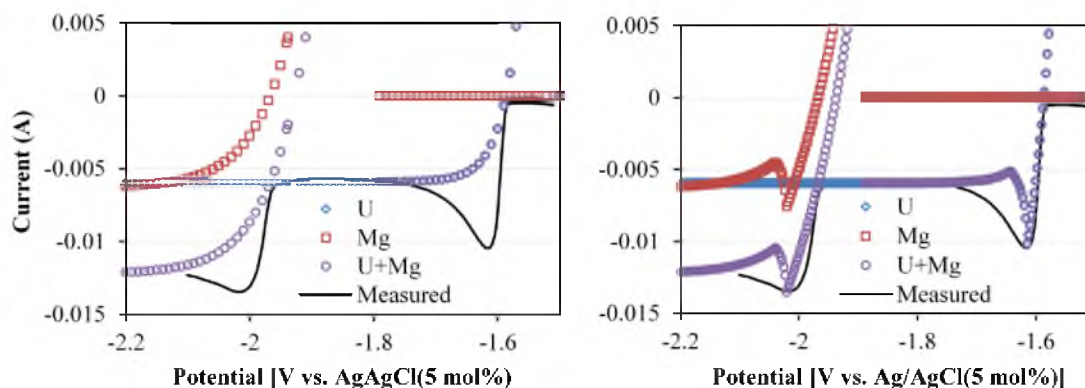


Figure 8.12 DREP simulated HD-LSV using static (left) and transient (right) diffusion layer thickness at 20 mV/s and 250 RPM in mixture RCE2

$$\delta = \sqrt{D\pi t} \quad (8.10)$$

This form of the diffusion layer thickness was used in Figure 8.12 by assuming that diffusion layer does not begin to grow until the peak potential is reached and the concentration profile is linear. The simulated peak is narrower, but equal in height, when compared to measured HD-LSV data. The incorporation of transient diffusion layer thickness could possibly allow DREP to be extended to higher concentrations where convection accelerates deposition and WE area growth occurs too rapidly.

Another noteworthy feature of Figure 8.12 is the oxidation current. Although not visible in the figure, it rises steeply to an unlimited value. The positive end of the y-axis was limited in the figure so that reduction currents could be clearly seen. There is no limit on the oxidation current in DREP. This permitted large negative concentrations of  $\text{Mg}^{2+}$  which in turn caused the large positive concentration and deposition rates of  $\text{U}^{3+}$ . To improve the model and prevent unrealistic solutions, a mechanism needs to be built into the model to account for limitations on the oxidizing metal, such as depletion and diffusion.

## 8.5. Conclusions

The use of an RCE was developed and implemented at high temperature (773 K) in the LiCl-KCl-UCl<sub>3</sub>-MgCl<sub>2</sub>. Electrochemical kinetic parameters were also determined for the first time for Mg<sup>2+</sup> ions. The initial application of DREP to experimental data yielded promising results. The ability of DREP to determine concentrations is dependent on potential and diffusion layer thickness which shifted and varied between mixtures. This occasionally caused large errors in the concentration which propagated through to the deposition rates. When ICP-MS measured concentrations were used in DREP the deposition rates for each mixture with a few exceptions were very accurate. Hence, the use of the current version of DREP is not recommended for concentration measurements, rather an electroanalytical technique such as CV or NPV should be used to measure concentrations and then DREP could predict the deposition rates. Improvement in both experimental setup and model structure are also recommended. An electrochemical cell setup was proposed to improve hydrodynamic measurements in high-temperature molten salts. Limitations on the oxidation current need to be incorporated into the model.

## 9. CONCLUSIONS AND FUTURE WORK

### 9.1. Conclusions

The Nuclear Pyrometallurgy Laboratory (NPL) has been setup to enable, among other things, electrochemical measurements of binary-analyte mixtures in eutectic LiCl-KCl. A large amount of electrochemical measurements have been made on binary-analyte mixtures at many different concentrations. In addition to electrochemical measurements, computer simulations of binary-analyte mixtures were also performed. The binary-analyte mixtures studied covered a range of standard apparent reduction potential spacing from 51 to 560 mV. In every case, the signals (current or potential) were able to be related to concentration. This was often done by fitting current electrochemical models, such as the Nernst and Berzins-Delahay equations, to the appropriate signal. However, when the spacing was very close, principal component regression (PCR) enabled the concentration to be accurately determined because signal separation was not necessary. On experimental data, a method to separate cyclic voltammetry (CV) peaks separated as little as 60 mV was developed for soluble-insoluble reduction to enable concentration correlations. Normal pulse voltammetry (NPV) and CV yielded the most accurate concentration measurements. Open-circuit potentiometry has many challenges, such as reference potential drift, that need to be resolved before it can be effectively implemented to measure concentrations in an electrorefiner (ER). Most important, the presence of multiple deposited metals on the working electrode (WE) does

not allow true open-circuit potentials to be measured for the more active ions.

Other significant contributions were made in addition to the development of concentration measurements on binary-analyte mixtures. One was the establishment of  $\text{MgCl}_2$  as an electrochemical surrogate for  $\text{PuCl}_3$  enabling experimental and analytical methods to be tested with a cheaper and more readily available chemical. Another was the development of the rotating cylinder electrode (RCE) for high-temperature molten salts which facilitated hydrodynamic electrochemistry measurements in eutectic  $\text{LiCl-KCl}$  and the validation of a method, DREP, to determine deposition rates in an electrorefiner (ER). However, these advancements have also revealed important challenges and issues confronting the application of electrochemical measurements in molten salts.

## 9.2. Future Work

First and foremost, the WE surface area measurements still contain a high level of uncertainty, even with the use of the vertical translator. This is in part due to an insufficient amount of CV peak height measurements at various immersion depths. To demonstrate the possible accuracy of electrochemical methods in measuring concentrations, the normalized CV peak heights of uranium and magnesium is plotted for mixtures P1-P4 for uranium and S4-S7 for magnesium are plotted in Figure 9.1. These CVs were all measured without disturbing the WE between analyte additions. Thus, WE surface area was as close to same at each concentration as possible. This results in a strong correlation between peak height and concentration. The average relative error of the concentrations measured using only the data in Figure 9.1 is 3.5% and 4.5% for uranium and magnesium, respectively, and as low as 1% for both. Similar results are



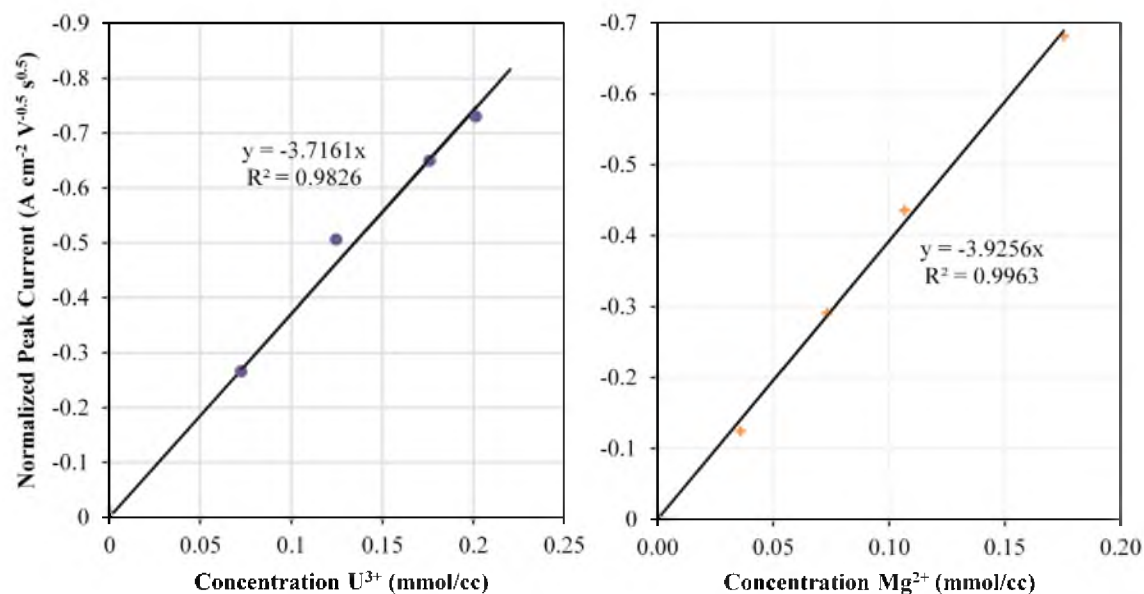


Figure 9.1 CV peak currents measured without disturbing WE between analyte additions in mixture P1-P4 for uranium (left) and mixtures S4-S7 for magnesium (right)

achieved in these mixtures for NPV as well. This shows the great improvement that can be made by more accurately measuring the WE surface area. However, in order to realize this improvement, significant strides in the reproducibility of WE surface and immersion depth need to be made.

In addition to current measurements, the potential of cell or an electrode can provide valuable data to determine concentration. However, the accuracy of potential in determining concentration was hampered by reference electrode (RE) drift and inconsistent AgCl concentration across all REs used. Despite the best efforts to accurately and precisely weigh out the same amount of AgCl and eutectic LiCl-KCl for each RE, the reference potential between each RE varied slightly. Even if REs could be consistently constructed, the vaporization and condensation of eutectic LiCl-KCl on the RE wall and the deposition of Ag<sup>+</sup> ions on the silver wire shift the reference potential over time. This drift can be accelerated when high currents are inadvertently charged

through the cell. Efforts were made to adjust for the shift in potential, but in all probability, the adjustment may have over or undercorrected the potential.

A truly stable and repeatable RE is required in order to use the valuable additional information that potential measurements provide. For this cause, a 100 mol% Ag/AgCl RE was constructed and tested to demonstrate its feasibility. One of the multiple CVs recorded using a 100 mol% AgCl RE is displayed in Figure 9.2. There appear to be no ill effects in the CV due to the use of 100 mol% AgCl. The uranium and magnesium peaks take on the same shape and height as those from mixture Q3 which used 5 mol% AgCl in RE. However, the lower temperature limit for the 100 mol% AgCl RE is set by the melting point of AgCl (455°C), but used nuclear fuel (UNF) ERs usually operate at 500°C.

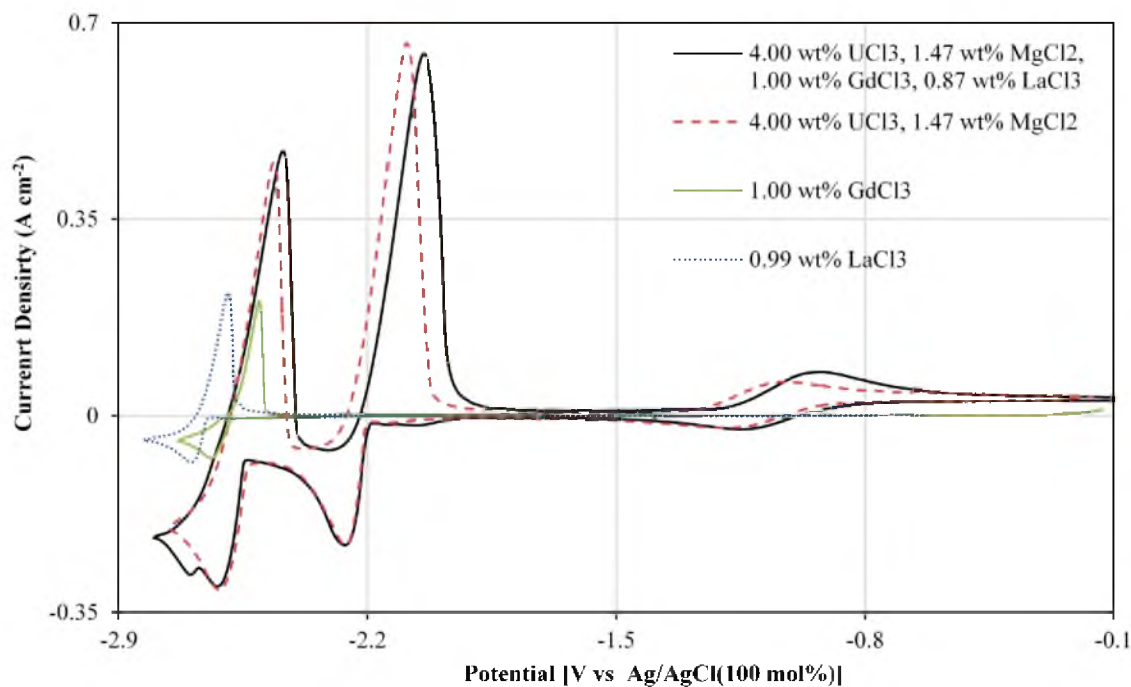


Figure 9.2 CV at 100 mV/s (Area =0.74 cm<sup>2</sup>) of a mixture (ID=MIX in Appendix A) containing four analytes with overlays of CVs from mixtures C1 (blue dashed), OCP-Gd (green), and Q3 (red dashed)

The introduction of Figure 9.2 also highlights another challenge: the interference of fission products (FP) and transuranics in a UNF ER. This black curve in Figure 9.2 is for a quaternary-analyte mixture containing uranium, magnesium (surrogate for plutonium), and two FP (lanthanum and gadolinium). Fortunately, the uranium and magnesium peaks are unaffected, unless the presence of gadolinium inflates magnesium's reduction peak. However, gadolinium's peaks are not discernable, even after semi-differentiation. Lanthanum's reduction peak appears to rise up through the magnesium tail possibly aided by the tail of gadolinium's reduction peak. The concentration of  $\text{MgCl}_2$  is quite high in this mixture and peaks may be more discernable at lower  $\text{MgCl}_2$  contents. It should also be noted that concentration values in Figure 9.2 are based on the amount of salt weighed out because ICP measurements are yet to be made on the quaternary-analyte salt mixture.

The CV measurement in Figure 9.2 highlights the importance of establishing PCR as a viable analytical method. Imagine separating all four of those peaks and then adding in a few more peaks. If the baseline for all of these peaks cannot be established, then peak heights will not yield accurate concentration measurements. PCR removes the need to find each peak. The challenge facing PCR is whether the variance of conditions unrelated to concentration (e.g., temperature, area, etc.) can be accurately accounted for or tightly controlled.

The application of electrochemical techniques to an actual ER for process monitoring, nuclear material accountancy, and safeguards will most likely involve the use of multiple techniques. Ideally, an algorithm would be developed for each ion of interest similar to the one proposed in Figure 9.3. CV has broad application and provides a

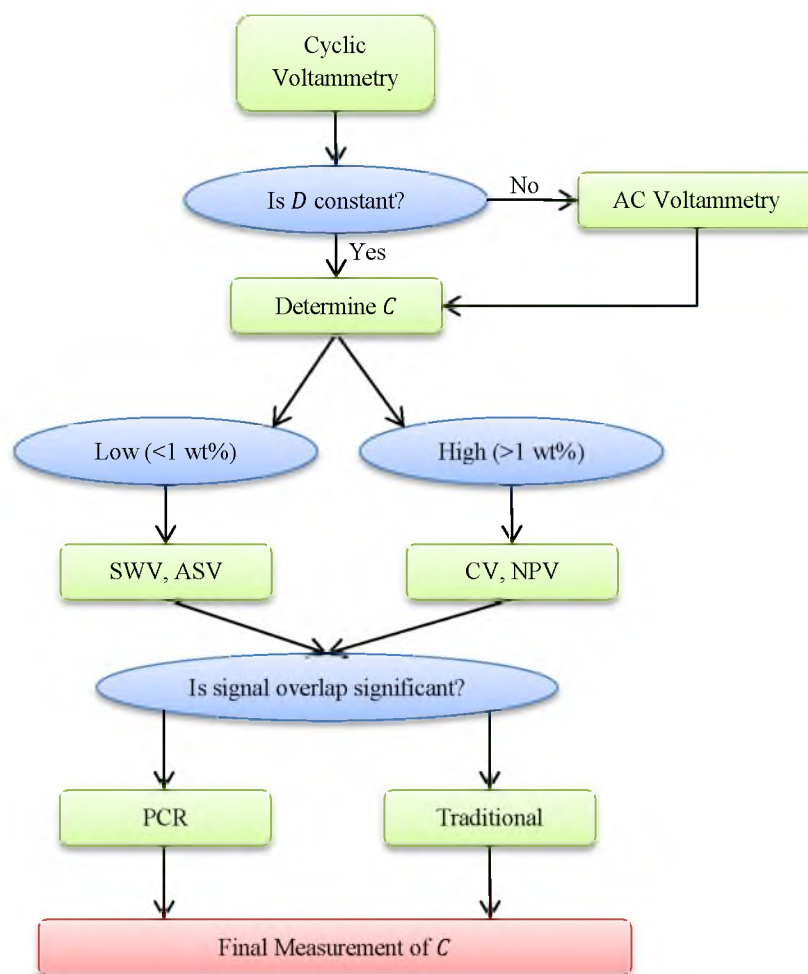


Figure 9.3 Voltammetry decision tree

general idea of the behavior of the ions in the system. From the trend of CV peak heights with concentration, the assumption of a constant diffusion coefficient can be validated or disproven. If disproven, then an alternating current (AC) technique could be used to determine the diffusion coefficient separately, such as AC voltammetry. Alternatively, OCP could be used to determine concentration, if a stable RE is developed. If the diffusion coefficient is constant, then the concentration can be measured directly. If the measured concentration is low, then a more sensitive technique could be used to obtain a more accurate measurement. On the other hand, if the concentration is high, a different

set of techniques could be used to measure the concentration. Lastly, if the recorded signals overlap significantly, then PCR could be used to determine the concentration. Otherwise, traditional methods such as peak heights could be used to measure the concentration. In such manner, the use of voltammetry to measure concentrations could be optimized so that the most accurate measurements are made based on the ER conditions.

Clearly, further development is still needed, but the use of electrochemical signals in measuring metal ion concentrations in binary-analyte mixtures has shown great promise throughout this work and in other studies. The improvement of electrochemical measurements is dependent upon the successful development of a stable RE and accurate methods of measuring WE surface area. With progress already being made on both of those fronts, it seems very likely that electrochemical measurements will be a valuable tool for process monitoring, nuclear material accountancy, and international safeguards.

## APPENDIX A

### EXPERIMENTAL DETAILS

The following tables (Tables A.1-A.10) detail the experimental setup and observations for each experimental matrix presented in Chapter 3 of the dissertation (see Table 3.3, 3.4, and 3.5). Reading the descriptions of the electrochemical cells in Section 3.3 will lend greater clarity to the following tables. Note that stainless steel, alumina tubes, vertical translator, and eutectic LiCl-KCl are abbreviated by SS, ALT, VT, and LiCl-KCl, respectively, in the tables.

Table A.1 Experimental setup details for GdCl<sub>3</sub>-LaCl<sub>3</sub>-LiCl-KCl mixtures

Mixture ID	Date	Furnace Plug	CE	WE	RE
A1	6/17/2014	alumina	Gd Rod in SS basket	1 mm Mo wire	1 wt% AgCl in Pyrex
A2	6/25/2014	alumina	Gd Rod in SS basket	1 mm Mo wire	1 wt% AgCl in Pyrex
A3	7/8/2014	alumina	Gd Rod in SS basket	1 mm Mo wire	1 wt% AgCl in Pyrex
A4	7/10/2014	alumina	Gd Rod in SS basket	1 mm Mo wire	1 wt% AgCl in Pyrex
B1	6/23/2014	alumina	2mm W rod	1 mm Mo wire	1 wt% AgCl in Pyrex
B2	7/2/2014	alumina	Gd Rod in SS basket	1 mm Mo wire	1 wt% AgCl in Pyrex
B3	7/15/2014	alumina	Gd Rod in SS basket	1 mm Mo wire	1 wt% AgCl in Pyrex
B4	7/17/2014	alumina	Gd Rod in SS basket	1 mm Mo wire	1 wt% AgCl in Pyrex
C1	7/28/2014	alumina	Gd Rod in SS basket	1 mm Mo wire	1 wt% AgCl in Pyrex
C2	8/1/2014	alumina	Gd Rod in SS basket	1 mm Mo wire	1 wt% AgCl in Pyrex
D1	8/19/2014	alumina	Gd Rod in SS basket	1 mm Mo wire	1 wt% AgCl in Pyrex
D2	8/27/2014	alumina	Gd Rod in SS basket	1 mm Mo wire	1 wt% AgCl in Pyrex
D3	8/29/2014	alumina	Gd Rod in SS basket	1 mm Mo wire	1 wt% AgCl in Pyrex
D4	9/2/2014	alumina	Gd Rod in SS basket	1 mm Mo wire	1 wt% AgCl in Pyrex
D5	9/4/2014	alumina	Gd Rod in SS basket	1 mm Mo wire	1 wt% AgCl in Pyrex
D6	9/9/2014	alumina	Gd Rod in SS basket	1 mm Mo wire	1 wt% AgCl in Pyrex
D7	9/17/2014	alumina	Gd Rod in SS basket	1 mm Mo wire	1 wt% AgCl in Pyrex
OCP-Gd	11/17/2014	alumina	Gd Rod in SS basket	1 mm Mo wire	1 wt% AgCl in Pyrex
OCP-La	11/19/2014	alumina	2mm W rod	1 mm Mo wire	1 wt% AgCl in Pyrex
OCP-Gd2	1/20/2015	alumina	Gd Rod in SS basket	1 mm Mo wire	5 mol% AgCl in Pyrex
OCP-La2	1/22/2014	alumina	2mm W rod	1 mm Mo wire	5 mol% AgCl in Pyrex
OCP-Gd3	2/23/2015	alumina	Gd Rod in SS basket	1 mm Mo wire	1 wt% AgCl in Pyrex

Table A.2 Experimental setup details for ThCl<sub>4</sub>-LaCl<sub>3</sub>-LiCl-KCl mixtures

Mixture ID	Date	Furnace Plug	CE	WE	RE
L1	1/13/2015	alumina	2 mm W rod	2 mm W rod	5 mol% AgCl in Pyrex
L2	1/14/2015	alumina	2 mm W rod	2 mm W rod	5 mol% AgCl in Pyrex
L3	1/15/2015	alumina	2 mm W rod	2 mm W rod	5 mol% AgCl in Pyrex
L4	1/15/2015	alumina	2 mm W rod	2 mm W rod	5 mol% AgCl in Pyrex
T1	12/11/2014	alumina	Th metal in SS basket	2 mm W rod	1 wt% AgCl in Pyrex
U1	3/24/2015	alumina	Th metal in SS basket	2 mm W rod	5 mol% AgCl in Pyrex
U2	3/26/2015	alumina	Th metal in SS basket	2 mm W rod	5 mol% AgCl in Pyrex
U3	3/26/2015	alumina	Th metal in SS basket	2 mm W rod	5 mol% AgCl in Pyrex
U4	4/1/2015	alumina	Th metal in SS basket	2 mm W rod	5 mol% AgCl in Pyrex
U5	4/2/2015	alumina	Th metal in SS basket	2 mm W rod	5 mol% AgCl in Pyrex
U6	5/4/2015	alumina	Th metal in SS basket	2 mm W rod	5 mol% AgCl in Pyrex
U7	5/5/2015	alumina	Th metal in SS basket	2 mm W rod	5 mol% AgCl in Pyrex
U8	5/19/2015	alumina	Th metal in SS basket	2 mm W rod	5 mol% AgCl in Pyrex
U9	5/29/2015	alumina	Th metal in SS basket	2 mm W rod	5 mol% AgCl in Pyrex
V1	6/17/2015	alumina	Th metal in SS basket	2 mm W rod	5 mol% AgCl in Pyrex
V2	6/18/2015	alumina	Th metal in SS basket	2 mm W rod	5 mol% AgCl in Pyrex
V3	6/18/2015	alumina	Th metal in SS basket	2 mm W rod	5 mol% AgCl in Pyrex
W1	6/26/2015	alumina	Th metal in SS basket	2 mm W rod	5 mol% AgCl in Pyrex
W2	6/26/2015	alumina	Th metal in SS basket	2 mm W rod	5 mol% AgCl in Pyrex
W3	6/26/2015	alumina	Th metal in SS basket	2 mm W rod	5 mol% AgCl in Pyrex
W4	6/27/2015	alumina	Th metal in SS basket	2 mm W rod	5 mol% AgCl in Pyrex
W5	6/27/2015	alumina	Th metal in SS basket	2 mm W rod	5 mol% AgCl in Pyrex
W6	6/27/2015	alumina	Th metal in SS basket	2 mm W rod	5 mol% AgCl in Pyrex
W7	6/27/2015	alumina	Th metal in SS basket	2 mm W rod	5 mol% AgCl in Pyrex



Table A.3 Experimental setup details for mixtures for U/Mg pairing in eutectic LiCl-KCl

Mixture ID	Date	Furnace Plug	CE	WE	RE
M1	7/29/2014	alumina	Mg Rod in SS basket	1 mm Mo wire	1 wt% AgCl in Pyrex
N1	3/4/2015	SS w/ALT	U metal in SS basket	2 mm W rod	5 mol% AgCl in Pyrex
N2	3/4/2015	SS w/ALT	U metal in SS basket	2 mm W rod	5 mol% AgCl in Pyrex
O1	5/6/2015	SS w/ALT	U metal in SS basket	2 mm W rod	5 mol% AgCl in Mullite (M-1)
O2	5/6/2015	SS w/ALT	U metal in SS basket	2 mm W rod	5 mol% AgCl in Mullite (M-1)
O3	5/6/2015	SS w/ALT	U metal in SS basket	2 mm W rod	5 mol% AgCl in Mullite (M-1)
O4	5/6/2015	SS w/ALT	U metal in SS basket	2 mm W rod	5 mol% AgCl in Mullite (M-1)
O5	5/6/2015	SS w/ALT	U metal in SS basket	2 mm W rod	5 mol% AgCl in Mullite (M-1)
O6	5/20/2015	SS w/ALT	U metal in SS basket	2 mm W rod	5 mol% AgCl in Mullite (M-1)
P1	5/27/2015	SS w/ALT	U metal in SS basket	2 mm W rod	5 mol% AgCl in Mullite (M-2)
P2	5/27/2015	SS w/ALT	U metal in SS basket	2 mm W rod	5 mol% AgCl in Mullite (M-2)
P3	5/27/2015	SS w/ALT	U metal in SS basket	2 mm W rod	5 mol% AgCl in Mullite (M-2)
P4	5/27/2015	SS w/ALT	U metal in SS basket	2 mm W rod	5 mol% AgCl in Mullite (M-2)
P5	6/30/2015	SS w/ALT	U metal in SS basket	2 mm W rod	5 mol% AgCl in Mullite (M-2)
P6	6/30/2015	SS w/ALT	U metal in SS basket	2 mm W rod	5 mol% AgCl in Mullite (M-2)
P7	6/30/2015	SS w/ALT	U metal in SS basket	2 mm W rod	5 mol% AgCl in Mullite (M-2)
P8	6/30/2015	SS w/ALT	U metal in SS basket	2 mm W rod	5 mol% AgCl in Mullite (M-2)
Q1	7/9/2015	SS w/ALT	U metal in SS basket	2 mm W rod	5 mol% AgCl in Mullite (M-1)
Q2	7/9/2015	SS w/ALT	U metal in SS basket	2 mm W rod	5 mol% AgCl in Mullite (M-1)
Q3	7/9/2015	SS w/ALT	U metal in SS basket	2 mm W rod	5 mol% AgCl in Mullite (M-1)
R1	8/19/2015	SS w/ALT	U metal in SS basket	2 mm W rod	5 mol% AgCl in Mullite (M-1)
R2	8/19/2015	SS w/ALT	U metal in SS basket	2 mm W rod	5 mol% AgCl in Mullite (M-1)
R3	8/19/2015	SS w/ALT	U metal in SS basket	2 mm W rod	5 mol% AgCl in Mullite (M-1)
R4	8/19/2015	SS w/ALT	U metal in SS basket	2 mm W rod	5 mol% AgCl in Mullite (M-1)
RCE1	9/3/2015	SS w/ALT	U metal in SS basket	2 mm W rod	5 mol% AgCl in Mullite (M-1)
RCE2	9/14/2015	SS w/ALT	U metal in SS basket	2 mm W rod	5 mol% AgCl in Mullite (M-3)
RCE3	9/16/2015	SS w/ALT	U metal in SS basket	2 mm W rod	5 mol% AgCl in Mullite (M-3)
RCE4	9/17/2015	SS w/ALT	U metal in SS basket	2 mm W rod	5 mol% AgCl in Mullite (M-3)
MIX	9/18/2015	SS w/ALT	Coiled 0.5 W wire	2 mm W rod	100 wt% AgCl in Pyrex
S1	10/1/2015	SS w/ALT	U metal in SS basket	2 mm W rod	5 mol% AgCl in Mullite (M-3)
S2	10/2/2015	SS w/ALT	U metal in SS basket	2 mm W rod	5 mol% AgCl in Mullite (M-2)
S3	10/2/2015	SS w/ALT	U metal in SS basket	2 mm W rod	5 mol% AgCl in Mullite (M-2)
S4	10/2/2015	SS w/ALT	U metal in SS basket	2 mm W rod	5 mol% AgCl in Mullite (M-2)
S5	10/2/2015	SS w/ALT	U metal in SS basket	2 mm W rod	5 mol% AgCl in Mullite (M-2)
S6	10/2/2015	SS w/ALT	U metal in SS basket	2 mm W rod	5 mol% AgCl in Mullite (M-2)
S7	10/2/2015	SS w/ALT	U metal in SS basket	2 mm W rod	5 mol% AgCl in Mullite (M-2)
S8	10/8/2015	SS w/ALT	U metal in SS basket	2 mm W rod	5 mol% AgCl in Mullite (M-2)

Table A.4 Key experimental observations for GdCl<sub>3</sub>-LaCl<sub>3</sub>-LiCl-KCl mixtures

Mixture ID	Salts	Amount (g)	WE Depth (mm)	Method	Notes
A1	GdCl <sub>3</sub> LaCl <sub>3</sub> LiCl-KCl	0.88 0.58 56.84	17	Dip	No Anodic Cleaning of WE
A2	Add to A1 GdCl <sub>3</sub> LaCl <sub>3</sub>	0.89 0.01	9	Dip	
A3	Add to A2 GdCl <sub>3</sub> LaCl <sub>3</sub>	0.02 0.59	17	Dip	
A4	Add to A3 GdCl <sub>3</sub> LaCl <sub>3</sub>	0.02 0.59	17	Dip	
B1	LaCl <sub>3</sub> LiCl-KCl	0.58 57.72	11	Dip	No Anodic Cleaning of WE
B2	Add to B1 GdCl <sub>3</sub> LaCl <sub>3</sub>	1.00 0.01	14	Dip	
B3	Add to B2 LaCl <sub>3</sub> LiCl-KCl	0.73 7.00	10	Dip	
B4	Add to B3 GdCl <sub>3</sub> LaCl <sub>3</sub>	0.01 0.72	16	Dip	
C1	LaCl <sub>3</sub> LiCl-KCl	0.58 57.72	13	Dip	
C2	Add to C1 GdCl <sub>3</sub> LaCl <sub>3</sub>	0.88 0.01	N/A	None	Mg Contamination and broken RE
D1	GdCl <sub>3</sub> LaCl <sub>3</sub> LiCl-KCl	0.91 0.58 56.85	9	Dip	
D2	Add to D1 GdCl <sub>3</sub>	0.11	12	Dip	
D3	Add to D2 GdCl <sub>3</sub> LaCl <sub>3</sub>	0.78 0.01	14	Dip	
D4	Add to D3 GdCl <sub>3</sub> LaCl <sub>3</sub>	0.92 0.01	9	Dip	
D5	Add to D4 LaCl <sub>3</sub>	0.59	11	Dip	
D6	Add to D5 GdCl <sub>3</sub> LaCl <sub>3</sub>	0.04 0.61	11	Dip	
D7	Add to D6 LiCl-KCl	12.03	18	Dip	
OCP-Gd	GdCl <sub>3</sub> LiCl-KCl	0.50 49.50	9.5	Dip	
OCP-La	LaCl <sub>3</sub> LiCl-KCl	0.49 49.60	Unkown	Dip	Area not measured
OCP-Gd2	Repeat test of OCP-Gd	No salt added	4	Dip	5 mol% AgCl in RE
OCP-La2	Repeat test of OCP-La	No salt added	9	Dip	5 mol% AgCl in RE

Table A.4 Continued

Mixture ID	Salts	Amount (g)	WE Depth (mm)	Method	Notes
OCP-Gd3	Add to OCP-Gd2 GdCl <sub>3</sub>	0.37	4	Dip	

Table A.5 Key experimental observations for ThCl<sub>4</sub>-LaCl<sub>3</sub>-LiCl-KCl mixtures

Mixture ID	Salts	Amount (g)	WE Depth (mm)	Method	Notes
L1	LaCl <sub>3</sub> LiCl-KCl	0.56 55.00	8	Dip	
L2	Add to L1 LaCl <sub>3</sub> LiCl-KCl	0.89 3.40	8	Dip	
L3	Add to L2 LaCl <sub>3</sub> LiCl-KCl	1.55 2.50	12	Dip	
L4	Add to L3 LaCl <sub>3</sub> LiCl-KCl	1.64 1.40	8	Dip	
T1	ThCl <sub>4</sub> LiCl-KCl	0.28 58.34	16	Dip	
U1	LaCl <sub>3</sub> ThCl <sub>4</sub> LiCl-KCl	0.59 0.37 54.72	7	Dip	
U2	Add to U1 LaCl <sub>3</sub>	0.53	7	Dip	
U3	Add to U2 LaCl <sub>3</sub>	0.55	6	Dip	
U4	Add to U3 LaCl <sub>3</sub> ThCl <sub>4</sub> LiCl-KCl	0.55 0.04 0.46	6	Dip	
U5	Add to U4 LaCl <sub>3</sub>	0.55	6	Dip	
U6	Add to U5 LaCl <sub>3</sub> ThCl <sub>4</sub> LiCl-KCl	0.47 0.19 4.87	6	Dip	
U7	Add to U6 LaCl <sub>3</sub> ThCl <sub>4</sub> LiCl-KCl	0.20 0.31 3.91	5	Dip	
U8	Add to U7 LaCl <sub>3</sub> ThCl <sub>4</sub> LiCl-KCl	0.25 0.35 4.38	5	Dip	
U9	Add to U8 LaCl <sub>3</sub> ThCl <sub>4</sub> LiCl-KCl	0.30 0.40 5.00	5	Dip	
V1	LaCl <sub>3</sub> ThCl <sub>4</sub> LiCl-KCl	0.56 0.51 56.43	6	Dip	

Table A.5 Continued

Mixture ID	Salts	Amount (g)	WE Depth (mm)	Method	Notes
V2	Add to V1		7	Dip	
	LaCl <sub>3</sub>	0.03			
	ThCl <sub>4</sub>	0.22			
	LiCl-KCl	2.76			
V3	Add to V2		5	Dip	
	LaCl <sub>3</sub>	0.04			
	ThCl <sub>4</sub>	0.24			
	LiCl-KCl	3.22			
W1	LaCl <sub>3</sub>	0.59	5	Dip	
	ThCl <sub>4</sub>	1.52			
	LiCl-KCl	56.07			
W2	Add to W1		4.5	Dip	
	LaCl <sub>3</sub>	0.59			
	ThCl <sub>4</sub>	0.03			
	LiCl-KCl	0.27			
W3	Add to W2		4.5	Dip	
	LaCl <sub>3</sub>	0.61			
	ThCl <sub>4</sub>	0.05			
	LiCl-KCl	0.40			
W4	Add to W3		5	Dip	
	LaCl <sub>3</sub>	0.60			
	ThCl <sub>4</sub>	0.04			
	LiCl-KCl	0.35			
W5	Add to W4		5	Dip	
	LaCl <sub>3</sub>	0.44			
	LiCl-KCl	10.56			
W6	Add to W5		5	Dip	
	LiCl-KCl	14.00			
W7	Add to W6		3.5	Dip	
	LiCl-KCl	18.00			

Table A.6 Key experimental observations for UCl<sub>3</sub>-MgCl<sub>2</sub>-LiCl-KCl mixtures

Mixture ID	Salts	Amount (g)	WE Depth (mm)	Method	Notes
M1	MgCl <sub>2</sub>	0.69	13	Dip	
	LiCl-KCl	57.61			
N1	UCl <sub>3</sub>	0.51	11.63	VT	CVs cut short
	LiCl-KCl	49.53	11.40	Dip	
N2	Add to N1		11.63	VT	RE broke
	MgCl <sub>2</sub>	0.19			
O1	UCl <sub>3</sub>	0.50	12.37	VT	
	MgCl <sub>2</sub>	0.15	10.35	Dip	
	LiCl-KCl	49.35			
O2	Add to O1		12.37	VT	Temperature spike before test*
	MgCl <sub>2</sub>	0.16			
O3	Add to O2		12.37	VT	
	MgCl <sub>2</sub>	0.14			
O4	Add to O3		12.37	VT	
	MgCl <sub>2</sub>	0.15			
O5	Add to O4		12.37	VT	Temperature spike before test*
	MgCl <sub>2</sub>	0.15			
O6	Add to O5		N/A		Furnace ran away
	UCl <sub>3</sub>	0.50			

Table A.6 Continued

Mixture ID	Salts	Amount (g)	WE Depth (mm)	Method	Notes
P1	UCl <sub>3</sub>	0.99	12.46	VT	
	MgCl <sub>2</sub>	0.15	10.16	Dip	
	LiCl-KCl	48.84			
P2	Add to P1		12.46	VT	
	UCl <sub>3</sub>	0.67			
P3	Add to P2		12.46	VT	
	UCl <sub>3</sub>	0.49			
P4	Add to P3		12.46	VT	
	UCl <sub>3</sub>	0.54			
P5	Add to P4		11.15	VT	
	MgCl <sub>2</sub>	0.16	11.39	Dip	
P6	Add to P5		11.15	VT	
	MgCl <sub>2</sub>	0.16			
P7	Add to P6		11.15	VT	
	MgCl <sub>2</sub>	0.16			
P8	Add to P7		11.15	VT	
	MgCl <sub>2</sub>	0.16			
Q1	UCl <sub>3</sub>	1.02	12.70	VT	
	MgCl <sub>2</sub>	0.75	12.00	Dip	
	LiCl-KCl	48.26			
Q2	Add to Q1		12.70	VT	
	UCl <sub>3</sub>	0.48			
Q3	Add to Q2		12.70	VT	
	UCl <sub>3</sub>	0.53			
R1	MgCl <sub>2</sub>	0.15	9.71	VT	
	LiCl-KCl	49.85	11.00	Dip	
R2	Add to R1		13.17	VT	
	UCl <sub>3</sub>	1.16			
	MgCl <sub>2</sub>	0.16			
R3	Add to R2		13.17	VT	
	UCl <sub>3</sub>	0.51			
	MgCl <sub>2</sub>	0.15			
R4	Add to R3		11.14	VT	
	UCl <sub>3</sub>	0.99	9.96	Dip	
	MgCl <sub>2</sub>	0.15			
RCE1	UCl <sub>3</sub>	0.20	12.43	Dip	
	MgCl <sub>2</sub>	0.30			
	LiCl-KCl	49.52			
RCE2	UCl <sub>3</sub>	0.25	11.78	Dip	
	MgCl <sub>2</sub>	0.08			
	LiCl-KCl	49.69			
RCE3	Add to RCE2		11.80	Dip	
	UCl <sub>3</sub>	0.25			
	MgCl <sub>2</sub>	0.08			
RCE4	Add to RCE2		13.78	Dip	
	UCl <sub>3</sub>	0.25			
	MgCl <sub>2</sub>	0.15			
S1	UCl <sub>3</sub>	1.01	15.17	VT	
	MgCl <sub>2</sub>	0.15	14.75	Dip	
	LiCl-KCl	48.89			
S2	Add to S1		15.66	VT	
	UCl <sub>3</sub>	0.46	15.70	Dip	
S3	Add to S2		15.66	VT	
	UCl <sub>3</sub>	0.44			

Table A.6 Continued

Mixture ID	Salts	Amount (g)	WE Depth (mm)	Method	Notes
S4	Add to S3 UCl <sub>3</sub>	0.59	15.66	VT	
S5	Add to S4 MgCl <sub>2</sub>	0.18	15.66	VT	
S6	Add to S5 MgCl <sub>2</sub>	0.16	15.66	VT	
S7	Add to S6 MgCl <sub>2</sub>	0.29	15.66	VT	
S8	Add to S7 LiCl-KCl	10.99	14.82 14.82	VT Dip	

\*Temperature of salt allowed to settle to 500°C before testing

Table A.7 Concentrations of salt samples for the GdCl<sub>3</sub>-LaCl<sub>3</sub>-LiCl-KCl mixtures based on ICP-OES measurements and amounts weighed out on scales

Mixture ID	ICP-OES		Scale	
	GdCl <sub>3</sub>	LaCl <sub>3</sub>	GdCl <sub>3</sub>	LaCl <sub>3</sub>
A1	1.32%	0.78%	1.51%	0.99%
A2	2.57%	0.96%	3.00%	1.00%
A3	3.08%	1.49%	3.00%	1.99%
A4	3.19%	2.95%	2.99%	3.00%
B1	---	---	0.00%	0.99%
B2	1.53%	0.96%	1.70%	0.99%
B3	1.49%	1.52%	1.50%	1.99%
B4	1.65%	2.21%	1.54%	3.06%
C1	-0.01%	0.96%	0.00%	0.99%
C2	---	---	---	---
D1	1.53%	0.89%	1.49%	0.99%
D2	1.81%	0.97%	1.68%	0.99%
D3	2.84%	0.95%	3.00%	1.00%
D4	3.94%	0.92%	4.53%	1.00%
D5	4.49%	1.38%	4.48%	1.98%
D6	4.69%	2.45%	4.50%	3.00%
D7	3.64%	2.33%	3.73%	2.49%
OCP-Gd	1.10%	0.00%	1.00%	0.00%
OCP-La	0.00%	0.97%	0.00%	1.00%
OCP-Gd2	Repeat of OCP-Gd		Repeat of OCP-Gd	
OCP-La2	0.00%	0.85%	0.00%	1.00%
OCP-Gd3	1.72%	0.00%	1.74%	0.00%

Table A.8 Calculated concentrations of salt samples for Th/La pairing based on ICP-OES measurements and amounts weighed out on scales

Mixture ID	ICP-OES (wt%)		Scale (wt%)	
	ThCl <sub>4</sub>	LaCl <sub>3</sub>	ThCl <sub>4</sub>	LaCl <sub>3</sub>
L1	---	0.97%	---	1.01%
L2	---	2.68%	---	2.42%
L3	---	4.15%	---	4.69%
L4	---	6.38%	---	6.93%
T1	---	---	0.48%*	---
U1	0.69%	1.01%	0.66%	1.06%
U2	0.67%	1.83%	0.66%	1.99%
U3	0.68%	2.65%	0.65%	2.94%
U4	0.78%	3.73%	0.71%	3.84%
U5	0.73%	4.68%	0.70%	4.75%
U6	1.12%	5.43%	0.94%	5.07%
U7	1.60%	4.97%	1.33%	5.04%
U8	2.13%	4.75%	1.72%	5.03%
U9	2.86%	5.17%	2.10%	5.05%
V1	0.91%	0.94%	0.89%	0.97%
V2	1.37%	0.97%	1.21%	0.98%
V3	1.70%	1.22%	1.59%	0.98%
W1	2.55%	1.11%	2.61%	1.01%
W2	2.52%	1.99%	2.62%	2.00%
W3	2.55%	2.84%	2.66%	2.98%
W4	2.53%	3.77%	2.68%	3.91%
W5	0.96%	1.76%	2.27%	3.92%
W6	1.46%	2.69%	1.90%	3.29%
W7	2.07%	3.74%	1.58%	2.72%

\*Uncertain due to oxides, estimated to be 1/10<sup>th</sup> from CV peak height

Using the bulk salt weight fraction of  $\text{UCl}_3$  and  $\text{MgCl}_2$  in Table A.9, the calculation of deposited metal on a WE in Table A.10 is accomplished. The salt adhering to the WE was assumed to have same composition as the bulk salt (see Table A.9). The adhering salt was determined by using the measured amount of Li and K dissolved in 10 vol%  $\text{HNO}_3$  (trace metal grade) solution and the following equation:

$$m_{\text{salt}} = \frac{m_{\text{LiCl}} + m_{\text{KCl}}}{1 - w_{\text{MgCl}_2} - w_{\text{UCl}_3}}$$

where  $w$  is the weight fraction of the subscripted salt.

Table A.9 Calculated concentrations of salt samples for the U/Mg pairing based on ICP-MS measurements and amounts weighed out on scales

Mixture ID	ICP-MS (wt%)			Scale (wt%)	
	$\text{UCl}_3$	$\text{MgCl}_2$ (High)*	$\text{MgCl}_2$ (Low)*	$\text{UCl}_3$	$\text{MgCl}_2$
M1	0.00%	1.17%	---	0.00%	1.18%
N1	0.83%	0.38%	---	1.02%	0.00%
N2	0.83%	0.88%	---	1.02%	0.38%
O1	0.83%	0.59%	0.19%	1.00%	0.30%
O2	0.91%	0.72%	0.30%	1.00%	0.62%
O3	0.93%	0.81%	0.49%	0.99%	0.89%
O4	0.78%	1.11%	0.57%	0.99%	1.19%
O5	0.89%	1.81%	0.96%	0.99%	1.48%
O6	---	---	---	---	---
P1	1.53%	0.89%	---	1.98%	0.30%
P2	2.61%	0.69%	---	3.28%	0.30%
P3	3.65%	0.56%	---	4.20%	0.29%
P4	4.16%	0.51%	0.25%	5.21%	0.29%
P5	4.45%	1.11%	0.40%	5.19%	0.58%
P6	4.10%	1.20%	0.59%	5.18%	0.87%
P7	4.44%	1.45%	0.80%	5.16%	1.15%
P8	4.18%	1.68%	0.92%	5.15%	1.43%
Q1	2.08%	1.79%	---	2.04%	1.50%
Q2	2.61%	1.62%	---	2.97%	1.48%
Q3	3.24%	1.53%	---	3.98%	1.47%
R1	0.00%	0.67%	0.21%	0.00%	0.30%
R2	2.12%	0.99%	0.42%	2.00%	0.60%
R3	2.76%	1.05%	0.56%	3.00%	0.90%



Table A.9 Continued

Mixture ID	ICP-MS (wt%)			Scale (wt%)	
	UCl <sub>3</sub>	MgCl <sub>2</sub> (High)*	MgCl <sub>2</sub> (Low)*	UCl <sub>3</sub>	MgCl <sub>2</sub>
R4	3.47%	1.25%	0.66%	5.00%	1.20%
RCE1	0.51%	0.53%	---	0.40%	0.60%
RCE2	0.48%	0.44%	0.10%	0.53%	0.17%
RCE3	1.02%	0.53%	0.23%	1.06%	0.34%
RCE4	0.89%	0.74%	---	1.05%	0.65%
S1	2.11%	0.60%	---	2.02%	0.30%
S2	2.37%	0.66%	---	2.91%	0.30%
S3	3.65%	1.79%	---	3.75%	0.29%
S4	4.42%	2.32%	0.20%	4.85%	0.29%
S5	4.50%	0.77%	0.42%	4.83%	0.64%
S6	4.32%	1.11%	0.61%	4.82%	0.94%
S7	4.53%	1.71%	1.00%	4.79%	1.50%
S8	3.47%	1.53%	0.81%	3.96%	1.23%

\*High = High dilution, sample ppm close to detection limit for Mg; Low = Low dilution, more accurate

Table A.10 ICP-MS measured concentration of dissolved WE deposits in 10 vol% HNO<sub>3</sub> solution

Deposit ID	Concentration in 10 vol% HNO <sub>3</sub> Solution (mg/kg)				Solution Mass (g)
	Li	Mg	K	U	
RCE1	12.82	0.7605	52.91	10.7923	26.40
RCE2	17.93	0.3517	77.16	9.3123	27.08
RCE3	25.65	0.3646	110.9	35.6055	23.29
RCE4	34.46	3.7332	150.9	59.5829	28.02

Deposit ID	Masses (mg)				Adhering Salt (mg)
	LiCl	Mg	KCl	U	
RCE1	2.067	0.0201	2.664	0.2850	4.781
RCE2	2.967	0.0095	3.984	0.2522	6.991
RCE3	3.649	0.0085	4.925	0.8292	8.682
RCE4	5.898	0.1046	8.062	1.6697	14.19

Deposit ID	Metal in Salt (mg)		Metal Deposited (mg)		Total Deposited (mg)
	Mg	U	Mg	U	
RCE1	0.0065	0.0169	0.0136	0.2681	0.2817
RCE2	0.0018	0.0230	0.0077	0.2292	0.2370
RCE3	0.0050	0.0611	0.0035	0.7681	0.7716
RCE4	0.0268	0.0869	0.0778	1.5828	1.6606

## APPENDIX B

### DENSITY MEASUREMENTS

The density measurements of molten salt at 500°C at varying concentrations of  $\text{UCl}_3$  and  $\text{LaCl}_3$  have been made at NPL (143). The details of these measurements are being prepared for publication. They are only included here to demonstrate the accuracy of the additive volume model. The maximum error between the model and measurements in these plots is 1.5%.

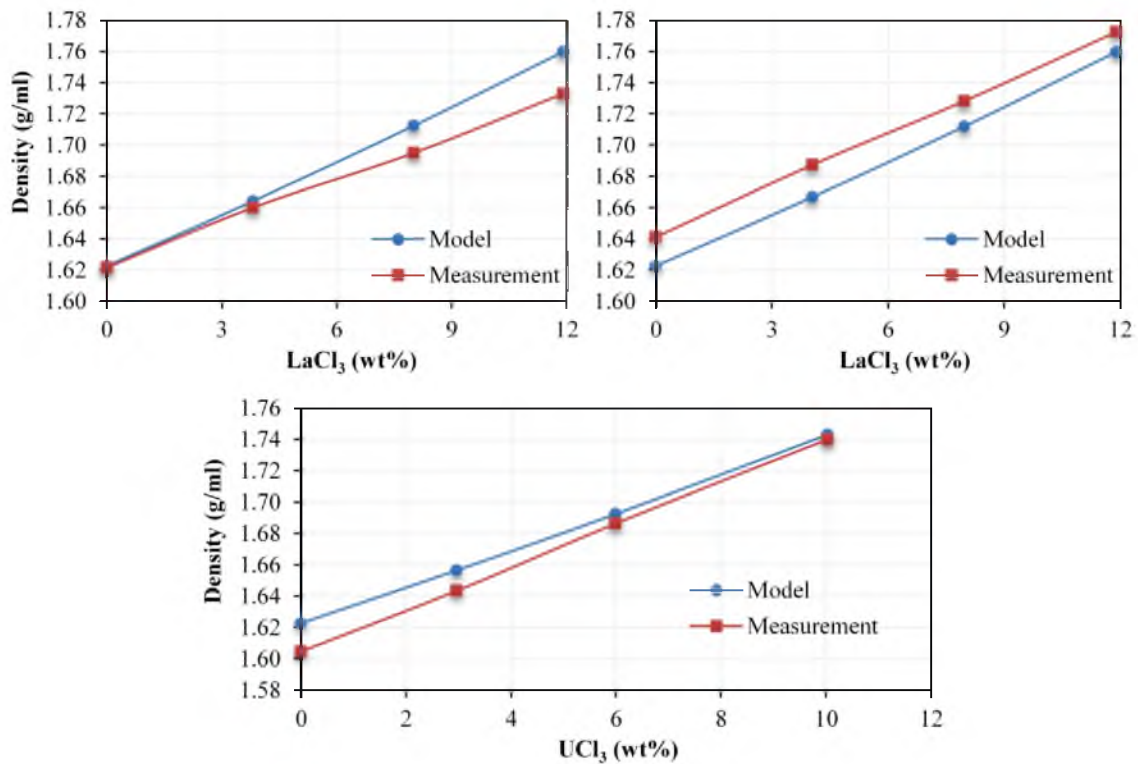


Figure B.1 Density measurements for  $\text{LaCl}_3$  test 1 (top left), test 2 (top right), and  $\text{UCl}_3$  (bottom) in eutectic  $\text{LiCl-KCl}$  at 500°C

## REFERENCES

1. Bishop, J. Engineers Take Different Path In Search for Safer Reactor. *The Wall Street Journal*, May 2, 1986, 23.
2. Till, C. E.; Chang, Y. I. *Plentiful Energy*; CreateSpace Independent Publishing Platform: North Charleston, 2011.
3. Stevenson, C. E. *The EBR-II Fuel Cycle Story*; American Nuclear Society: La Grange Park, 1987.
4. Westfall, C. Vision and Reality: The EBR-II Story. *Nuclear News*, February 2004, 25-32.
5. Simpson, M. F. *Development of Spent Nuclear Fuel Pyroprocessing Technology*; Idaho National Laboratory: Idaho Falls, ID, 2012.
6. Taylor, R., Ed. *Reprocessing and Recycling of Spent Nuclear Fuel*; Elsevier Ltd.: Cambridge, 2015.
7. Guoan, Y.; Hui, H.; Rushan, L.; Wenbin, Z. R&D Activities on Actinide Separation in China. *Procedia Chem.* **2012**, 7, 215-221.
8. Nagarajan, K.; Reddy, B. P.; Ghosh, S.; Ravisankar, G.; Mohandas, K. S.; Mudali, U. K.; Kutty, K.; Viswanathan, K.; Babu, C.; Kalyanasundaram, P.; Rao, P.; Raj, B. Development of Pyrochemical Reprocessing for Spent Metal Fuels. *Energy Procedia* **2011**, 7, 431-436.
9. *South Korea: International Energy Data and Analysis*; U.S. Energy Information Administration (EIA): Washington D.C., 2015.
10. Lee, H.; Park, G.-I.; Lee, J.-W.; Kang, K.-H.; Hur, J.-M.; Kim, J.-G.; Paek, S.; Kim, I.-T.; Cho, I.-J. Current Status of Pyroprocessing Development at KAERI. *Sci. Technol. Nucl. Install.* **2013**, 2013, 1-11.
11. Park, S. W. Why South Korea Needs Pyroprocessing. *Bulletin of the Atomic Scientists*, October 26, 2009.
12. Koyama, T.; Sakamura, Y.; Iizuka, M.; Kato, T.; Murakami, T.; Glatz, J.-P.

- Development of Pyro-processing Fuel Cycle Technology for Closing Actinide Cycle. *Procedia Chem.* **2012**, *7*, 772-778.
13. Inoue, T.; Koyama, T.; Arai, Y. State of the Art of Pyroprocessing in Japan. *Energy Procedia* **2011**, *7*, 405-415.
  14. *4th Strategic Energy Plan*; Ministry of Economy, Trade and Industry: Tokyo, 2014.
  15. Iizuka, M.; Koyama, T.; Sakamura, Y.; Uozumi, K.; Fujihata, K.; Kato, T.; Murakami, T.; Tsukada, T.; Glatz, J.-P. Development of Pyro-processing technology at CRIEPI for Carving out the Future of Nuclear Fuel Cycle. *Proc. GLOBAL 2013*, Salt Lake City, UT, Sept 29- Oct 3, 2013; American Nuclear Society: La Grange Park, IL, 2013.
  16. Beech, M. GE Hitachi and Iberdrola Sign MoU on Nuclear Project. *Utility Week*, July 21, 2014.
  17. Gray, J. Game Changer: PRISM Aims to Dethrone MOX. *Utility Week*, March 13, 2015, 22-23.
  18. International Atomic Energy Agency. Regular Budget Appropriations for 2015: GC(58)/22. *Proceedings of the 58th Regular Session of General Conference*, Vienna, Sept 25, 2014.
  19. Reaves, B. A.; Hickman, M. J. *Police Departments in Large Cities, 1990-2000*; Bureau of Justice Statistics, U.S. Department of Justice: Washington D.C., 2002.
  20. *Electrometallurgical Techniques for DOE Spent Nuclear Fuel: Final Report*; National Research Council, The National Academy Press: Washington DC, 2000.
  21. Ackerman, J. P.; Johnson, T. R.; Chow, L. S.; Carls, E. L.; Hannum, W. H.; Laidler, J. J. Treatment of Wastes in the IFR Fuel Cycle. *Prog. Nucl. Energy* **1997**, *31* (1/2), 141-154.
  22. Plambeck, J. A. Electromotive Force Series in Molten Salts. *J. Chem. Eng. Data* **1967**, *12* (1), 77-82.
  23. Adams, C. H.; Beitel, J. C.; Birgersson, G.; Bucher, R. G.; Derstine, K. L.; Toppel, B. J. The Mass Tracking System - Computerized Support for MC&A and Operations at FCF. *Proc. Am. Nucl. Soc. Top. Mtg on DOE Spent Nuclear Fuel and Fissile Material Management*, Reno, NV, June 16-20, 1996; American Nuclear Society: La Grange Park, IL, 1996.
  24. McKnight, R. D. ANL Computational Methodologies for Determining Spent Nuclear Fuel Source Term. *Proc. Am. Nucl. Soc. 4th Top. Mtg on DOE Spent Nuclear Fuel*

- and Fissile Material Management*, San Diego, CA, June 4-8, 2000; American Nuclear Society: La Grange Park, IL, 2000.
25. McKnight, R. D.; Krsul, J. R. Validation Results Based on the Spent Fuel Demonstration Program at FCF. *Proc. Am. Nucl. Soc. 4th Top. Mtg on DOE Spent Nuclear Fuel and Fissile Material Management*, San Diego, CA, 2000; American Nuclear Society: La Grange Park, IL, 2000.
  26. Vaden, D. Fuel Conditioning Facility Electrorefiner Process Model. *Sep. Sci. Technol.* **2006**, *41*, 2003-2012.
  27. *IAEA Safeguards Glossary - 2001 Edition*; International Atomic Energy Agency, IAEA: Vienna, 2002.
  28. Cipiti, B. B.; Duran, F. A.; Key, B.; Liu, Y.; Lozano, I.; Ward, R. *Modeling and Design of Integrated Safeguards and Security of an Electrochemical Reprocessing Facility*; SAND2012-9303; Sandia National Laboratories, U.S. Department of Energy: Albuquerque, 2012.
  29. Durst, P. C.; Ehinger, M. H.; Boyer, B.; Therios, I.; Bean, R.; Dougan, A.; Tolk, K. *Advanced Safeguards for New TRU Fuel Fabrication Facilities*; PNNL-17151; Pacific Northwest National Laboratory, U.S. Department of Energy: Richland, WA, 2007.
  30. Cook, M. T.; Jones, S. J.; Lux, J. E.; Baruzzini, M. L.; Skutnik, S. E.; Hall, H. L. Current and Future State of Pyrochemical Reprocessing for Spent Nuclear Fuel. *Proc. Inst. Nucl. Mater. Manage. 54th Ann. Meet.*, Palm Desert, CA, July 14-18, 2013; Institute of Nuclear Material Management: Oakbrook Terrace, IL, 2013.
  31. Bean, R. *Project Report on Development of a Safeguards Approach for Pyroprocessing*; INL/EXT-10-20057; Idaho National Laboratory: Idaho Falls, ID, 2010.
  32. Gonzalez, M.; Hansen, L.; Rappleye, D.; Cumberland, R.; Simpson, M. F. Application of a 1D Transient Electrorefiner Model to Predict Partitioning of Plutonium from Curium in a Pyrochemical Spent Fuel Treatment Process. *Nucl. Technol.* **2015**, *192* (2).
  33. Hanson, C.; Phongikaroon, S.; Scott, J. R. Temperature Effect on Laser-Induced Breakdown Spectroscopy Spectra of Molten and Solid Salts. *Spectrochim. Acta, Part B* **2014**, *97*, 76-85.
  34. Smith, N. A.; Savina, J. A.; Williamson, M. A. Application of Laser Induced Breakdown Spectroscopy to Electrochemical Process Monitoring of Molten Chloride Salts. *2014 Symposium on International Safeguards (IAEA-CN-220)*,

Vienna, Oct 20-24, 2014; International Atomic Energy Agency: Vienna, 2014

35. Gerts, D.; Paff, M.; Bean, R. Nuclear Material Accountability Applications of a Continuous Energy and Direction Gamma Ray Detector. *Proc. Inst. Nucl. Mater. Manage. 51st Annu. Meet.*, Baltimore, July 11-15, 2010; Institute of Nuclear Material Management: Oakbrook Terrace, IL, 2010.
36. Wigeland, R.; Bjornard, T.; Castle, B. *The Concept of Goals-Driven Safeguards*; INL/EXT-09-15511; Idaho National Laboratory: Idaho Falls, ID, 2009.
37. Simpson, M. F.; Rappleye, D.; Blandford, E. D.; Garcia, H. Signature Based Safeguards Alternative to Nuclear Material Accountancy. *Proc. Inst. Nucl. Mater. Manage. 55th Ann. Meet.*, Atlanta, GA, July 20-24, 2014; Institute of Nuclear Material Management: Oakbrook Terrace, IL, 2014.
38. Kim, D.-H.; Bae, S.-E.; Park, T.-H.; Kim, J.-Y.; Lee, C.-W.; Song, K. Real-time monitoring of metal ion concentration in LiCl–KCl melt using electrochemical techniques. *Microchem. J.* **2014**, *114*, 261-265.
39. Hoover, R. O.; Shaltry, M. R.; Martin, S.; Sridharan, K.; Phongikaroon, S. Electrochemical Studies and Analysis of 1-10 wt% UCl<sub>3</sub> Concentrations in Molten LiCl-KCl Eutectic. *J. Nucl. Mater.* **2014**, *452* (1-3), 389-396.
40. Iizuka, M.; Inoue, T.; Shirai, O.; Iwai, T.; Arai, Y. Application of Normal Pulse Voltammetry to On-line Monitoring of Actinide Concentrations in Molten Salt Electrolyte. *J. Nucl. Mater.* **2001**, *297*, 43-51.
41. Zhang, J. Electrochemistry of Actinides and Fission Products in Molten Salts--Data Review. *J. Nucl. Mater.* **2014**, *447*, 271-284.
42. Li, S. X.; Simpson, M. F. Anodic Process of Electrorefining Spent Driver Fuel in Molten LiCl-KCl-UCl<sub>3</sub>/Cd System. *Miner. Metall. Process.* **2005**, *22* (4), 192.
43. Li, S. X.; Vaden, D.; Westphal, B. R.; Frederickson, G. L.; Benedict, R. W.; Johnson, T. A. Integrated efficiency test for pyrochemical fuel cycles. *Nucl. Technol.* **2009**, *166*, 180-186.
44. Simpson, M. F.; Sachdev, P. Development of electrorefiner waste salt disposal process for the EBR-II spent fuel treatment project. *Nucl. Eng. Technol.* **2008**, *40* (3), 175-181.
45. Tylka, M. M.; Willit, J. L.; Williamson, M. A. Application of Voltammetry for Quantitative Analysis of Actinides in Molten Salts. *J. Electrochem. Soc.* **2015**, *162* (12), H852-H859.

46. Yang, Y.; Zhang, M.; Han, W.; Sun, P.; Liu, B.; Jiang, H.; Jiang, T.; Peng, S.; Li, M.; Ye, K.; Yan, Y. Selective Electrodeposition of Dysprosium in LiCl-KCl-GdCl<sub>3</sub>-DyCl<sub>3</sub> Melts at Magnesium Electrodes: Application to Separation of Nuclear Wastes. *Electrochim. Acta* **2014**, *118*, 150-156.
47. Cai, Y.; Liu, H.; Xu, Q.; Song, Q.; Xu, L. Investigation on the Reaction Progress of Zirconium and Cuprous Chloride in the LiCl-KCl Melt. *Electrochim. Acta* **2015**, *161*, 177-185.
48. Gese, N.; Serrano, B. Idaho National Laboratory, Idaho Falls, ID. U.S. DOE MPACT meeting presentation, Oak Ridge, TN, March 25, 2015.
49. Gese, N. J.; Jue, J. F.; Serrano, B. E.; Fredrickson, G. L. Potentiometric Sensor for Real-Time Remote Surveillance of Actinides in Molten Salts. *Proc. Inst. Nucl. Mater. Manage. 53rd Annu. Meet.*, Orlando, FL, July 15-19, 2012; Institute of Nuclear Material Management: Oakbrook Terrace, IL, 2012.
50. Tang, H.; Yan, Y.-D.; Zhang, M.-L.; Xue, Y.; Zhang, Z.-J.; Du, W.-C.; He, H. Electrochemistry of MgCl<sub>2</sub> in LiCl-KCl Eutectic Melts. *Acta Phys.-Chim. Sinica* **2013**, *29* (8), 1698-1704.
51. Shukla, A. K.; Kumar, T. P. Pillars of Modern Electrochemistry. *Electrochem. Soc. Interface* **2008**, *17* (3), 31-39.
52. Bard, A. J.; Faulkner, L. R. *Electrochemical Methods: Fundamentals and Applications*, 2nd ed.; John Wiley & Sons, Inc.: New York, 2001.
53. IUPAC. *IUPAC Compendium of Chemical Terminology (Gold Book)* [Online]; 2nd ed.; IUPAC: Research Triangle Park, NC, 2014; <http://goldbook.iupac.org> (accessed October 3, 2015).
54. Popov, K. I.; Keca, D. N.; Vidojkovic, S. I.; Lazarevic, B. J.; Milojkovic, V. B. Mathematical Model and Digital Simulation of Pulsating Overpotential Copper Electrodeposition. *J. Appl. Electrochem.* **1976**, *6* (4), 365-370.
55. Avaca, L. A.; Kaufmann, S.; Kontturi, K.; Murtoimaki, L.; Schiffrin, D. J. Theory of Cyclic Voltammetry for Quasi-Reversible Electrodeposition Reactions with Insoluble Products. *Ber. Bunsen Ges. Phys. Chem.* **1993**, *97* (1), 70-76.
56. Park, B.-G. A Time-Dependent Simulation of Molten Salt Electrolysis for Nuclear Wastes Transmutation. Ph.D. Dissertation, Seoul National University, Seoul, South Korea, 1999.
57. Laitinen, H. A.; Roe, D. K. Exchange Current Density in KCl-LiCl Eutectic Melt. *J. Electrochem. Soc.* **1960**, *107* (6), 546-555.

58. Lantelme, F.; Berghoute, Y. Electrochemistry Studies of  $\text{LaCl}_3$  and  $\text{GdCl}_3$  Dissolved in Fused  $\text{LiCl-KCl}$ . *J. Electrochem. Soc.* **1999**, *146* (11), 4137-4144.
59. Reddy, B. P.; Vandarkuzhali, S.; Subramanian, T.; Venkatesh, P. Electrochemical Studies on the Redox Mechanism of Uranium Chloride in Molten  $\text{LiCl-KCl}$  Eutectic. *Electochim. Acta* **2004**, *49* (15), 2471-2478.
60. Van Artsdalen, E. R.; Yaffe, I. S. Electrical Conductance and Density of Molten Salt Systems:  $\text{KCl-LiCl}$ ,  $\text{KCl-NaCl}$  and  $\text{KCl-KI}$ . *J. Phys. Chem.* **1955**, *59* (2), 118-127.
61. Matsuda, H.; Ayabe, Y. Zur Theorie der Randles-Sevcikschen Kathodenstrahl-Polarographie. *Z. Elektrochem.* **1955**, *59* (6), 494-503.
62. Nicholson, R. S.; Shain, I. Theory of Stationary Electrode Polarography. *Anal. Chem.* **1964**, *36* (4), 706-723.
63. Randles, J. E. B. A Cathode Ray Polarograph. Part II—The Current-Voltage Curves. *Trans. Faraday Soc.* **1948**, *44*, 327-338.
64. Berzins, T.; Delahay, P. Oscillographic Polarographic Waves for the Reversible Deposition of Metals on Solid Electrodes. *J. Am. Chem. Soc.* **1953**, *75* (3), 555-559.
65. Delahay, P. Theory of Irreversible Waves in Oscillographic Polarography. *J. Am. Chem. Soc.* **1953**, *75* (5), 1190-1196.
66. Masset, P.; Bottomley, D.; Konings, R.; Malmbeck, R.; Rodrigues, A.; Serp, J.; Glatz, J.-P. Electrochemistry of Uranium in Molten  $\text{LiCl-KCl}$  Eutectic. *J. Electrochem. Soc.* **2005**, *152* (6), A1109-A1115.
67. Kuznetsov, S. A.; Hayashi, H.; Minato, K.; Gaune-Escard, M. Electrochemical Behavior and Some Thermodynamic Properties of  $\text{UCl}_4$  and  $\text{UCl}_3$  Dissolved in a  $\text{LiCl-KCl}$  Eutectic Melt. *J. Electrochem. Soc.* **2005**, *152* (4), C203-C212.
68. Marsden, K. C.; Pesic, B. Evaluation of the Electrochemical Behavior of  $\text{CeCl}_3$  in Molten  $\text{LiCl-KCl}$  Eutectic Utilizing Metallic Ce as an Anode. *J. Electrochem. Soc.* **2011**, *158* (6), F111-F120.
69. Yang, L.; Hudson, R. G. Some Investigations of the  $\text{Ag/AgCl}$  in  $\text{LiCl-KCl}$  Eutectic Reference Electrode. *J. Electrochem. Soc.* **1959**, *106* (11), 986-990.
70. Shirai, O.; Nagai, T.; Uehara, A.; Yamana, H. Electrochemical Properties of the  $\text{Ag}^+|\text{Ag}$  and Other Reference Electrodes in the  $\text{LiCl-KCl}$  Eutectic Melts. *J. Alloys Compd.* **2008**, *456*, 498-502.
71. Caravaca, C.; de Cordoba, G.; Tomas, M. J.; Rosado, M. Electrochemical Behavior



- of Gadolinium Ion in Molten LiCl-KCl Eutectic. *J. Nucl. Mater.* **2007**, *360* (1), 25-31.
72. Rutherford, E. Forty Years of Physics. In *Background to Modern Science*; University Press: Cambridge, 1938.
73. Willit, J. L.; Miller, W. E.; Battles, J. E. Electrorefining of Uranium and Plutonium—A Literature Review. *J. Nucl. Mater.* **1992**, *195*, 229-249.
74. Cassayre, L.; Serp, J.; Soucek, P.; Malmbeck, R.; Rebizant, J.; Glatz, J.-P. Electrochemistry of Thorium in LiCl-KCl Eutectic Melts. *Electrochim. Acta* **2007**, *52* (26), 7432-7437.
75. Chiotti, P.; Jha, M. C.; Tschetter, M. J. Reaction of Thorium and ThCl<sub>4</sub> with UO<sub>2</sub> and (Th, U)O<sub>2</sub> in Fused Chloride Salts. *J. Less-Common Met.* **1975**, *42* (2), 141-161.
76. *HSC Chemistry*, version 7.10; Outotec Research: Finland, 2009.
77. Castrillejo, Y.; Bermejo, M. R.; Barrado, E.; Martinez, A. M.; Arocas, P. D. Solubilization of Rare Earth Oxides in the Eutectic LiCl-KCl Mixture at 450°C and in the Equimolar CaCl<sub>2</sub>-NaCl Melt at 550°C. *J. Electroanal. Chem.* **2003**, *545*, 141-157.
78. Hayashi, H.; Minato, K. Stability of Lanthanide Oxides in LiCl-KCl Eutectic Melt. *J. Phys. Chem. Solids* **2005**, *66* (2-4), 422-426.
79. Shishalov, V. I.; Kovalevski, A. V. The Properties of the Surface of Molten Mixtures of the LiCl-KCl Eutectic with Praseodymium, Samarium, Erbium, and Ytterbium. *Russ. J. Phys. Chem. A* **2011**, *85* (1), 108-111.
80. James, D. F. The Meniscus on the Outside of a Small Circular Cylinder. *J. Fluid Mech.* **1974**, *63* (4), 657-664.
81. Gabriel, J. C.; Vincent, D.; Bouteillon, J.; Poinet, J. C.; Volkovich, V. A.; Griffiths, T. R. Molybdenum Chemistry in Molten LiCl-KCl Eutectic: An Electrochemical and Adsorption Spectroscopy Study of the Concentration Dependent Stability of Solutions of K<sub>3</sub>MoCl<sub>6</sub>. *Electrochim. Acta* **1999**, *44*, 4619-4629.
82. Metropolis, N. The Beginning of the Monte Carlo Method. *Los Alamos Sci.* **1987**, *15*, 125-130.
83. Serge, E. *From X-Rays to Quarks: Modern Physicists and Their Discoveries*; W. H. Freeman: San Francisco, 1980.
84. Ackerman, J. P. Chemical Basis for Pyrochemical Reprocessing of Nuclear Fuel.

- Ind. Eng. Chem. Res.* **1991**, *30* (1), 141-145.
85. Kobayashi, T.; Tokiwai, M. Development of TRAIL, a simulation code for the molten salt electrorefining of spent nuclear fuel. *J. Alloys Compd.* **1993**, *197*, 7-16.
  86. Ahluwalia, R.; Hua, T. Q.; Geyer, H. K. Behavior of Uranium and Zirconium in Direct Transport Tests with Irradiated EBR-II Fuel. *Nucl. Technol.* **1999**, *126*, 289-302.
  87. Cumberland, R.; Yim, M.-S. Development of a 1D Transient Electrorefiner Model for Pyroprocess Simulation. *Ann. Nucl. Energy* **2013**, *71*, 52-59.
  88. Cumberland, R. 1D and 3D Simulation of Electrochemical Behavior of U/UCl<sub>3</sub> and Pu/PuCl<sub>3</sub> in Molten Salt Systems. M.S. Thesis, Korean Advanced Institute of Science and Technology, Daejeon, South Korea, 2013.
  89. Rappleye, D.; Simpson, M.; Cumberland, R.; McNelis, D.; Yim, M.-S. Simulated Real-Time Process Monitoring of a Molten Salt Electrorefiner. *Nucl. Eng. Des.* **2014**, *273*, 75-84.
  90. Cumberland, R.; Yim, M. S. A Computational Meta-Analysis of UCl<sub>3</sub> Cyclic Voltammograms in LiCl-KCl Electrolyte. *J. Electrochem. Soc.* **2014**, *161* (4), D147-D149.
  91. Koyama, T.; Kinoshita, K.; Inoue, T.; Ougier, M.; Malmbeck, R.; Glatz, J.-P.; Koch, L. Study of Molten Salt Electrorefining of U-Pu-Zr Alloy Fuel. *J. Nucl. Sci. Technol.* **2002**, *39* (Suppl. 3), 765-768.
  92. Iizuka, M.; Kinoshita, K.; Koyama, T. Modeling of Anodic Dissolution of U-Pu-Zr Ternary Alloy in the Molten LiCl-KCl Electrolyte. *J. Phys. Chem. Solids* **2005**, *66*, 427-432.
  93. Peterson, D. E.; Foltyn, E. M. The Pu-U (Plutonium-Uranium) System. *Bull. Alloy Phase Diagrams* **1989**, *10* (2), 160-164.
  94. Peterson, D. E. The Th-U (Thorium-Uranium) System. *Bull. Alloy Phase Diagrams* **1985**, *6* (5), 443-445.
  95. Rough, F. A.; Bauer, A. A. *Constitution of Uranium and Thorium Alloys*; Technical Report for Battle Memorial Institute: Columbus, OH, June 1958.
  96. Palys, M.; Kobra, T.; Bos, M.; Van Der Linden, W. E. The Separation of Overlapping Peaks in Cyclic Voltammetry by Means of Semi-Differential Transformation. *Talanta* **1991**, *38* (7), 723-733.

97. Rappleye, D. S.; Stika, M.; Simpson, M. F. Simulated Response of Electrochemical Sensors for Monitoring Molten-Salt Fueled Reactors. *Proc. Inst. Nucl. Mater. Manage. 55th Annu. Meet.*, Atlanta, GA, July 20-24, 2014; Institute of Nuclear Material Management: Oakbrook Terrace, IL, 2014.
98. Keithley, R. B.; Heien, M. L.; Wightman, R. M. Multivariate Concentration Determination using Principal Component Regression with Residual Analysis. *TrAC, Trends Anal. Chem.* **2009**, *28* (9), 1127-1136.
99. Kramer, R. *Chemometric Techniques for Quantitative Analysis*; Marcel Dekker, Inc.: New York, 1998.
100. SourceForge. <http://plotdigitizer.sourceforge.net> (accessed March 3, 2014).
101. *Matlab R2013a*; Mathworks Inc.: Natick, MA, 2013.
102. Montgomery, D. C.; Runger, G. C.; Hubele, N. F. Chapter 6: Building Empirical Models. In *Engineering Statistics*, 3rd ed.; John Wiley & Sons, Inc.: Hoboken, NJ, 2006.
103. Transatomic Power. *Technical White Paper*; version 1.0.1, Transatomic Power: Cambridge, MA, 2014. [http://transatomicpower.com/white\\_papers/TAP\\_White\\_Paper.pdf](http://transatomicpower.com/white_papers/TAP_White_Paper.pdf) (accessed April 14, 2014).
104. Ignatiev, V.; Feynberg, O.; Gnidoi, I.; Merzlyakov, A.; Smirnov, V.; Surenkov, A.; Tretiakov, I.; Zakirov, R. Progress in Development of Li,Be,Na/F Molten Salt Actinide Recycler & Transmuter Concept. *Proc. Int. Congr. Adv. Nucl. Power Plants*, Nice, May 13-18, 2007; Curran Associates Inc: Red Hook, NY, 2008.
105. Merle-Lucotte, E.; Heuer, D.; Allibert, M.; Ghetta, V.; Le Brun, C.; Brissot, R.; Liatard, E.; Mathieu, L. The Thorium Molten Salt Reactor: Launching the Thorium Cycle While Closing the Current Fuel Cycle. *Proc. Eur. Nucl. Conf.*, Brussels, Sept 16-20, 2007.
106. Endicott, N. Thorium-Fuelled Molten Salt Reactors, 2013. The Weinberg Foundation. <http://www.the-weinberg-foundation.org/wp-content/uploads/2013/06/Thorium-Fuelled-Molten-Salt-Reactors-Weinberg-Foundation.pdf> (accessed April 18, 2014).
107. Griffiths, T.; Tomlinson, J.; O'Sullivan R. *MSR Review: Feasibility of Developing a Pilot Scale Molten Salt Reactor in the UK*; Energy Process Developments Ltd.: London, 2015.
108. Bettis, E. S.; Robertson, R. C. The Design and Performance Features of a Single-Fluid Molten-Salt Breeder Reactor. *Nucl. Appl. Tech.* **1970**, *8*, 190-207.

109. Carter, W. L.; Nicholson, E. L. *Design and Cost Study of a Fluorination--Reductive Extraction--Metal Transfer Processing Plant for the MSBR*; ORNL-TM-3579; Oak Ridge National Laboratory: Oak Ridge, 1972.
110. Masset, P.; Konings, R.; Malmbeck, R.; Serp, J.; Glatz, J.-P. Thermochemical Properties of Lanthanides (Ln = La, Nd) and Actinides (An = U, Np, Pu, Am) in the Molten LiCl-KCl Eutectic. *J. Nucl. Mater.* **2005**, *344*, 173-179.
111. Morss, L. R.; Edelstein, N. M.; Fuger, J. *The Chemistry of the Actinide and Transactinide Elements*; Springer: Dordrecht, Netherlands, 2006; Vol. 4.
112. Clayton, F. R.; Mamantov, G.; Manning D. L. Electrochemical Studies of Uranium and Thorium in Molten LiF-NaF-KF at 500° C. *J. Electrochem. Soc.* **1974**, *121* (1), 86-90.
113. Stika, M.; Rappleye, D.; Jeong, S.-M.; Simpson, M. F. Development of On-line Pyroprocessing for Liquid Thorium Fueled Reactors. *AIChE J.* **2016**, *62* (4), 1236-1243.
114. Curie, I.; Savitch, P. Concerning the Nature of the Radioactive Element with 3.5-Hour Half-Life, Formed from Uranium Irradiated by Neutrons. *Comptes Rendus* **1938**, *206*, 1643.
115. Graetzer, H. G.; Anderson, D. L. *The Discovery of Nuclear Fission: A Documentary History*; Van Norstrand Reihhold Company: New York, 1971.
116. Iizuka, M. Diffusion Coefficients of Cerium and Gadolinium in Molten LiCl-KCl. *J. Electrochem. Soc.* **1998**, *145* (1), 84-88.
117. Bermejo, M. R.; Gomez, J.; Medina, J.; Martinez, A. M.; Castrillejo, Y. The Electrochemistry of Gadolinium in the Eutectic LiCl-KCl on W and Al electrodes. *J. Electroanal. Chem.* **2006**, *588*, 253-266.
118. Tang, H.; Pesic, B. Electrochemistry and Electrocrystallization of Gadolinium on Mo Substrate in LiCl-KCl Eutectic Salts. *J. Electrochem. Soc.* **2014**, *161* (9), D429-D436.
119. Castrillejo, Y.; Bermejo, M. R.; Martinez, A. M.; Arocas, P. D. Electrochemical Behavior of Lanthanum and Yttrium Ions in Two Molten Chlorides with Difference Oxoacidic Properties: the Eutectic LiCl-KCl and the Equimolar Mixture CaCl<sub>2</sub>-NaCl. *J. Min. Met.* **2003**, *39* (1-2), 109-135.
120. Vandarkuzhali, S.; Gogoi, N.; Ghosh, S.; Reddy, B. P.; Nagarajan, K. Electrochemical Behavior of LaCl<sub>3</sub> at Tungsten and Aluminium Cathodes in LiCl-KCl Eutectic Melt. *Electrochim. Acta* **2012**, *59*, 245-255.

121. Tang, H.; Pesic, B. Electrochemical Behavior of LaCl<sub>3</sub> and Morphology of La Deposit on Molybdenum Substrate in Molten LiCl-KCl Eutectic Salt. *Electrochim. Acta* **2014**, *119*, 120-130.
122. Wang, Z.; Rappleye, D.; Simpson, M. F. Voltammetric Analysis of Mixtures of Molten Eutectic LiCl-KCl Containing LaCl<sub>3</sub> and ThCl<sub>4</sub> for Concentration and Diffusion Coefficient Measurement. *Electrochim. Acta* **2016**, *191*, 29-43.
123. Gschneider, K. A.; Calderwood, F. W. The Gd-La (Gadolinium-Lanthanum) system. *Bull. Alloy Phase Diagrams* **1982**, *2* (4), 448-451.
124. Wojdyr, M. Fityk: A General-Purpose Peak Fitting Program. *J. Appl. Cryst.* **2010**, *43*, 1126-1128.
125. Gao, F.; Wang, C.; Liu, L.; Guo, J.; Chang, S.; Chang, L.; Li, R.; Ouyang, Y. Electrode Process of La(III) in Molten LiCl-KCl. *J. Rare Earths* **2009**, *27* (6), 986-990.
126. Dalrymple-Alford, P.; Goto, M.; Oldham, K. B. Peak Shapes in Semidifferential Electroanalysis. *Anal. Chem.* **1977**, *49* (9), 1390-1394.
127. Fontani, M.; Costa, M.; Orna, M. V. *Lost Elements: The Periodic Table's Shadow Side*; Oxford University Press: New York, 2014.
128. Okamoto, H. La-Th (Lanthanum-Thorium). In *Binary Alloy Phase Diagrams*, 2nd ed.; Massalski, T. B., Ed.; ASM International: Materials Park, OH, 1990; Vol. III.
129. Hahn, O.; Strassmann, F. Concerning the Existence of Alkaline Earth Metals Resulting from Neutron Irradiation of Uranium. *Naturwiss.* **1939**, *27*, 11.
130. Shirai, O.; Iwai, T.; Suzuki, Y.; Sakamura, Y.; Tanaka, H. Electrochemical Behavior of Actinide Ions in LiCl-KCl Eutectic Melts. *J. Alloys Compd.* **1998**, *271-273*, 685-688.
131. Gao, F.; Wang, C.; Guo, J.; Chang, S.; Chang, L.; Ouyang, Y. Electrode Processes of Uranium Ions and Electrodeposition of Uranium in Molten LiCl-KCl. *J. Radioanal. Nucl. Chem.* **2009**, *280* (1), 207-218.
132. Tylka, M. M.; Willit, J. L.; Prakash, J.; Williamson, M. A. Method Development for Quantitative Analysis of Actinides in Molten Salts. *J. Electrochem. Soc.* **2015**, *162* (9), H625-H633.
133. Store, T.; Haarberg, G. M.; Tunold, R. Determination of Diffusion Coefficients of Depositing Ions in Molten Chlorides by Transient Electrochemical Techniques. *J. Appl. Electrochem.* **2000**, *30*, 1351-1360.

134. Martinez, A. M.; Borresen, B.; Haarberg, G. M.; Castrillejo, Y.; Tunold, R. Electrodeposition of Magnesium from the Eutectic LiCl-KCl Melt. *J. Appl. Electrochem.* **2004**, *34*, 1271-1278.
135. Nayeb-Hashemi, A. A.; Clark, J. B. Mg-U (Magnesium-Uranium). In *ASM Alloy Phase Diagrams Database*; Villars, P., Okamoto, H., Cenzual, K., Eds.; ASM International: Material Park, OH, 2006.
136. Rappleye, D. Developing Safeguards for Pyroprocessing: Detection of a Plutonium Co-deposition on Solid Cathode in an Electrorefiner by Applying the Signature-Based Safeguards Approach. M.S. Thesis, North Carolina State University, Raleigh, 2013.
137. Eisenberg, M.; Tobias, C. W.; Wilke, C. R. Ionic Mass Transfer and Concentration Polarization at Rotating Electrodes. *J. Electrochem. Soc.* **1954**, *101* (6), 306-320.
138. Kinoshita, K.; Inoue, T.; Fusselman, S. P.; Grimmitt, D. L.; Krueger, C. L.; Storvick, T. S. Electrodeposition of Uranium and Transuranic Elements onto Solid Cathode in LiCl-KCl/Cd System for Pyrometallurgical Partitioning. *J. Nucl. Sci. Technol.* **2003**, *40* (7), 524-530.
139. Choi, S.; Park, J.; Kim, K. R.; Jung, H.; Hwang, I.; Park, B.; Yi, K.; Lee, H. S.; Ahn, D.; Paek, S. Three-Dimensional Multispecies Current Density Simulation of Molten-Salt Electrorefining. *J. Alloys Compd.* **2010**, *503* (1), 177-185.
140. Lee, J. H.; Oh, K. H.; Kang, Y. H.; Hwang, S. C.; Lee, H. S.; Shim, J. B.; Kim, E. H.; Park, S. W. Assessment of a High-Throughput Electrorefining Concept for a Spent Metallic Nuclear Fuel-II: Electrohydrodynamic Analysis and Validation. *Nucl. Technol.* **2009**, *165* (3), 370-379.
141. Phillips, J. R.; Gale, R. J.; Wier, R. G.; Osteryoung, R. A. Glassy Carbon Rotating Ring-Disc Electrode for Molten Salt Studies. *Anal. Chem.* **1976**, *48* (8), 1266-1268.
142. Kim, J. Y.; Bae, S. E.; Kim, D. H.; Choi, Y. S.; Yeon, J. W.; Song, K. High-Temperature Viscosity Measurement of LiCl-KCl Molten Salts Comprising Actinides and Lanthanides. *Bull. Korean Chem. Soc.* **2012**, *33* (11), 3871-3874.
143. Zhang, C. Density Measurements in Ternary Molten Salts. University of Utah: Salt Lake City, UT. Unpublished work, 2015.
144. Rappleye, D.; Jeong, S.-M.; Simpson, M. Application of multivariate analysis techniques to safeguards of the electrochemical treatment of used nuclear fuel. *Ann. Nucl. Energy* **2015**, *77*, 265-272.